SANDIA REPORT

SAND2000-0091
Unlimited Release
Printed January 2000

MEMS Reliability: Infrastructure, Test Structures, Experiments, and Failure Modes

Danelle M. Tanner, Norman F. Smith, Lloyd W. Irwin, William P. Eaton,
Karen S. Helgesen, J. Joseph Clement, William M. Miller, Jeremy A. Walraven,
Kenneth A. Peterson, Paiboon Tangyunyong, Michael T. Dugger, and Samuel L. Miller

Prepared by
Sandia National Laboratories
Albuquerque, New Mexico 87185 and Livermore, California 94550

Sandia is a multiprogram laboratory operated by Sandia Corporation,
a Lockheed Martin Company, for the United States Department of
Energy under Contract DE-AC04-94AL85000.

Sandia National Laboratories

Issued by Sandia National Laboratories, operated for the United States Department of Energy by Sandia Corporation.

Available to DOE and DOE contractors from
Office of Scientific and Technical Information
P.O. Box 62
Oak Ridge, TN 37831

Prices available from (703) 605-6000
Web site: http://www.ntis.gov/ordering.htm

Available to the public from
National Technical Information Service
U.S. Department of Commerce
5285 Port Royal Rd
Springfield, VA 22161

DISCLAIMER

Portions of this document may be illegible in electronic image products. Images are produced from the best available original document.

1.5 Single package environmental test cell

A small chamber was constructed in order to permit quantitative friction measurements in controlled environments at atmospheric pressure. The device houses a single 24-pin DIP, and uses high vacuum materials and fittings to provide a clean, leak-free environment. A wide variety of gas compositions can be flowed through the chamber, and sensors allow oxygen and water vapor to be measured in the part per million range.

Cell Construction

A photograph of the environmental cell is shown in Figure 1.5.1. The body and lid of the cell are constructed from 6061 aluminum. A 10-pin electrical feed-through (toward the front in Figure 1.5.1) on a 3.38 cm diameter metal-sealed vacuum flange provides signals to the 24-pin zero insertion force socket at the center of the cell. The DIP socket is positioned so that a module mounted inside the package will sit near the

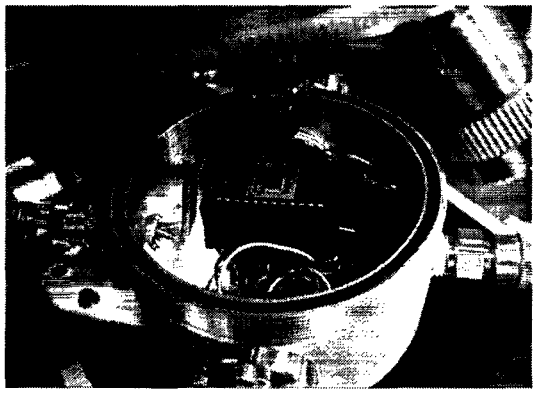

Figure 1.5.1. Photograph of the environmental cell with lid removed to show the package and connections inside.

center of the cell, and close to the lid. The number of devices that may be run depends upon the number of signal lines required per device. For example, each friction test structure requires 5 signal lines to operate, so two devices may be run simultaneously with different drive signals within this device. Input and output gas connections are 0.25-inch Swagelock fittings and either stainless steel or perfluoroalkoxy tubing.

A picture of the environmental cell with the lid attached is shown in Figure 1.5.2. A sapphire window 1.78 cm in diameter in the lid allows the structures to be viewed with a microscope while they are running in the controlled environment. The free volume of the environmental cell is 250 cm^3.

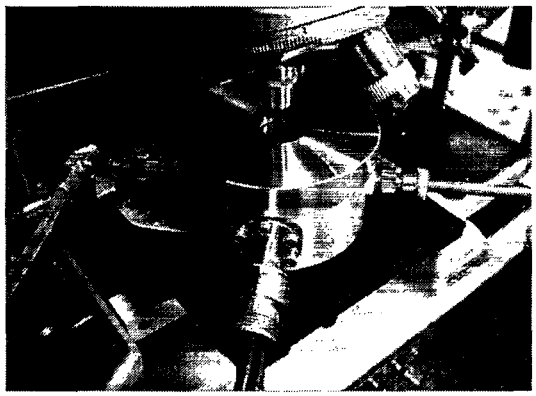

Figure 1.5.2. Photograph of the environmental cell with lid removed to show the package and connections inside.

Gas Handling and Sensors

For controlled environment experiments, gas was run first through a drying/humidifying manifold and then was provided to the input port of the cell from cylinders of ultra pure compressed gas at a supply pressure of 10 psig. This manifold contained separate columns of desiccant and deionized water. The amount of gas from the cylinder that went to the desiccant or deionized water was controlled with flow meters. Adjusting the flow rate of supply gas to the desiccant column and deionized water column allowed introduction of water vapor to the gas stream in a controlled way. The exhaust line of the cell was connected to a chilled mirror dew point monitor (General Eastern Hygro M4/D-2 sensor) and an electrochemical oxygen analyzer (Delta-F,

model FA31111XA) in series. Under ambient conditions of 12.5 psia and 25°C, water vapor sensitivity was 222±5 ppmv (0.6±0.1 %RH). Under the same conditions, oxygen concentration sensitivity was 2±0.5 ppmv.

Performance Characteristics

At a gas supply pressure of 10 psig, the volume flow rate through the environmental cell is 400 cm^3/min. Purging the gas cell for 15 minutes with dry nitrogen resulted in a water vapor concentration of 430 ppmv (1.2% RH) and an oxygen concentration of 30 ppmv. Purging for longer times could further reduce the water and oxygen concentration.

Conclusions

The single package environmental test cell permits testing of devices within a single package in controlled environments at atmospheric pressure. The detection limits for water vapor and oxygen permit control of these species to help determine mechanisms for wear in micromachines that are related to reactions with the environment.

SAND2000-0091
Unlimited Release
Printed January 2000

MEMS Reliability: Infrastructure, Test Structures, Experiments, and Failure Modes

Summary of work for LDRD: Integrated Approach to Develop MEMS Reliability Tools

Danelle M. Tanner, Norman F. Smith, Lloyd W. Irwin,
William P. Eaton, Karen S. Helgesen, J. Joseph Clement, and William M. Miller
Reliability Physics

Jeremy A. Walraven, Kenneth A. Peterson, Paiboon Tangyunyong
Failure Analysis

Michael T. Dugger
Materials Aging and Reliability of Interfaces

Samuel L. Miller
Intelligent Micromachines

Sandia National Laboratories
P.O. Box 5800
Albuquerque, NM 87185-1081

Abstract

The burgeoning new technology of Micro-Electro-Mechanical Systems (MEMS) shows great promise in the weapons arena. We can now conceive of micro-gyros, micro-surety systems, and micro-navigators that are extremely small and inexpensive. Do we want to use this new technology in critical applications such as nuclear weapons? This question drove us to understand the reliability and failure mechanisms of silicon surface-micromachined MEMS.

Development of a testing infrastructure was a crucial step to perform reliability experiments on MEMS devices and will be reported here. In addition, reliability test structures have been designed and characterized. Many experiments were performed to investigate failure modes and specifically those in different environments (humidity, temperature, shock, vibration, and storage). A predictive reliability model for wear of rubbing surfaces in microengines was developed. The root causes of failure for operating and non-operating MEMS are discussed. The major failure mechanism for operating MEMS was wear of the polysilicon rubbing surfaces. Reliability design rules for future MEMS devices are established.

Intentionally Left Blank

Acknowledgements

The authors thank the personnel of the Microelectronics Development Lab (MDL) for fabricating, releasing and packaging the devices used in these tests. In particular, we thank Peggy Clews and Sasha Summers for releasing over a thousand die and we thank Cathy Reber's team for packaging them. Steve Rodgers, Jim Allen, and Maarten de Boer have been extremely supportive and helpful throughout this project. We thank Chad O'Neal for his work on the storage life experiment during the summer of '99. We acknowledge Duane Bowman's work during the first year of the project. Special thanks for failure analysis work go to Tom Headley, Alex Pimentel, Ann Campbell, Paiboon Tangyunyong, and Dan Barton. We also appreciate Michael Callahan for funding the MEMS effort and Paul McWhorter for leading the creation of this technology at SNL.

Contents

Figures

Tables

Preface

Our team was involved in a three year LDRD investigation of MEMS reliability. The overall goals of this work were a) to perform statistical reliability characterization of MEMS devices, b) to identify failure modes, c) to develop reliability test structures, d) to develop predictive reliability models and e) to develop failure analysis techniques for MEMS.

A graphic representation of our approach is shown in Figure P.1. In order to identify the failure modes, we looked at statistically significant numbers of devices. We also designed test structures sensitive to certain aspects of failure. When we understood the failures from a physics perspective we can develop predictive reliability models. Performing all four functions in the large dashed box put us in a position to qualify MEMS for crucial applications.

This report will document all of the significant findings made during the investigation. Specifically, Chapter 1 will describe our creation of the infrastructure necessary to run reliability experiments. All of the test structures that we designed will be described in Chapter 2. Chapter 3 will document all of the reliability experiments performed in the three-year period. And finally, Chapter 4 will pull together all our findings, ordered according to failure mode or mechanism. Design rules for avoiding pitfalls will also be covered in this section.

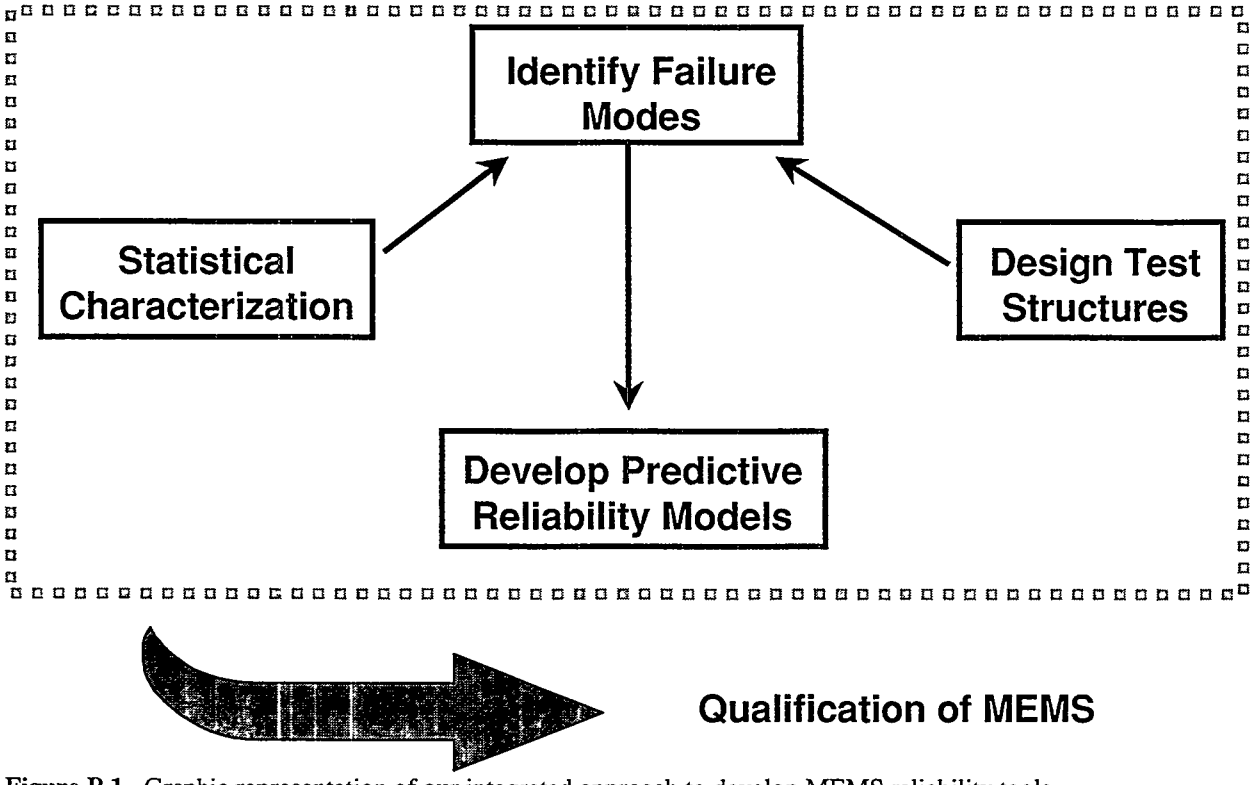

Figure P.1. Graphic representation of our integrated approach to develop MEMS reliability tools

Chapter 1. MEMS Testing Infrastructure

1.1 Introduction
1.2 SHiMMeR
1.3 SHiMMeR Lite
1.4 Environmental storage chambers
1.5 Single package environmental test cell
1.6 Super μDriver
1.7 Characterization Techniques
1.8 Image Analysis
1.9 Failure Analysis Techniques

Intentionally Left Blank

1.1 Introduction

This section will document the development of equipment and techniques for reliability testing of MEMS devices. Sections 1.2 to 1.5 describe the hardware developed for our tests. Included are our 'parallel testing' capability (SHiMMeR – section 1.2) and its smaller version (SHiMMeR Lite – section 1.3). We developed environmental chambers for storage (section 1.4) and testing (section 1.5)

In addition, software was developed to run (Super μDriver – section 1.6) MEMS devices. Characterization, including measurement of resonant frequency, is important and the techniques developed are documented in section 1.7. The ability to monitor degradation in microengines was developed and is described in section 1.8 (Image Analysis).

An understanding of failures is crucial to developing reliable MEMS devices and the final section 1.9 describes the techniques pursued.

1.2 SHiMMeR

The ability to acquire reliability data on a statistically significant number of devices was extremely important in the development of this LDRD. Lifetime studies of MEMS devices can be performed serially but this is a time consuming and very labor intensive operation. A method to test multiple devices simultaneously was needed.

A first generation multi-part MEMS test station was created before this LDRD was started. The original system is shown in Figure 1.2.1. This system consisted of a custom test fixture to hold the devices and a biological-type microscope. This system suffered from many shortcomings. Focus changed as the operator removed their hands from the microscope. Quality images were almost impossible to acquire due to non-coaxial lighting and room vibrations were amplified through the cantilevered arm of the microscope. A greatly improved system was needed. This system became known as SHiMMeR (Sandia High Volume Measurement of Micromachine Reliability) [1].

SHiMMeR was created to address the shortcomings of the original system and to create a multi-part test system that could adequately address the need of flexibility of MEMS device types and ease of use.

The SHiMMeR system was designed and built to provide electrical drive signals to large numbers of packaged microactuators and to optically inspect them for functionality. SHiMMeR is subdivided into the electrical subsystem, which provides customized electrical signals to the packaged parts, and the optical subsystem, in which a microscope and camera are stepped from part to part to inspect functionality. The optical system for SHiMMeR consists of two major components; an X-Y gantry table, and a video microscope (Figure 1.2.2).

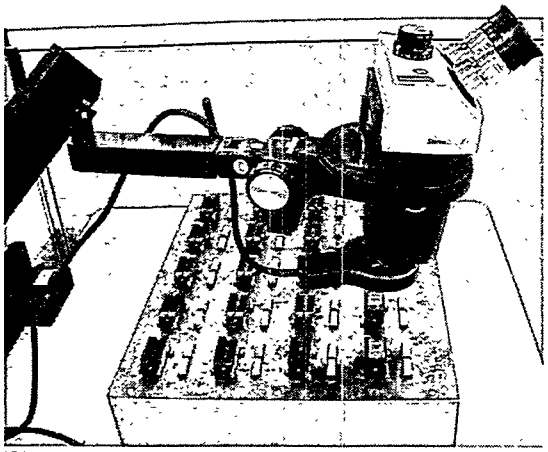

Figure 1.2.1. Original multi-device MEMS test system using biological-type microscope.

The X-Y gantry table used to build the SHiMMeR system is a Techno Isel Gantry System III table with a travel of 500 x 540 mm, a table size of 850 x 750 mm, and a 200 mm clearance under the Z axis. This table has a repeatability of 10 μm and can support a payload of 22.7 kg on the Y axis. The axes are driven by Parker Compumotor Indexers that provide a resolution of 1.25 μm, when used with the standard 5mm pitch ball screw on the table. The overall accuracy of the table is ±0.1 mm over 300 mm. A high accuracy table was not required for this application because MEMS devices have considerable variation when mounted inside packages and the test fixture mounting also varies somewhat. These variations prevent exact determination of where the part is located within the travel of the gantry table, thus negating the requirement for accurate linear distance moves. Currently the operator of the SHiMMeR system is required to

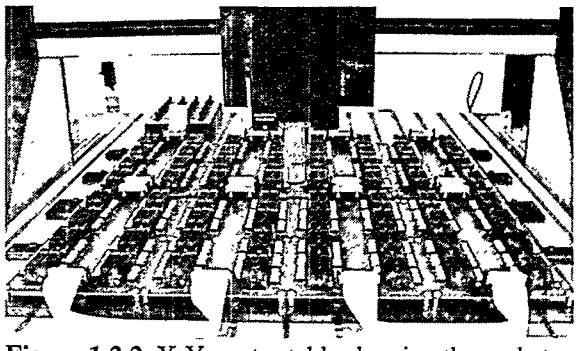

Figure 1.2.2. X-Y gantry table showing the socket arrangement and video microscope on SHiMMeR.

manually teach the system the location of each MEMS device being characterized prior to the start of a test.

The video microscope used in SHiMMeR is a 9x A-Zoom microscope from Ready Products Corporation. This microscope has many features that made it very useful in our system. It uses a single lens for its entire magnification range. In our configuration with a 20x long working distance objective, the magnification is continuously variable from 250x to 1800x with a field of view ranging from 1.1 mm to 150 μm. This allows the SHiMMeR system to look at a wide variety of MEMS devices without the operator having to change primary objectives, thus eliminating the possibility that a turret full of lenses would collide with other parts of the system. The microscope is equipped with motorized focus controls and illumination is provided through a 150W fiber optic light source and/or a stroboscopic light source. All aspects of the microscope can be controlled from a personal computer via an RS-232 port. A high-resolution black and white CCD camera is used for acquisition of the image.

The stimulus or stressing system is made up of several components: waveform synthesis, waveform amplification, and waveform distribution, all coupled to the MEMS device fixtures. Waveforms for driving the MEMS devices are created using four 20 MHz arbitrary waveform generators from Pragmatic Instruments. All four channels are phase-locked together and use a common clock. The custom model-based waveforms are downloaded via IEEE-488.2 bus to the waveform generators. These waveform generators allow multiple waveforms to be sequenced together to generate acceleration and deceleration profiles required for high speed operation of the SNL microengines [2].

The maximum output voltage from the waveform generators is limited to ±10V. Since this voltage is insufficient to actuate the current electrostatic comb drives of the microengine, the output waveforms must be amplified to a voltage sufficient to drive the device. Amplification is achieved with a custom 4-channel amplifier designed and built at SNL. The amplifier provides up to a 200-V drive signal for the electrostatic combs and has a bandwidth sufficient to drive the microengines up to 600,000 rpm.

The device fixture consists of modular printed circuit boards with eight 24-pin DIP sockets. All sockets on the board are wired in parallel with each pin isolated from the parallel bus via 1-MΩ resistors. This provides the needed isolation from one device short-circuiting and causing the remaining devices to stop functioning due to missing drive signals. The test bed consists of a 4 x 2 array of these printed circuit boards and can test up to 64 packages with a total of 256 parts (Figure 1.2.2). This arrangement of multiple small printed circuit boards rather than one large board provides great flexibility in the arrangement, device wiring, and signal optimization of MEMS devices under test.

Waveform distribution is controlled through a manual switch matrix. The current matrix is arranged in a 6 x 24 arrangement. This arrangement accommodates the four drive signals required for the SNL microengine, a ground line, and a line that disconnects the socket pin from any signal. Additional switch matrices can be added by breaking up the 4 x 2 arrangement of the test fixture boards allowing for greater flexibility in testing.

The optical subsystem and device fixtures are enclosed within a custom Plexiglas enclosure. This enclosure is humidity controlled. The humidity control range is from 2 to 90+ % RH. This control is accomplished through two separate systems. A gas bubble system (Figure 1.2.3) is used for humidity control between 2% to 45% RH. The hu-

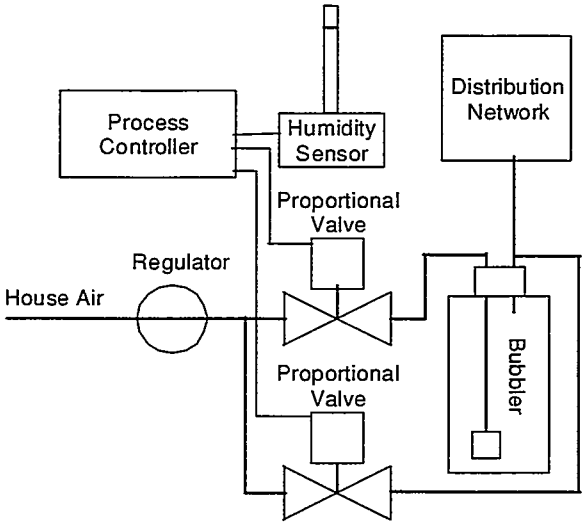

Figure 1.2.3. Schematic of humidity bubble system.

midity plane over the DUTs can be controlled to within ±0.2%. The second unit is a standard steam humidifier. This system is used above 45% RH and controls humidity levels to within ±5%. A chilled mirror hygrometer is used to measure the actual humidity levels encountered during testing.

The entire system (optics, DUTs, and the humidity enclosure) is mounted on a vibration isolation table. This provides us with the ability to remove any ambient laboratory vibration from entering into our experimental data. It also allows us to achieve high magnification of our devices without experiencing blurring due to external vibrations. The humidity and vibration isolation systems are illustrated in Figure 1.2.4.

SHiMMeR Control Software

The software developed to run the SHiMMeR system was written using Visual Basic. This software allows the operator to optimize and vary all engine drive signal parameters. The amplitude and shape of the drive signals can be viewed on the monitor, prior to application to the devices under test. Test fixture arrangements that can be made to fit within the travel of the X-Y gantry table as well as layouts of the MEMS device can be accommodated through description files created by the software.

The operator test screen allows stress and duration parameters to be defined and varied throughout the test. A running commentary can be kept on each device under test until it fails, at which time the software will skip the observation portion of the test unless set up to do otherwise. Device failures are currently broken down into three major categories (Not Used, Functional, and Failed) where each category can have one level of sub-categories.

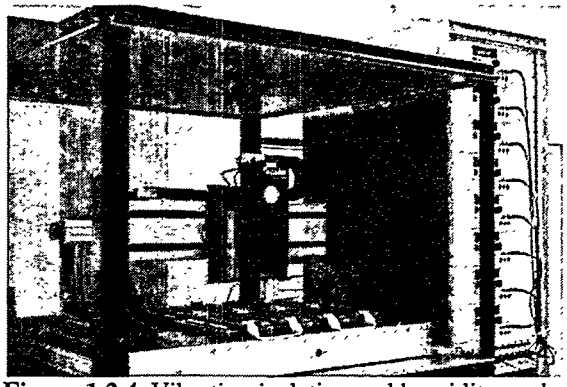

Figure 1.2.4. Vibration isolation and humidity enclosure for SHiMMeR. Doors have been removed for clarity.

The operator can use the predefined subcategories or add additional ones as the test progresses. A color-coded map of the test bed displays the current status of each package under test as well as the status of each

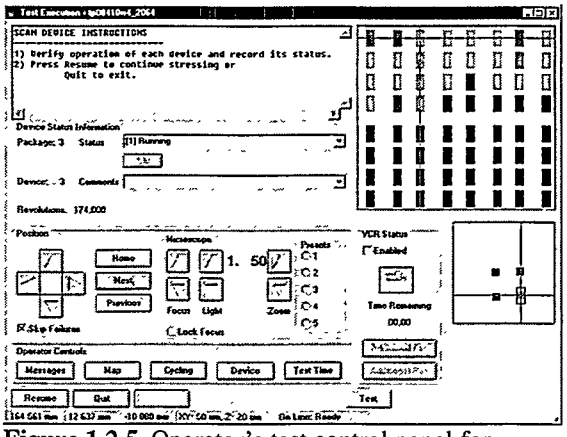

Figure 1.2.5. Operator's test control panel for SHiMMeR. This panel displays the currently status of the devices under test.

device in each package (Figure 1.2.5).

Currently, most of the data is taken manually from the SHiMMeR system, while an automated system is being completed. The operator defines the test by establishing a series of stress and inspection cycles. The stress cycles operate the microengine, while the inspection cycle slows the microengine down to 1 Hz, a speed that is easily viewable by the operator. The operator can then visually inspect each microengine and note its functionality. The operator has the option of using a stroboscopic light source to view the microengine during its high-speed stress cycle. This manual method to perform reliability experiments has been successfully employed [3].

---

[1] D. M. Tanner, N. F. Smith, D. J. Bowman W. P. Eaton, K. A. Peterson, "First Reliability Test of a Surface Micromachined Microengine Using SHiMMeR", *Proceedings SPIE Symposium on Micromachining and Microfabrication*, **Vol. 3224**, Austin, 1997, pp. 14-23.

[2] S. L. Miller, J. J. Sniegowski, G. LaVigne, and P. J. McWhorter, "Performance tradeoffs for a surface micromachined microengine", *Proc. SPIE Micromachined Devices and Components II*, **Vol. 2882**, Austin, October. 14-15, pp. 182-191, 1996.

[3] D. M. Tanner, W. M. Miller, W. P. Eaton, L. W. Irwin, K. A. Peterson, M. T. Dugger, D. C. Senft, N. F. Smith, P. Tangyunyong, and S. L. Miller, "The Effect of Frequency on the Lifetime of a Surface Micromachined Microengine Driving a Load", *Proceedings International Reliability Physics Symposium*, Reno, 1998, pp. 26-35.

1.3 SHiMMeR Lite

A second system similar to SHiMMeR (section 1.2) was needed with the ability to acquire reliability data on a statistically significant number of devices. This system needed to be smaller and more mobile than SHiMMeR with the ability to be easily moved from one lab to another. This system was created and given the name SHiMMeR Lite (Figure 1.3.1). SHiMMeR Lite allows us to perform smaller/quicker experiments while SHiMMeR is in use.

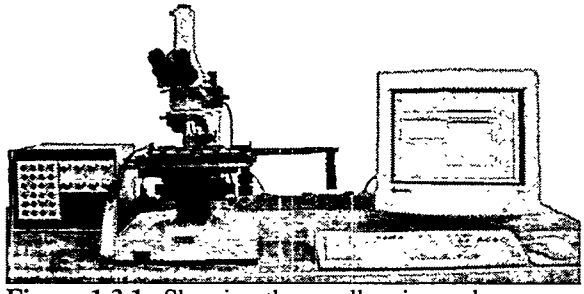

Figure 1.3.1. Showing the smaller size and more flexible arrangement of ShiMMeR Lite.

SHiMMeR Lite has the capacity for 8 DIP packages for a total of 32 micromachines. The device fixture consists of one modular printed circuit board (identical to the boards used in the full SHiMMeR system), with eight 24-pin DIP sockets, which is mounted on a manually operated table under an optical microscope.

The SHiMMeR Lite computer uses an analog output card to produce custom waveforms to drive the micromachines under test. Use of the analog output card allows SHiMMeR Lite to execute two tests simultaneously. Lifetime experiments with a maximum frequency of about 800 Hz can easily be performed in this configuration. Waveforms are amplified using a custom 4-channel amplifier designed and built at SNL (see Figure 1.3.2).

SHiMMeR Lite uses the Super μDriver software (section 1.6). This software allows the operator to optimize and vary all engine drive signal parameters. Micromachine devices can be viewed during testing either through the eyepieces of the Nikon microscope or on a TV monitor attached to a video camera atop the microscope.

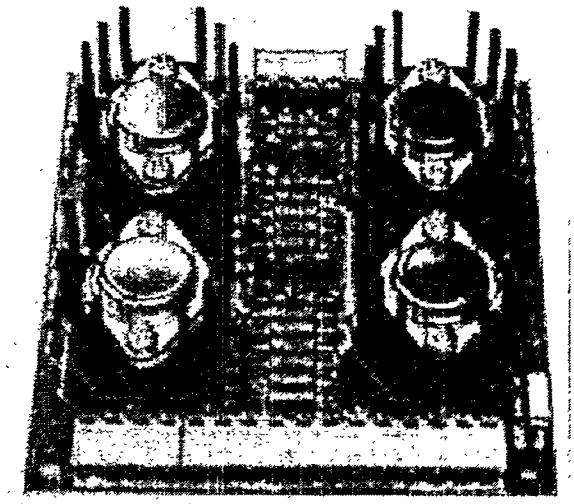

Figure 1.3.2. The four-channel amplifier board provides a 15 times gain to the input voltage.

1.4 Environmental Storage Chambers

Incoming MEMS components, either as gel-packs containing individual die or packaged as DIPs, are stored in a humidity controlled environment. This provides a history of the environmental conditions the components have experienced before they are placed into reliability or characterization experiments.

Six plexiglas containers (Figure 1.4.1) manufactured by Plas Labs are currently used. Five of the boxes are configured as dry storage only. The sixth box has the capacity to control the humidity. Humidity is controllable from 0% to 100% RH, however condensation will occur at very high RH levels. All of the boxes are purged using dry nitrogen via individual flow meters. Purge rates are continuously variable from 0.1 to 3.0 cubic feet per hour (CHF).

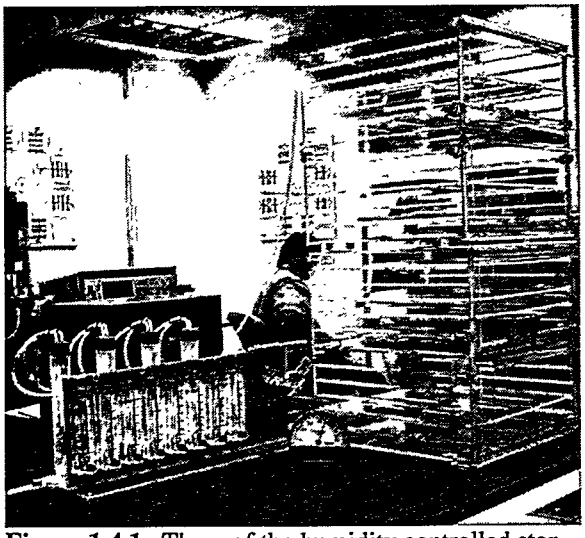

Figure 1.4.1. Three of the humidity controlled storage boxes.

The humidity system uses 2 separate flow meters with one of the flow meters controlling the rate of N2 bubbling through de-ionized water (Figure 1.4.2). The use of two flow meters allows greater control of the desired humidity. All of the enclosures are equipped with portable humidity and temperature meters. Each meter can track both min/max temperature and humidity.

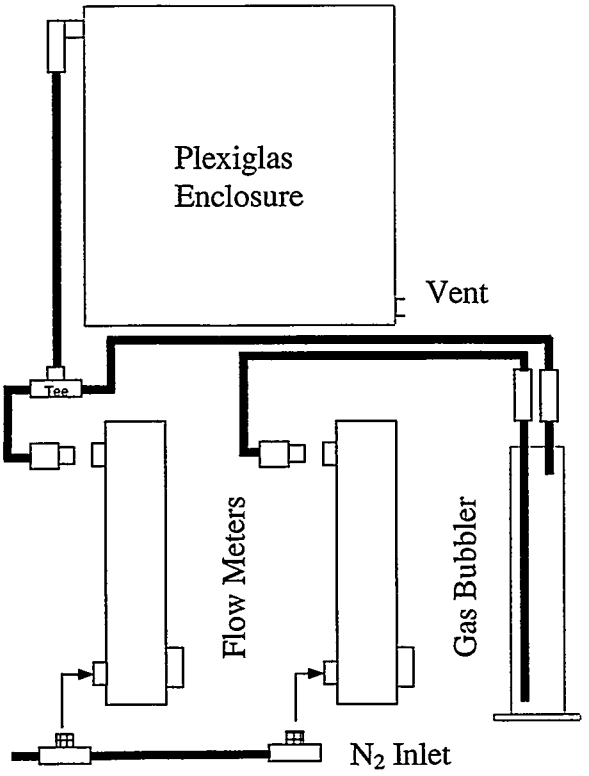

Figure 1.4.2 Diagram of the gas connections for the nitrogen storage boxes.

1.6 Super μDriver

Simple MEMS devices such as cantilevered beams and comb drives can easily be actuated with a standard function generator whose output has been sufficiently amplified to control the device. The addition of multiple comb drives working together increase the complexity of the required actuation signals. Additional function generators phase-locked together are required to operate these devices. However, the waveforms that standard function generators provide can cause unwanted forces to be applied to the device under test.

These unwanted forces can severely shorten the life of the device. Complex or model-based drive signals that account for the device's geometry as well as other aspects of the device are required to enhance its lifetime (Figure 1.6.1) [4]. This requirement has led to the development of flexible waveform generation software and hardware that can generate model-based drive signals as well as standard function generator waveforms. This system is referred to as Super μDriver.

Super μDriver provides standard function generator type waveforms that can be used to operate simple MEMS devices. These standard waveforms include sine, square, triangular and DC voltage. Since these standard waveforms are generated as arbitrary waves, enhancements to them have been incorporated which allow for simplified controls of MEMS devices.

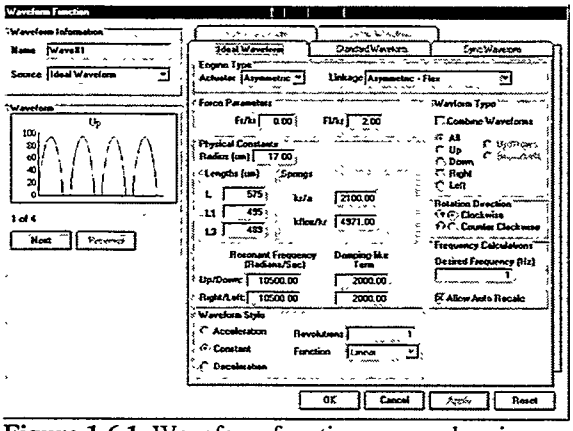

Figure 1.6.1. Waveform function screen showing drive signal parameters required to properly operate the microengine.

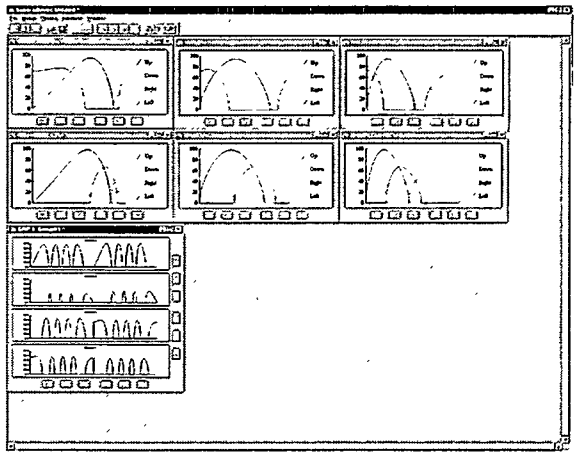

Figure 1.6.2. An example of linking drive signals together to create useful motion. These signals are used to move a linear rack assembly back and forth (Figure 1.6.3).

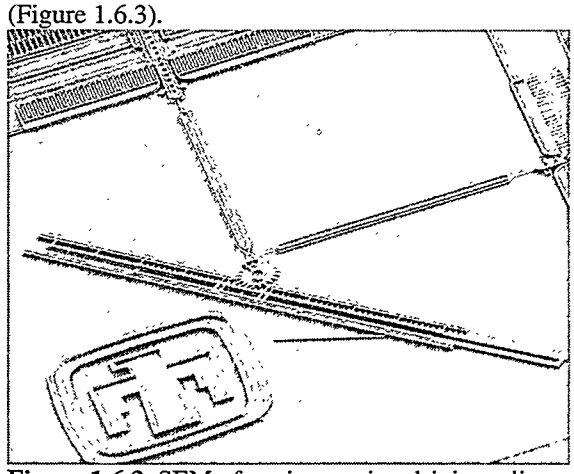

Figure 1.6.3. SEM of a microengine driving a linear rack assembly.

Super μDriver also has the capability to control the Sandia developed microengine with model-based drive signals. By using the model-based drive signal for the microengine we are allowed fine control of the device's operation. Physical constants, such as geometric lengths, spring constants, resonant frequency, etc., can be controlled to operate various design iterations. Radial and tangential forces can be varied to study the effects of forces applied to the gear hub. Additionally, acceleration and deceleration

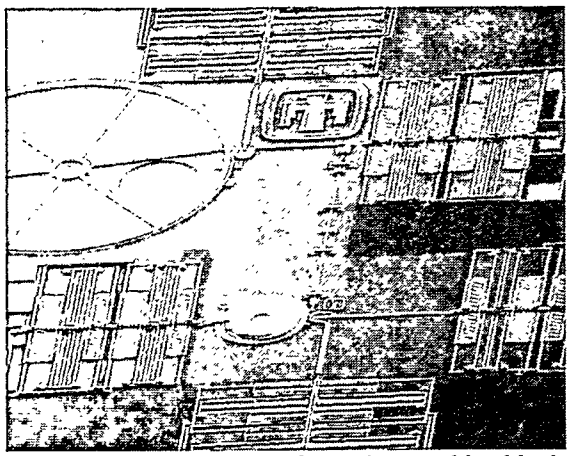

Figure 1.6.4. SEM of a surface micromachined lock and optical shutter assembly

waveform profiles are available to account for inertial effects of high-speed operation.

Multiple waveforms can be linked together and repeated. This provides the capability to perform linear motion. Figures 1.6.2 and 1.6.3 show an example of linked drive signals can be used to operate a linear rack assembly that is driven by a microengine. Additionally Super μDriver can synchronize motion of multiple devices to control a complex microsystem. Figure 1.6.4 shows an example of a complex microsystems device that requires multiple synchronized drive signals.

Super μDriver currently supports 16 synchronized channels of waveform generation and two separate types of arbitrary waveform generation hardware. The two separate hardware platforms address the need for a high-performance reliability system and a low-cost characterization system that can easily be duplicated for use in multiple laboratories.

[4] S. L. Miller, J. J. Sniegowski, G. LaVigne, and P. J. McWhorter, "Performance tradeoffs for a surface micromachined microengine", *Proceedings of SPIE Micromachined Devices and Components II*, **Vol. 2882**, Austin, October 14-15, 1996, pp. 182-191.

1.7 Characterization Techniques

Much of the characterization associated with microengines and other MEMS actuators revolves around determining parameters for the proper electrical drive signals. While the subject of electrical drive signals has been discussed in detail elsewhere [5, 6, 7], many of the concepts will be repeated here for convenience.

Electrical Drive Signals

Optimized electrical drive signals for microengines can be derived from simple Newtonian physics. They account for the electrostatic force of the comb drives, the restoring force of the folded comb drive springs, and the damping force associated with air damping. Furthermore, tangential and radial forces at the gear are included. The net equations generated by this ideal model are **NOT** simple sine waves, and their shape changes as a function of speed. The drive signals are:

$$V_x^2 = \frac{1}{\gamma}\frac{kr}{a}\left\{\begin{array}{l}\frac{\gamma^2}{\omega_0^2}\left[\left(\ddot{\theta}+2\delta\dot{\theta}\right)\cos(\theta)-\dot{\theta}^2\sin\theta\right] \\ +\left(\frac{F_r}{kr}+\gamma^2\right)\sin\theta+\frac{F_l}{kr}\cos\theta\end{array}\right\} \quad (1)$$

and

$$V_y^2 = \frac{kr}{a}\left\{\begin{array}{l}\frac{1}{\omega_0^2}\left[\left(\ddot{\theta}+2\delta\dot{\theta}\right)\sin(\theta)-\dot{\theta}^2\cos\theta\right] \\ +\left(\frac{F_r}{kr}+1\right)\cos\theta+\frac{F_l}{kr}\sin\theta\end{array}\right\}, \quad (2)$$

where V_x and V_y are x voltage (right and left) and y voltage (up and down), respectively. The variables k, a, and ω_0 are the spring constant, electrostatic force constant, and resonant frequency, respectively, associated with the comb drives. The radius of the gear is represented by r and the radial and tangential forces on the gear are F_l and F_r, respectively. The term γ is a geometric term that represents the coupling location of the two linkage arms. It is 1 for newer engine designs. The gear angle, angular velocity and angular acceleration are given by θ, $\dot{\theta}$, and $\ddot{\theta}$ respectively.

The unknown terms in equations 1 and 2 are kr/a and ω_0. The remaining terms are either well known or specified by the user. Hence for microengine characterization, these two terms are the most important.

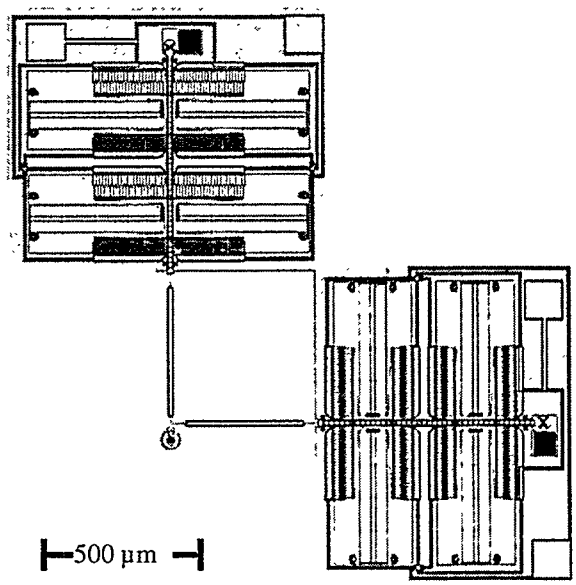

Figure 1.7.1. Photomicrograph of Sandia microengine.

Normalized Spring Constant

To determine the spring constant of the microengine, we start with the static drive signal equations (i.e. $\dot{\theta}$, $\ddot{\theta}$, F_l, $F_r = 0$)

$$V_x^2 = \frac{kr}{a}\gamma\sin\theta \quad (8)$$

$$V_y^2 = \frac{kr}{a}(1-\cos\theta) \quad (9)$$

If $\gamma = 1$ and we pick a "magic" angle where $V_x^2 = V_y^2$ then we can determine the *lumped* or normalized spring constant, kr/a. This magic angle is 90°. And V_x^2 and V_y^2 both degenerate to kr/a. Hence, if DC voltages of equal magnitude are applied to both comb drives of the microengine until the gear reaches an angle of 90°, then the square of

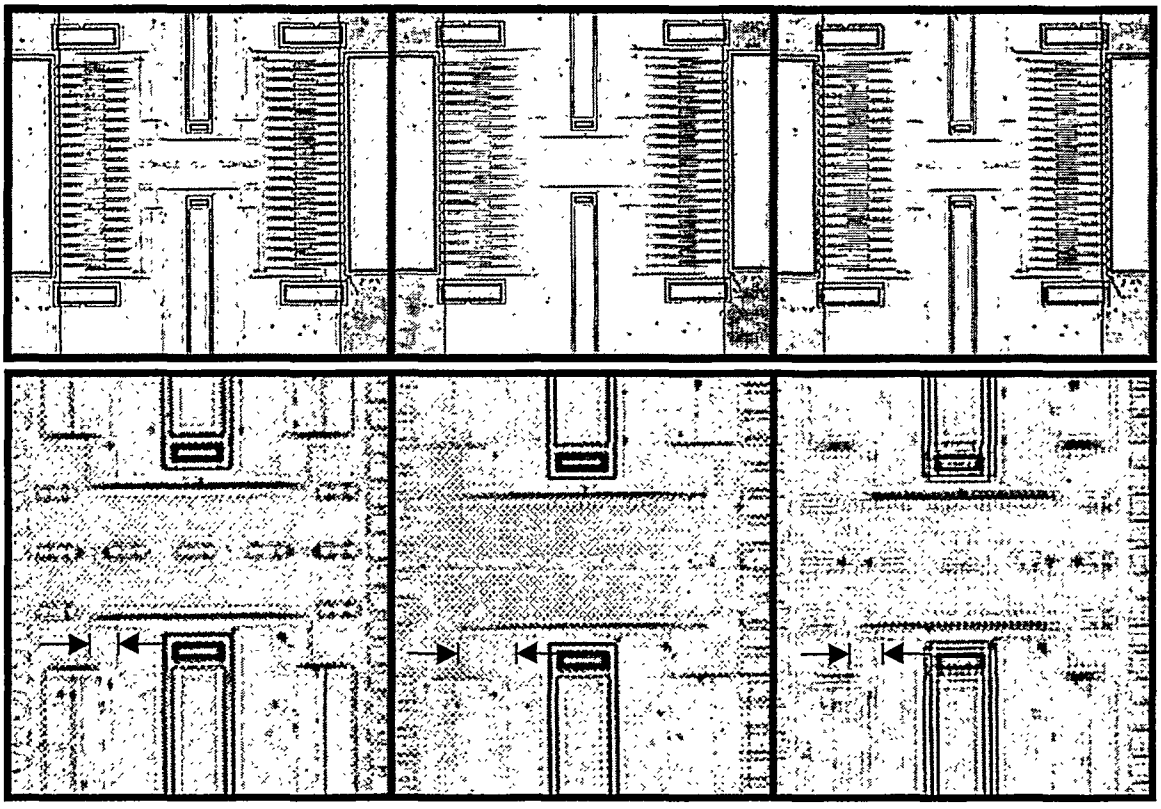

Figure 1.7.2. Blur envelope technique. A sine wave electrical drive signal is applied to the part. The amplitude is kept constant, while the frequency is swept. (left) 3.5 kHz. (middle) 4 kHz. (right) 4.5 kHz. The amount of blur is indicated by the arrows. The middle picture has the largest blur, and hence the largest amount of deflection.

the voltage required is precisely the lumped spring constant.

An alternate method to measuring spring constants using a test structure is described in section 2.6.

Resonant Frequency

Perhaps the most common way of measuring resonant frequency of a MEMS device is using the "blur envelope" technique. By this method (Figure 1.7.2), a sine wave electrical drive signal is applied to the part to force it to actuate. The amplitude of the signal is held constant while the frequency is swept. As the device passes through its resonant frequency, its amplitude of vibration will go through a maximum.

Unfortunately, the blur envelope technique has two major flaws: (1) poor accuracy and resolution and (2) difficulty of automation. The resolution of this technique is about 50-100 Hz at best and accuracy is limited by operator variability. One operator might see a different resonant frequency than another. And because of the visual nature of the measurement – automation, while not impossible, would be very difficult. Despite these weaknesses, the blur envelope technique is convenient since it is relatively simple.

It is generally desirable to have an electrical measurement of the resonant frequency. Electrical measurements are complicated by the presence of large parasitics in the presence of small signals. Clark Nguyen *et al.* [8, 9] have reported a technique which has high resolution and can be easily automated. This technique takes advantage of the rate of change of capacitance with time ($\partial C/\partial t$) of a moving microme-

chanical structure. This technique is shown schematically in Figure 1.7.3 and spectrally in Figure 1.7.4. It is a modulation/demodulation scheme, where the electrical signal driving the structure into resonance is first modulated by the structure itself and then demodulated using a mixer.

Referring to Figure 1.7.3, a drive signal with frequency near the resonance of the structure is applied to the stationary comb fingers. A carrier signal with a DC offset and AC frequency much larger than the resonant frequency of the structure is applied to the shuttle and underlying ground plane. The sense signal is picked off the other set of stationary comb fingers.

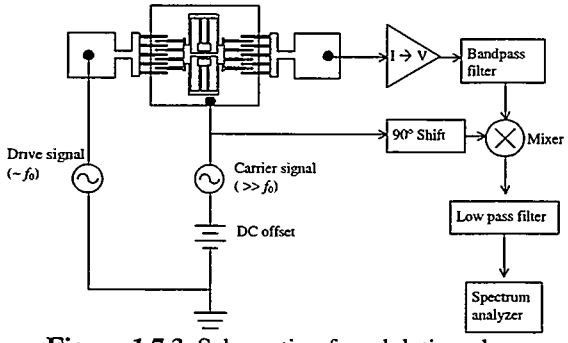

Figure 1.7.3. Schematic of modulation–demodulation measurement scheme.

The moving shuttle will induce charge on the sense fingers, which will give rise to a current. This current is converted to a voltage and amplified by a transimpedance amplifier. Referring to Figure 1.7.4(a), the spectral response will contain undesired feedthrough terms at the drive and carrier frequencies ω_d and ω_c. Modulated sideband terms at $(\omega_c - \omega_d)$ and $(\omega_c + \omega_d)$ will also be generated. The signal is then passed through a bandpass filter with center frequency near the carrier frequency to eliminate the drive signal component(Figure 1.7.4b). It is noted that the drive signal component at this stage is due to unwanted parasitics inherent in the device and measurement scheme itself.

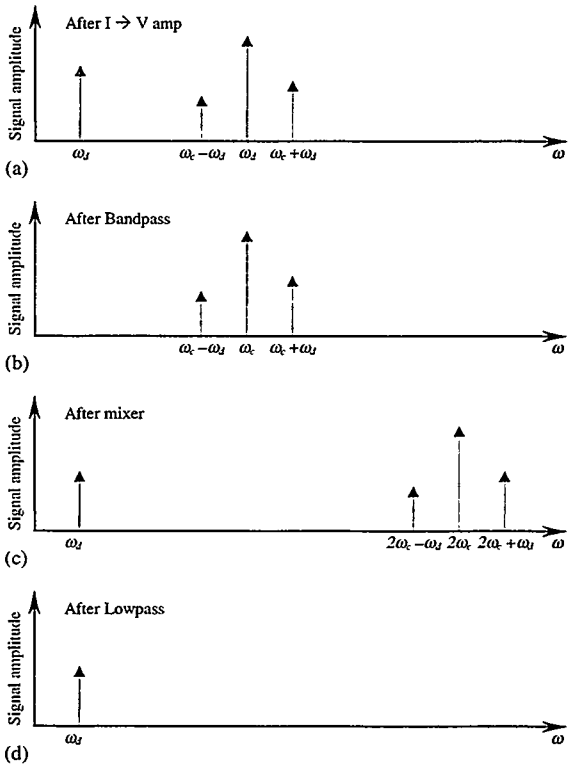

Figure 1.7.4. Spectral components graphs from different stages of measurement (a) after I → V amplifier (b) after bandpass filter (c) after mixer (d) after lowpass filter.

After bandpass filtering, the resultant signal is mixed with the carrier signal that has been phase shifted by 90°. This phase shift has been shown to yield optimal signal amplitude [8]. At this point the spectral components contain peaks at ω_d, $2\omega_c$, $(2\omega_c - \omega_d)$, and $(2\omega_c + \omega_d)$ (Figure 1.7.4c). The height of the peak at ω_d is proportional to $(\partial C/\partial t)$ and will increase with increasing amplitude of motion. If the signal after the mixer is fed through a low pass filter, only the ω_d peak survives and its height can be monitored with a spectrum analyzer. The spectrum analyzer itself can supply the drive signal for the measurement. Used in a swept sine mode, the spectrum analyzer will sweep the drive signal frequency and measure the resultant peak height. In this manner the frequency response of the structure can be measured.

FQ

FQ is a program compatible with Microsoft Windows 95/NT, which is used for measuring resonant frequency, f_0, and quality factor, Q (hence the name FQ). It was developed using the Visual Basic programming environment and can be applied to electrostatic drives or resonators that are electrostatically driven. Because the measurement technique shown in Figure 1.7.3 can be difficult to implement, we created FQ to simplify the process. Most of the difficulty arises from (1) the complexity of operating a signal analyzer and (2) the variability among drive signals among various devices. By using computer control to narrow down the number of functions of the signal analyzer to only those that are needed for making resonant frequency measurements, we greatly simplify the operation of the signal analyzer. And by allowing the user to save the settings necessary to drive a given device, we greatly simplify the variables to input.

Figures 1.7.5 through 1.7.9 show how FQ works. Measurements of resonant frequency are much more reproducible and have a resolution at least an order of magnitude finer than the blur envelope technique. Frequency spectra are shown for various devices in Figures 1.7.10 through 1.7.12.

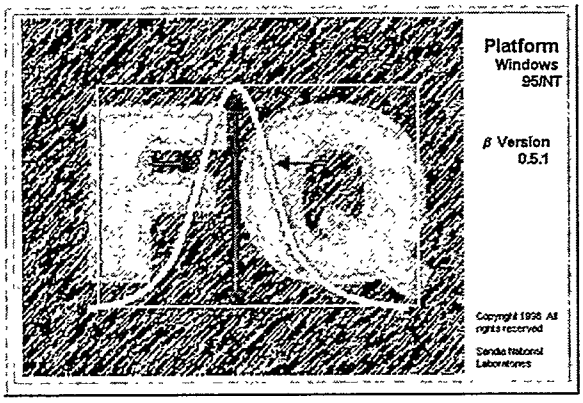

Figure 1.7.5. "Splash Screen" for FQ.

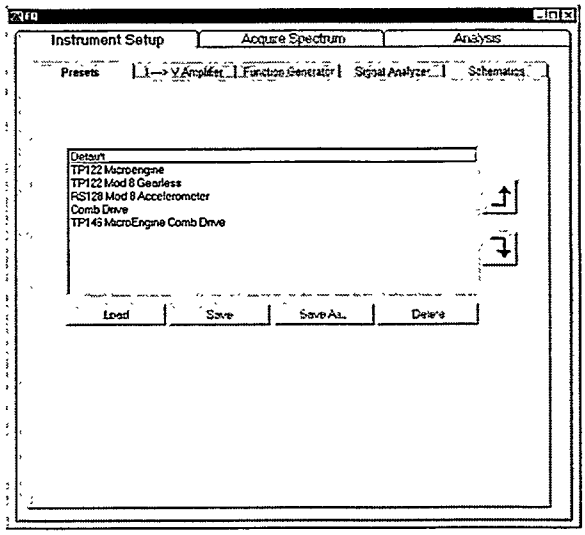

Figure 1.7.6. "Preset" window allows user to Load, Save, and Delete sets of instrument settings.

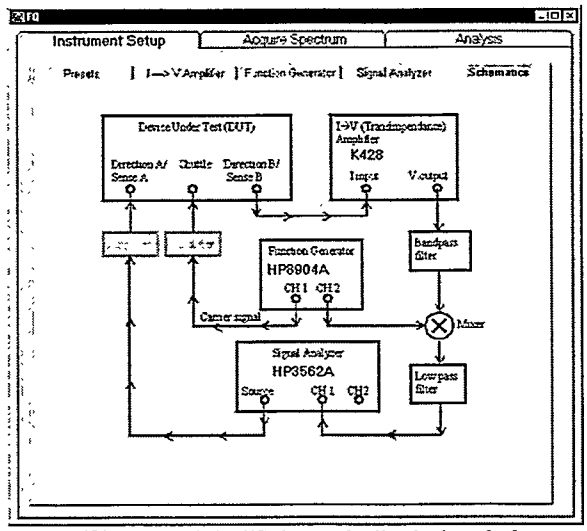

Figure 1.7.7. "Schematics" window helps user to connect instruments correctly.

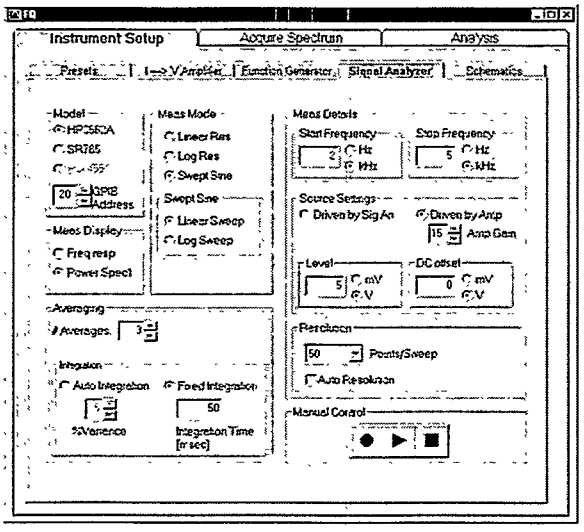

Figure 1.7.8. "Signal analyzer" window contains all of the settings important for making resonant frequency measurements.

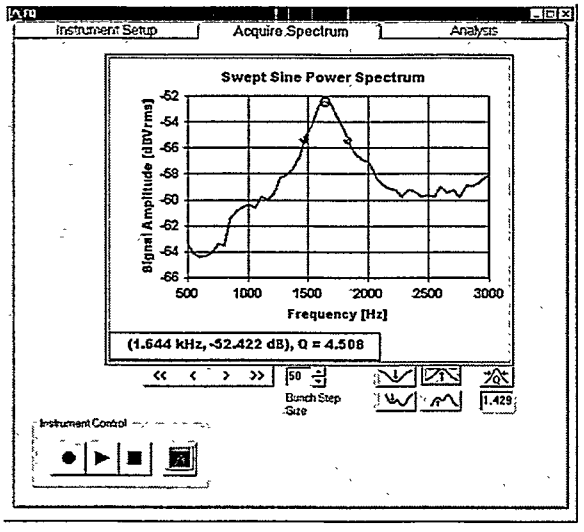

Figure 1.7.9. "Acquire spectrum" window allows user to operate all instruments simultaneously to acquire frequency spectrum. The open circle marks the resonant frequency. The filled circles mark the 3 dB points.

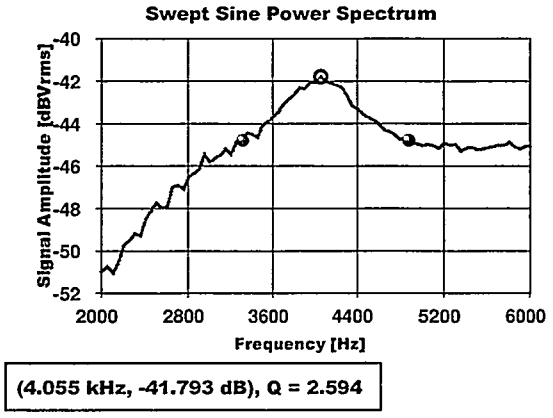

Figure 1.7.10. Power spectrum of the same comb drive from Figure 1.7.1.

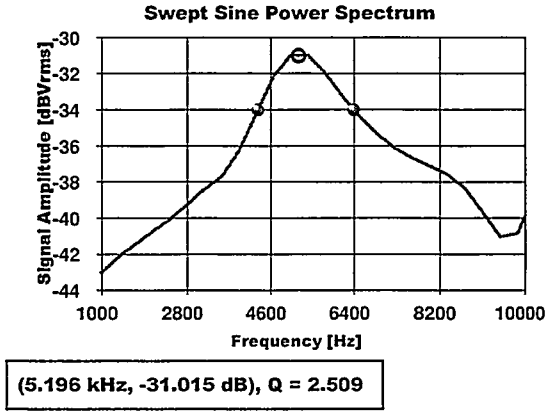

Figure 1.7.11. Power spectrum of an accelerometer.

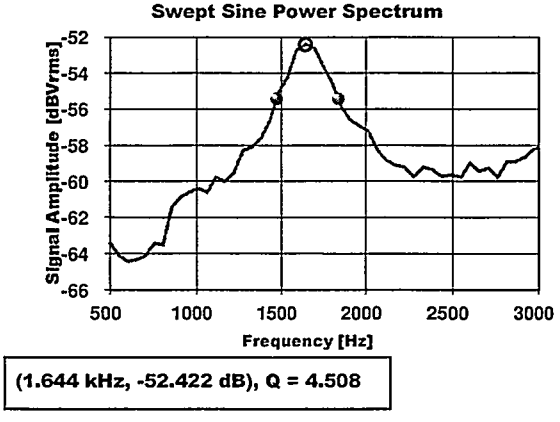

Figure 1.7.12. Power spectrum of a 'gearless' micro-engine.

[5] S. L. Miller, J. J. Sniegowski, G. LaVigne, and P. J. McWhorter, "Friction in Surface Micromachined Microengines", *Proc. SPIE Smart Electronics and MEMS*, **Vol. 2722**, p. 197-204(Feb. 1996).

[6] S. L. Miller, J. J. Sniegowski, G. LaVigne, and P. J. McWhorter, "Performance Tradeoffs for a Surface Micromachined Microengine", *Proc. SPIE Micromachined Devices and Components*, **Vol. 2882**, 1996, p. 182-191(Oct 1996).

[7] J. J. Allen, S. L. Miller, G. F. LaVigne, M. S. Rodgers, and W. P. Eaton, "Dynamic Effects of Linkage Joints in Electrostatic Microengines", Presented at *Modeling and Simulation of Microsystems 1998*, Santa Clara, CA, April 6-8, 1998.

[8] T.-C. Nguyen, "Electromechanical Characterization of Microresonators for Circuit Applications", *Final Report Masters Project*, The University of California at Berkeley, 1991.

[9] C.T.-C Nguyen, "Micromechanical Signal Processors", *Ph.D. Dissertation*, The University of California at Berkeley, 1994.

1.8 Image Analysis

Qualitative assessment of device operation is critical in understanding the underlying mechanisms of failure. The SHiMMeR system requires that an operator views the device in operation and make narrative assessment of its condition and marking it as failed when appropriate. While this system is quite effective several issues have been encountered.

An automated image capture system and tools to analyze these images has been developed. These tools help to remove variances in the narrative description as well as how different operators assess the device. Others have reported similar systems [10,11]. The analysis software provides the capability to track the motion of the gear or another feature. The ability to track motion at operational speeds allows angle versus time and angular error determinations to be made. This information can provide insight into drive signal optimization and friction as well as other types of reliability information.

Image Capture

An automated image capture system has been developed that is capable of handling the large number of images generated during the testing multiple devices. This system is capable of tracking the frequency of the drive signal and taking multiple snapshots of the device's rotation or linear motion. A block diagram of the system is presented in Figure 1.8.1. The system is fully computer controlled allowing for the images to be captured at very precise instances in time.

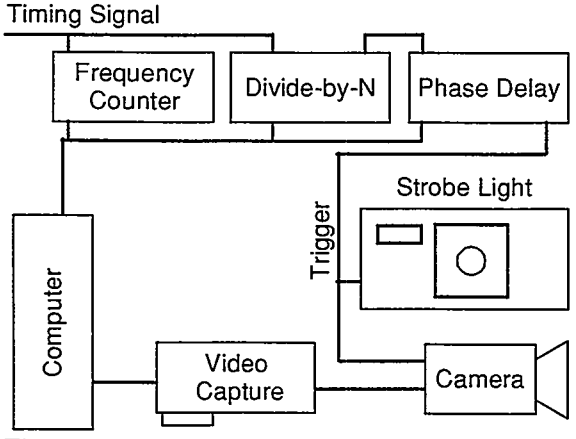

Figure 1.8.1. Block diagram of image capture system.

A high intensity stroboscopic light (Olympus ALS-12000S) source is used for illumination of the DUT at operational speeds. This light source is directly coupled into the same fiber optic bundle that is used for normal illumination. The flash rate of this strobe can be externally controlled with an approximate flash duration of 3-5μs. A National Instruments TCIO-10 timer/counter card and a National Instruments PCI-1408 monochrome video capture card handle the timing of the strobe and the image snapshots. A pair of counters is used to measure and tracks the actual drive signal operating the device through a timing signal generated by the arbitrary waveform generators. The strobe light is unable to fire at the drive rates routinely encountered, so an additional counter is configured as a divide-by-N. This generates a new flash rate that the strobe can constantly lock onto. One additional counter is configured to generate a finely controlled delayed pulse for the strobe and image capture card. This delay allows images to be acquired at any desired angle during the waveform period.

Software that allows the computer to control this image capture system has been developed (Figure 1.8.2). It allows images to be captured from both rotary and linear motion devices. The images can be either be viewed continuously in slow motion or a sequence can be saved to disk. It has the capability to automatically generate unique names for each device under investigation. Individual frames can be captured and stored through the software's built-in viewer.

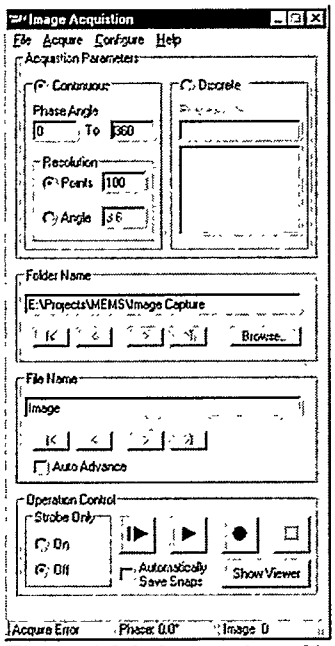

Figure 1.8.2. Screen shot of image capture controls.

Image Analysis

Once a series of image has been acquired, information must be extracted from them. A tool for analyzing the images has been created. This computer program (Figure 1.8.3) allows the images to be played backed at various frame rates. Binary threshold and image morphology tools are supported. Image tools have been created that can track the motion of a user-defined object in each of the images that was taken with the image capture software. These initial data points can be used to determine theta versus time and angular error measurements [11]. The theta versus time measurement is used to evaluate constant rotational velocity. The angular error measurement can be used to determine how well the device is tracking the drive signal. This information can be further evaluated to determine a coefficient of friction.

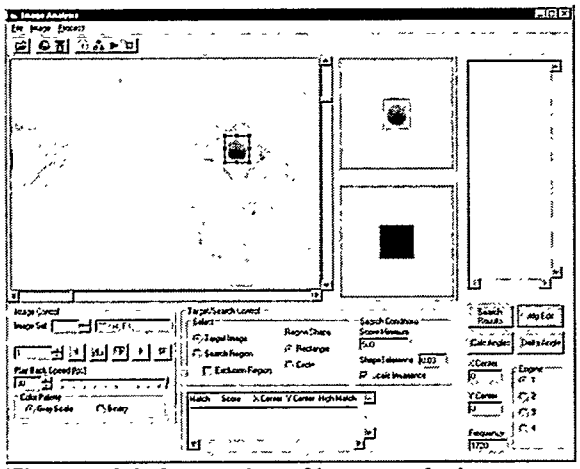

Figure 1.8.3. Screen shot of image analysis program.

The ability to analyze images captured at operational speeds allows a more qualitative

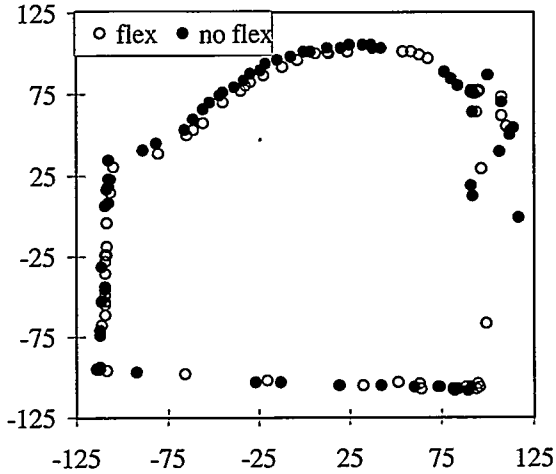

Figure 1.8.4. Position map of a gearless microengine with linear clamping and radius set to 17 µm. Horizontal and vertical axes are in pixels.

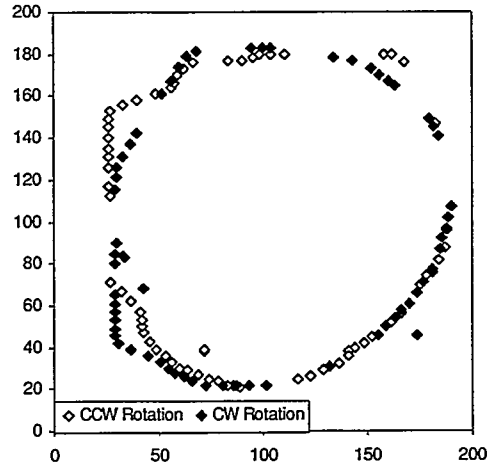

Figure 1.8.5. Position map of a gearless microengine without linear clamping and radius set to 17µm. Horizontal and vertical axes are in pixels. The flat sections in the rotation are due to increases in frictional forces of the shuttle against its guides.

assessment of microengine performance. It has also provided the ability to compare various design modifications against one another. This analysis has allowed design enhancements that increased the reliability of the microengine. In order to study unconstrained operation of the microengine, removal of the gear is necessary. This allows the drive signals and inherent device behavior to be determined. Figure 1.8.4 shows an example of a microengine design that exhibits linear clamping. The linear clamping is due to the fringe field forces becoming non-linear at the end of their full engagement. This design can be contrasted with the design shown in Figure 1.8.5. In this design the linear clamping problem has been eliminated. This device still exhibits some non-ideal effects due to frictional forces changing during the rotation of the device. The flat sections of the curves are where the shuttle is pressing against the guides with enough force to prevent them from sliding efficiently.

---

[10] D. M. Freeman and C. Q. Davis, "Using Video Microscopy to Characterize Micromechanics of Biological and Man-made Micromachines", *Technical Digest of the 1996 Solid-State Sensor and Actuator Workshop*, Hilton Head Isl., June 3-6, 1996, pp. 161-167.

[11] G. F. LaVigne and S. L. Miller, "A Performance Analysis System for MEMS using Automated Imaging Methods", *IEEE International Test Conference*, Washington DC, Oct. 18-23, 1998, pp. 442-447

1.9 Failure analysis techniques

Failure analysis (FA) tools have been applied to analyze failing polysilicon microengines. Many MEMS devices have been examined using techniques developed for integrated circuit failure analysis including optical microscopy, scanning electron microscopy (SEM), focused ion beam (FIB), transmission electron microscopy (TEM), energy dispersive x-ray spectroscopy (EDX), and atomic force microscopy (AFM). We first stressed these devices to failure under accelerated conditions in various environments. Analysis of these failed microengines found that wear debris was produced from friction on rubbing surfaces. We observed an increase in the amount of wear debris with decreasing humidity. The dominant failure mechanism of these microengines was identified as wear of rubbing surfaces. This often results in either seized microengines or microengines with broken pin joints. The pin joints typically fail through wear and thinning.

Optical Microscopy

As a preliminary measure for evaluating MEMS devices, optical microscopy serves as an easy, cost-effective method for quickly determining the integrity of a device. Optical microscopy can provide an initial view of defects such as fracture, displacement, debris, and abnormalities. Insight into the failure mechanism can be achieved in minutes.

For example, the failed spring in Figure 1.9.1a is clearly visible from optical inspection. However, more subtle changes in the MEMS elements, as shown for an overdriven spring in Figure 1.9.1b are also visible optically. This precursor to failure is due to arcing to the adjacent powered line. Contact from the grounded spring to the power line results in either a broken spring or residue. This failure mode has been remedied through design modifications which include the addition of spring stops, and reposition of the Y actuator. This resulted in a relocation of the power line yielding more space between it and the spring.

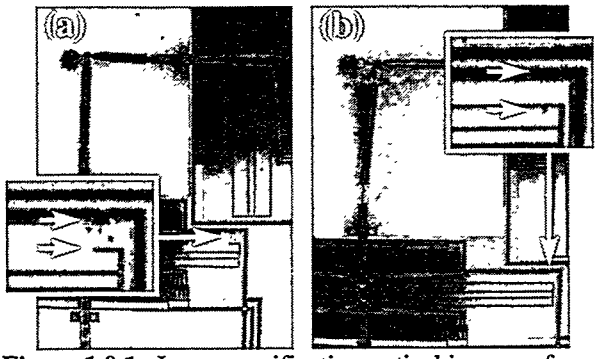

Figure 1.9.1. Low magnification optical images of degraded engines, with insets enlarged. (a) Engine with broken spring and debris from broken attachment. (b) Engine with debris due to less severe broken attachment.

Close examination of all movable parts can reveal exactly which connections might suffer sticking and which are free. For example, one pinned link may be able to reciprocate with a displacement equal to the tolerance of the pin joint, while the link to which it is pinned does not move. Videotapes of operating engines have also proven useful to track performance during tests of operating life [12].

In another example, a microengine that failed due to a broken pin joint can be distinguished from a microengine that failed by gear seizure. These two failure modes are illustrated in Figures 1.9.2a and b. In Figure 1.9.2a, the seized microengine reveals wear debris around the pin joint and hub. Figure 1.9.2b reveals a broken pin joint and like Figure 1.9.2a, wear debris is scattered across the entire gear. By imaging through a series of focal planes, the location of wear debris is observed on the gear surface as well as the substrate. Figures 1.9.2c & d represent the

same microengine with focal planes on the ground plane and gear surface respectively.

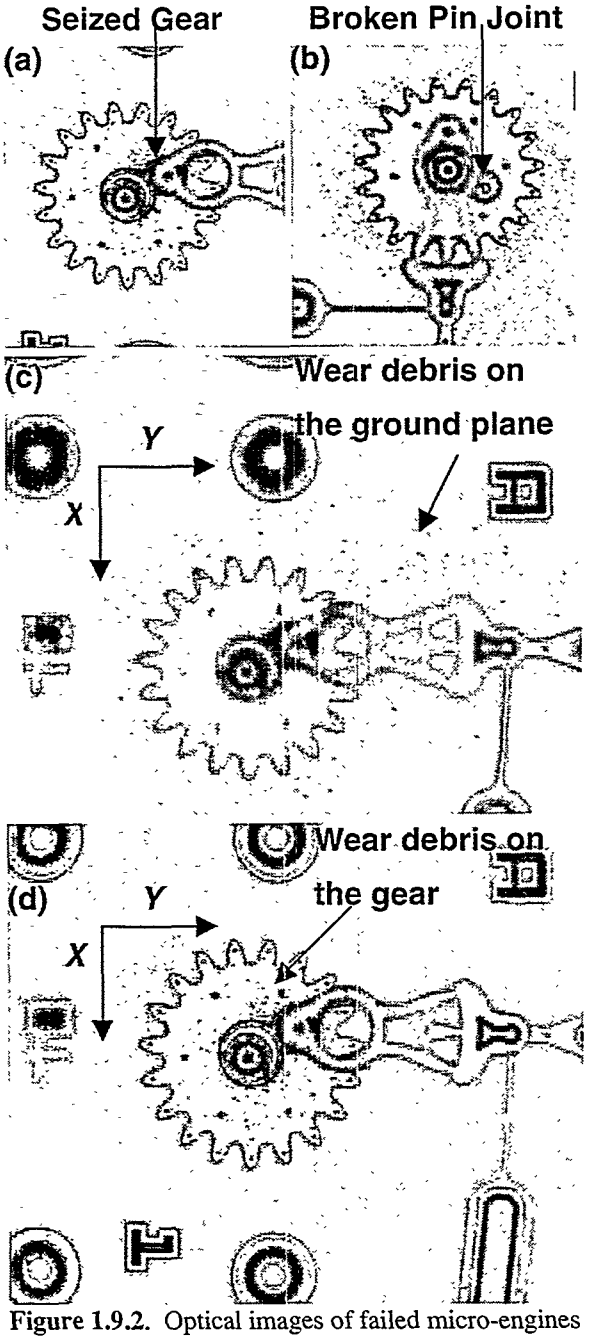

Figure 1.9.2. Optical images of failed micro-engines tested in dry nitrogen. Figures a and b show a seized microengine and broken pin joint respectively. Figures c & d focus on the ground plane and gear revealing debris on both surfaces as indicated by the arrows.

These images suggest the dominant mode of failure is wear of rubbing surfaces. The microengine illustrated in Figure 1.9.2c seized after 2,000,000 cycles. This may be the result of accumulation of wear debris along the rubbing surfaces of the microengine. Although wear debris can be observed, its morphology and structure are too small to be resolved using optical microscopy. A tool with higher magnification is needed to discern the debris morphology.

Scanning Electron Microscopy

Scanning electron microscopy (SEM) is a useful tool for imaging defects and debris at high magnification. SEM analysis provides a larger depth of focus and higher magnification than optical microscopy. This enables debris on both the substrate and gear surface to be in focus at the same time. SEM imaging is also useful for determining the electrical continuity of MEMS devices in static and operating conditions.

General inspection of a failed MEMS device using the SEM has revealed stuck springs, fractured and broken elements as well wear debris from accelerated testing. Just as the spring elements are susceptible to stiction, the comb fingers of a drive actuator can also exhibit sticking behavior to the substrate. As illustrated in figure 1.9.3, the last comb finger on the x axis actuator is bent down and contacting the substrate. This defect can result in a short from the actuator drive signals (voltage) to the ground plane.

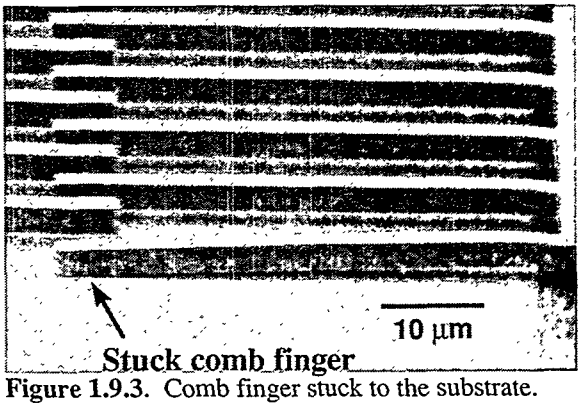

Figure 1.9.3. Comb finger stuck to the substrate.

Just as the comb fingers are susceptible to stiction, spring elements of a drive actuator can also exhibit sticking behavior to the substrate. Figure 1.9.4a and b illustrate two sets of spring elements. The first set is shown contacting the substrate, making the MEMS device inoperative. The other set of springs is suspended above the substrate, allowing the MEMS device to function normally. Designing double level springs that are much stiffer eliminated this stiction problem.

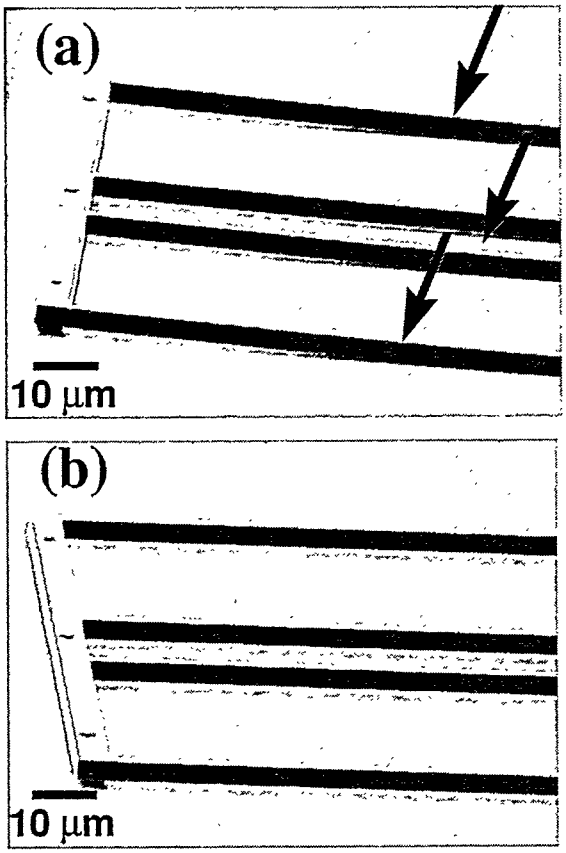

Figure 1.9.4. SEM image of spring elements. (a) Defective spring (arrows show points of contact with substrate). (b) Spring element suspended properly above the substrate.

Figures 1.9.5a and b identify chipped spring elements in a failed binary counter. These chipped springs were evident before the test and were due to the pressure of the wash stream on the wafer-sawing tool. The upper level of polysilicon had no protective covering when the wafer was sawed. To prevent this effect on future die, photoresist is now spun on all wafers at the end of fabrication. Figure 1.9.5b provides a magnified view of the fractured polysilicon surface.

In one experiment, plan view inspection of microengines tested in low humidity showed wear debris was produced and accumulated at the hub and pin joint regions. Debris had also accumulated on the surface of the gears, linkage arms, and substrate. SEM imaging showed larger pieces of debris found on the substrate and top surface of the gear. In this experiment, increasing the percent relative humidity (%RH) decreased the amount of wear debris produced. At 30% RH, debris is located primarily around the

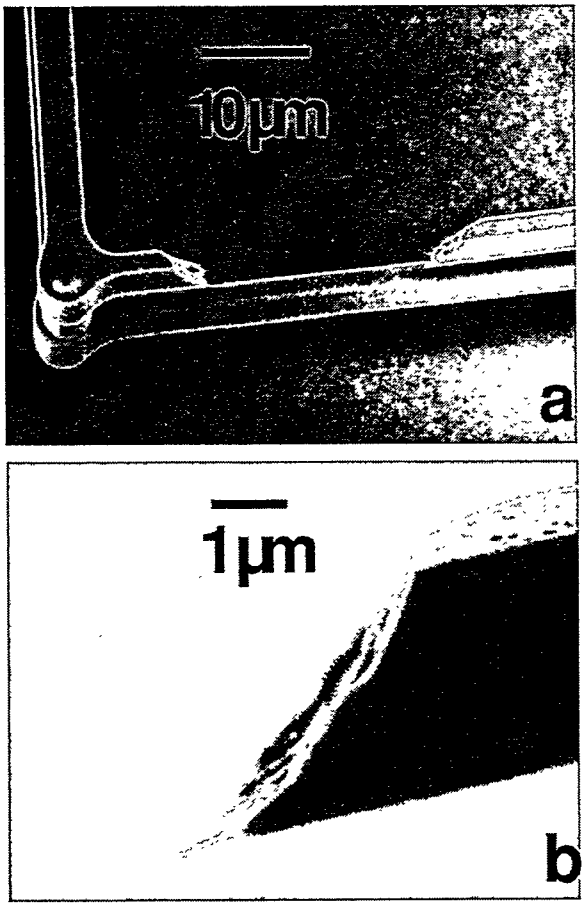

Figure 1.9.5. SEM images of chipped upper levels on spring elements caused by the pressure of the wash stream on wafer-sawing tool. Note the fracture surface in figure b.

hub and pin joint regions. Figures 1.9.6a and b are characteristic of microengines operated in these environments.

SEM imaging revealed that changes in the testing environment affect the morphology of the wear debris. As illustrated in figures 1.9.7a & b, the wear debris morphology appears "particulate" when the microengine is operated in a dry environment (1.8% RH) and "stringy" or "fibrous" when operated in a humid (39% RH) environment. These results show a strong dependence of debris morphology with varying humidity.

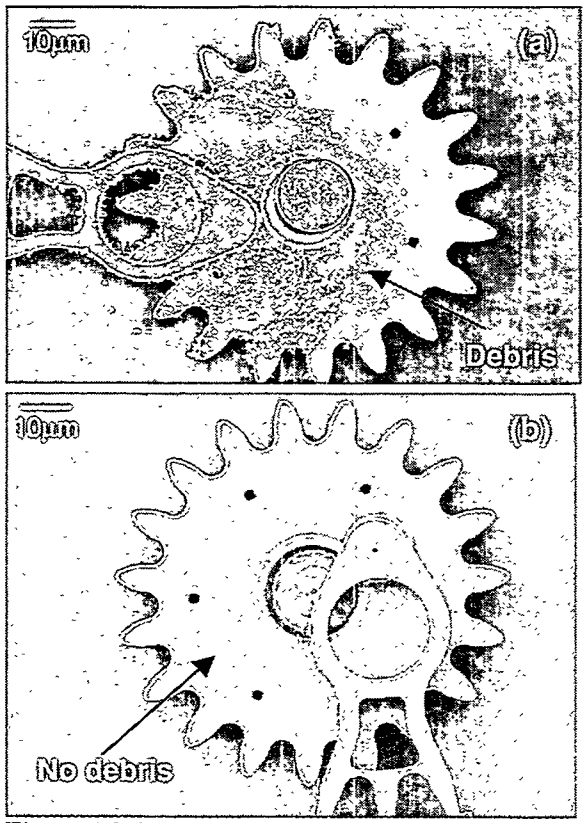

Figure 1.9.6. SEM images of polysilicon microengines stressed to ~ 600,000 cycles at 1.8% (a) and 30% (b) RH at 25°C. Note the accumulation of wear debris on the surface of a compared to b.

To assess the behavior of non-oxidizing atmospheres on microengines, MEMS devices were operated in nitrogen-rich environments. These microengines show significant wear occurring around the pin joint and hub regions. A large amount of wear debris is found on the surface of the gear and the substrate. Figure 1.9.8 shows debris accumulating on the surface of the gear as well as the ground plane. This experiment will be discussed further in the FIB section.

To reduce the effects of oxidation on the polysilicon microengine surfaces, MEMS devices were operated in vacuum. To conduct these experiments, a fixture that was capable of running up to eight microengines was mounted inside the SEM chamber. Using a computer equipped with the Super μdriver software [12], we were able to apply the appropriate power and drive signals to the microengines. The SEM chamber vacuum pump was on overnight (14 hrs.) prior to testing. This pump down time yielded a pressure of ~10^{-6} torr (with a partial pressure of oxygen at ~10^{-9} torr).

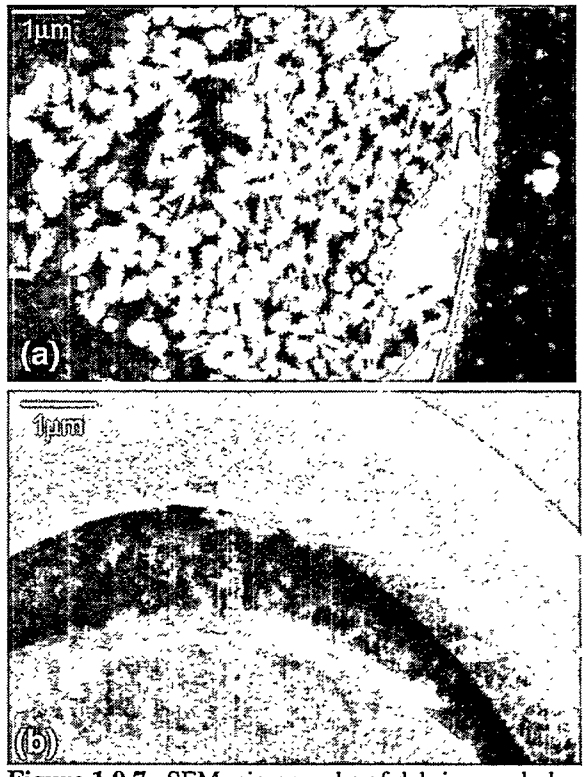

Figure 1.9.7. SEM micrographs of debris morphology for 1.8% RH (a) and 30% RH (b) samples.

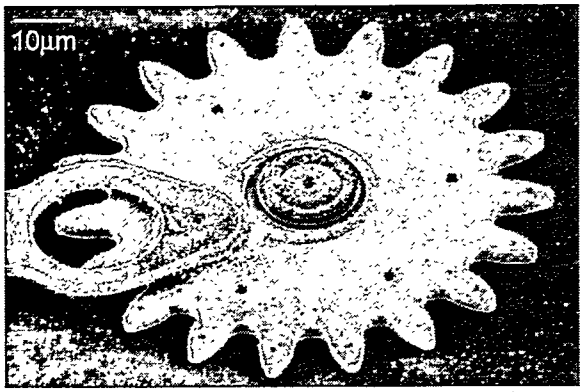

Figure 1.9.8. Debris accumulated along the substrate and surface of the gear of a microengine operated to failure in dry nitrogen.

As illustrated in figures 1.9.9 a & b, a microengine operated to failure in vacuum shows debris accumulating along the hub and pin joint regions. Consistent with results from low humidity testing, the morphology appears to be spherical and particulate. However, it appears that the amount of debris formed is considerably less than that found in 1.8% RH. This result is consistent with our hypothesis that oxygen has a pronounced affect on the wear properties of microengines.

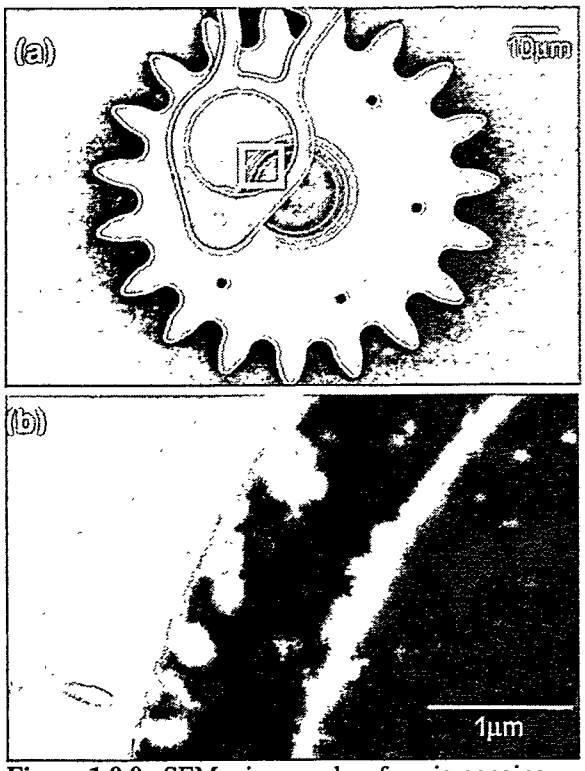

Figure 1.9.9. SEM micrographs of a microengine operated in vacuum over 2,000,000 cycles. Note the lack of debris compared to the 1.8% RH sample in Figure 1.9.6a and its morphology.

SEM failure analysis of a microengine with a broken pin joint has revealed uneven wear along the pin joint. By over-stressing the microengines (by running them at 1720 Hz), the frictional forces between the pin joint connecting the gear to the linkage arm change severely [13]. These forces directly impact the friction-bearing surfaces throughout the microengine which may cause the gear to fail by seizure or breakage of the pin joint. Previous results [13] have shown that these microengines exhibited linear clamping. By optimizing the drive signals, thus creating a fluent circular motion of the pin joint and gear, the wear along the pin joint and hub regions can be reduced substantially.

As illustrated in figure 1.9.10a, the pin has rubbed against the gear's pin joint causing significant wear along the y-axis. The preferential wear of the pin joint may be a result of abrupt changes in acceleration that the gear experiences during each revolution. This may be a result of inadequately optimized drive signals, linear clamping of the actuators, manufacturing variation, or a combination thereof. This mode of failure can be detected in the optical microscope by tracing the location of the debris along the substrate. Figure 1.9.2c illustrates small particles of wear debris on the substrate. This debris is preferentially distributed along the y-axis (actuator) of this microengine as we expected due to the y-axis clamping. Through design modifications and further optimization of drive signals, issues involved with linear clamping have been resolved.

Illustrated in figure 1.9.10b is a higher magnification SEM image of the fractured pin joint in the boxed region of figure

1.9.10a. Notice the significant wear along the bottom of the pin joint. This non-concentric wear indicates strong forces occur along that direction resulting in preferential wearing. This type of wearing process can cause the pin joint to fracture, seize (with the accumulation of wear debris), or rock about the worn region. In a rocking failure, the gear will move but not make a complete revolution at the inspection frequency.

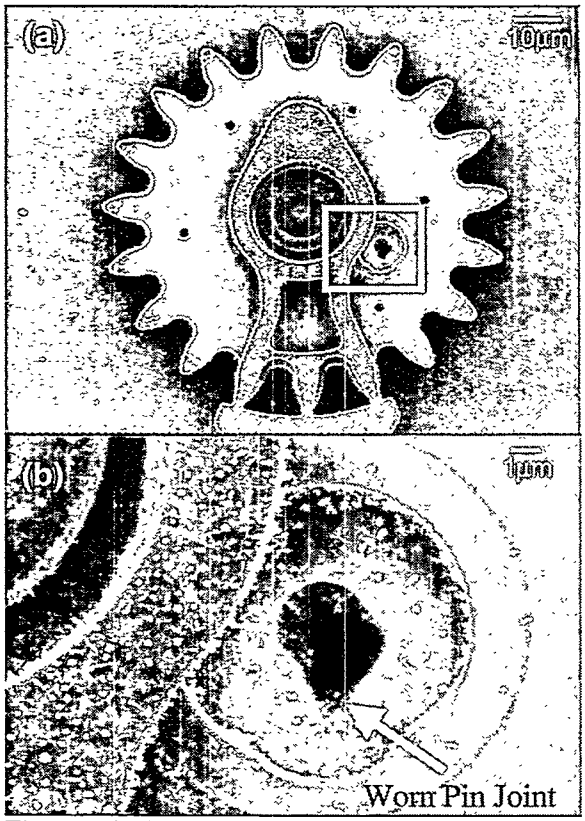

Figure 1.9.10. Non-circular wearing of the pin joint connecting the gear to the linkage arm caused by overstressing the microengine.

Focused Ion Beam

Focused ion beam (FIB) systems are extremely valuable tools in the failure and yield analysis of MEMS devices [14,15]. FIB systems use a focused beam of Ga+ ions (typically 25 – 50 keV) for precise material removal (by physical sputtering), material deposition (by ion beam assisted chemical vapor deposition), and for imaging (by detection of secondary electrons or ions generated during beam exposure). The FIB system provides the best method for producing clean cross sections of the precise area of interest in MEMS structures; cross sections can be made of both large and small structures with submicron accuracy. Further, the FIB can also be used to free, and in some cases remove, portions of the device to enable the analysis of otherwise inaccessible areas. [14,15]

We have used the FIB system extensively in the evaluation of the amount and location of wear debris formed during the operation of microengines. FIB cross sections have revealed debris located throughout the pin joint and hub regions of the microengine. Illustrated in figure 1.9.11 is a FIB cut through a gear tested at 1.8% RH. This image illustrates the debris on the surface of the gear as well as revealing a cross section of the pin joint and hub regions. Figures 1.9.12a, b, c, and d show four cross-sections of microengines from various humidity levels. Note the change in the amount of wear debris produced within the microengine with varying humidity.

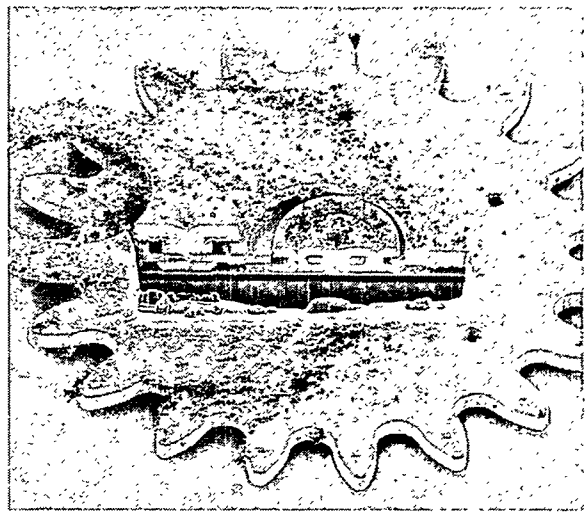

Figure 1.9.11. MEMS device with an exposed cross-section of the gear produced from FIB machining.

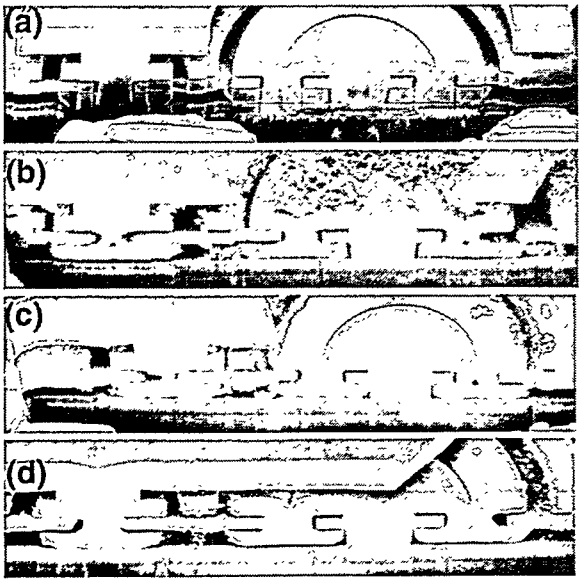

Figure 1.9.12. MEMS gears tested in: 1.8% (b), 24% (c), and 39% RH (d) environments (control (a)). Note the accumulation of debris in as a function of humidity.

The FIB also helps resolve the root cause of failure for various microengines. In instances where the microengine is seized up, it is important to determine the region most susceptible to sticking.

Using the FIB, it became apparent that the majority of seized regions occurred at the pin joint. In this case, either worn material from the pin joint accumulated and caused the microengine to seize or the wearing away of material allowed a protruding part of the gear to get stuck in the pin joint. Another cause of seized microengines can be attributed to induced motion or displacement along the z-axis of the device causing the bottom of the pin joint to contact and adhere to the substrate.

Figures 1.9.13a and b illustrate seized portions of the microengines occurring at the pin joint. The severe wear of the pin joint revealed by the FIB cross-section indicates that worn material had been accumulated around the portion of the gear that contacts the pin joint. The as-fabricated geometry has changed from 90° sidewalls to rounder, sharper ends protruding into the pin joint, leading to excessive wear and damage. This

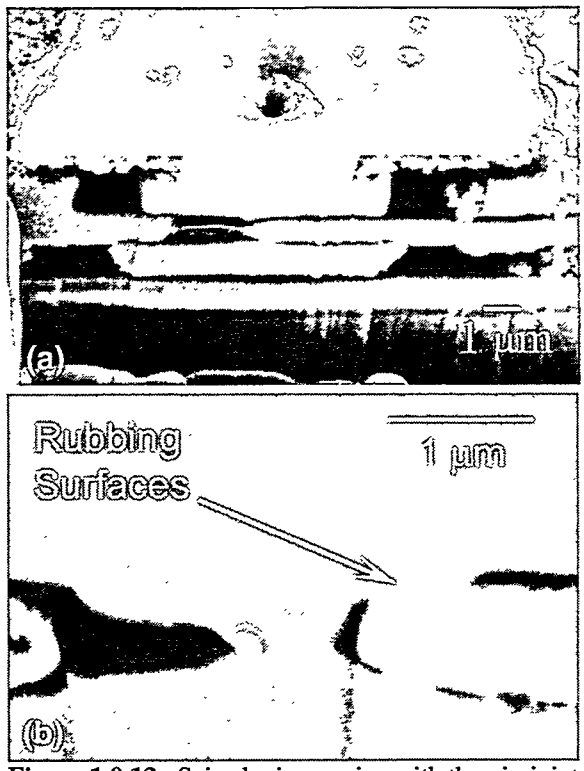

Figure 1.9.13. Seized microengine with the pin joint sheared through (a). A microengine with the seized region exposed (b). Note the wear along the pin joint.

mechanism may also be the root cause in the fracture of pin joints.

Another failure mode exhibited in earlier generations of MEMS revealed wear along the shuttle/guide regions. As illustrated in figure 1.9.14a and b (FIB and optical images), wear tracks and debris were observed along the shuttle area closest to the guide. Upon FIB sectioning of the guide portion closest to the shuttle (a), the shuttle became mobile, and moved to its equilibrium position (b).

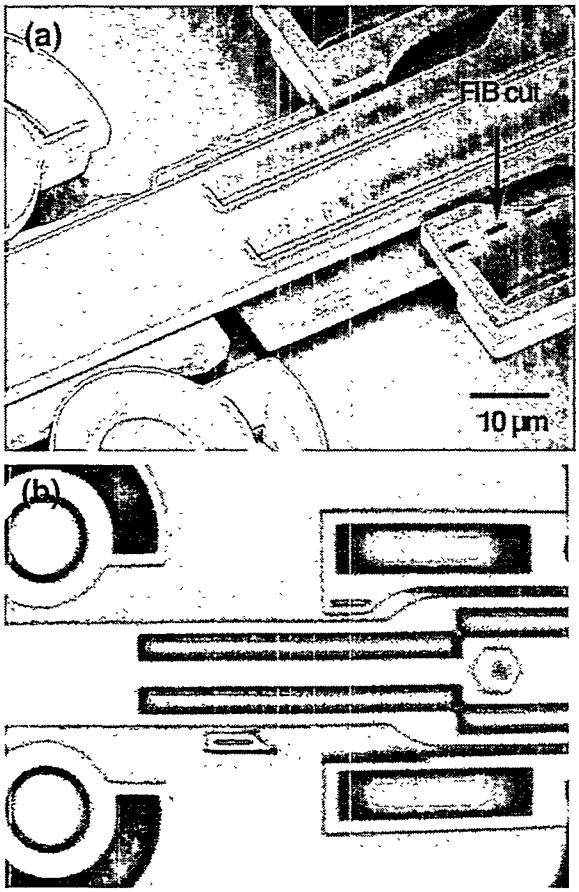

Figure 1.9.14. (a) Location of FIB cut on the pinned link microengine guide of the up-down shuttle in a failed binary counter. (b) Optical image showing portion of the guide was severed by FIB cut and moved to the left. The FIB cut freed the shuttle from the guide.

Using the FIB, we have found tracks of wear debris around the hub and outer perimeter of the pin joint as illustrated in figures 1.9.15a and b. Of primary interest was evidence that a pin joint is firmly adhered to the ground plane. This result indicates undesirable displacement has occurred along the z-axis resulting in the pin contacting the ground plane. This motion may have occurred when the hub and pin joint regions were significantly worn away resulting in wobbling along the z-axis during operation. The end result is friction welding of the pin to the substrate.

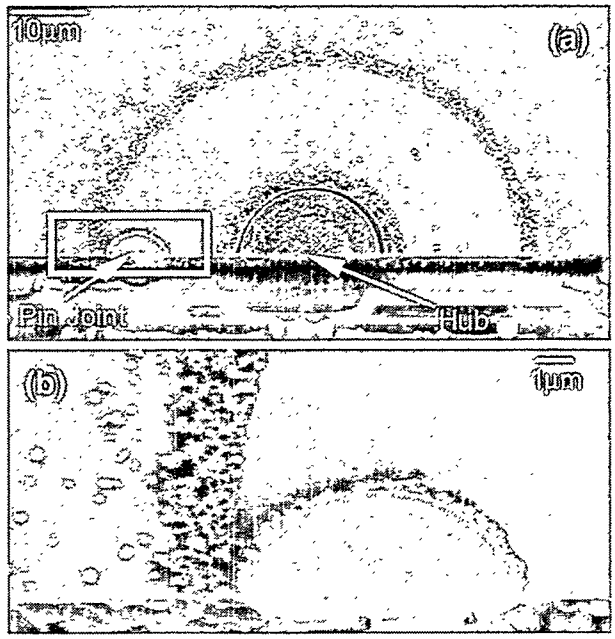

Figure 1.9.15. Debris tracks along the outer perimeter of the pin joint and hub on the surface of the substrate.

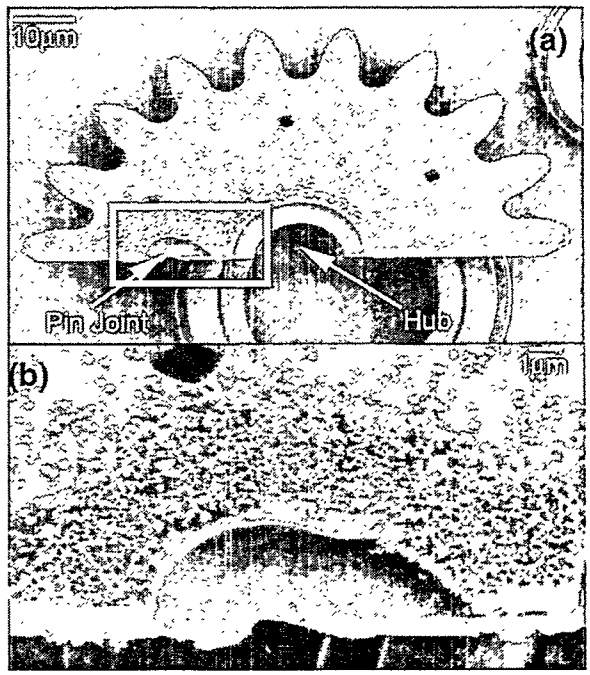

Figure 1.9.16. Debris located on the bottom gear surface (top) with debris accumulating along the worn pin joint. Note the lack of circular shape around the pin joint.

The bottom half of the gear also shows accumulation of debris around the hub and pin joint regions. Figures 1.9.16a and b il-

lustrates significant wear along the hub and pin joint with the build up of debris at the pin joint. Initially, the gear failed by seizing up as opposed to fracture of the pin joint. However, while performing a FIB cut through the hub and pin joint, the microengine freed up and became mobile indicating the FIB cut freed up the seized portion of the polysilicon microengine.

Transmission Electron Microscopy

Transmission electron microscopy (TEM) has been used to characterize the debris morphology, crystal structure and chemical composition. TEM was used to gain further insight into the debris morphology because of its high magnification and diffraction capabilities. Using a Philips CM30 300 keV transmission electron microscope, the debris morphology at low relative humidity has been identified as either spherical or rod-like structures. Spherical wear debris has been found to be as large as 250 nm in diameter. Rod-like debris was found to be up to 500 nm long with a diameter of 50 nm.

The morphology of the wear debris was determined by imaging the various particulate geometries while rotating them through angles of +/-25° and +/-30° in orthogonal x and y directions, respectively. By tilting the debris, no significant deviation from its initial geometry could be observed indicating that the morphology is homogeneous throughout a large degree of rotation.

TEM plan-view specimens were prepared using a replica-stripping technique. A thin section of poly-acetate film softened with a drop of acetone was placed on the gear and then stripped to remove the gear and linkage arms from the microengine. The parts were then coated with a thin carbon film and transferred to a TEM specimen grid. The remaining polyacetate film was dissolved with acetone, allowing the gear and associated debris to rest on the carbon film supported by the TEM specimen grid.

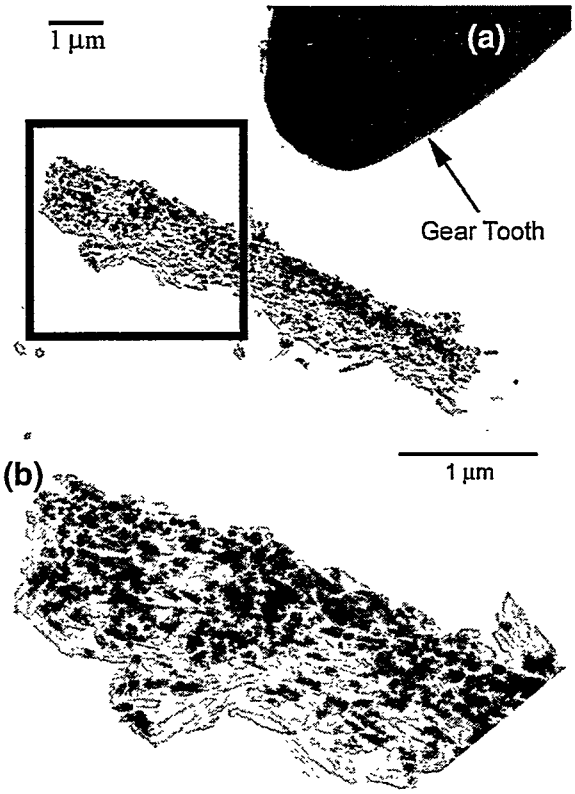

Figure 1.9.17. Plan-view TEM images of a large sliver of debris (a). Note the length of the sliver and the smaller particles comprising this debris (b).

As illustrated in figures 1.9.17 a and b, plan-view TEM reveals a large sliver of material removed from the hub region of a microengine tested in a 1.8% RH environment and displaced just beyond a gear tooth. The large sliver appears to be comprised of smaller spherical and rod-like debris. This debris accumulated along the sidewall of the hub region (as illustrated in the SEM and FIB images). We believe the debris was torn off from within the hub region and thrown outside the gear during testing. Further chemical analysis of this debris using EDX and EELS indicates it is oxidized silicon. Diffraction analysis has shown that this debris is amorphous.

High-resolution electron microscopy did not reveal any boundaries or other features

to indicate that the spherical or rod-like constituents are comprised of even smaller debris. One drawback to this technique is that at high magnifications, high-energy electron transmission can change the sample morphology due to localized heating. In essence, if smaller pieces of debris made up the spherical and rod-like structures, any boundaries in them may have been "fused" together during imaging.

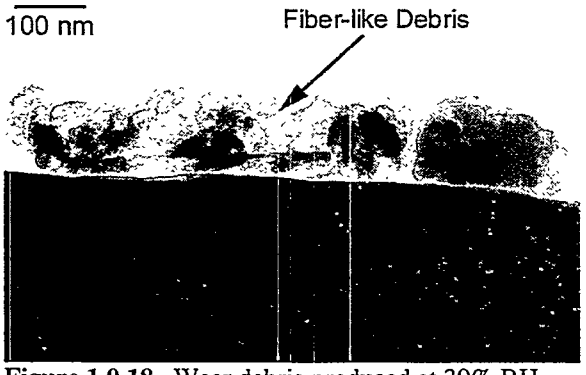

Figure 1.9.18. Wear debris produced at 39% RH. Note the stringy piece of debris.

Comparing wear debris produced during various humidities revealed a difference in debris morphology. At higher humidities, the debris appeared to be fibrous or stringy as illustrated in the SEM micrograph of figure 1.9.7b. Upon TEM examination of the wear debris, there were several regions where these fiber-like structures existed. As illustrated in figure 1.9.18, the wear debris from a 39% RH sample shows an area with fiber-like or filament-like debris. More detailed microscopy (not shown) in these regions indicated that the fiber-like debris is part of the sample and not an artifact resulting from sample preparation.

Electron diffraction analysis was used to assess the crystalline properties of the debris. Diffraction patterns obtained from wear debris formed at low and high humidities revealed the debris is amorphous (non-crystalline) in both instances. As illustrated in figure 1.9.19, diffuse halos characteristic of amorphous material are observed in diffraction patterns taken from debris found in 1.8% and 39% RH (not shown). These results are compared with the diffraction pattern taken from a portion of the gear. Note the diffraction spots form sharp rings from the polycrystalline silicon gear.

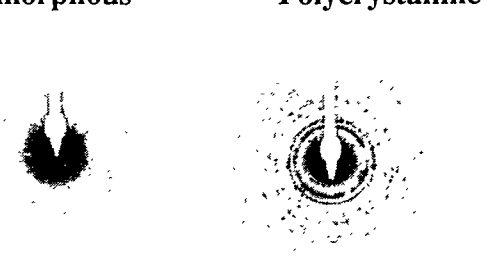

Figure 1.9.19. Diffraction patterns illustrating the amorphous structure of wear debris (left) compared to a diffraction pattern of the polysilicon gear tooth (right).

Energy Dispersive X-ray Spectroscopy

To identify the chemical constituents comprising the wear debris, both energy dispersive x-ray spectroscopy (EDX) and electron energy loss spectroscopy (EELS) were employed. EDX in conjunction with diffraction analysis indicated the presence of amorphous oxidized silicon along the worn surfaces. This indicates that the friction bearing surfaces are becoming oxidized during this experiment. As illustrated in figure 1.9.20, the chemical composition for wear debris formed at 1.8% (not shown) and 39% RH is oxidized silicon. This spectrum is shown with a spectrum from the gear tooth to illustrate an increase in the oxygen peak on the stress-tested samples. The carbon peak represented in both spectra is an artifact resulting from the sample preparation technique. We believe localized heating is occurring along the friction bearing surfaces resulting in the formation of silicon oxide. Contacting asperities along these friction-bearing surfaces may oxidize them during operation leading to wearing of oxi-

dized surfaces. By operating microengines in vacuum the oxidizing environment is removed from the system.

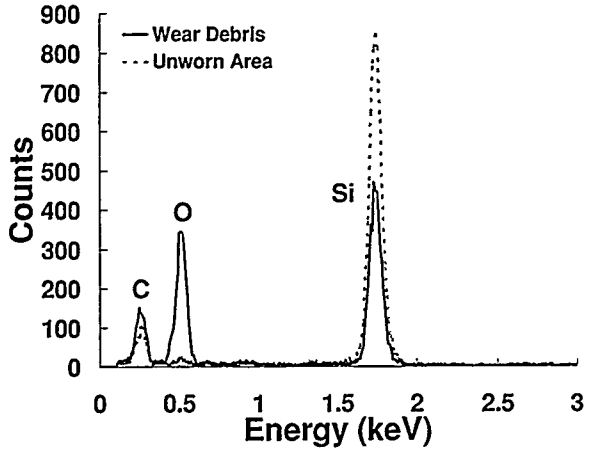

Figure 1.9.20. X-ray spectrum comparing chemical compositions of wear debris at high humidity with an unworn region of the gear. Note the oxide peak in the high humidity spectrum.

Electron Energy Loss Spectroscopy

Electron energy loss spectroscopy (EELS) analyzes the distribution of energy lost by beam electrons as they interact with atoms in the analyzed volume of the sample. The high energy loss region of the EELS spectrum will contain a series of energy-loss "edges" characteristic of the different atomic species present, superimposed on an exponentially decaying back-ground.

EELS analysis of the debris formed at ~0.4% RH (nitrogen environment) indicates the debris is still oxidized silicon. In the presence of a non-oxidizing atmosphere, enough oxygen was present to provide passivation for the friction bearing surfaces of the microengine during operation. Figure 1.9.21 shows a portion of the EELS spectrum from this debris exhibiting a strong oxygen-K signal at 532 eV onset. Note the absence of any nitrogen signal, which would occur at 401 eV onset. The lower energy portion of this spectrum (not shown) contained a strong silicon signal ($L_{2,3}$ edge) at 99 eV onset. Electron diffraction analysis showed that this debris is also amorphous.

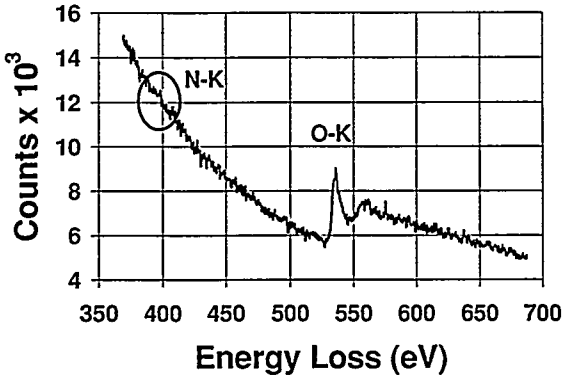

Figure 1.9.21. EELS spectrum of debris formed in a nitrogen rich environment. Note the absence of a nitrogen signal from the wear debris at 401 eV.

Atomic Force Microscopy

The atomic force microscope (AFM) provides very detailed topographic images and surface traces across the sample. Figure 1.9.22 shows the wear debris produced in a microengine on the drive gear of a failed binary counter. AFM was also used to measure the surface roughness wear tracks produced along the guide of the microengines. Figure 1.9.23 shows a topology image of an area, which includes the wear track. Smoothing was observed in the track, compared to the region just outside of the track. A line scan is also shown in figure 1.9.24.

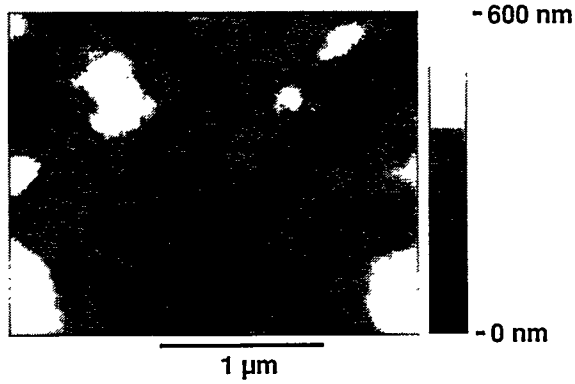

Figure 1.9.22. AFM topographic image of wear debris produced in a failed binary counter.

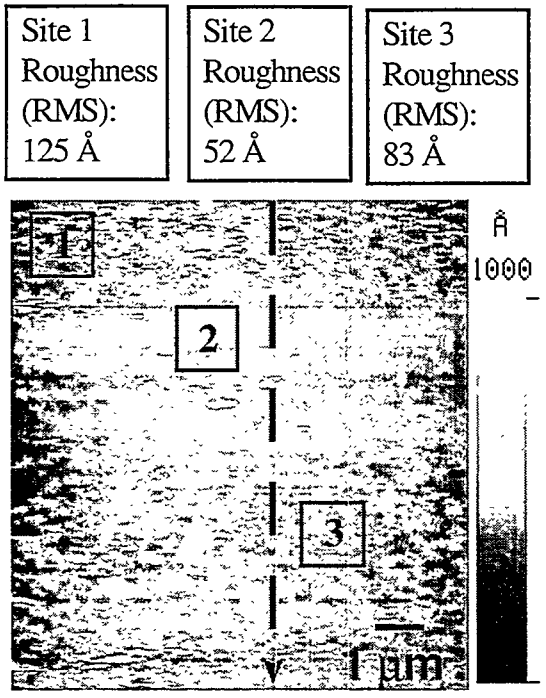

Figure 1.9.23. AFM topology image of a wear track. The dashed line indicates the position of line scan of Figure 1.10.7.3.

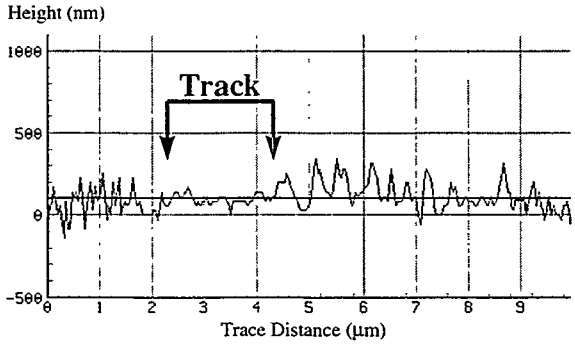

Figure 1.9.24. Topology line scan of the wear track.

Acoustic Emission

Acoustic emission was also evaluated on several engines while they were running. This involved the attachment of a sensor to the package containing the microengines and "listening" for acoustic events as microengines were operated. No signal was resolvable above the background noise level, but changes in vertical displacement were observed.

Acoustic Microscopy

Acoustic microscopy was employed on stationary microengines in an attempt to resolve contact between stuck gears and links and the substrate. This technique is more destructive to the sample due to the introduction of water as a coupling fluid. The acoustic signal could not be translated into evidence of sticking, although morphological features were resolved.

Figure 1.9.25 shows a sample of the visual output for a gear that had tilted, causing a gradient in its intensity across the image.

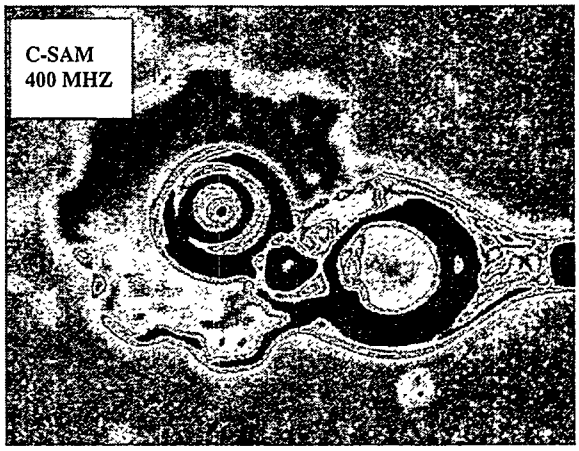

Figure 1.9.25. Acoustic microscopy resolves the tilt of a gear, but no contact.

Combs were also resolved, but no information was gained regarding points of contact.

Scanning Laser Microscopy

Scanning laser microscopy has been used primarily to obtain confocal images. A confocal image is an image with a very limited depth of field (depth of focus) created by inserting an aperture in the optical path. By taking a series of confocal images at different focal planes, an extended depth of focus image can be constructed. The extended depth of focus image is particularly useful in resolving elements that have abnormal verti-

cal displacements. Figure 1.9.26 shows an example where a malfunctioning comb drive was not free to translate in plane, but did deform out of plane under power. The image in Figure 1.9.26 (a) was obtained by subtracting an unpowered extended depth of focus image from the powered one.

The grayscale in the image represents different sample heights. Bright areas indicate a larger height. Both the low-magnification and high magnification images of the comb drives and shuttle reveal significant vertical displacement. The bright region shown in the shuttle and movable comb areas indicates that these two components of the microengine levitates under power. The fixed combs do not change height under power and appear dark in the image.

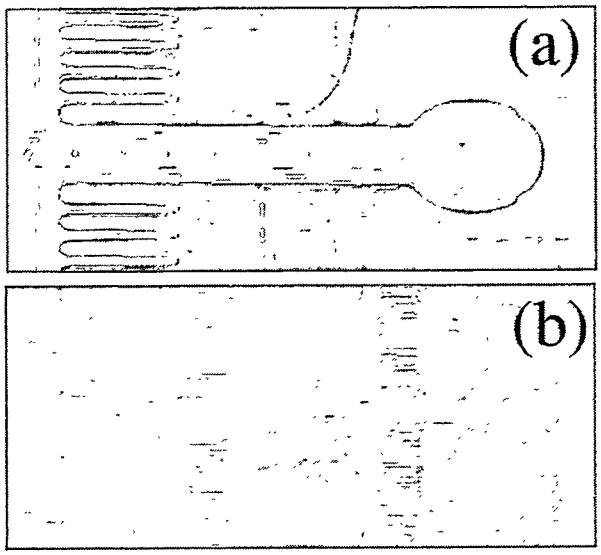

Figure 1.9.26. (a) Levitation of tail end of shuttle and movable combs. (b) Gradient of shuttle levitation with larger field of view.

Infrared Microscopy

Several operating microengines were examined using an infrared microscope to construct thermal images based on the infrared radiance emitted from the structures. Figure 1.9.27 shows a thermal image of the x-comb drives of an early version of the microengine during operation. The attached gear was rotating irregularly with a pause in the rotation cycle. Hot spots (areas where the radiance increased in the image) were found in the X-comb drives. We suspect the hot spots were caused by intermittent contact of the comb fingers. In gray scale, the hot spots appear dark, and are indicated by arrows in figure 1.9.27.

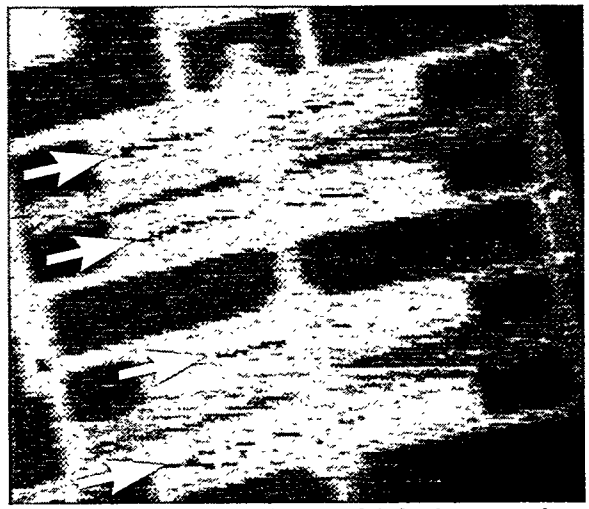

Figure 1.9.27. Infrared image of defective operating engine showing hot spots (dark in appearance) in X comb drive area.

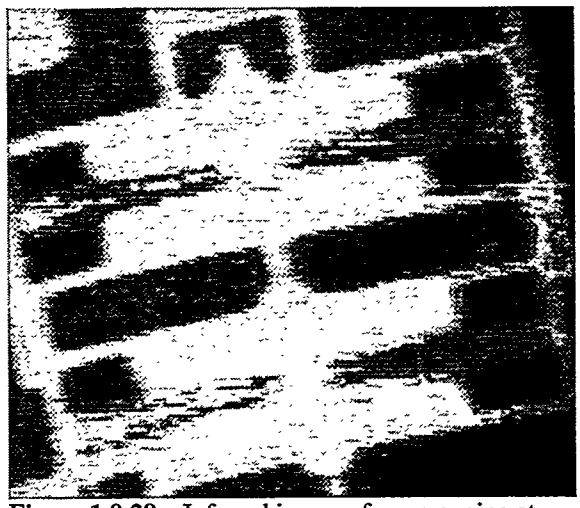

Figure 1.9.28. Infrared image of same engine at rest.

No hot spots were found in the y-comb drives, nor were found in the comb drives of engines operating with smooth rotation or at rest (figure 1.9.28).

This technique was also utilized to detect comb fingers sticking to the substrate. As illustrated in figure 1.9.29, the arrow points to a comb finger, which is not at the appropriate z-height from the substrate. This indicates displacement along the z-axis and in this instance, the comb finger is stuck to the substrate by stiction related forces.

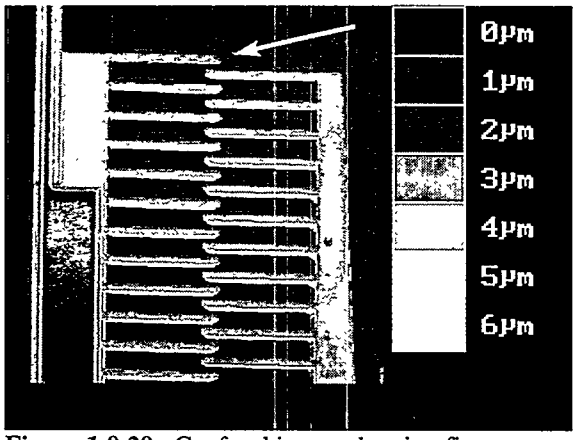

Figure 1.9.29. Confocal image showing finger which is displaced out of plane (arrow, darker contrast) and is in contact with the substrate.

Light Emission

The possibility of arcing at combs suggested the use of light emission analysis, (common in FA of ICs). The same microengine that exhibited the hot spots in Figure 1.9.27 was analyzed using LE, but no emitted light was resolved under the same operating conditions.

Laser Cutting

A laboratory laser cutter has been used to excise portions of circuits and sever connections to determine which elements are free or stuck. It has also been used to impart energy to members such as gears and links which moves like a shock wave to agitate discrete portions of the overall system (Figure 1.9.30).

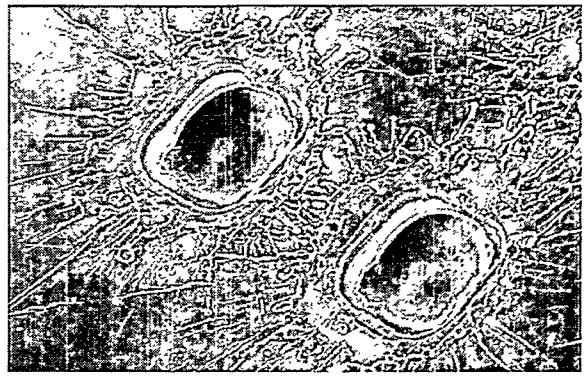

Figure 1.9.30. Laser marks used to free up a region of the microengine.

Lift-off techniques

Carefully removing elements using a conductive laboratory adhesive tape used for SEM mounting has added another dimension to post-mortems of microengines. By looking at the bottom surfaces of engines, details of operation such as the accumulation of wear debris or out of round damage to pin receiver holes can be checked. Figures 1.9.31 and 1.9.32 illustrate the lift out technique looking at the underside of a gear half (1.9.31) and the bottom side of a shuttle (1.9.32).

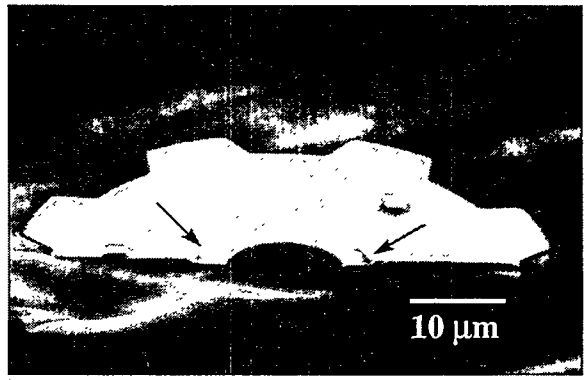

Figure 1.9.31. Microengine gear that has been microsectioned in the FIB and separated for SEM examination of bearing surfaces.

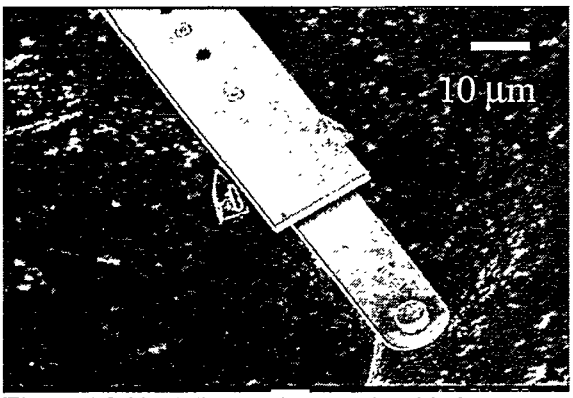

Figure 1.9.32. Microengine shuttle with the gear microsectioned off in the FIB.

[12] D. M. Tanner, N. F. Smith, D. J. Bowman, W. P. Eaton, and K. A. Peterson, "First Reliability Test of a Surface Micromachined Microengine using ShiMMeR", *SPIE Symposium on Micromachining and Microfabrication*, **Vol. 3224**, Austin, TX 1997, pp. 14-23.

[13] S. L. Miller, M. S. Rodgers, G. Lavigne, J. J. Sniegowski, P. Clews, D. M. Tanner, and K. A. Peterson, "Failure Modes in Surface Micro-machined MicroElectroMechanical Actuators", *IEEE International Reliability Physics Symposium Proceedings*, San Diego CA, 1998, pp. 26-35.

[14] K. A. Peterson, P. Tangyunyong, and A. Pimentel, "Failure Analysis of Surface-Micromachined Microengines", *Materials and Device Character-ization in Micromachining Symposium*, SPIE Proceedings, Santa Clara CA, 1998, **Vol. 3512**, pp. 190-200.

[15] K. A. Peterson, P. Tangyunyong, and D. L. Barton, "Failure Analysis for Micro-Electrical-Mechanical Systems (MEMS)", Proc. *Proceedings from the 23rd International Symposium for Testing and Failure Analysis*, Santa Clara CA, 1997, pp. 133-142.

Intentionally Left Blank

Chapter 2. Test Structure Development

Intentionally Left Blank

2.1 Introduction

This section will document the development of reliability test structures. By far, the most used device for studying reliability has been the Sandia microengine [16]. The microengine is the actuator used in most of our applications, devices like transmissions, gear trains, linear racks, and pop-up mirrors [17].

The microengine consists of orthogonal linear comb drive actuators mechanically connected to a rotating gear as seen in Figure 2.1.1. By applying model-based voltages, the linear displacement of the comb drives is transformed into circular motion of a gear [18]. The X and Y linkage arms are connected to the gear via a pin joint. The gear rotates about a hub, which is anchored to the substrate.

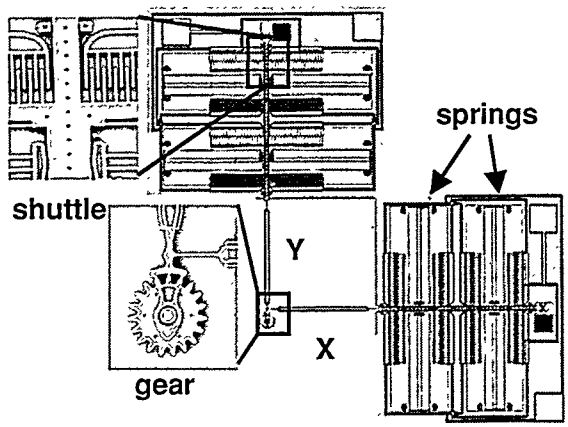

Figure 2.1.1. Sandia microengine with expanded views of the comb actuator (top left) and the rotating gear (bottom left).

The following subsections will describe the modules designed specifically to perform reliability work. Because we are interested in large sample sizes, we typically pack as many devices of the same variety into one module as possible.

Subsection 2.2 describes the module using the standard microengine. In subsection 2.3, we report on a module with a newer symmetric microengine. Subsection 2.4 will describe a device developed to easily observe wear using comb actuators. A modified symmetric actuator and an actuator gage designed to measure displacement are reported in subsection 2.5.

A new method and apparatus to measure force in MEMS devices was developed and is described in subsection 2.6. The method uses the actuator gage for spring constant measurement.

---

[16] E. J. Garcia and J. J. Sniegowski, "Surface micromachined microengine", Sensors and Actuators A, **Vol. 48**, 1995, pp. 203-214.

[17] http://www.mdl.sandia.gov/Micromachine

[18] S. L. Miller, J. J. Sniegowski, G. LaVigne, and P. J. McWhorter, "Performance tradeoffs for a surface micromachined microengine", *Proceedings of SPIE Micromachined Devices and Components II*, **Vol. 2882**, Austin, October. 14-15, 1996, pp. 182-191.

2.2 TP122 module 8

This was the first module designed for reliability testing. A photograph of the entire module is shown in Figure 2.2.1. It consists of 3 microengines with gears and 1 microengine without a gear. In order to make the bond pads accessible, each microengine is rotated by 90° and positioned in the adjacent quadrants of the module. The microengines are numbered for reference.

The structures seen inside the microengine perimeter were various types of alignment marks. Many types and sizes were fabricated so that we could choose the mark most recognizable for automated positioning.

Microengine 1 and 2 are identical. An image of the gear is shown in Figure 2.2.2. The gear is in its fabricated (or 'rest') position defined to be 0°. Microengine 3, also shown in the figure, has no gear. It is used for set-up purposes (see sections 1.7 and 3.6) and can be run in conjunction with the

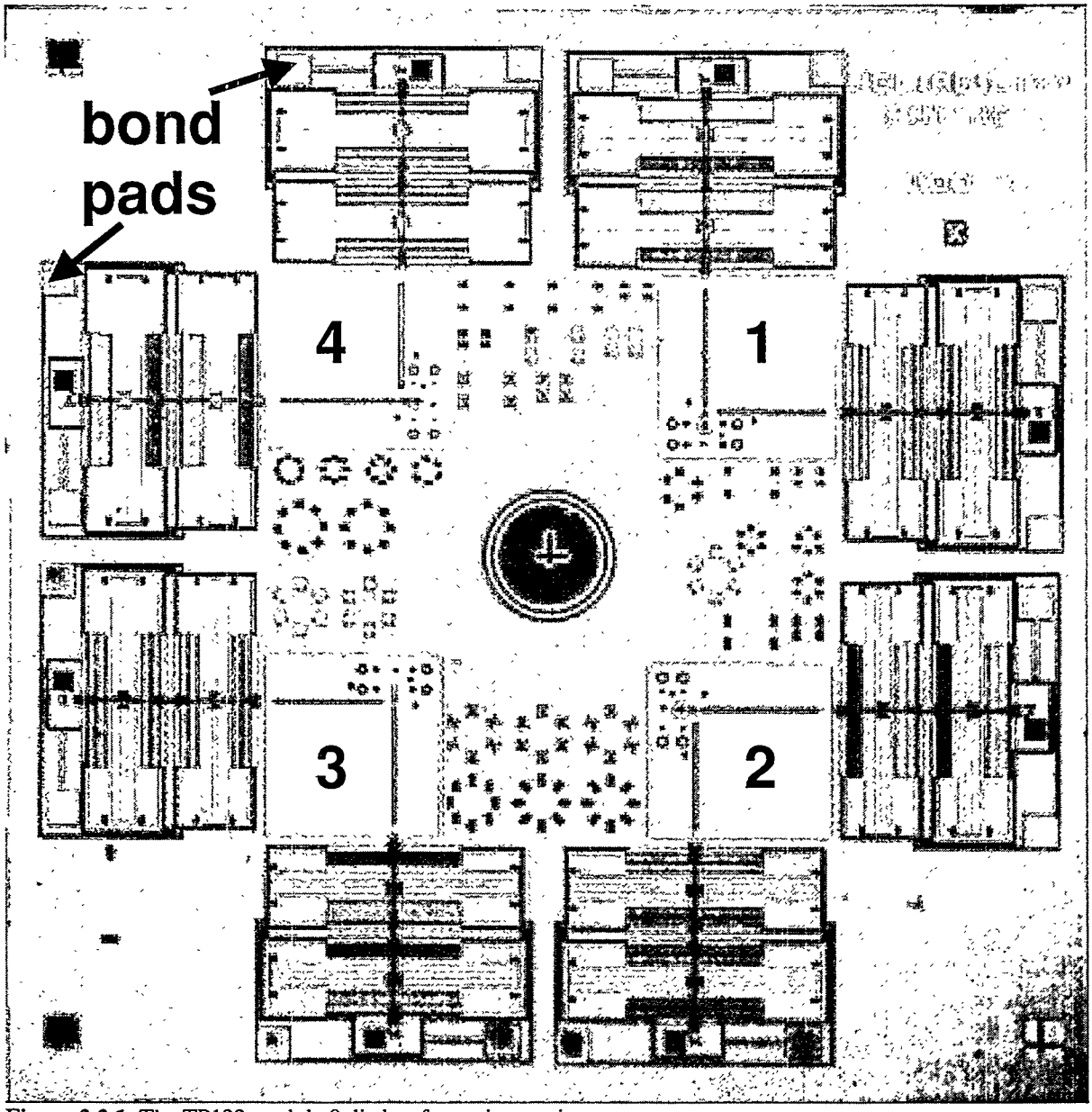

Figure 2.2.1 The TP122 module 8 die has four microengine structures.

other microengines to separate out failures associated with the gear-hub mechanism versus the actuators.

An image of microengine 4 is shown in Figure 2.2.3. This gear was modified for use with a micromachine optical probe (MOP) which consists of a laser and detector developed to sense the motion of the

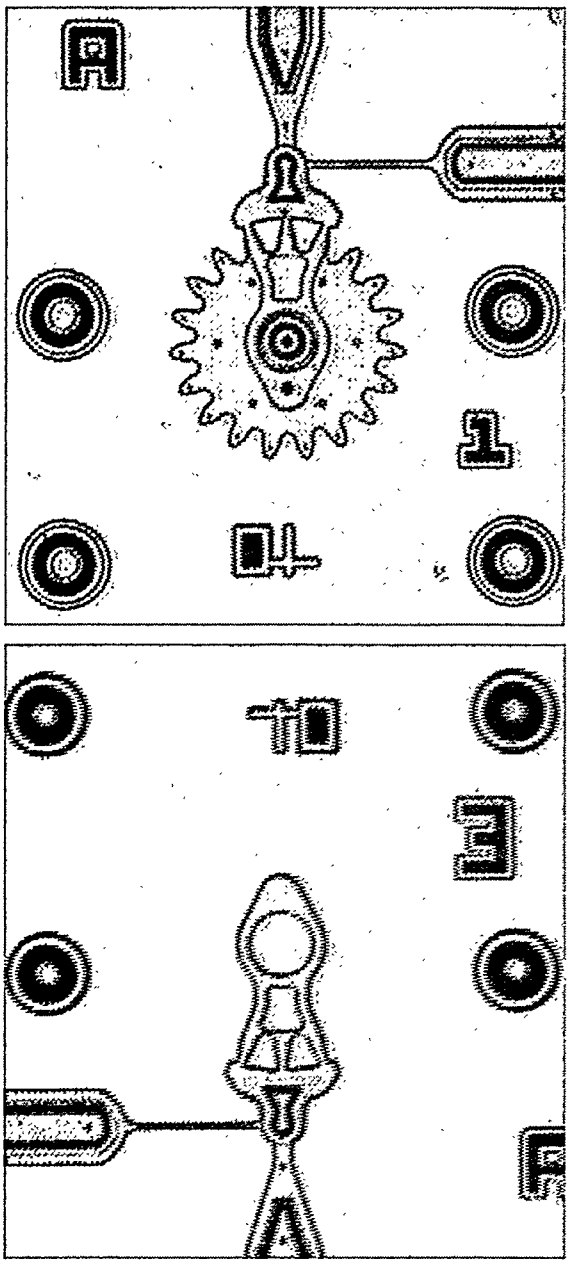

Figure 2.2.2 The top image shows the standard microengine gear of engine 1 and 2. The bottom image shows the gearless microengine, which is used for set-up purposes.

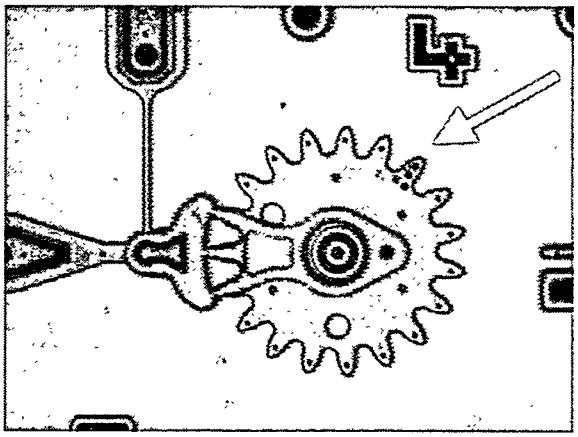

Figure 2.2.3 The arrow indicates the tooth with the etched holes for identification in microengine 4.

teeth [19]. One of the gear teeth has etched holes for identification purposes using MOP. The holes scatter the laser light differently than the other teeth, which provides a marker in the reflected light.

The two large etched holes in the gear face were intended for image analysis. All of the gears have dimples under the gear teeth to prevent wobble.

This module was used for many of the experiments documented in section 3. During the course of this work, it was experimentally determined that the Y comb drive "linearly clamps" during a portion of rotation of the gear [20]. The clamping was due to the force from the fringing fields at the ends of the comb fingers that occur when the combs are fully engaged. This effect increases the force on the drive pin joint.

---

[19] Scott Holswade and Fred Dickey, "Optical measurement of micromachine engine performance," *SPIE Proceedings*, Vol. 3224, 1997, pp.131-140.

[20] S. L. Miller, M. S. Rodgers, G. LaVigne, J. J. Sniegowski, P. Clews, D. M. Tanner, K. A. Peterson, "Failure Modes in Surface Micromachined MicroElectroMechanical Actuators," *Proc. 1998 IEEE International Reliability Physics Symposium,* Reno, NV, 1998, pp. 17-25.

2.3 TP122 module 9

This was the first module designed for reliability testing using a newer version of the microengine with symmetric drives. These actuators do not clamp (either linearly or laterally). A photograph of the entire module is shown in Figure 2.3.1. It consists of 3 microengines with gears and 1 microengine without a gear. In order to make the bond pads accessible, each microengine is rotated by 90° and positioned in the next quadrant of the module. The microengines are numbered for reference.

The structures seen inside the microengine perimeter were various types of alignment marks. Many types and sizes were fabricated so that we could choose the mark most recognizable for automated positioning..

Microengine 1 and 2 are identical. An image of the gear is shown in Figure 2.3.2. Note the change from Figure 2.2.2 for the fabricated ('rest') position of the gear. Because symmetric actuators are used, the gear is rotated 45° from its previous position.

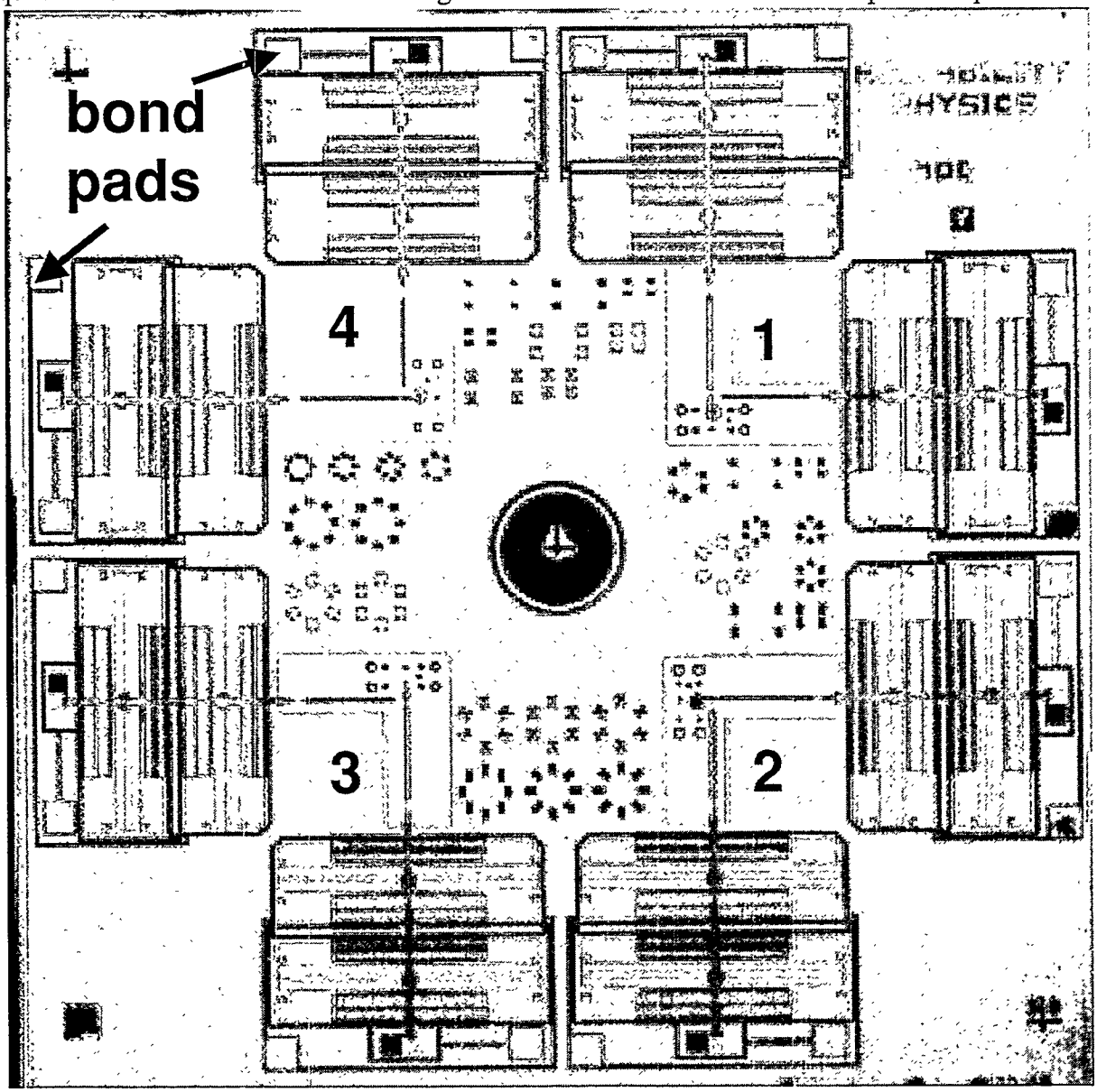

Figure 2.3.1 The TP122 module 9 die has four microengine structures.

The gear diameter is 80 μm. Microengine 3, also shown in the figure, has no gear. It is used for set-up purposes (see sections 1.7 and 3.6) and can be run in conjunction with the other microengines to separate out failures associated with the gear-hub mechanism versus the actuators.

An image of microengine 4 is shown in Figure 2.3.3. This gear was modified for use with a micromachine optical probe (MOP) which consists of a laser and detector developed to sense the motion of the teeth [21]. One of the gear teeth has an etched hole for identification purposes using MOP. The hole scatters the laser light differently than the other teeth, which provides a marker in the reflected light. The etch hole here is different from TP122 module 8.

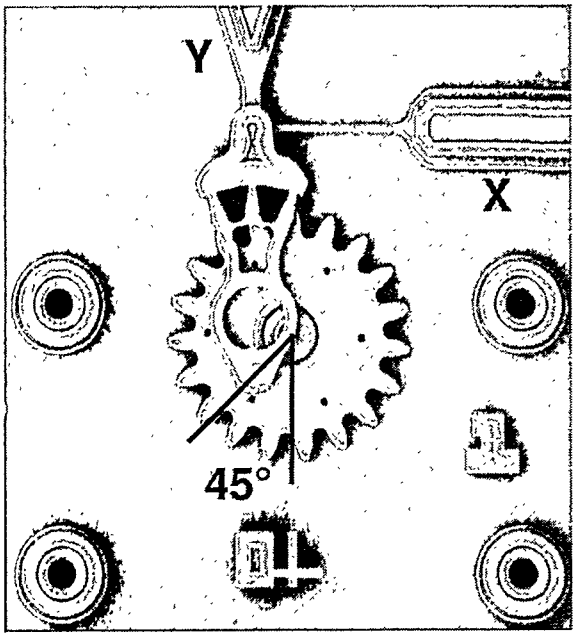

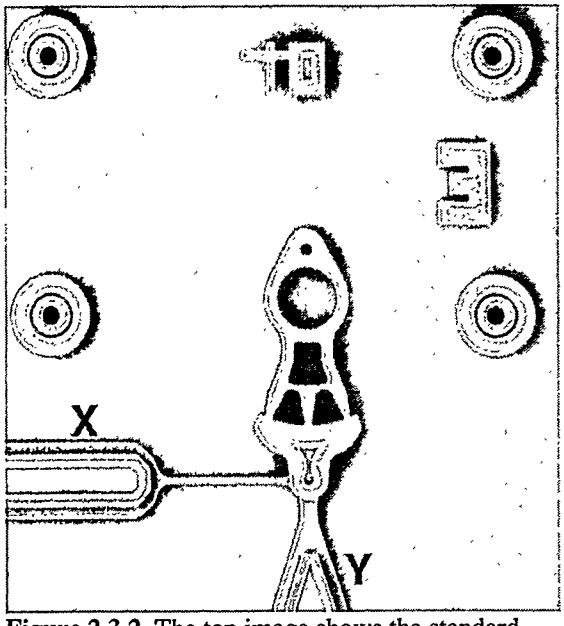

Figure 2.3.2 The top image shows the standard microengine gear of engines 1 and 2. The bottom image shows the gearless microengine, which is used for set-up purposes.

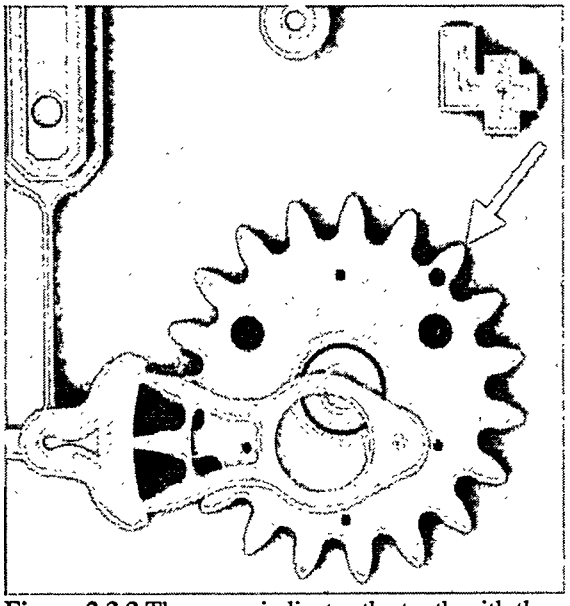

Figure 2.3.3 The arrow indicates the tooth with the etched holes for identification in microengine 4.

The two large etched holes in the gear face were intended for image analysis. All of the gears have dimples under the gear teeth to prevent wobble.

The symmetric actuators employed a different guide system with more lateral constraint and an attempt at vertical constraint. It is shown in Figure 2.2.3. The two guides prevent lateral motion of the shuttle. In the figure, the shuttle moves up and down. Our fabrication design rules require 1-micron gaps, which is shown with the shuttle in the rest position. When the shuttle moves up or down that gap reduces to 0.25-micron.

Also shown in the figure are the layer indentations where dimples are formed. The typical separation between polysilicon layers is 2 micron. The dimple protrudes down

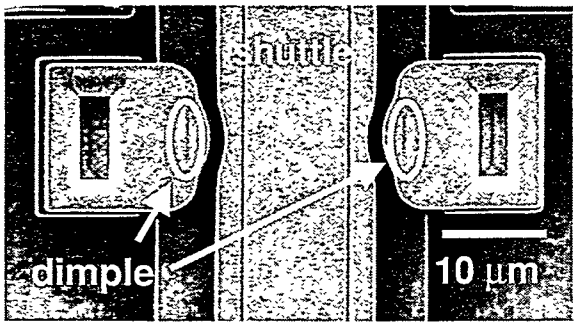

Figure 2.3.4 This SEM image of the shuttle and guides shows the indentation made by the long dimples to reduce vertical motion.

into this separation thus reducing it to 0.5-micron. The dimple was originally designed to serve as vertical restraint to control the levitation of the combs.

It was hoped that these microengines would be much more reliable than TP122 module 8. However, the new actuator guides added friction and another source of rubbing. The initial experiment with this module had a lifetime an order of magnitude worse than TP122 module 8.

The dimple and the tighter lateral tolerance both caused excessive wear and adhesion. A later version, TP157, eliminated the dimple and increased the gap to 0.5 micron hoping to improve the lifetime results.

---

[21] Scott Holswade and Fred Dickey, "Optical measurement of micromachine engine performance," *SPIE Proceedings*, Vol. 3224, 1997, pp.131-140.

2.4 TP157 module 3

After it became evident that wear was a substantial factor in failed microengines, we developed a device to mimic the wear inside the hub of the microengine. Probing inside the hub required a FIB cut which was expensive and time consuming. Development of this wear device allowed direct viewing of the worn surfaces.

The wear device was fabricated as a reliability-testing module. It used a newer version of the microengine with symmetric drives that do not clamp. A photograph of the entire module is shown in Figure 2.4.1. It consists of a wear device with a smooth rubbing surface (1), two wear devices with defined surfaces (2 and 3) and a gearless microengine (4). In the center of the die is a 'Force Detector,' which will be described fully in section 2.6.

In order to make the bond pads accessible, each device was rotated by 90° and positioned in the adjacent quadrant of the

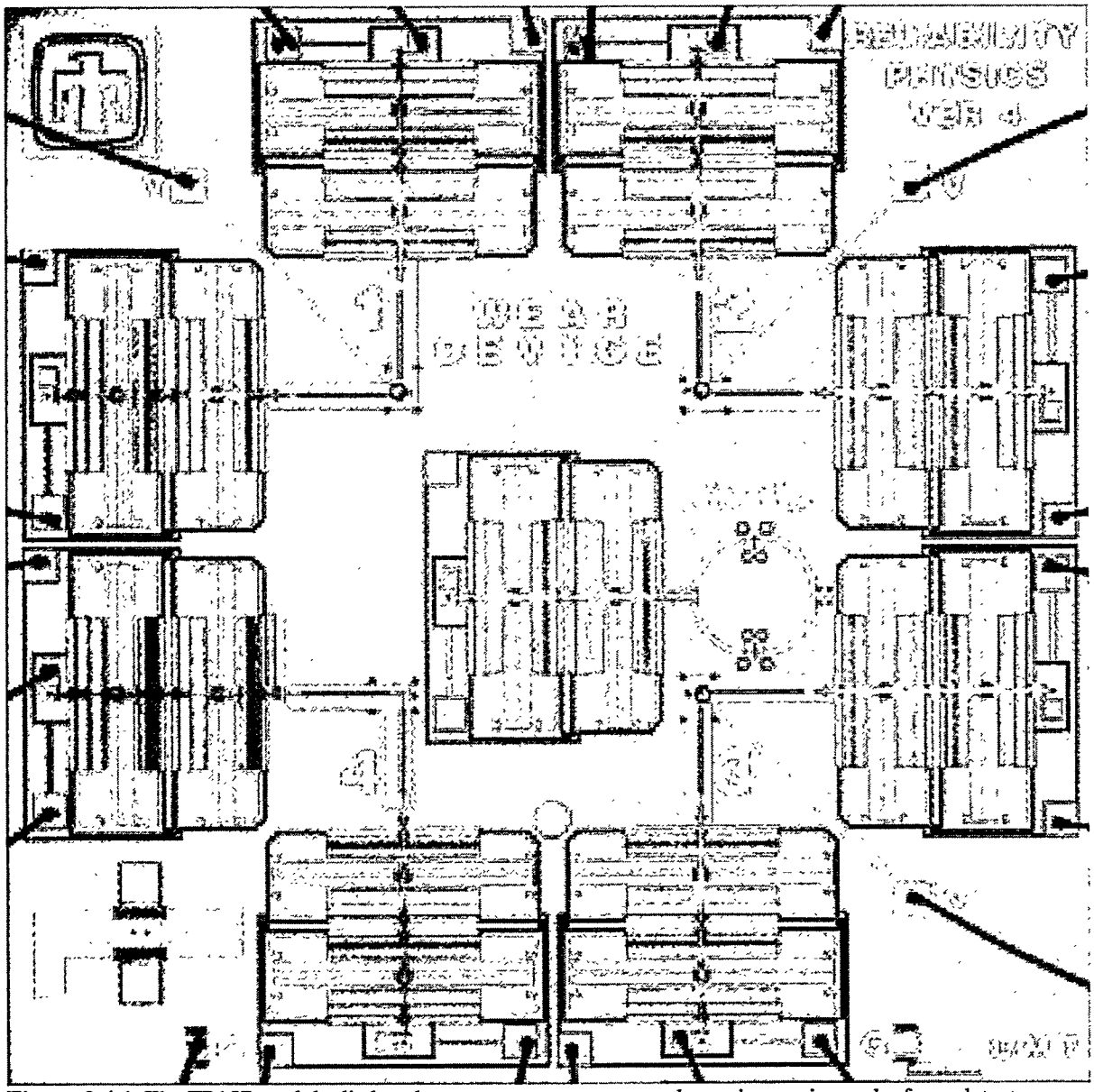

Figure 2.4.1 The TP157 module die has three wear structures, a gearless microengine and a force detector.

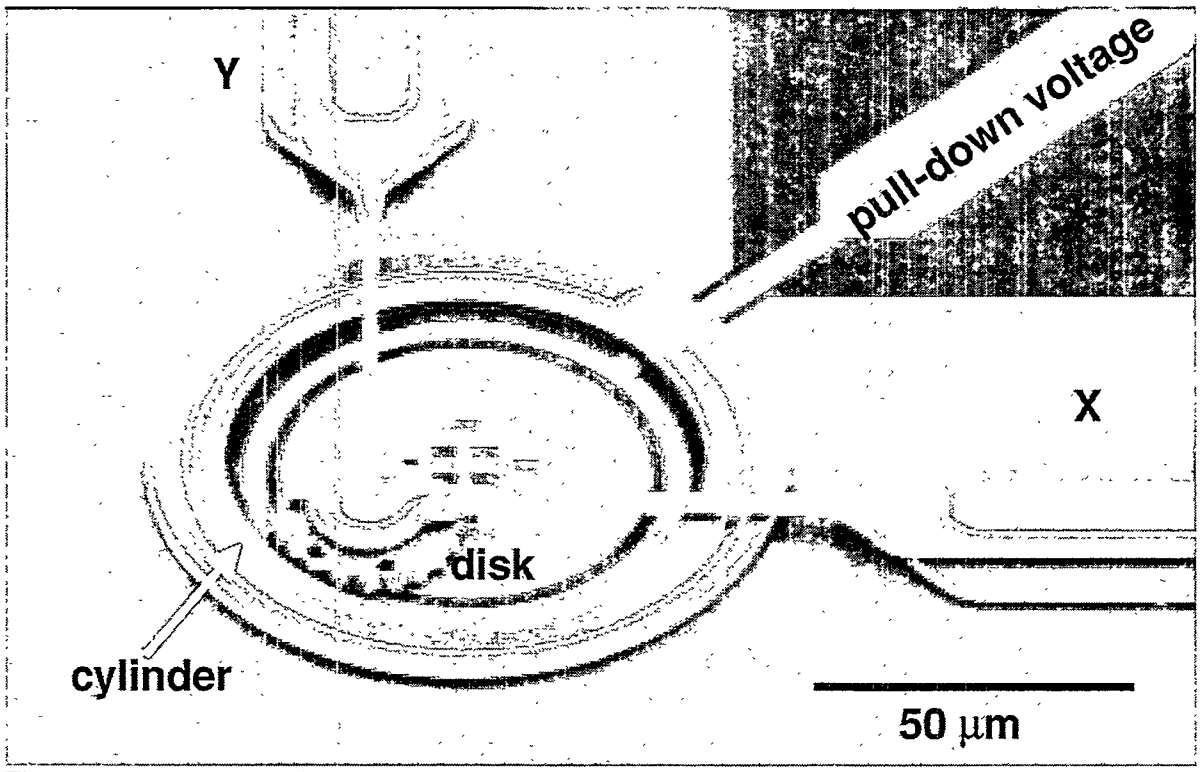

Figure 2.4.2 SEM image of the wear device which shows the wavy-edged disk that rotates against the inner wall of the cylinder.

module. The devices are numbered for reference. Bond wires appear as dark lines in Figure 2.4.1.

A view of the wear device is shown in Figure 2.4.2. The x and y linkage arms are connected to a fixed disk. By applying the proper voltages to the actuators connected to the other end of the linkages, we can move the disk so that it rubs against the inner surface of the cylinder. There is a lead to apply a pull-down voltage if the disk tends to pop out of the cylinder. In order to prevent charge build-up on the disk, the center of the ground plane was grounded to the substrate through the square array of nitride cuts. To inspect for wear debris, we simply lift the disk out of the cylinder and look at each surface.

The disks were fabricated with two surface morphologies. The smooth-edged disk is shown in Figure 2.4.3. This represents the surfaces of the microengine and can be used for inspection of wear tracks. The wavy-

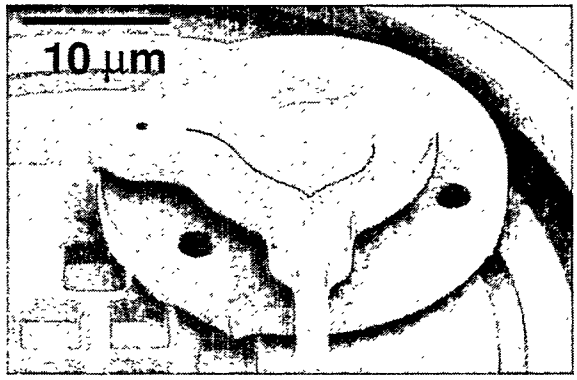

Figure 2.4.3 SEM image of the smooth disk that rubs against the cylinder.

edged disk has 20 equally spaced curves on the rubbing surface and is shown in Figure 2.4.4. Each curve has a defined radius of curvature of 1 μm. The wavy-edge disk allows determination of the contact angle of the rubbing surfaces so that the coefficient of friction may be calculated.

Using model-based drive signals with no radial or longitudinal force, the wear device will move in the same 17-μm circle as the microengine without touching the cylinder

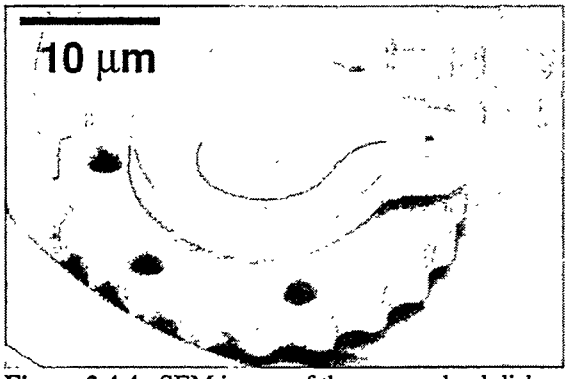

Figure 2.4.4. SEM image of the wavy-edged disk that rubs against the cylinder.

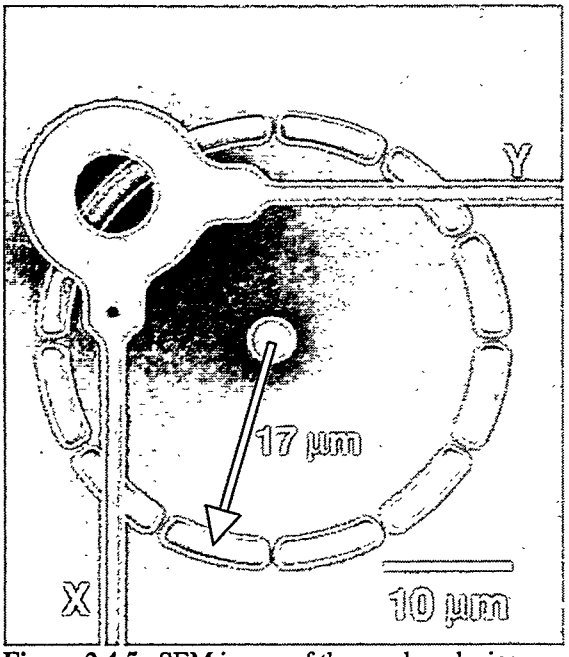

Figure 2.4.5. SEM image of the gearless device. The circle was defined by ground plane cuts to have a radius of 17-µm.

walls. Inputting a radial force into the equations will provide a normal force to the rubbing surfaces.

The other crucial device on this module is a gearless microengine. The only way to check the model-based drives signals is to track a microengine that's not constrained with a gear and hub. The device shown in Figure 2.4.5 allows tracking of the movement of the linkage arms. The 17-µm circle formed by etch holes in the ground plane defines ideal motion. The circular post in the center and the large etch hole in the linkage arm joint provide good marks for image analysis.

We discovered that the guides in the wear device were contributing friction that was not accounted for in the equations. We have successfully broken off the guides and can map out a perfect circle using our model-based drive signals.

Our preliminary testing of the device revealed an inadequacy in the design. The pull down voltage ring does not provide the proper area to yield enough electrostatic force to hold the device in the cylinder. This will be fixed in the redesign.

We also found that the image analysis routine could use better defined circles to track the center of the cylinder and the center of the disk. Again, this is an easy redesign fix.

2.5 TP157 module 4

This was another module designed for reliability testing using a newer version of the microengine with symmetric drives that do not clamp. A photograph of the entire module is shown in Figure 2.5.1. It consists of two microengines driving load gears and two simple microengines. In order to make the bond pads accessible, each microengine is rotated by 90° and positioned in the next quadrant of the module. The microengines are numbered for reference.

The structure seen inside the microengine perimeter is an actuator with a gage to measure displacement. The structures in the lower corners of the module are resonators.

The improvements made over TP122 module 9 were a) removal of the dimple in the guide, b) widening the tolerance in the guide to 0.5 micron, c) providing separate grounds for each microengine, d) adding another flexure, and e) using a triangular grouping of the alignment marks near each gear.

Microengines 1 and 2 are identical. An

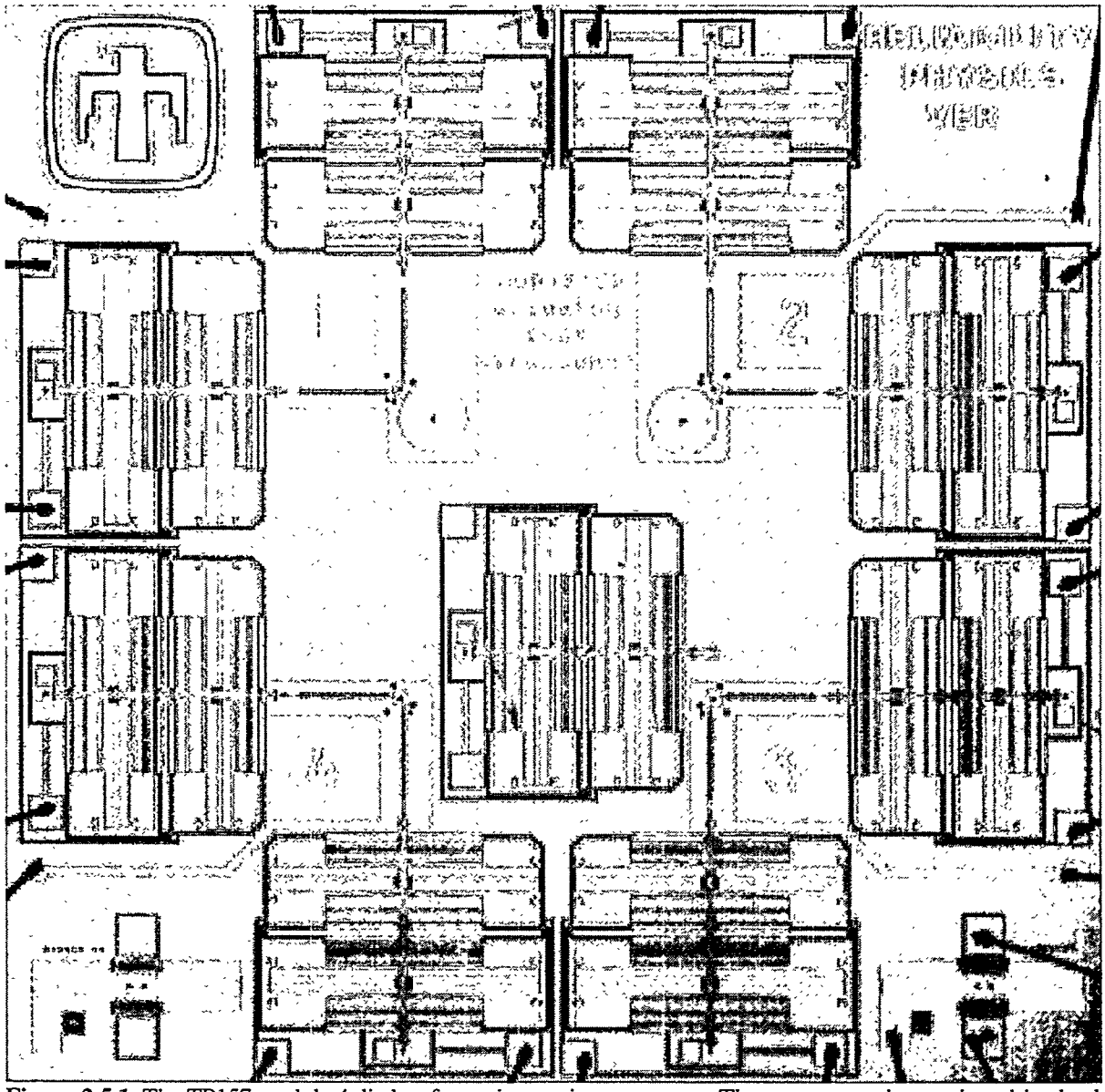

Figure 2.5.1. The TP157 module 4 die has four microengine structures. The upper two microengines drive load gears.

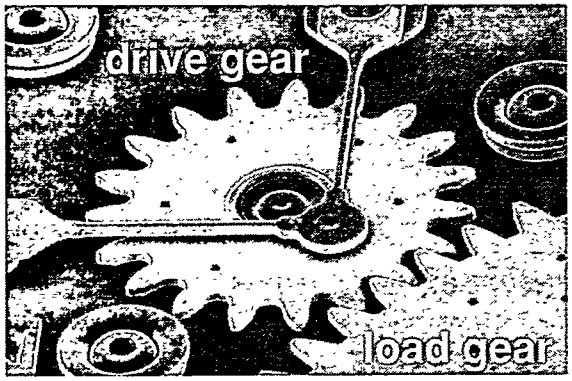

Figure 2.5.2. SEM image of the coupling between the drive gear and the load gear.

image of the drive gear and a portion of the load gear are shown in Figure 2.5.2. The drive gear in the picture has 19 teeth and a diameter of 80-μm. The linkage arm flexures are 2-μm wide and 40-μm long.

The simple microengine is shown in Figure 2.5.3. Note the new flexure in the y linkage arm and the triangular array of alignment marks. The rest position of the gear is rotated 45° from the position in the standard microengine.

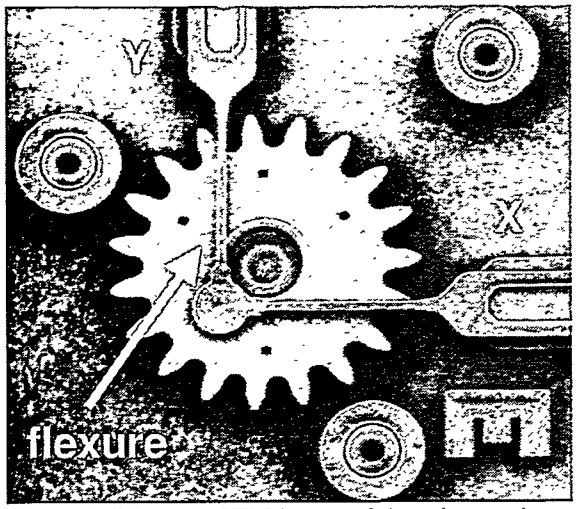

Figure 2.5.3. This SEM image of the microengine shows the new flexure for the y linkage arm and the triangular array of alignment marks. The gear has a diameter of 80-μm.

The actuator gage shown near the center of the die allows the measurement of voltage applied to the electrostatic combs versus displacement. The actuator and gage are

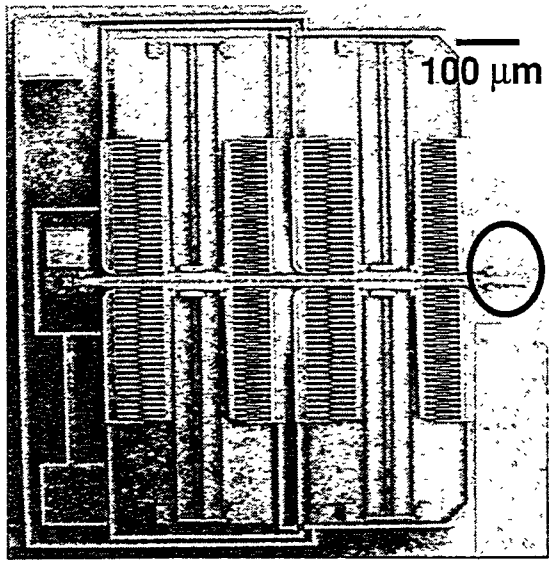

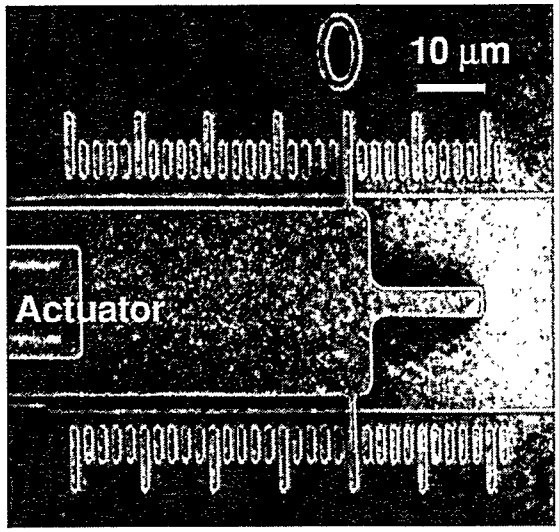

Figure 2.5.4. The top view is an image of the actuator. A close-up of the gage (circled region) is shown in the lower figure.

shown in the top of Figure 2.5.4 and a closer view of the gage is shown on the bottom.

Applying voltage to the lower left pad of the actuator causes the gage to move left (pull). The opposite effect will happen when applying voltage to the upper left pad (push). The gage was designed to measure more pull than push because of the functionality of the actuator.

In our first test of the gage and actuator, we applied voltage to pull the gage to the left in 2-micron steps. Data from this test is shown in Figure 2.5.5. We plotted voltage squared versus displacement to achieve a straight line. This gage was used in conjunction with the force detector described in the next subsection.

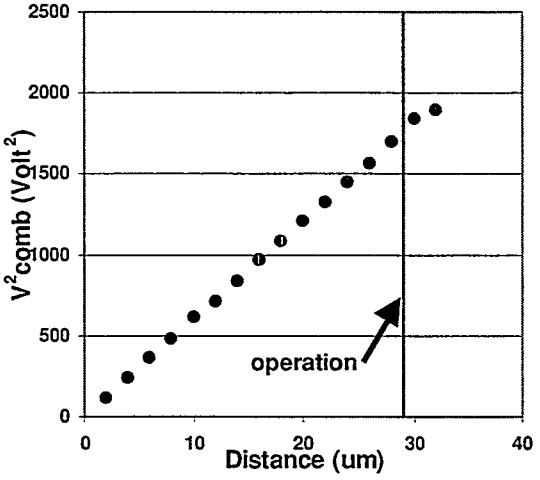

Figure 2.5.5. This data was taken with the actuator and gage. Voltage was applied to pull the gage back in 2-micron steps. The distance it must move for proper operation is noted on the graph.

2.6 Force Detector

In order to characterize an electrostatic actuator, the spring constant and force output of the actuator must be determined. The measurement of force output requires the actuator to move a known structure (typically a cantilever beam) a measurable distance. Bending equations are then used to calculate the force. We will describe a novel test structure called the 'force detector' and the complete techniques used to determine force and spring constant.

The force detector consists of a ring of polysilicon anchored to the substrate at one location and attached to the actuator 180 degrees from the anchor as shown in Figure 2.6.1. The ring radius is 250 μm and the width of the ring was 4 μm. The ring thickness was defined in our process to be 2.5 μm. Pulling from the actuator end will elongate the ring, with deflections measured in three locations (X, Y1, and Y2). A closer view of the calibration tick marks (each mark is 1 μm wide and they are separated by 1 μm) are shown in Figure 2.6.2. The upper

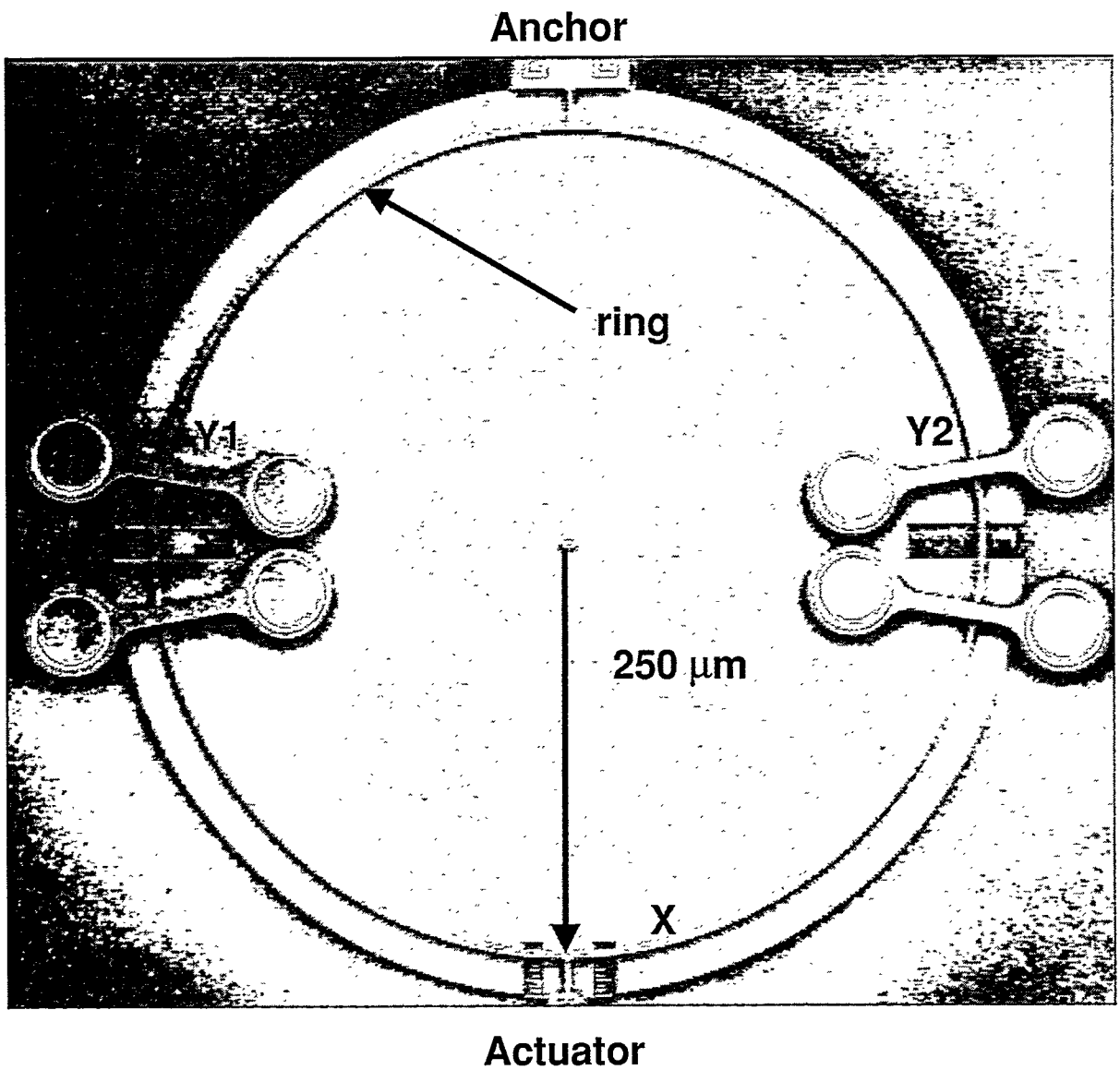

Figure 2.6.1 This SEM image of the force detector shows the ring and the location of the anchor and actuator. The force detector ring has gages at the three locations of X, Y1, and Y2.

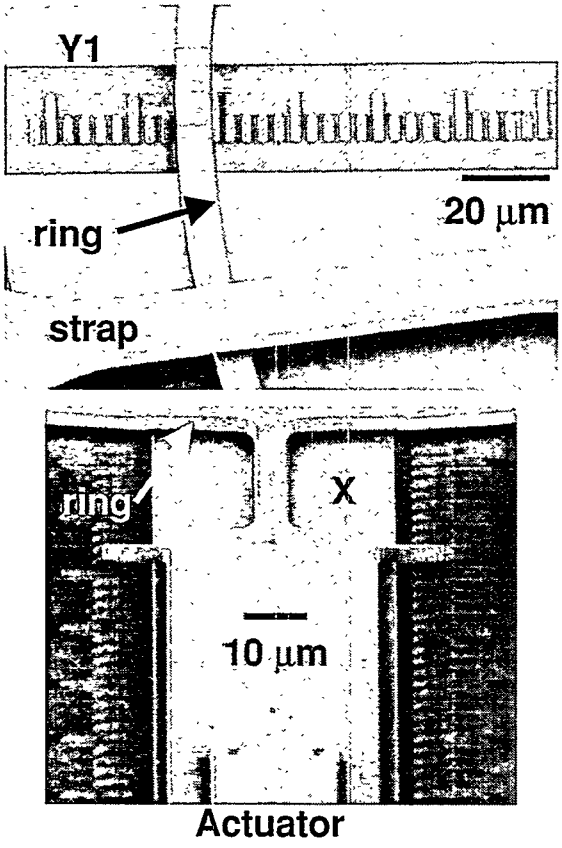

Figure 2.6.2. The upper SEM image shows the Y1 deflection measurement. Note the ring and the higher-level polysilicon strap. The X deflection measurement arm that attaches to the actuator is shown in the lower SEM image.

SEM image shows the ring in relation to the tick marks and the higher level polysilicon strap used to prevent curl in the structure. The lower SEM image is a closer view of the actuator attachment to the ring. Note the tick marks used for deflection measurement.

Standard formulas for circular rings were used to calculate the force necessary to cause deflection [22]. For deflection toward the actuator (D_x), we have

$$D_X = 0.137\frac{Fr^3}{EI} \qquad (1)$$

where r is the radius of the ring, E is Young's modulus for polysilicon (0.155 N/μm^2), and I is the bending moment. A similar equation exists for deflections in the y direction (D_Y),

$$D_Y = D_{Y1} + D_{Y2} = -0.149\frac{Fr^3}{EI} \qquad (2)$$

where the negative sign indicates movement toward the center of the ring. The bending moment, I, is

$$I = bw^3/12 \qquad (3)$$

where w is the width of the ring (4 μm) in the plane and b is the polysilicon layer thickness (2.5 μm).

Equations 1 and 2 can be solved for force, F, so that when we apply a voltage and measure a deflection, calculating the force is straightforward. In electrostatics,

$$F = -aV^2 \qquad (4)$$

where the minus sign indicates an attractive force. The constant, a, is simply the slope of F versus V^2.

The determination of spring constant, k, requires a simpler structure consisting of an actuator and a gage. Figure 2.5.4 in the previous subsection shows the gage used for this measurement; the actuator was located to the left of the figure and is not shown. The tick marks were fabricated in the poly0 level and the movable gage was fabricated in an upper poly2 level. Voltage was applied to the actuator which caused deflections, x, in the gage. We then plot V^2 versus x and use the equations,

$$F = kx = aV^2 \qquad (5)$$

to calculate the slope, k/a. The earlier value of a combined with this result will yield a value for k.

The voltage was adjusted on the force detector actuator to yield displacement steps in the X gage of 2 μm. Data from five force detectors is shown in Figure 2.6.3. Each set of data was analyzed using linear regression and the slope was determined. The average a using this technique was $1.34 \pm .06 \times 10^{-4}$ μN/V^2.

Data from the gage was acquired in the same manner. The voltage in the actuator was adjusted to yield displacement steps of

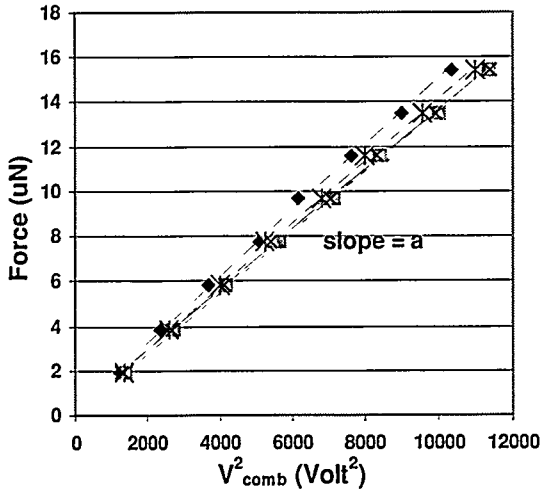

Figure 2.6.3. Data from the force detector. The electrostatic constant, *a*, was determined from the slope.

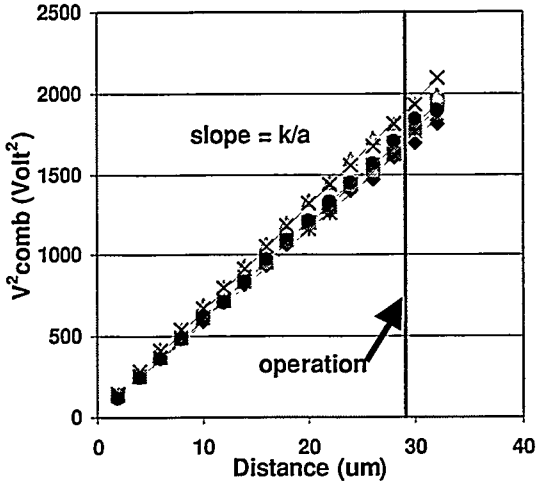

Figure 2.6.4. Data from the actuator and gage are shown. The actuator must move to the operation line in order for a microengine to run.

2 μm. Data from five gages is shown in Figure 2.6.4 where each slope was determined. The average *k/a* was 60.2 ± .3.9 $V^2/\mu m$. For operation of a microengine, the actuator must move at least 29 μm and that displacement is noted on the graph.

Both data sets reveal the variation in the fabricated devices. The value of spring constant was calculated as .083 ± .0065 N/m that has a combined error of roughly 10%.

---

[22] R. J. Roark, "*Formulas for Stress and Strain*," Fourth Version, McGraw-Hill Book company, p. 172, 1965.

Intentionally Left Blank

Chapter 3. Reliability Experiments

Intentionally Left Blank

3.1 Introduction

All of the sections that follow are data and discussions of the reliability experiments that we have performed. Our experiments started with an attempt to answer the question, "how do these MEMS devices fail?", and ended with a focus on environmental effects.

Section 3.2 describes the first reliability test performed on the Sandia microengine. In section 3.3, we describe the stressing of many microengines at various frequencies, which led to our first reliability model.

In section 3.4, we show how the design of a guide linkage led to a reliability problem. Actuator reliability (a microengine without a gear) is addressed in section 3.5.

The drive signals, which cause circular movement of the gear in a microengine, must be optimized for proper performance. Section 3.6 discusses some of the aspects of this optimization.

The next six sections document our work with various environments. Section 3.7 discusses temperature cycling effects and section 3.8 documents the shock experiments performed. Vibration is addressed in section 3.9 and humidity in section 3.10.

A chamber specifically designed for experimentation on MEMS devices in very well controlled environments is described in section 3.12.

Experiments involving the newer non-clamping microengine are described in section 3.13.

3.2 First reliability test

Below we describe the first-ever reliability stress test on surface micromachined microengines [23]. We stressed 41 microengines at 36,000 RPM and inspected the functionality at 60 RPM. We have observed an infant mortality region, a region of low failure rate (useful life), and no signs in the data of wearout. The majority of the failures were a result of lateral clamping of the comb finger actuation system. This clamping failure occurred before wearout could be observed. A design change preventing lateral motion of the shuttle was recommended.

Experiment Description

The structure tested was the SNL microengine, which consists of orthogonal linear comb drive actuators mechanically connected to a rotating gear as seen in Figure 3.2.1. These microengines are a useful test vehicle to identify failure modes and methods since they possess the rotational/sliding friction components found in many devices. Based on previous work [24], quantifying the process of degradation by observing the changes in behavior of the microengine to failure should yield significant results.

In our experiment to study a statistically significant number of microengines, 52 packages with glass observation covers were put on test. The unsealed covers prevented particle contamination, however the microengines were exposed to the ambient environments of temperature and humidity of the laboratory.

There were two microengines, representing different flexure types, on each die attached in each package. The flexure was either thin (1 μm wide by 25 μm long, as seen in Figure 3.2.1) or thick (2 μm wide by 50 μm long). The flexures are located near the gear where the linkage arms meet and where the shuttle attaches to each linkage arm. In our initial scan to check functionality, we identified 41 working engines to perform the stress test.

The stress test involves a repeated process of stressing the engines at 36,000 RPM for a defined number of revolutions and then observing functionality at 60 RPM. The stress speed of 36,000 RPM was chosen to be below the resonance of the comb drives. In the transition from one speed to the other, we decelerated in one revolution, momentarily stopped the gear (for roughly one sec-

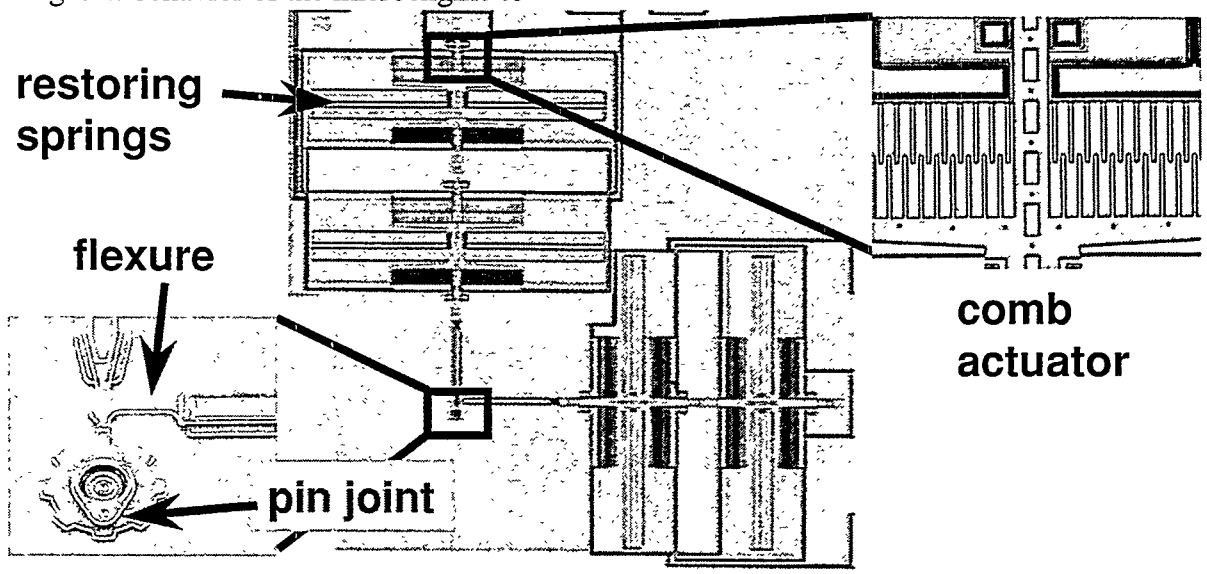

Figure 3.2.1. The microengine with expanded views of the comb actuator (top right) and the rotating gear (bottom left) shown in what we define as the 6 o'clock (or 0°) position.

ond) and then accelerated, again in one revolution, to the other speed. We made the assumption that the stress during the observation period was negligible.

Our criterion for a failed part was the inability to complete a revolution (cycle). During the observation period, we made a decision about the functionality of the engine, flagged the failed engine or commented on the motion of a functioning engine, and recorded the motion of the microengine on video for post test analysis.

At the beginning of the test we stressed for a short duration expecting the weaker parts to fail quickly. As the test progressed, the duration of the stress was increased. The entire test lasted for 28 days with a total of 32 separate stress periods.

The progression to failure was similar in most of the microengines that we observed. The gear went from rotating smoothly to momentarily sticking but completing a revolution. This erratic behavior then led to either the gear oscillating, typically between the 7 o'clock and 11 o'clock positions, or freezing in one position.

Data Analysis

The long-term reliability test resulted in over a billion "stress" cycles (revolutions) on the longest running engines. The last 'record-breaking' failure was at 7 billion cycles. Because the parts were observed at fixed inspection times, common to all the parts, the results fall in the category of reliability data called "interval" data. This is also commonly known as "grouped" or "inspection" data. Useful methods for analyzing this type of data are documented in Nelson [25,26] and Peck [27].

All of the 41 working engines that started the test eventually failed. They exhibited a decreasing failure rate, with no sign of wearout evident in the data. Figure 3.2.2 shows two separate views of the same estimated hazard rate (i.e. instantaneous failure

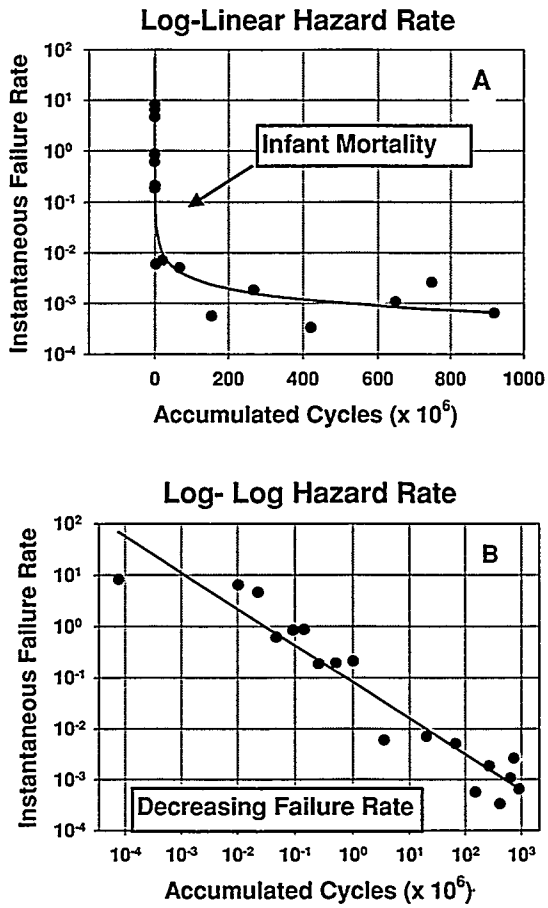

Figure 3.2.2. The instantaneous failure rate (failures per million cycles) was plotted on different scales. The top curve (A) shows the early failure infant mortality region. The bottom curve (B) shows a more detailed representation of the decreasing failure rate throughout the life test.

rate) data from this test. The units on the vertical axis are failures expressed in parts per million (ppm) cycles, i.e. the estimated number of failures that would be expected in one million total device-cycles. This data is "smoothed" by averaging any failures over the stress interval since the last observed failure, providing a conceptual plot of the decreasing failure rate typically associated with the first part of the familiar "bathtub" curve [28]. The "accumulated cycles" axis represents the geometric midpoints in the stress intervals, which is a somewhat arbitrary choice of where to assign the failure times, but consistent with the observed de-

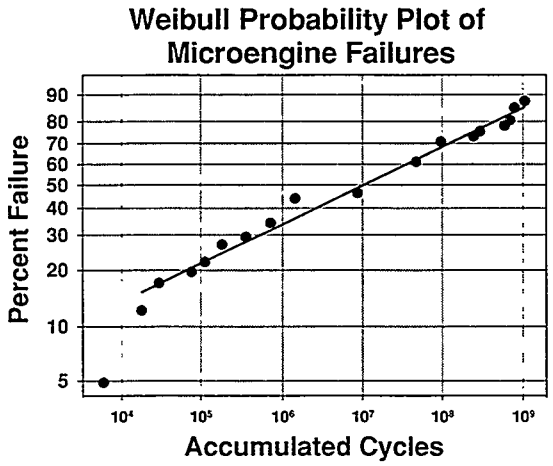

Figure 3.2.3. Microengine failure data fit to a Weibull distribution.

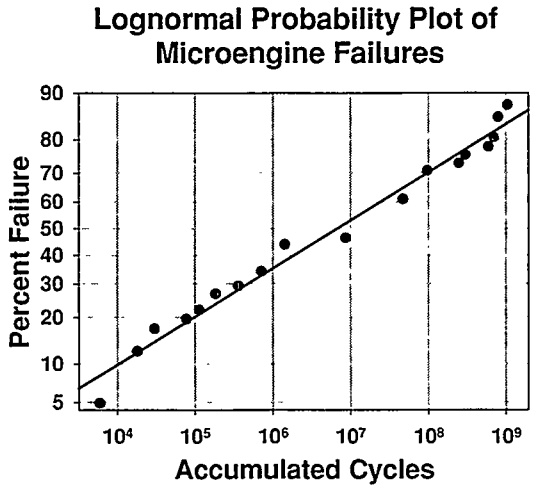

Figure 3.2.4. Microengine failure data fit to a lognormal distribution.

pendency of failure rate on logarithmic time. Figure 3.2.2A uses a linear "accumulated cycles" scale to illustrate a generally decreasing failure rate up to about 1 billion cycles; Figure 3.2.2B uses a log-log scale to show the decreasing tendency in failure rate throughout the life test.

The fact that a straight line could be reasonably fit through the data on the log-log plot of Figure 3.2.2B indicates that an inverse power-law can describe the hazard rate, and in fact the Weibull distribution for decreasing failure rates has a hazard rate function of that form. This curve is primarily meant to be illustrative of a generally decreasing failure rate, and is not a robust curve from which to derive a distribution model. Figures 3.2.3 & 3.2.4 show attempts to fit the data to classical distribution models.

Weibull Distribution

Figure 3.2.3 depicts the fit of our microengine failure data to the Weibull distribution model. The resulting straight-line fit indicates that the Weibull distribution is a reasonable model for cycles-to-failure of these devices. The Weibull fit results in an estimate for the "characteristic life" of $\alpha =$ 66 million cycles (the characteristic life is defined as the point in time when $(1\text{-}e^{-1})$ 100% = 63.2% of the parts are expected to fail), and an estimate for the shape parameter of $\beta = 0.22$. The shape parameter is essentially a measure of dispersion, and lower values correspond to greater spread in logarithmic lifetime. Typical values of β for production-ready electronic and mechanical products fall in the range of 0.5 to 5 [28]. The considerably wide dispersion in lifetimes for the microengines is to be expected because there is still considerable process learning to occur in this infant technology.

Lognormal Distribution

Figure 3.2.4 depicts the fit of our microengine failure data to the lognormal distribution model. The resulting straight-line fit indicates that the lognormal distribution is also a reasonable model. The lognormal fit results in an estimate of a median lifetime of $t_{50\%} = 7{,}800{,}000$ cycles, which means that 50% of the parts would be expected to fail by 7,800,000 cycles. The estimate for the lognormal shape parameter is $\sigma = 5.2$. In this case, the relatively high value of the lognormal standard deviation again indicates a large spread in the log lifetimes. Typical semiconductor products show lognormal

standard deviations in the range of 0.1 to 1.0 [28].

In the case of the lognormal distribution fit it is not simple to determine if the failure rate is decreasing, constant or increasing, since the lognormal distribution can manifest all of these in a single unimodal case. By physical argument, it is reasonable to expect that a transition from infant mortality (decreasing failure rate) to wearout (increasing failure rate) would be due to a change in physical failure mechanism and bimodality would be observed in the distribution fit. Still, increasing and decreasing failure rates cannot be easily discriminated on a lognormal probability plot.

If we examine the lognormal plot more closely, we observe a bimodal distribution as seen in Figure 3.2.5. This is a typical 's-shaped' curve, which implies the presence of two populations. The slopes are equivalent implying one dominant failure mode. The upper population had a median time to failure of $t_{50\%}$ of 2.5 x 10^8 with a sigma of 0.8. The lower population had a median time to failure of 1.4 x 10^5 with a sigma of 1.0.

Further examination of the data showed that most of the thick flexures were the earlier failures. The thin flexures were the population that lasted longer. This will be explained later.

Data Analysis Results

Across the range of failure probability estimates generated from this data, the two distributions turn out to be almost indistinguishable, i.e. the Weibull and lognormal distributions both fit the observed data equally well. In fact, visual comparisons of the probability density function, cumulative distribution functions and failure rate plots of the lognormal distribution (in the high σ case) and the Weibull distribution (in the low β case) show that they can have very similar shapes. So, with consistent characteristic lifetimes (as is necessarily the case here, since we are using the same data) and the respective shape parameters that were derived from the lognormal and Weibull distribution fits, the two distributions are evidently nearly indistinguishable across the observed range of failure data.

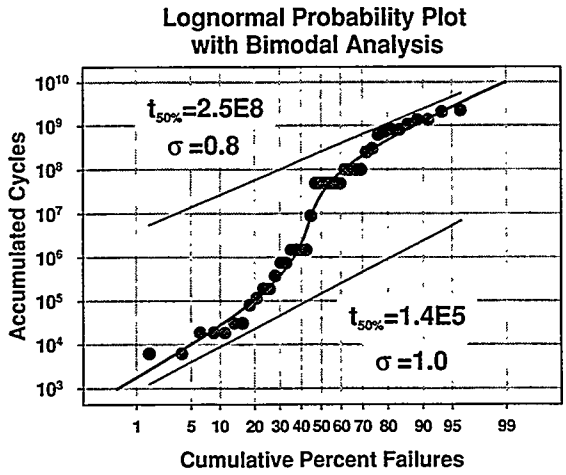

Figure 3.2.5 There were two populations leading to a bimodal distribution which coincided with the flexure type.

The fact that the failure rate is consistently decreasing indicates that the parts contain defects that result in the observed failures. This "weeding out" process is typically called infant mortality and necessarily results in a decreasing failure rate because each loss of a defective part renders the remaining sample more defect-free.

Another implication of the observed decreasing failure rate is that effective burn-in schedules can be devised, once the manufacturing process is sufficiently under control that stationary statistics can be applied. The goal would then be to weed out enough defective parts that the failure rate of the remaining parts is acceptably low, usually expressed as a FIT (failures-in-time) or ppm (parts per million) requirement. Such a burn-in schedule would have to be periodically supplemented by long-term life tests to ensure that wearout (increasing failure rates) never starts occurring unacceptably soon,

impinging on the required lifetime of the parts.

There is one potentially important caveat to the conclusions stated, and that lies in the method in which the data was obtained. As explained previously, the parts were stressed at high speed (36000 rpm), and then slowed down to a slow speed (60 rpm) to observe their operation. In fact, due to the nature of the experimental apparatus, the engines were actually decelerated to a stop for one second during any transition in speed. The analysis presented assumes that degradation accumulated during the high-speed "stress" intervals, and was negligible during the slow speed inspection intervals, the very brief pauses, and the deceleration and acceleration periods. (This is analogous to the concerns raised commonly in product life tests when parts that are stressed at high temperature are brought down to room temperature for inspection, resulting in undesired thermal cycling.) An attempt to analyze the failure data as a function of these deceleration, stop, slow speed, stop, acceleration cycles was inconclusive, but showed a generally constant failure rate.

A constant failure rate is indicative of a failure mechanism that has no "memory", i.e. it is due to random external events and is not heavily influenced by defectivity or wear. For example, the chance encounter of obstructing contaminant particles with sliding surfaces could result in a constant failure rate, if the likelihood of such encounters were nearly equal for all microengines. Hence, there remains the possibility that the decreasing failure rate reported here is an artifact of the approximately logarithmic "stress" intervals that were chosen for the test.

Failure Analysis

After each microengine failed, we recorded the position of the pin joint relative to its rest position. The upper portion of Figure 3.2.6 shows the gear with the pin joint in the rest position defined as 0°. The lower portion of the figure shows a map of locations of failure. The gear was 'stuck' with the pin joint in these locations. Notice that the failure locations are grouped around 0° or 165° implying that the microengines fail in preferred positions.

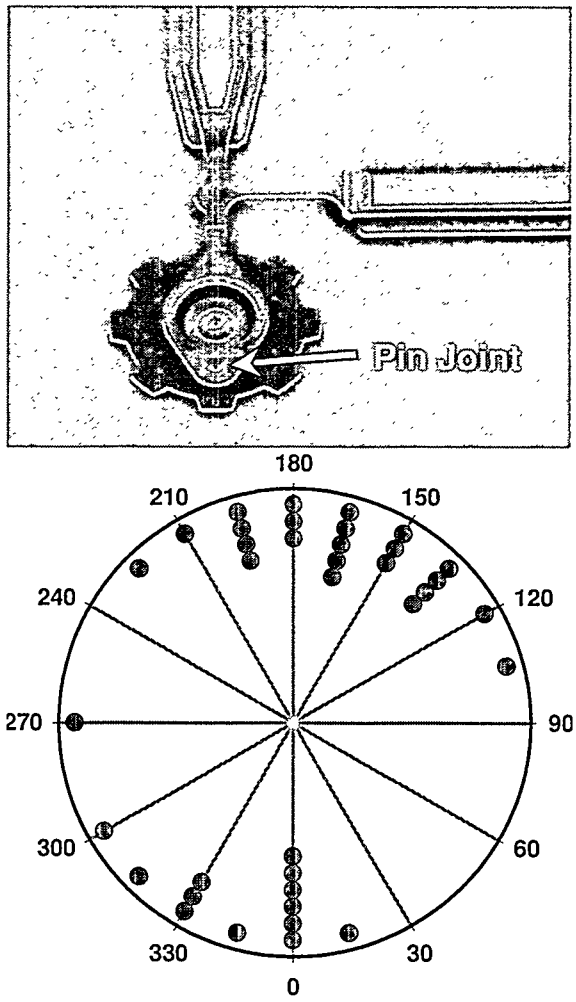

Figure 3.2.6 The upper image shows the location of the pin joint at rest which is defined at 0°. The lower plot shows the pin joint location at failure.

Further examination of the comb fingers of 30 microengines revealed that 24 had laterally clamped comb fingers as shown in Figure 3.2.7. The left image in the figure shows the moving shuttle and combs centered between the pull-up and pull-down stationary combs. However, the upper right image shows the movable fingers shifted to

the left. The arrow indicates the comb finger that is shorted. The lower right image also shows a shorted comb finger. The fingers touched during operation allowing current to flow and the result was welding of the polysilicon material. In order to assure ourselves that this was the failure mode, we used a focussed ion beam (FIB) to cut through the welded area and that microengine returned to its rest position.

As mentioned earlier, the thin flexures outlived, for the most part, the thick flexures. This may have been due to greater compliance which prevented the comb teeth from touching.

Other failure analysis (FA) activities have consisted of examination of several failures from the first lifetime test which appeared to be stuck at some location on the microengine structure. "Stuck" as it is used here, means surfaces adhering to each other (i.e., as opposed to failing to complete a revolution). Usually this is a permanent condition, however two types of exceptions were observed. One may have been a failure mechanism wherein a gear stuck momentarily at some point in its rotation, and then freed itself due to a combination of increased force or mixed motion between rocking and rotation. A second is the reversible cyclic contact between opposing combs. Permanent lateral sticking of a single comb finger coincided with stopping the operation of two microengines during FA troubleshooting.

Two scanning electron microscopy (SEM) techniques, new in the application to MEMS, have been utilized to study the microengines. The first was passive voltage contrast (VC), where no external voltage was applied to the packaged part and all the pins were grounded. Contrast arose from the fact that electrically isolated elements attained a different potential, due to charge injection from the electron beam, than did ground elements. The secondary electron yield, which was used to construct the image, depended on this potential. Figure

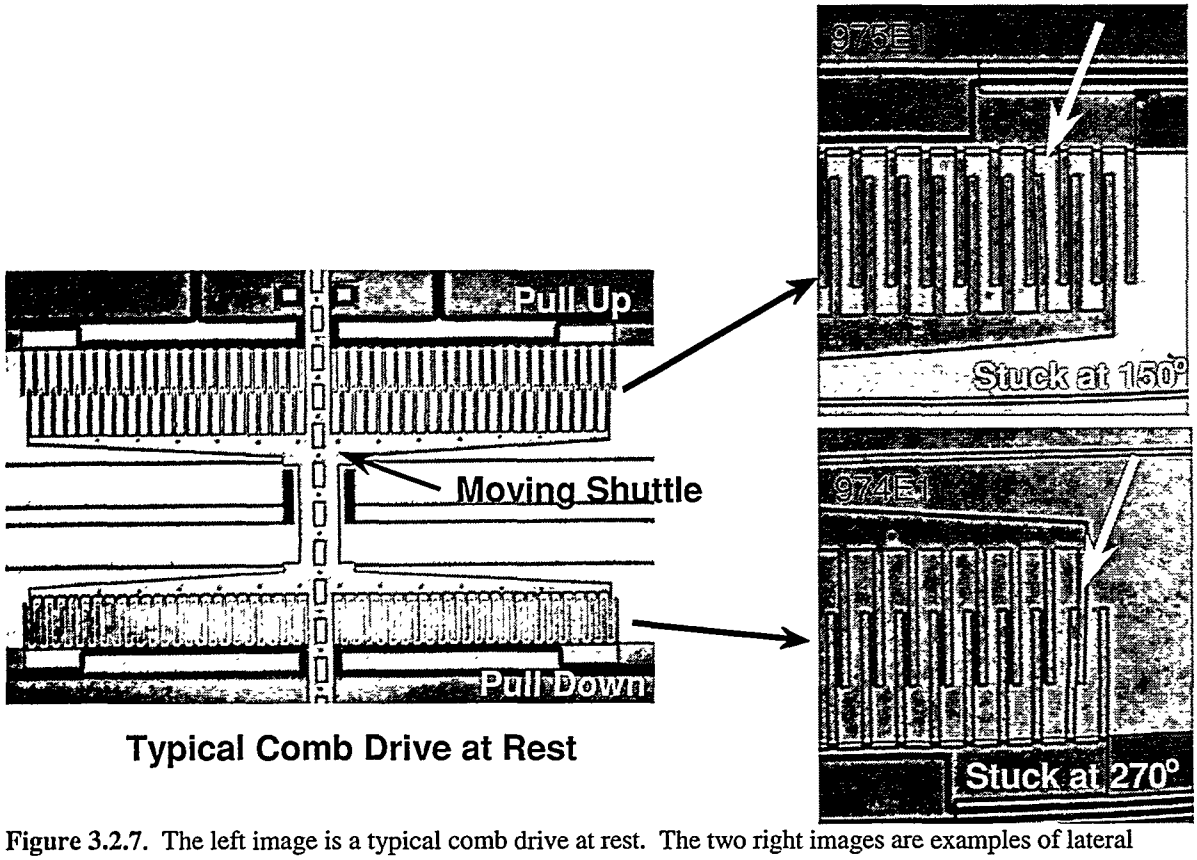

Figure 3.2.7. The left image is a typical comb drive at rest. The two right images are examples of lateral clamping of the comb fingers with arrows indicating welded fingers caused by current flow through the fingers.

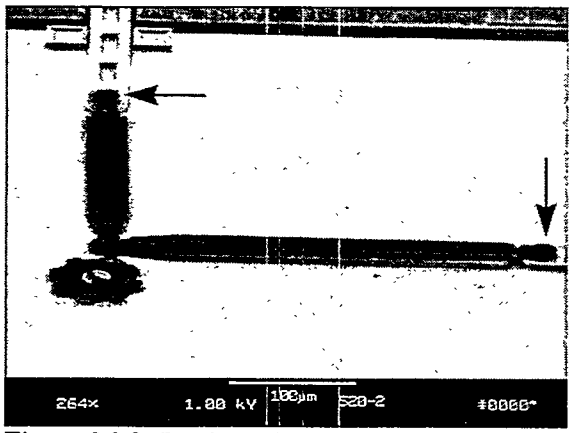

Figure 3.2.8. Passive voltage contrast image of pin joint micromachine showing charging of links, gear with respect to sample. Arrows show change of potential due to pin joints.

3.2.8 shows such an image at 1keV accelerating potential, where the isolated two link arms and gear charged to a positive potential with respect to the rest of the sample, resulting in a dark appearance of those elements. The shuttles were grounded through their springs, and the hub was grounded through its attachment to the substrate. The links and gear were only grounded if the physical contact at pin joints resulted in electrical contact, which was not occurring in this case. On the contrary, Figure 3.2.9 shows that the electrical connection provided by the flexible links drains charge from the link arms, but that the gear still charged positively, as it was not directly coupled to either the link arms or the hub.

Passive VC imaging also identified one comb drive and associated interconnect line which have charged to a positive potential with respect to the opposing comb drive and the rest of the sample, even though all the package pins were grounded. Figure 3.2.10 shows a darker appearance on the Y comb on the left, compared to the comb on the right, which is attached to the shuttle. Tracing this line in the SEM, the effect seemed to be due to the resistance of the line, as it gradually equilibrated toward the wirebonded pad. Figure 3.2.11 shows a crossover of lines feeding opposing combs,

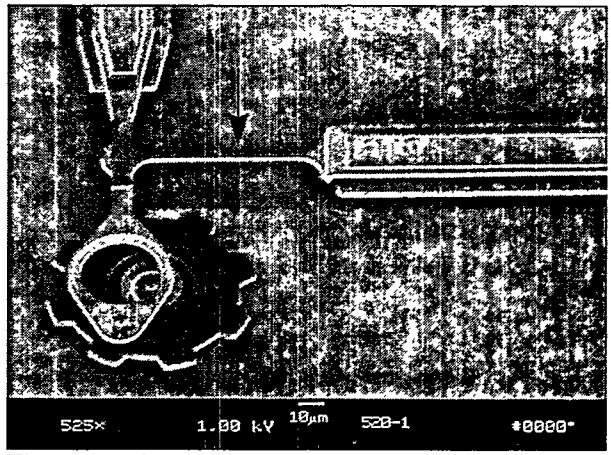

Figure 3.2.9. Passive voltage contrast of flexible link micromachine showing charging of gear with respect to links and the rest of the sample. Arrow shows flexible link.

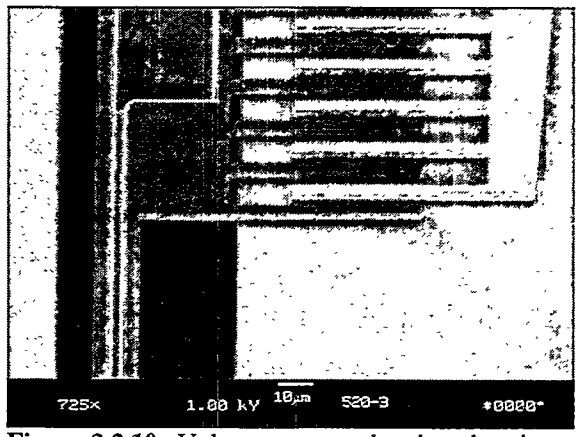

Figure 3.2.10. Voltage contrast showing charging of the comb on the left.

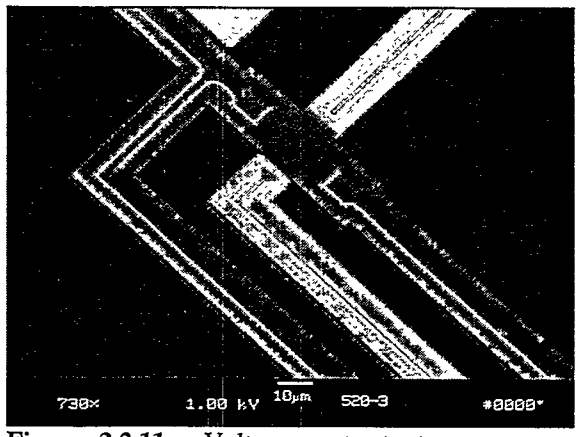

Figure 3.2.11. Voltage contrast at a crossover, showing charging of an interconnect line (all pins grounded).

where the passive voltage contrast effect was still visible.

The second new technique employed, was active voltage contrast, wherein external voltages were applied to microengine elements as they were examined in the SEM. The charging behavior of the electrically isolated elements of the operating microengines was observed with this technique. One gear, which was electrically floating at rest, changed as it was run counter-clockwise. It charged during the portion of its rotation from the 12:00 position to the 6:00 position, and then discharged and recharged during the portion from the 6:00 position to the 12:00 position. While the electron beam seemed to interfere significantly with a few microengines, as found in previous work, certain engines were successfully run for several hours in the SEM with no attempt to limit electron beam illumination to any portion of the microengine.

Voltage contrast has also been used to observe static and operating microengines in the positive ion beam used in the FIB. More importantly, it has been demonstrated in the FIB that it is possible to electrostatically clamp a gear at high beam current, presumably when the positively charged gear is attracted to the grounded substrate. Charge neutralization (via an electron flood gun) has been used to mitigate the positive charging from the ion beam. Microengines have been observed to operate smoothly using charge neutralization, then fail to rotate when the neutralization is suspended. This is a reversible phenomenon.

Conclusions

The microengine failure data showed no evidence of wearout in the distributions but there was a significant infant mortality region. The lognormal distribution was bimodal indicating two populations, but the similar slopes imply one dominant failure mode. This failure mode of lateral clamping was large enough to overshadow any wearout.

The thin flexures produced the longest-lived microengines, but could not be fabricated reproducibly. In the process the 1 mm width was over-etched to 0.7 mm and was susceptible to breakage.

Several FA techniques developed for microelectronics have proven useful in the analysis of MEMS. The dominant failure mode was lateral clamping of the comb fingers. The secondary mode of failure was the gear sticking either to the substrate or to the hub. This was determined due to the presence of motion in the comb drives, but no translation of that motion to the gear. Voltage contrast in the SEM and in the FIB has been used to identify charging on the gears and links of stationary and operating engines. This charging may be related to the erratic behavior in the rotation of the microengine as observed in the FIB.

[23] E. J. Garcia and J. J. Sniegowski, "Surface micromachined microengine", Sensors and Actuators A, **Vol. 48**, pp. 203-214 1995.

[24] S. L. Miller, J. J. Sniegowski, G. LaVigne, and P. J. McWhorter, "Performance tradeoffs for a surface micromachined microengine", Proc. SPIE Micromachined Devices and Components II, Vol. 2882, Austin, October. 14-15, pp. 182-191, 1996.

[25] W. Nelson, *Applied Life Data Analysis*, Chapter 9, J. Wiley & Sons, New York, 1982.

[26] W. Nelson, *Accelerated Testing*, Chapter 3, J. Wiley & Sons, New York, 1990.

[27] D. S. Peck and O. D. Trapp, *Accelerated Testing Handbook*, Chapter 6, Technology Associates, Portola Valley, 1987.

[28] P. A. Tobias, D. Trindade, *Applied Reliability*, Van Nostrand Reinhold, New York, 1986.

3.3 Frequency effect and a wear model

Experiments were performed on surface micromachined microengines driving load gears to determine the rotational frequency dependence on median cycles to failure. These microengines were a later version where the lateral clamping seen in section 3.2 was eliminated by design changes. A sample of 272 microengines, each driving a load, was stressed at eight different frequencies. Frequency dependence was observed and a model was developed based on fundamental wear mechanisms and forces exhibited in resonant mechanical systems. Stressing loaded microengines caused observable wear in the rotating joints and in a few instances led to fracture of the pin joint in the drive gear when the pin was worn through.

Introduction

The objective of this work was to determine the fundamental correlation between the operational drive frequency (microengine speed) and the lifetime of the microengine. The microengine consists of orthogonal linear comb drive actuators mechanically connected to a rotating gear as seen in Figure 3.3.1. The comb drives of these microengines have springs, which restore any deflections back to the rest position. The polysilicon comb drive exhibits a resonant frequency, as does any mechanical oscillating system. By selecting frequencies above and below resonance, we have collected data for the median lifetime of the microengine driving a load as a function of f/f_o where f is the stress frequency and f_o is the resonance frequency. We have developed a predictive model for the number of revolutions to failure that is based on the fundamental principles of the physics of wear in a mechanically resonating system.

Experimental Approach

Lifetime Experiment

This study used the electrostatically driven microactuator (microengine) devel-

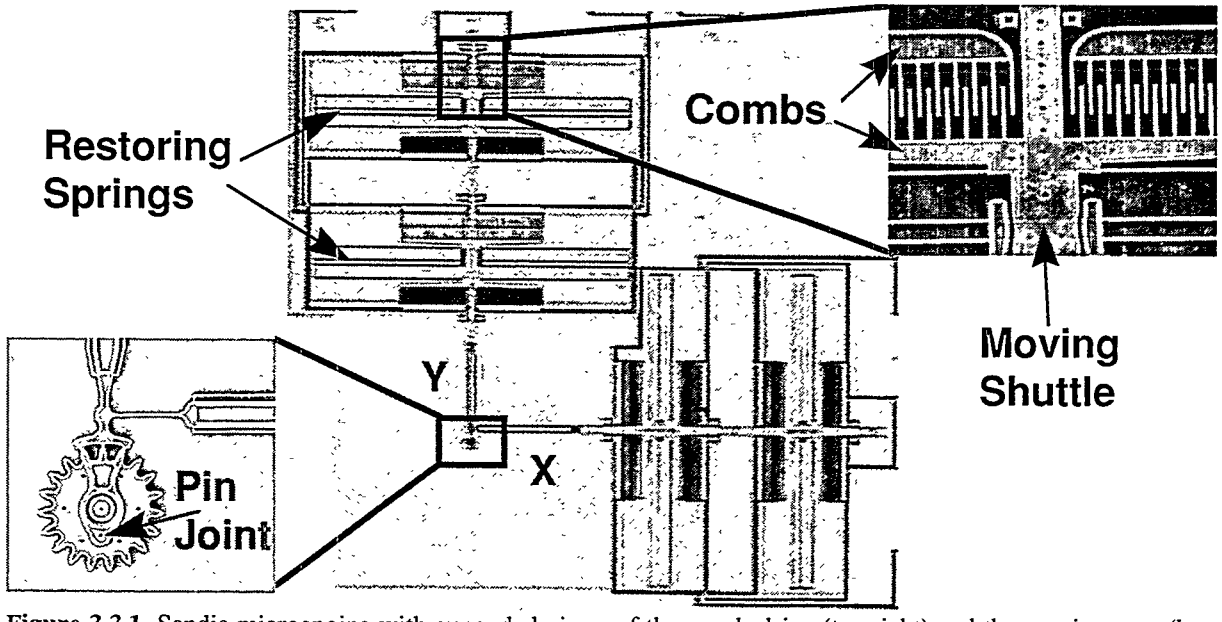

Figure 3.3.1. Sandia microengine with expanded views of the comb drive (top right) and the rotating gear (bottom left) shown in what we define as $\theta = 0$.

oped at Sandia National Laboratories [29] as seen in Figure 3.3.1. By applying the proper drive voltages, the linear displacement of the comb drives is transformed into circular motion. The X and Y linkage arms are connected to the gear via a pin joint. The gear rotates about a hub that is anchored to the substrate. The microengine has been the focus of much investigation for MEMS devices experiencing sliding friction [30,31].

We used the microengine to drive the load gear depicted in Figure 3.3.2a. A close-up view of the drive gear meshing with the load gear is shown in 3.3. 2b. The radius of the microengine drive gear is 38 μm and the load gear is four times as large.

One of the many issues associated with the reliability of microengines is the method used to operate them [32]. If the drive signals supplied to the comb drives are not optimized, there will be excessive forces on the hub and pin joint of the gear, which promote early failures. In the optimization procedure, we characterized the microengines by measuring parameters [2] from a sample of 5 devices. Model-based drive signals were calculated using the measured parameters, and these drive signals were maintained throughout the experiment. For all experiments, we accelerated the load gear to full speed in three rotations of the drive gear. This method was necessary to account for the inertia of the large gear.

The dice were packaged with glass covers to allow viewing of the rotating gears. The covers prevented external particle contamination but allowed access of the ambient environment in the laboratory. The relative humidity in the laboratory fluctuated slowly between 10% and 45% throughout the experiment. The packages were stored in a dry nitrogen environment before the test. The tester, Sandia High Volume Measurement of Micromachine Reliability (SHiMMeR - see section 1.2), was used to provide electrical signals to large numbers

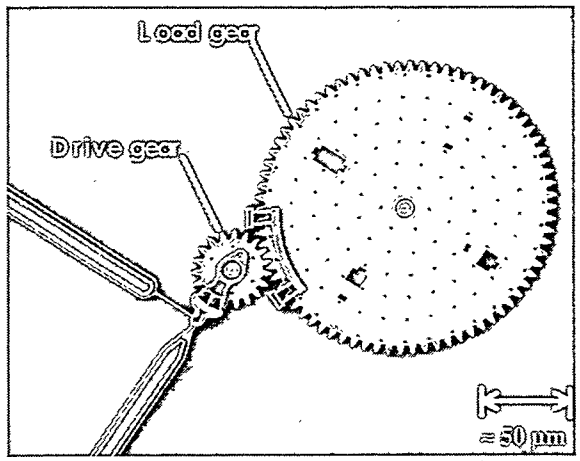

Figure 3.3.2a. The microengine drive gear shown with the load gear. The right bracket ( ]) shaped guide on the load gear mitigates out-of-plane wobble to ensure proper meshing of teeth.

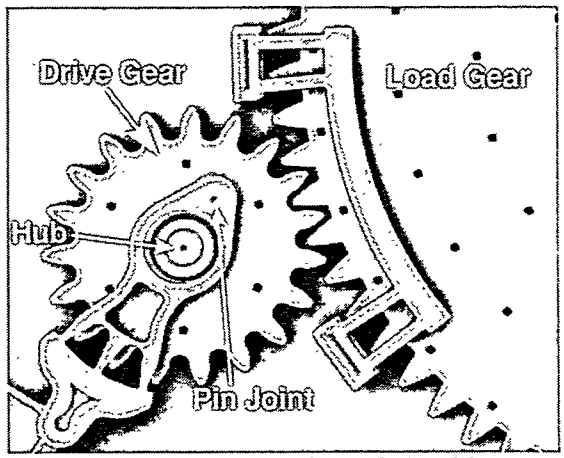

Figure 3.3.2b. Close-up view of the drive gear meshing with the load gear. The hub is anchored to the substrate and the pin joint connects the actuator linkage to the drive gear.

of packaged microengines driving loads and to optically inspect them for functionality.

We performed stress tests at eight frequencies, 860, 1204, 1500, 1720, 2064, 2200, 2408, and 3000 Hz. As the resonant frequency of the system was 1150 Hz, data for stresses both above and below resonance were taken. Prior to the first stress, the parts were checked for functionality. The stress intervals followed roughly the same sequence for all the experiments, and were 2000, 4000, 8000, 16000, ..., rotations of the drive gear. If more than 4 parts failed during a particular interval, we repeated that

stress interval. The devices were stressed at high speed and then slowed to 1 Hz to inspect for functionality. A failure was defined as the inability of the microengine drive gear to make a complete revolution at the 1 Hz inspection speed. During the inspection interval, we noted any observed changes or degradation in the motion of the gears.

Wear Structure Experiment

To compare the worn surface morphology found in actual devices with that occurring under well-defined contact conditions, experiments were run on a specialized "sidewall" friction test device [33], shown in Figure 3.3.3. In this device, the sidewall of a beam having trapezoidal cross-section is brought into contact with the cylindrical surface of a vertical post using an electrostatic comb drive to apply a load force. A second electrostatic comb drive is used to reciprocate the beam against the post.

Conditions in the friction experiments were chosen to duplicate as closely as possible the loading conditions found in the gear hubs of the microengine for the lifetime experiments. The maximum force exerted by the drive linkage on the microengine gear was estimated to be 2.5 μN. Based on the geometry of the microengine, assuming linear contact between the conformal polycrystalline silicon structural elements, and using an elastic modulus of 155 GPa and Poisson's ratio 0.23, the peak Hertzian contact pressure was therefore 27 MPa at the gear hub and 140 MPa at the pin joint.

In this experiment, a normal force of 4 μN was applied between the beam and post resulting in a peak contact pressure of 144 MPa in the sidewall device. The device was run at 127 Hz for a cumulative sliding distance of 10 m, equivalent to $1x10^6$ revolutions of the pin joint.

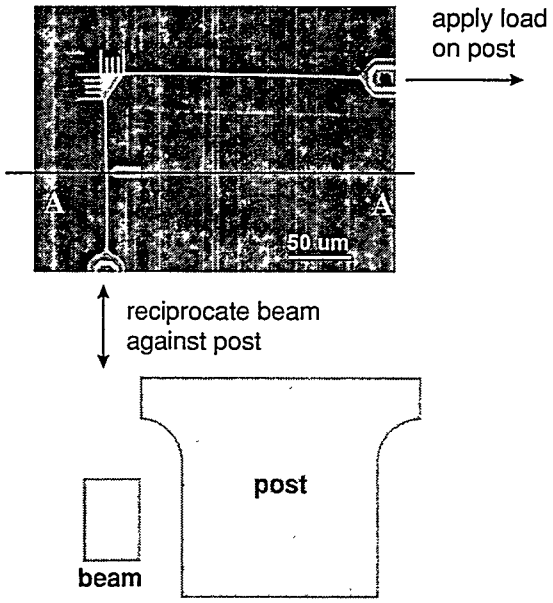

Figure 3.3.3. SEM micrograph showing the top view of the sidewall friction tester and a schematic cross-sectional view (A-A) of the contacting members.

Results

Experimental Observations

The behavior of the microengines as they were stressed followed a consistent pattern. Initially the microengines ran smoothly. With the accumulation of stress, the operation of the microengines became erratic at inspection frequencies, with occasional sticking followed by release. Some of the microengines would actually overcome the sticky behavior and become smooth again. Near the end of its life, rotation became more erratic until the microengine failed by sticking or rocking back and forth through a small angle. After failure, the part remained stimulated by the drive signals. By optically panning across the entire microengine we could obtain evidence about the failure. In some cases, the drive gear/load gear combination appeared stuck because we could see slight movement in the adjoining comb drives and shuttles. In other cases, the pin joint appeared to be adhered to the drive gear.

The lifetime behavior of the parts was markedly different for frequencies above and below 2400 Hz. This frequency is roughly twice the resonant frequency. The behavior at high frequencies was monitored using an Olympus ALS 12000S strobe light to "slow down" the motion for visual inspection. Below 2400 Hz, the microengines initially operated smoothly at inspection and stress frequencies. With the accumulation of stress (approximately 20,000 cycles), the motion became jerky at the inspection frequency of 1 Hz, but was smooth at the higher frequency. Eventually, the motion of the gears froze at both inspection and stress frequencies.

Above 2400 Hz, the parts initially operated smoothly at inspection and stress frequencies. After approximately 1,000,000 cycles, they would begin to chatter at stress frequencies; that is, the gears would vibrate about one position. This effect was greatest for the stress frequency of 3000Hz. We used a strobe light to observe the gear as it came up to high speed. The gears typically rotated smoothly for 10-15 seconds before the chatter began. At the onset of high-speed chatter, the parts would still operate normally at inspection speed. Eventually, however, the motion of the gears froze at both inspection and stress frequencies.

Data Analysis of Lifetime Experiment

Because the parts were observed at fixed inspection times, common to all the parts, the results fall into the category of reliability data called "interval" data. We plotted the accumulated number of cycles to failure against the cumulative percent failure for each stress frequency. The lognormal fit resulted in an estimate of t_{50}, the median cycles to failure. The estimate for the lognormal shape parameter, σ, was also determined.

Table 3.3.1. Series of frequency experiments performed.

f (Hz)	f/f_o	# Parts on test	# Parts Failed	# stress intervals
860	.75	34	28	30
1204	1.05	47	28	23
1500	1.30	9	9	21
1500	1.30	39	37	30
1720	1.49	25	25	30
2064	1.79	46	45	40
2200	1.91	28	28	17
2408	2.09	35	35	27
3000	2.60	15	14	23
3000	2.60	44	44	23

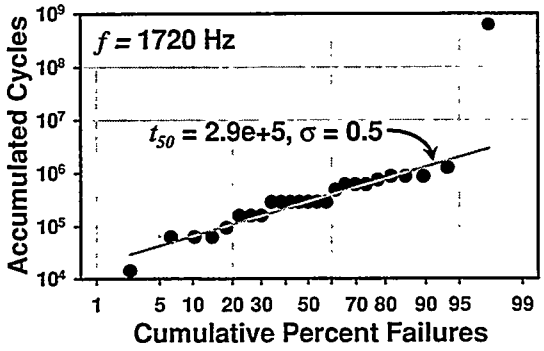

Figure 3.3.4. Lognormal distribution of accumulated cycles to failure for the resonant frequency stress. The last data point was omitted from the regression analysis.

The experimental results are summarized in Table 3.3.1. We performed eight experiments; we caused a total of 272 parts to fail. Most of the data at a given frequency could be described by a simple unimodal distribution such as seen in Figure 3.3.4. In this figure, the last point is roughly two orders of magnitude higher than the rest and was omitted from the fit. The regression analysis yielded a median number of cycles to failure of 2.9×10^5 with $\sigma = .51$.

However, there were three frequencies where the distribution was bimodal. This occurred for stress frequencies of 860, 1204, and 2408 Hz. In these instances, we deconvolved the data to determine the median number of cycles to failure for each population. Figure 3.3.5 shows the data with the upper and lower lines representing the two populations. The bimodal analysis fit using

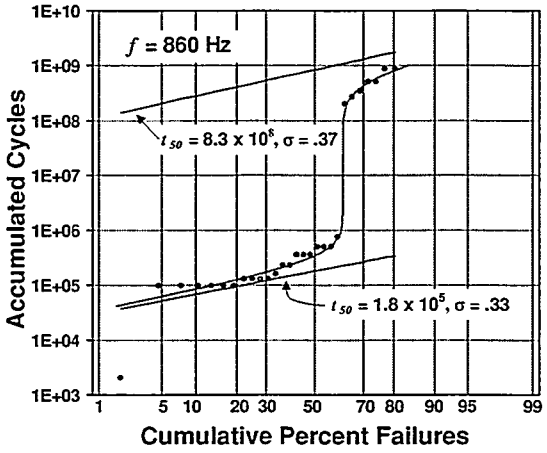

Figure 3.3.5. Lognormal probability plot for the 860 Hz test showing a bimodal distribution. The first data point was omitted from the deconvolution calculation.

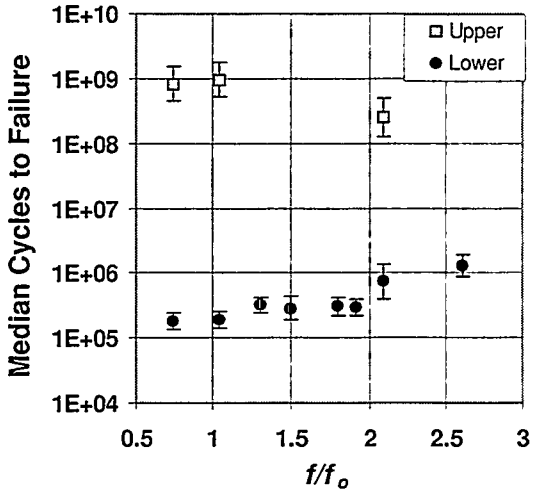

Figure 3.3.6. The frequency dependence of the lifetime of the microengine driving a load experiments. The error bars represent 90% confidence bounds.

a separation of the two distributions at the cumulative percent failure of 62% is also shown in the figure. Because the values of σ for both populations are similar, we believe that the underlying failure modes are the same, but that we have two populations, one of weak parts and the other of strong parts. There was inherent variability in the population of microengines. Additionally, the optimization technique described earlier is performed on a small number of devices. We speculate that the final drive parameters may be extremely well matched to some microengines leading to long lives (strong parts) and not well matched to other microengines leading to short lives (weak parts).

Table 3.3.2 shows the results of lognormal fits to all of the frequency experiments. For the cases where we observed a bimodal distribution, the lower and upper t_{50} are presented. The data are also graphically represented in Figure 3.3.6 with 90% confidence bounds represented by error bars. As in the table, the unimodal distributions are grouped with the lower portion of the bimodal distribution. The upper portions of the bimodal distribution are only seen at three frequencies. The bimodal distributions were observed on parts from different wafers of the same fabrication lot.

For the stress frequencies of 1500 and 3000Hz, we repeated the experiments and the results of the second experiment were

Table 3.3.2. Results of median number of cycles to failure from all frequency experiments performed.

		Unimodal or Lower		Bimodal Upper	
f (Hz)	f/f_o	t_{50}	σ	t_{50}	σ
860	.75	$1.8x10^5$	.33	$8.4x10^8$	.37
1204	1.05	$2.9x10^5$	.28	$9.6x10^8$	.53
1500	1.30	$3.2x10^5$	.45		
1720	1.49	$2.9x10^5$	.51		
2064	1.79	$3.1x10^5$	.54		
2200	1.91	$3.0x10^5$	.38		
2408	2.09	$1.2x10^6$	.29	$2.5x10^8$	.32
3000	2.60	$1.3x10^6$	.70		

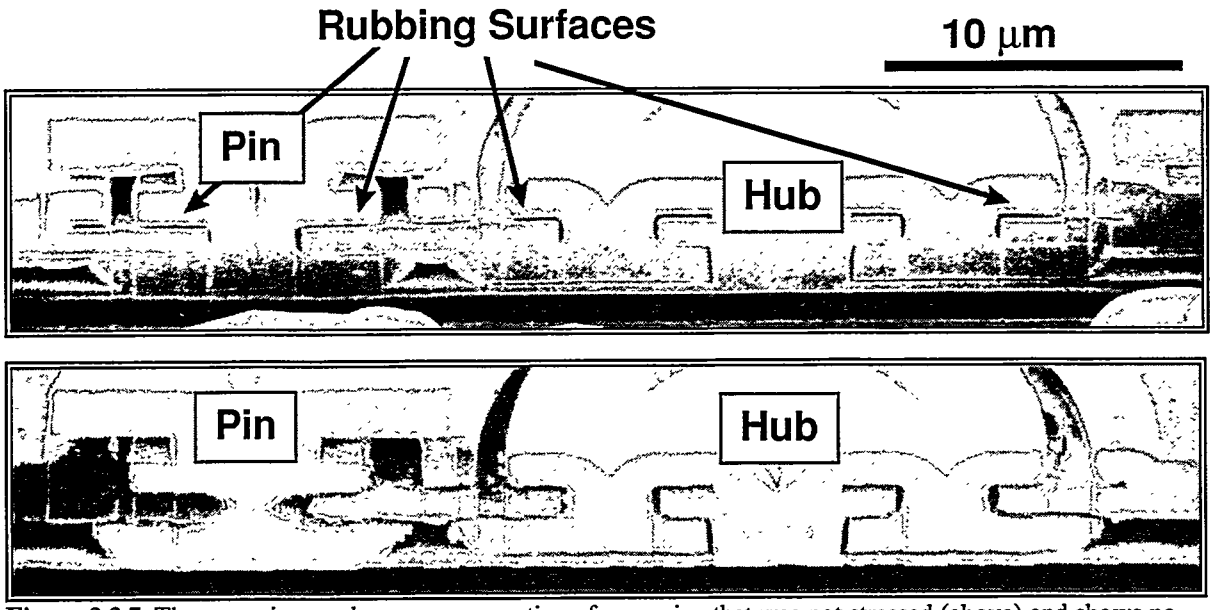

Figure 3.3.7. The upper image shows a cross section of an engine that was not stressed (above) and shows no wear debris. The hub is anchored to the substrate and the pin (diameter = 3 μm) rotates in the pin hole as the gear revolves around the hub. The lower image shows an engine that was tested to failure in 480k cycles. Severe wear of the pin joint and wear debris near the rubbing surfaces was evident.

within the 90% confidence bounds of the first experiment. We then averaged the two results. This was a demonstration of lot-to-lot repeatability since the microengines in the second experiment were from a different fabrication lot but of the same technology and design.

Failure Analysis of Lifetime Experiment

Wear of rubbing surfaces was the dominant mode of failure for these microengines. The images in Figure 3.3.7 show focused ion beam (FIB) cross sections for two samples with identical processing history. The drive gear (see Figure 3.3.2b) was sectioned along the line between the center of the hub and the pin joint. The upper image is from a control part which was not stressed, and does not show any evidence of wear or other processing artifacts, while the lower image is from a part which was tested to failure in 480,000 cycles. The tested part shows abundant wear debris on bearing surfaces and surrounding areas as well as severe

Figure 3.3.8. Severe pin hole damage in drive gear tested to failure (SEM).

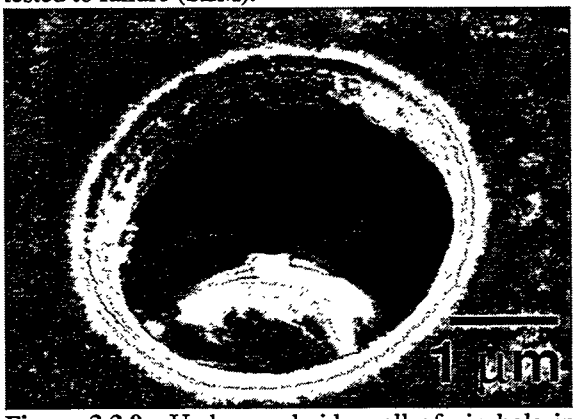

Figure 3.3.9. Undamaged side wall of pin hole in drive gear on control sample (SEM). This gear was not stressed.

damage that reduced the minimum diameter of the pin. This circumferential notch on the pin concentrates subsequent stresses, which is consistent with the result that broken pins typically show reduced diameters on both fracture surfaces.

Severe drive pin wear and occasional breakage of drive pins was characteristic of these devices when tested to failure. An example of such wear is seen in Figure 3.3.8, where the bore of the hole in the drive gear which accepts the drive pin is shown after a pin has been fractured (after testing). This wear has produced an out-of-round shape both by wearing material away and by depositing debris on the side wall of this hole. This out-of-roundness suggests repeated impact in one area. For comparison, a similar hole is shown in Figure 3.3.9 for a control sample with similar processing history that has not been stressed. The view shown is from the bottom of the gear, but the bore of the hole is undamaged by wear. The particle at the left of the image is the result of purposely breaking the pin during sample preparation.

Pin joint breakage was seen in 3 of 220 microengines driving a load and only when the stress frequency was greater than the resonant frequency of 1150 Hz. Pin joint breakage probably resulted from a combination of effects. The drive pins were worn down to a smaller diameter, which weakened the structure. Additionally, the load gear supplied a large inertial force to the drive gear when exhibiting erratic motion.

Microengines driving loads tested to failure typically exhibited wear debris that could be resolved optically. An example of this debris is shown in a SEM image in Figure 3.3.10. The left arrow in Figure 3.3.10 indicates a location where the debris has been moved out to the top surface of the hub on a drive gear. The right arrow indicates a site where debris can be seen in the gap

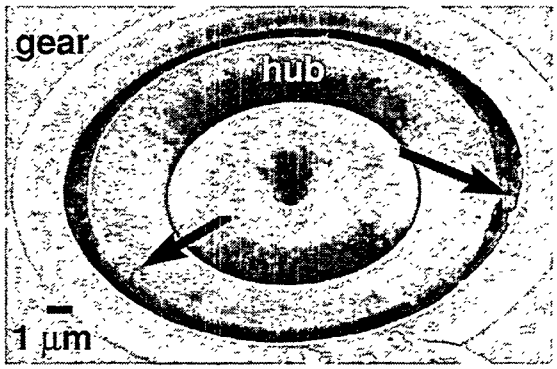

Figure 3.3.10. Top view SEM image of characteristic wear debris on drive gear and hub.

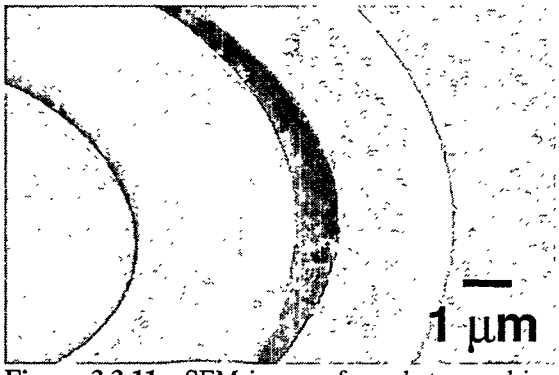

Figure 3.3.11. SEM image of gap between drive gear and hub showing characteristic accumulation of wear debris.

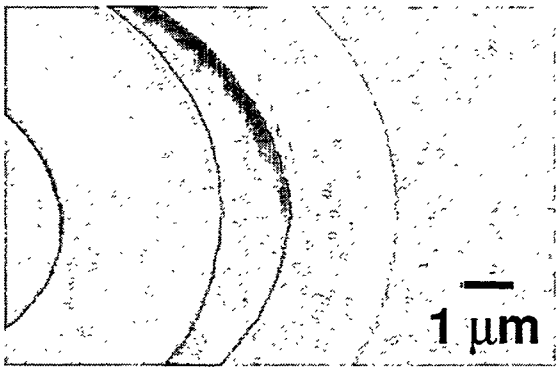

Figure 3.3.12. SEM image of gap between load gear and hub showing characteristic absence of wear debris.

between the vertical sidewalls of the drive gear and its hub.

Figures 3.3.11 and 3.3.12 show a result from a comparison of drive gears and load gears from several devices tested to failure. The light contrast debris is characteristically evident in the gap on the drive gear of Figure 3.3.11 and is characteristically absent in

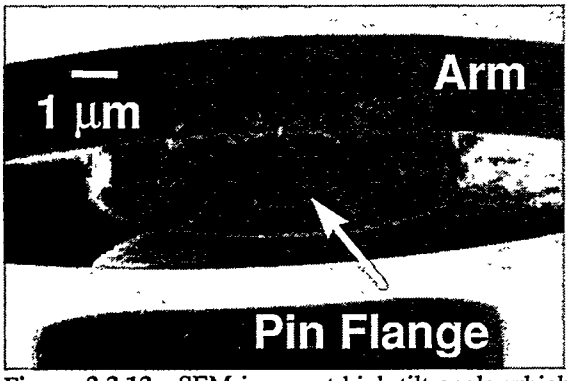

Figure 3.3.13. SEM image at high tilt angle which reveals wear debris adhering to the upper drive pin flange beneath the drive arm of a binary counter tested to failure due to pin breakage.

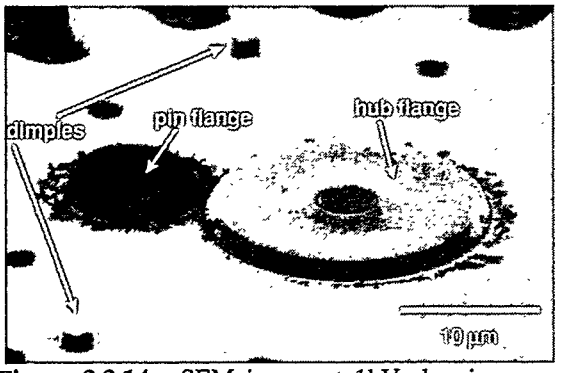

Figure 3.3.14. SEM image at 1kV showing wear debris on bottom of drive gear

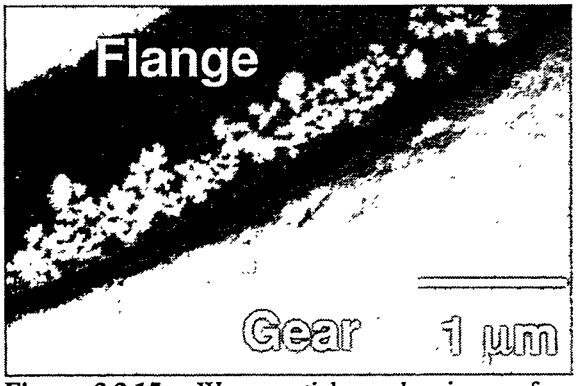

Figure 3.3.15. Wear particles a bearing surface flange on the underside of a drive gear.

a similar gap from the load gear of Figure 3.3.12.

Wear debris at drive pins was also resolved optically when it occasionally was broadcast from beneath the drive arm. It can also be seen in the SEM by tilting the sample to look under the drive arm. Figure 3.3.13 shows such an image, where a broken pin has come to rest between the teeth of a gear. The debris covers the sidewall of the upper pin flange and has spread to a sidewall of the drive arm.

Wear debris was examined from a different perspective by using a conductive double-sided adhesive laboratory tape to remove several gears and other components for examination of the undersides and the substrates from which they were removed. Figure 3.3.14 shows a SEM image from such a drive gear. The wear debris is attached to the sidewalls of the lower hub flange and the pin-retaining flange. It has radiated out from the perimeter of each of these flanges and has adhered to the bottom side of the drive gear. Gear teeth can be seen at the top of the image. This image was generated at 1 kV accelerating potential and shows interesting passive voltage contrast [34]. The dark contrast of the wear debris and the pin flange indicate that they are not grounded to the gear and are charging positively due to the 1 kV accelerating voltage. The pin flange and the hub flange by design must be free to move in the gear and therefore were not expected to be well connected electrically. The dark pin flange indicated pin join fracture during sample preparation. The dark contrast of the wear debris indicates that it is electrically insulating.

Similar flanges from the load gear hub and from drive gears on engines that share processing history, but have not been exercised show pristine sidewalls free from such particles. The two dimples extend downward from the bottom of the gear to minimize the rubbing area in the event of contact with the substrate. No other evidence of wear has been observed at these dimples or any other surfaces on the gear or on the substrate beneath the gear. The dark circle in the center of the lower hub flange is the anchor point for the gear that was broken in order to obtain this view. It is darker than

its surroundings due to a resistance path between the point of illumination of the electron beam and the electrical ground provided by the gear and hub.

A higher magnification image of the particles on a flange is shown in Figure 3.3.15. This SEM image was generated at 5 kV, and shows two size ranges for the wear debris seen at this location. Many of the particles are on the order of 50 nm in size and are elongated. A second size of feature are the rounder agglomerations of debris which are 200 nm and larger. Other agglomerations of wear debris have been observed which are submicron in size, but the morphology has not been resolved distinctly at this time. This may be caused by the low density, or perhaps, porosity of the debris that inhibits a high-resolution image at the surface. The particles appear light in contrast due to negative charging from the 5 kV accelerating potential.

Wear debris has also been observed on the shuttles and guides attached to the Y linkage arms. An example is shown in Figure 3.3.16. Although the debris lines up in this case, and can be seen to bridge the entire gap between shuttle and guide in Figure 3.3.17, it was not the reason for the shuttle being stuck in this position. This was shown by delicately severing the flexible link between this shuttle and the engine with a xenon-cutting laser. The springs attached to the comb drive then returned the shuttle to its rest position.

Data Analysis of Wear Structure Experiment

The results of the sliding wear test of the sidewall friction device are shown in figures 3.3.18 and 3.3.19. The unworn surfaces shown in Figure 3.3.18a reveal smooth sidewall morphology for the cylindrical post where silicon is deposited into a hole etched in oxide. There are no visible particles or scratches on this silicon surface. The beam

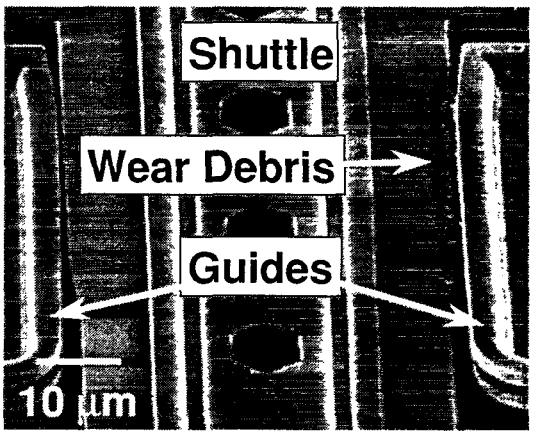

Figure 3.3.16. SEM image of wear debris on shuttle and guide.

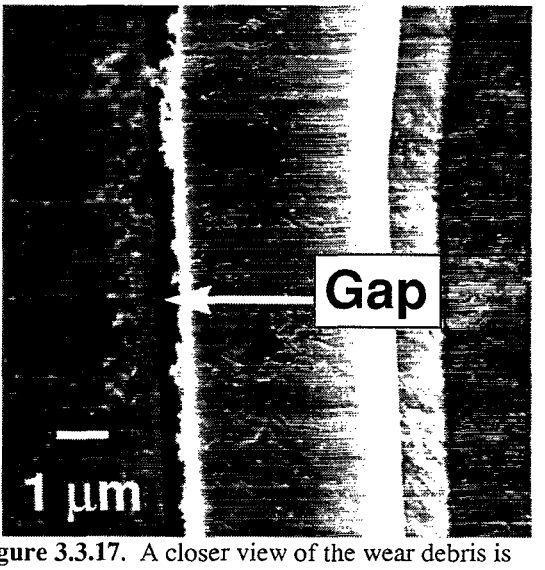

Figure 3.3.17. A closer view of the wear debris is shown under a higher magnification SEM view at the shuttle/guide location.

shown in Figure 3.3.18b was formed by reactive ion etching of silicon, and exhibits some texture due to the etching process. However, there are no attached particles or lateral scratches in the unworn side of the beam. Texture on the top surface of the silicon layers, in the form of small bumps, is inherent in the processing of the devices.

By comparison, the worn surfaces of the post and beam in Figure 3.3.19a and 3.3.19b show evidence of both attached particles and damage to the sliding surfaces. A scratch, probably due to the trapezoidal shape of the

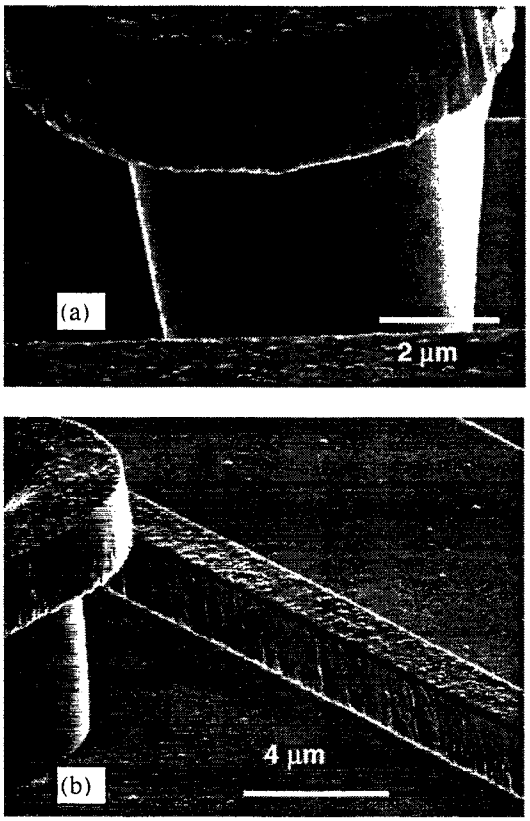

Figure 3.3.18. SEM micrograph of the contacting surfaces in the sidewall device prior to testing showing the movable cylindrical post (a) and the rectangular beam (b).

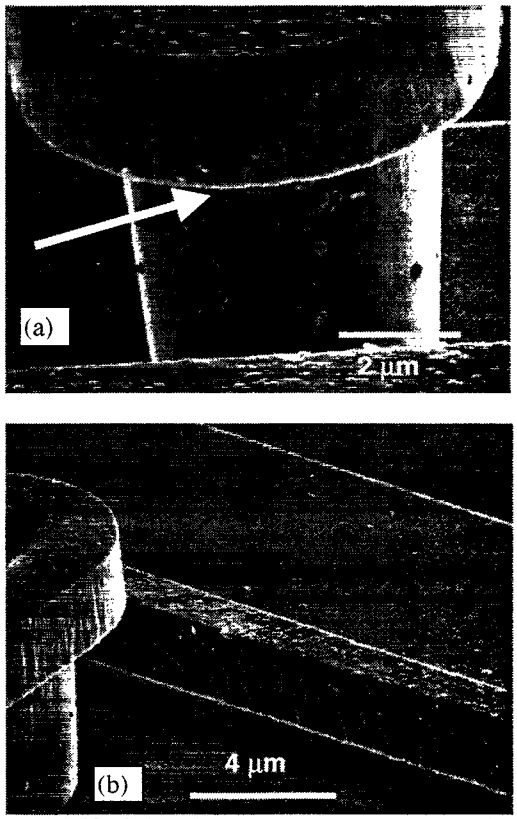

Figure 3.3.19. SEM micrographs of the sidewall device after reciprocation sliding for a total of 10 meters at 140 MPa. Collections of wear particles are on the post surface in (a) and a few particles were collected on the beam surface in (b).

beam, is evident near the top of the post in the micrographs of Figure 3.3.19a and 3.3.20a. The particles shown in Figures 3.3.20a and 3.3.20b are agglomerates, roughly 200 nm in size, made up of much smaller particles on the order of tens of nanometers in size. The particles are collected at the entry and exit zone of the sliding contact on the vertical post.

The surfaces in Figures 3.3.19 and 3.3.20 represent clear evidence of wear between the beam and post in the sidewall device, under contact conditions similar to those present in the microengine. The presence of wear particle agglomerates is expected in air, even though the wear process likely involves the initial removal of individual ~ 10 nm particles from the surface. After removal, individual wear particles are attracted to one another and the device surfaces by capillary and Van der Waals forces.

The morphology of the particles alone is

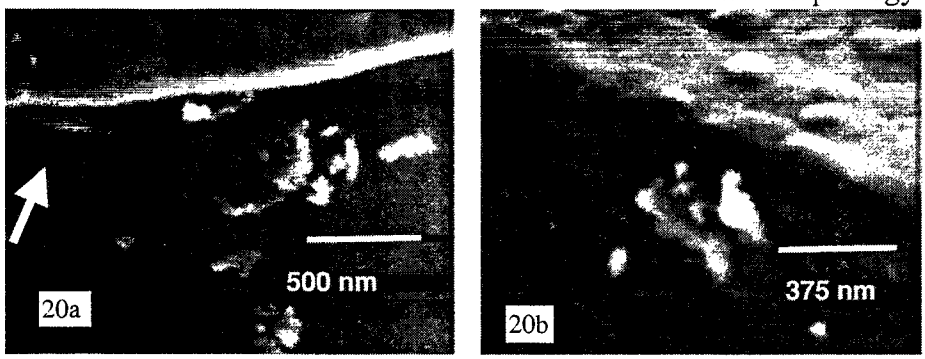

Figure 3.3.20. Magnified images of particles on the post (a) and beam (b) are shown.

insufficient to determine whether they are generated by asperity-to-asperity adhesion followed by tensile fracture, by asperity fatigue due to cyclic stresses, or simply by abrasion of one surface by the other. In fact, the wear process likely involves a combination of these mechanisms, such that surface degradation and adhesion or fatigue is responsible for creating the initial wear particles, and particles trapped at the interface during sliding result in abrasion to create additional wear particles.

Discussion

The large amount of wear debris observed during failure analysis focussed our investigation on wear mechanisms as a potential model to describe the failure data. Wear may be defined simply as the removal of material from solid surfaces as a result of mechanical action. In this section, we will present the derivation of a frequency-dependent wear model that predicts failure and compare this model to the lifetime data. An adhesive wear model will then be derived from the general frequency-dependent wear model and comparison to the data will be made. We will then discuss the implications of the friction structure experiment, describe some additional sources of wear, and comment on the bimodal distribution observed.

Failure Model: Types of Mechanisms

There are seven primary wear mechanisms observed for macroscopic mechanical systems [35]: adhesion, abrasion, corrosion, surface fatigue, deformation, impact and fretting wear. Due to the microscopic nature of each of these mechanisms, we would expect that one or a combination of them (as opposed to a non-wear mechanism) would be responsible for the wear-out of the micromachines studied in this paper.

Surface fatigue, deformation and impact wear typically require pressures in excess of those applied or predicted to have been present in the drive gear (roughly 30 MPa). There was no evidence of material flow or plastic deformation in any SEM images. In this experiment, the predominant motion between surfaces is sliding, not impact. Fretting wear occurs where machine elements experience small amplitude reciprocating motion, leading to microcracks and ultimately failure by fatigue.

Failure Model: Frequency-Dependent Wear

Most models of wear between two contacting or rubbing surfaces include the relationship between the wear volume, ΔV, and the length of the motion producing the wear, ΔL, and F, the force between the contacting surfaces. The model can be expressed as [36]:

$$\Delta V = cF\Delta L \qquad (1)$$

where c is a variable which is directly proportional to the wear coefficient and inversely proportional to the hardness of the material.

Following this general relationship, the total length of the motion creating the wear is related to the radius of the joint, r, and the number of revolutions, R, that the engine makes by:

$$\Delta L = 2\pi rR \qquad (2)$$

The derivation of the model for failure by wear begins by assuming that there is some critical volume, V_c, of material that must be worn in order to stop the motion of the micromachine. We anticipate that V_c is not a single number but is a distribution of values.

Bringing equations (1) and (2) together, setting ΔV to V_c, the critical volume for failure and R to R_f, the number of revolutions to failure and solving for R_f we get:

$$R_f = \left(\frac{1}{2\pi}\right)\left(\frac{1}{c}\right)\frac{V_c}{rF} \qquad (3)$$

In such a case, the net force on the joint will increase as the frequency approaches the critical frequency as [37]:

$$F = F_n \left[\frac{1}{\sqrt{\left[1-\left(\frac{\omega}{\omega_o}\right)^2\right]^2 + \left(\frac{1}{Q}\frac{\omega}{\omega_o}\right)^2}} \right] \quad (4)$$

where the term in large square brackets represents a "magnification factor" caused by approach to resonance and

F_n is the nominal force applied to the joint,

Q is the quality factor of the damped harmonic mechanical system and

ω/ω_o is the ratio of the driving frequency to the resonant frequency of the system.

Combining equations (3) and (4) we now arrive at the complete description for the reliability of a MEMS actuator failing due to wear at the pin joint, where again R_f represents the median number of revolutions to failure.

$$R_f = \left(\frac{1}{2\pi}\right)\left(\frac{1}{c}\right)\frac{V_c}{rF_n} \times \left[\sqrt{\left[1-\left(\frac{\omega}{\omega_o}\right)^2\right]^2 + \left(\frac{1}{Q}\frac{\omega}{\omega_o}\right)^2}\right] \quad (5)$$

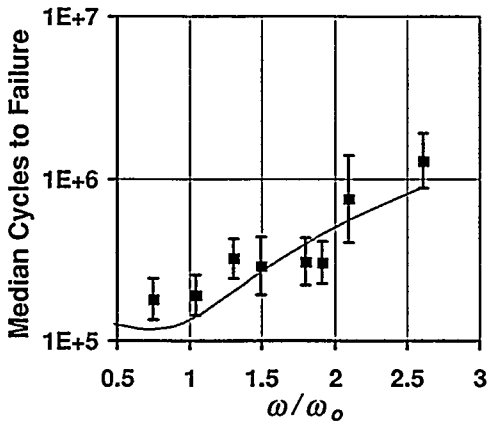

Figure 3.3.21. The failure data and the proposed wear model comparison shows good agreement. The value of c = 3 x 10^{-4} μm²/N was used in the model to generate the solid line.

Note that there are no adjustable parameters. The operative wear mechanism and the properties of the materials in contact determine the value of c. The physical constants that are material dependent are known or can be estimated. The other variables have been measured or calculated. Table 3.3.3 has the values of the model parameters and the corresponding references. Also V_c, the critical volume of adhered material, can be estimated from known physical parameters (see Appendix of this subsection).

In order to confirm the model derived above, we compare it to the actual failure data for the unimodal or lower distributions given in Table 3.3.2. This comparison is shown in Figure 3.3.21. The solid line is the shape that we get by simply using our

Table 3.3.3. Failure Model Parameters

Variable	Parameter	Value	Ref.
V_c	critical volume	~1.25x10^{-4} μm³	Section appendix
r	pin joint radius	1.5 μm	design
F_n	applied force	3x10^{-6} N	[30]
ω_o	resonant freq.	1150 Hz	measured
Q	quality factor	1.1	measured
σ_{yp}	uniaxial yield strength	1.2x10^{-3} N/μm²	[38]
K	adhesive wear constant	(5-60)x10^{-7}	[36]

best estimates of the physical parameters (from Table 3.3.3) in equation (5) and adjusting the variable c to minimize χ^2. The value of $c = 3 \times 10^{-4}$ $\mu m^2/N$ provided the curve that best describes the data with a χ^2 of 1.5.

There are two important characteristics in the data versus model comparison. First, the agreement supports the conclusion that the failures are associated with wear and not some other physical mechanism. However, the specific wear mechanism or combinations of mechanisms are as yet undetermined. Second, the functional dependence is correct, with the model clearly predicting the decrease in the number of revolutions to failure around the resonant frequency and the increase in the number of revolutions to failure above resonant frequency.

Failure Model: Adhesive Wear – A Step Further

For the specific mechanism of adhesive wear, the variable c in equation (5) is [35]:

$$c = \frac{K}{9\sigma_{yp}} \tag{6}$$

where K is the adhesive wear coefficient and σ_{yp} is the uniaxial yield strength of polysilicon. Adhesive wear occurs when the asperities between two surfaces (Figure 3.3.22a) form an adhesive bond (Figure 3.3.22b). The asperity then tears away, leaving a particle transferred to one surface (Figure 3.3.22c) or freed to become debris. In this way, material can transfer from one surface to another and result in regions where the micromachine can begin to stick and seize, as observed.

If equation (6) is substituted into equation (5) we then have a predictive model for the reliability of a MEMS actuator failing due to adhesive wear. R_f is the median number of revolutions to failure.

$$R_f = \left(\frac{9}{2\pi}\right)\left(\frac{\sigma_{yp}}{K}\right)\frac{V_c}{rF_n} \times \left[\sqrt{\left[1-\left(\frac{\omega}{\omega_o}\right)^2\right]^2 + \left(\frac{1}{Q}\frac{\omega}{\omega_o}\right)^2}\right] \tag{7}$$

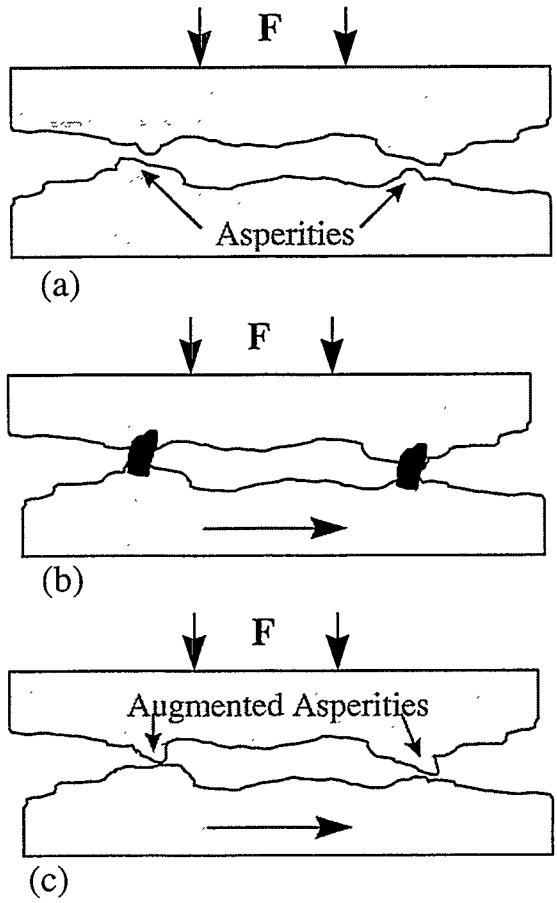

Figure 3.3.22. (a) A force, F, brings the two surfaces into contact at the asperities. (b) As the lower surface moves, the asperities adhesively bond together. (c) As the lower surface continues to move, the material breaks free again, leading to the augmented asperities on the upper surface.

Values of K for adhesive wear range from 5×10^{-7} to 6×10^{-6} for nonmetal sliding on an identical nonmetal using the tabulated values published in [36]. Nonmetal examples are nylon, alumina, or SiC. K has not been measured for polysilicon rubbing on polysilicon. If a value of $K = 3.4 \times 10^{-7}$, which is slightly out of the range, is used

with the value of σ_{yp} found in Table 3.3.3 an **identical** curve to that shown in Figure 3.3.21 is achieved.

A linear wear measurement was performed in which a polished silica sphere was rubbed on a blanket polysilicon-coated silicon wafer with a normal force of 98 mN. The value of K from this experiment was found to be 2.3×10^{-4} which is three orders of magnitude larger than the value in the model. This will shift the model down by three orders of magnitude implying that the microengines should fail much sooner if this value of K is correct.

The magnitude of K greatly affects the scale of the model and its uncertainty prevents validation of an adhesive wear model. The recent measurement described above used forces that are extreme (98 mN) compared to the peak forces in the microengines (μN), but the contact pressures and sliding velocities were similar to within an order of magnitude. The main difference between the macroscopic experiment to measure K and the microscopic lifetime experiment was the constraint of wear-generated debris. A particle generated in the center of the macroscopic experiment would have to travel 50 μm to exit the contacting surfaces, but in the microengine, the particle need only travel a few microns. The dramatic influence of third body wear upon tribological processes is well known [39]. Additionally, the macroscopic experiment used silica on polysilicon, which are not the same contacting surfaces in the microengines.

Additional Wear

There were two effects which could lead to additional wear that were not included in the model. First, it has been experimentally determined that the Y comb drive "linearly clamps" during a portion of rotation of the gear [40]. The clamping was due to the force from the fringing fields at the ends of the comb fingers that occur when the combs are fully engaged. This effect increases the force on the drive pin joint and will increase wear effects. Second, with our parallel data acquisition system, the device continues to be stimulated with voltages after failure. There is no means to power down a single device. This stimulation could give rise to further wear debris even when the gear not able to make a full rotation. While this impacts wear debris generation, it does not change the observed median number of cycles to failure.

Wear Structure Experiment

The experiment performed on the much simpler "sidewall" device revealed clear evidence of wear between the beam and the post at roughly the same forces experienced by the pin joint in the microengine. The agglomerates of wear particles were roughly 200 nm in diameter, from which we calculated a wear volume of 4.2×10^{-3} μm^3 (assuming spherical agglomerates). This was clearly greater than the critical volume, V_c, needed to stick a gear indicating that, at these forces, there was ample wear debris produced in the rubbing surfaces of the microengine to cause failure.

Bimodal Distributions

At three drive frequencies, two separate distributions of the devices were observed. The difference in the median number of cycles to failure between the lower and upper distributions was roughly three orders of magnitude. Examination of the longer-life devices showed no significant differences in wear debris compared to the shorter-life devices, indicating a slower average wear rate. Equation (5) indicates that a slower wear rate (longer life) would be achieved by smaller values of r, F_n, Q, or ω_o. The radius of the pin joint, r, is defined through a photolithography mask, hence has very little variation. The measured values of Q and ω_o

have some variation between samples, but not more than 0.1 for Q and 100 Hz for ω_o. However, it is possible for the nominal force, F_n, to vary. As mentioned earlier, the drive-signal optimization was based on a small sample of devices. These long-lived devices might be better optimized than their counterparts leading to smaller forces on the gears.

Conclusions

We have presented and validated the first quantitative and predictive model for MEMS actuator reliability. This first-principles, frequency-dependent wear model accurately describes statistically significant data over a wide range of frequencies, both above and below resonance. The model, which is based on the concept of wear coupled with mechanical resonance effects, correctly describes both our qualitative and quantitative observations of wear.

The large amounts of debris we observed in the areas of rubbing surfaces led to the failures in the drive gears of the microengines as detailed in numerous SEM images. The FIB cross sections of the drive gear showed severe notching in the pin joint, which probably lead to eventual breakage of the pin joint in 3 of the 220 parts stressed.

The results from the sidewall structure indicate that there was ample wear debris produced at these forces to form an agglomerate and cause failure.

Wear observed in the pin joints was successfully duplicated in simpler structures driven under similar conditions. The morphology of the wear particles was insufficient to determine whether they are due to adhesive or abrasive wear. The wear process most likely involves a combination of mechanisms, such that the initial wear particles result from surface degradation and adhesion and then particles trapped at the interface during rubbing cause abrasive wear to create additional particles.

Appendix

The critical volume, V_c, is a measure of the total amount of material that must be transferred by adhesive wear before a failure can occur. This is an unknown quantity. However, we have estimated it by calculating the size of asperity needed to stop the motion of the joint after an adhesive bond occurs, as in Figure 3.3.22b. The cross-sectional area of such a bond that can just stop the motion of the joint is given as:

$$A_c = F_n / \sigma_{yp} \qquad (6)$$

where A_c is the "critical area" of the adhesive bond.

If one assumes a roughly cubic mass of material with this critical area and all wear material contributes to the volume, then the critical volume of this mass is given by:

$$V_c = A_c^{3/2} = \left[F_n / \sigma_{yp}\right]^{3/2} \qquad (7)$$

Which for the values of force and yield strength in table 3.3.3, give a value of 1.25 x 10^{-4} μm^3.

[29] E. J. Garcia and J. J. Sniegowski, "Surface micromachined microengine", Sensors and Actuators A, **Vol. 48**, 1995, pp. 203-214.

[30] S. L. Miller, J. J. Sniegowski, G. LaVigne, and P. J. McWhorter, "Friction in Surface Micromachined Microengines", *Proceedings of SPIE Smart Electronics and MEMS* **Vol. 2722**, San Diego, Feb. 28-29, 1996, pp. 197-204.

[31] D. M. Tanner, W. M. Miller, W. P. Eaton, L. W. Irwin, K. A. Peterson, M. T. Dugger, D. C. Senft, N. F. Smith, P. Tangyunyong, and S. L. Miller, "The Effect of Frequency on the Lifetime of a

Surface Micromachined Microengine Driving a Load," *1998 IEEE International Reliability Physics Proceedings,* Reno, NV, 1998, pp. 26-35.

[32] S. L. Miller, J. J. Sniegowski, G. LaVigne, and P. J. McWhorter, "Performance tradeoffs for a surface micromachined microengine", *Proceedings of SPIE Micromachined Devices and Components II*, **Vol. 2882**, Austin, October. 14-15, 1996, pp. 182-191.

[33] D. C. Senft and M. T. Dugger, " Friction and wear in surface micromachined tribological test devices," Proceedings SPIE Symposium on Micromachining and Microfabrication, Vol. 3224, Austin, 1997, pp 31-38.

[34] K. A. Peterson, P. Tangyunyong, and D. L. Barton, "Failure Analysis for Micro-Electrical-Mechanical Systems (MEMS)," Proceedings of the 23rd International Symposium for Testing and Failure Analysis, October 1997, Santa Clara, pp. 133-142.

[35] J. A. Collins, Failure of Materials in Mechanical Design, New York, John Wiley & Sons, 1981.

[36] Ernest Rabinowicz, Friction and Wear of Materials, 2nd ed., New York, John Wiley & Sons, Inc., 1995.

[37] C. R. Freberg and E. N. Kemler, *Elements of Mechanical Vibration, 2nd ed.,* New York, John Wiley & Sons, Inc., 1949.

[38] W. N. Sharpe, Jr, B. Yuan, R. Vaidyanathan and R. L. Edwards, "Measurements of Young's Modulus, Poisson's Ratio and Tensile Strength of Polysilicon," *Proc. MEMS 97,* 10th *IEEE Inter. Workshop on MicroElectroMechanical Systems*, pp. 424-429.

[39] Irwin L. Singer, "How Third-Body Processes Affect Friction and Wear," MRS Bulletin, Vol. 23, No. 6, June 1998.

[40] S. L. Miller, M. S. Rodgers, G. LaVigne, J. J. Sniegowski, P. Clews, D. M. Tanner, K. A. Peterson, "Failure Modes in Surface Micromachined MicroElectroMechanical Actuators," *Proc. 1998 IEEE International Reliability Physics Symposium,* Reno, NV, 1998, pp. 17-25.

3.4 Linkage design effect

The reliability of microengines is a function of the design of the mechanical linkage used to connect the electrostatic actuator to the drive. We describe here a series of reliability stress tests on surface micromachined microengines driving an inertial load. In these experiments, we used microengines that had pin mechanisms with guides connecting the drive arms to the electrostatic actuators. Comparing this data to the previous result (see section 3.3) using flexure linkages revealed that the pin linkage design was less reliable. Significant amounts of wear debris were observed around both the hub and pin joint of the drive gear. Additionally, wear tracks were observed in the area where the moving shuttle rubbed against the guides of the pin linkage. A model was developed to describe the failure data based on fundamental wear mechanisms and forces exhibited in mechanical resonant systems.

Introduction

The objective of this work was to determine the effect of mechanical linkage design on the lifetime of the microengine driving a load (Figure 3.4.1). We have stressed a statistically significant number of microengines driving loads with two different linkages in the Y shuttle. One linkage was a flexure with simple guides and the other was a pin mechanism with complex guides.

The comb drives of these microengines have springs that restore any deflections back to the rest position. The polysilicon comb drive exhibits a resonant frequency

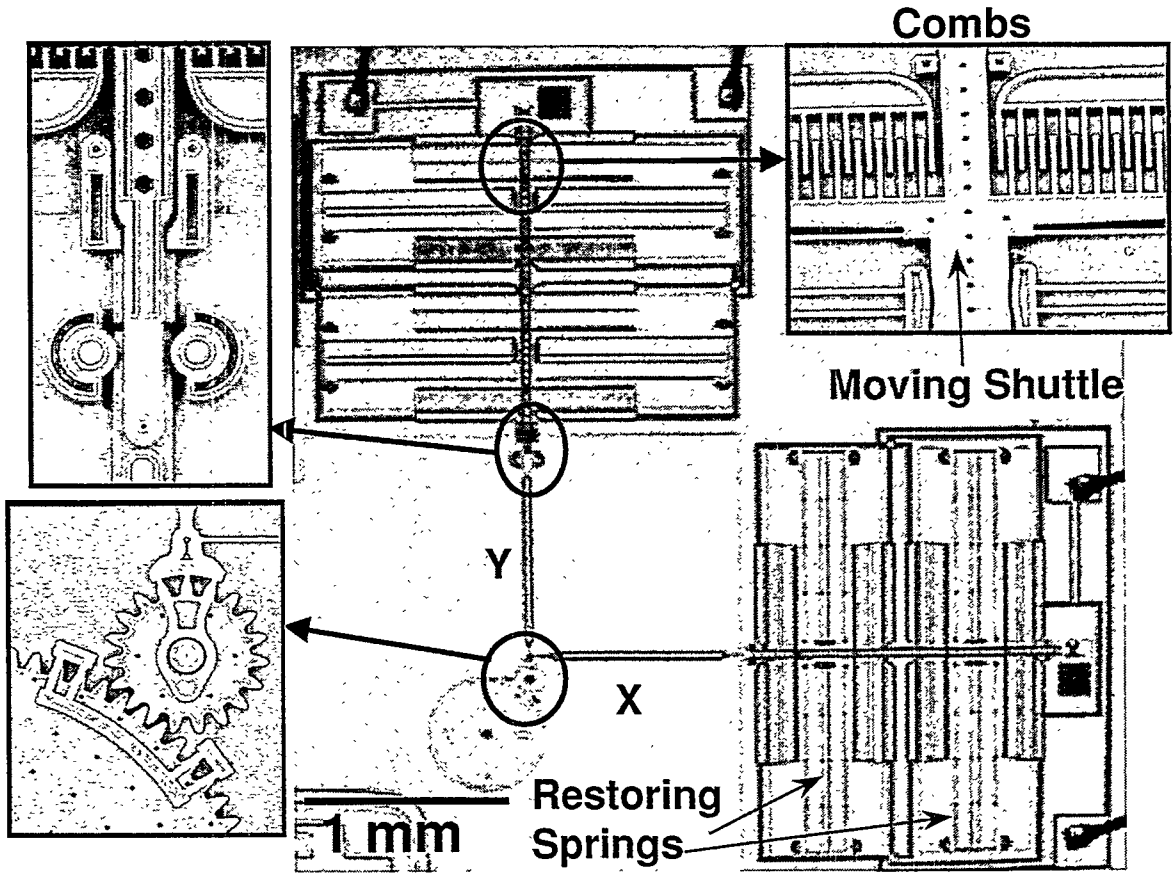

Figure 3.4.1. The microengine driving a load with expanded views of the combs (top right), the pin linkage (top left), and the drive gear and load gear (lower left).

(observed as the frequency of maximum displacement) like any mechanical oscillating system. By selecting frequencies above and below resonance, we have collected data for the median lifetime of the microengine driving a load as a function of f/f_o where f is the stress frequency and f_o is the resonance frequency.

We compared the lifetime results of the pin linkage design to the predictive model [41] for the number of revolutions to failure. We developed two models that are based on the fundamental principles of the physics of wear in a mechanically resonating system. One model describes the low-contact-pressure wear at the guides of the pin linkage in the Y shuttle and the other describes the high-contact-pressure wear at the same location.

Mechanical design

This study used the electrostatically driven microactuator (microengine) developed at Sandia National Laboratories [42]. The microengine consists of orthogonal linear comb drive actuators mechanically connected to a rotating gear as seen in Figure 3.4.1. By applying the proper drive voltages, the linear displacement of the comb drives was transformed into circular motion at the drive pin. The X and Y linkage arms are connected to the gear via a pin joint. The gear rotates about a hub that was anchored to the substrate.

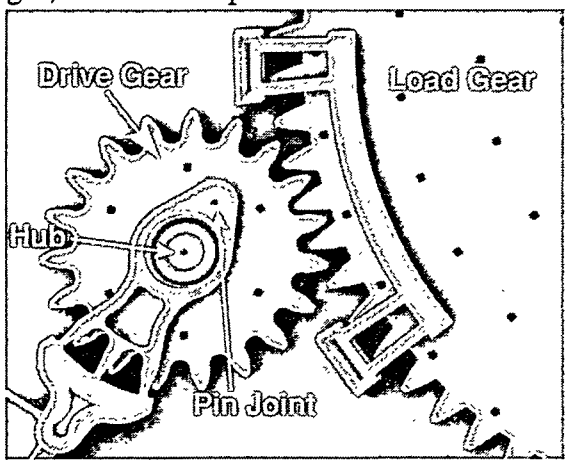

Figure 3.4.2. Close-up view of the drive gear meshing with the load gear. The right bracket ( ]) shaped guide on the load gear mitigates out-of-plane wobble to ensure proper meshing of teeth. The hub is anchored to the substrate and the pin joint connects the actuator linkage to the drive gear.

We used the microengine to drive the load gear depicted in the close-up view as shown in Figure 3.4.2. The radius of the microengine drive gear was 38 μm and the load gear was four times as large.

The pin and flexure linkages with guides are shown in Figure 3.4.3. The pin is 8 μm in diameter and was located in a 10 μm opening. It is free to move in the vertical direction unlike the pin joint in the drive gear that is constrained. In order to prevent pin displacement in the vertical direction, which would disconnect the shuttle from the linkage arm, the long guides (Figure 3.4.3a,

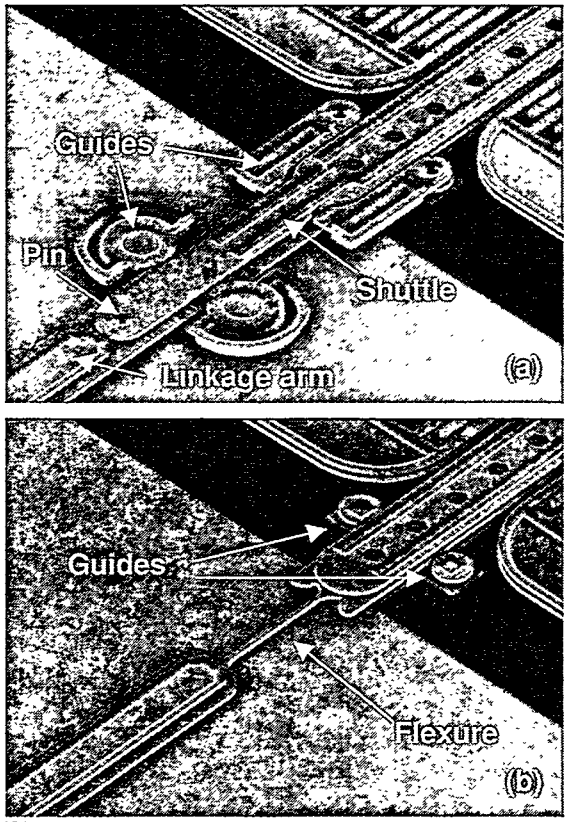

Figure 3.4.3. The top SEM shows the pin linkage (a) with guides deemed necessary to control the lateral motion of the shuttle. The lower SEM (b) shows the simpler design of the guides for the flexure linkage type.

right) were added to the design. The long guide is further constrained vertically to 0.5 μm by the use of dimples. The half-round guides constrain the vertical motion of the linkage arm to 2 μm and the lateral motion to 0.5 μm.

The simple guides shown in Figure 3.4.3b have only 0.5 μm lateral clearance and no vertical restraint. These guides are typically used for flexure linkage systems where there is no concern about vertical deflection. In this system, the shuttle is connected to the linkage arm by a 2 μm wide, 40 μm long link of polysilicon.

Experiment

We characterized the drive parameters fully by measuring both the resonant frequency and the normalized spring constant of the loaded microengine system. They were 1150 Hz and 1875, respectively. For all experiments, we accelerated the load gear to full speed in three rotations of the drive gear. This method was necessary to limit acceleration forces caused by the inertia of the large gear.

The dice were packaged with glass covers to allow viewing of the rotating gears. The covers were taped on so they prevented particle contamination but allowed access to the ambient environment of the laboratory. The packages were stored in a dry nitrogen environment before the test. The tester, Sandia High Volume Measurement of Micromachine Reliability (SHiMMeR – see section 1.2), was used to provide electrical signals to large numbers of packaged microengines driving loads and to optically inspect them for functionality.

We performed stress tests at eight frequencies, 860, 1204, 1500, 1720, 2064, 2200, 2408, and 3000 Hz. The resonant frequency of the system was 1150 Hz which allowed for stresses both above and below resonance. The stress intervals followed roughly the same sequence for all the experiments. The sequence was 2000, 4000, 8000, 16000, ..., rotation cycles of the drive gear per stress. If more than 4 parts failed during a particular stress, we repeated that stress interval. The devices were stressed at high speed and then slowed to 1 Hz to inspect for functionality. A failure was defined as the inability of the microengine drive gear to make a complete revolution at the 1 Hz inspection speed. During the inspection interval, we noted any observed changes or degradation in the motion of the gears for our records.

Results and Discussion

Data Analysis

Because the parts were observed at fixed inspection times, common to all the parts, the results fall into the category of reliability data called "interval" data. We plotted the accumulated number of cycles to failure against the cumulative percent failure for each stress frequency. The lognormal fit resulted in an estimate of t_{50}, the median cycles to failure. The estimate for the lognormal shape parameter, σ, was also determined.

The experimental results for the microengines driving loads with the pin linkage are listed in Table 3.4.1. We performed ten experiments and caused a total of 277 parts to fail.

Most of the data from each of the experiments could be described by a simple

Table 3.4.1. Series of frequency experiments performed.

f (Hz)	f/f_o	# Parts on test	# Parts Failed	# stress intervals
860	0.75	33	33	30
1204	1.05	45	41	23
1500	1.30	10	10	21
1500	1.30	42	42	30
1720	1.50	23	23	30
2064	1.79	32	32	40
2200	1.91	26	26	17
2408	2.09	28	27	27
3000	2.61	13	13	23
3000	2.61	40	40	23

unimodal distribution such as seen in Figure 3.4.4. In this figure, the first point and last two points were omitted from the fit as outliers. The regression analysis yielded a

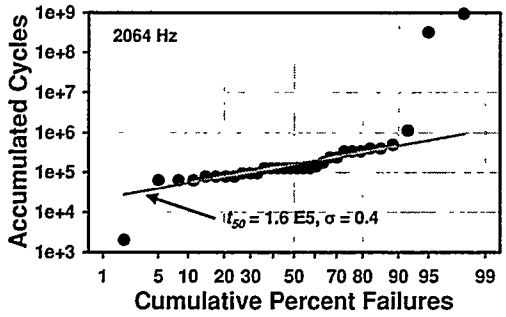

Figure 3.4.4. Lognormal distribution of accumulated cycles to failure for the 2064 Hz stress. The lower and upper freak data points were omitted from the regression analysis.

Table 3.4.2. Results of median number of cycles to failure from all frequency experiments performed.

f (Hz)	f/f_o	t_{50}	σ
860	0.75	8.50E4	0.35
1204	1.05	1.60E5	0.22
1500	1.30	1.29E5	0.65
1720	1.50	2.6E5	0.25
2064	1.79	1.60E5	0.37
2200	1.91	1.02E5	0.25
2408	2.09	7.20E4	0.26
3000	2.61	2.33E5	0.39

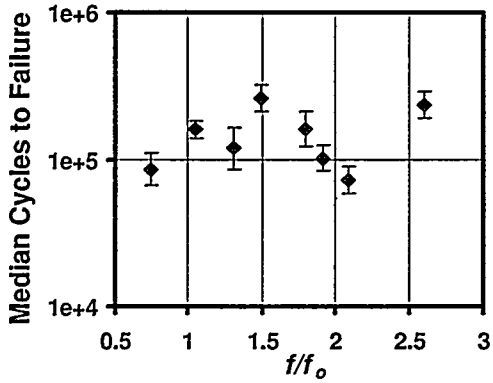

Figure 3.4.5. The frequency dependence of the lifetime of the microengines with pin linkages driving a load. The error bars represent 90% confidence bounds.

value of median cycles to failure of 1.6×10^5 cycles with σ = .37. The last two points could be the onset of another stronger population since bimodal distributions were observed in two of the frequency experiments.

Table 3.4.2 shows the results of lognormal fits to all of the frequency experiments. The data is also graphically represented in Figure 3.4.5 with 90% confidence bounds represented by error bars.

For the stress frequencies of 1500 and 3000Hz, we repeated the experiments and the results of the second experiment were within the 90% confidence bounds of the first experiment. We then averaged the two results. This was an excellent demonstration of lot to lot repeatability since the microengines in the second experiment were from a different fabrication lot but of the same technology and design.

Experimental Observations

The behavior of the microengines as they were stressed followed a consistent pattern. Initially the microengines ran smoothly. With the accumulation of stress, the operation of the microengines became sticky and jerky (stick-slip behavior) at inspection frequencies. Some of the microengines would actually work through the sticky behavior and become smooth again. Near the end of life, the rotation became more erratic until the microengine failed by sticking or rocking back and forth through a small angle.

After failure, the part was still being stimulated by the drive signals so we optically panned across the entire microengine to get clues about the failure. We observed cases where the drive gear/load gear combination appeared stuck since we could see slight movement in the adjoining comb drives and shuttles. In other cases, the pin joint of the drive gear appeared to be stuck. Nearly half of the devices in this experiment

failed with the Y shuttle stuck indicating that this was the dominant failure mode.

Comparison of flex to pin

The flexure microengine reliability study

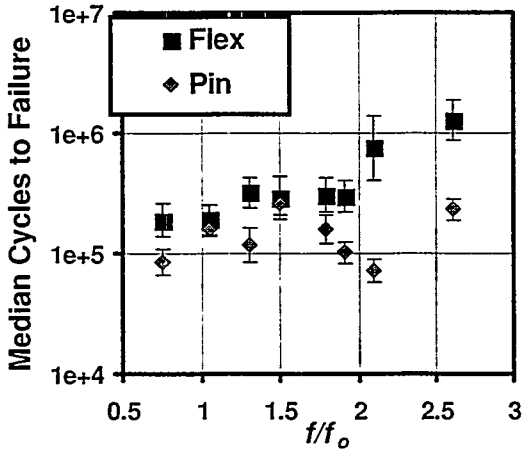

Figure 3.4.6. This comparison of median cycles to failure between the flexure linkage and the pin linkage shows the pin linkage to be less reliable.

was documented in section 3.3 of this report. We compare the two by plotting the median number of cycles to failure against the ratio of the stress frequency to the resonant frequency. As seen in Figure 3.4.6, all of the experiments with pin linkages have lower median cycles to failure than the flex linkage thus implying lower reliability.

Failure Analysis

Failure analysis on the pin linkage microengine driving a load has proceeded in much the same way as its counterpart, the flex linkage system. It was possible to optically document the existences of wear debris at drive gear hubs and, occasionally, its broadcast over the top of the gear from the drive pin region. It was also possible to document its absence from the load gear hub. These observations are from top view images into the gap between the hub and the gear.

Wear debris observations were corroborated in SEM imaging as shown in Figure 3.4.7. Arrows at right and in the center show wear debris in and on the hub of a drive gear that has been driven to 62,000 cycles. Lift-off techniques were used to remove drive gears for an inspection of the underside, as shown in Figure 3.4.8. The drive pin flange appears in the center of the image, with wear debris that has been broadcast over the horizontal surface between the flange and gear, and emerges at the perimeter of the pin flange. A similar effect occurs for the drive-gear hub lower flange, as seen in the lower right of the image.

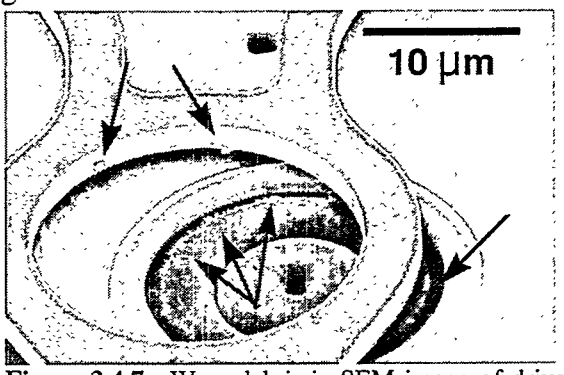

Figure 3.4.7. Wear debris in SEM image of drive gear and hub from pinned joint microengine tested to 62,000 cycles.

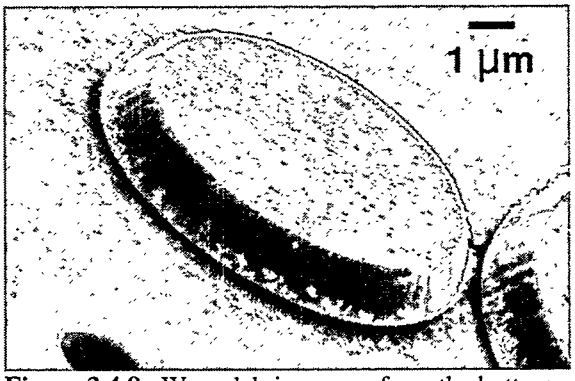

Figure 3.4.8. Wear debris as seen from the bottom of the gear, around the drive pin flange (center) and hub lower flange (lower right).

Load gear hubs were characteristically free from wear debris as in earlier work. A comparison of worn and wear-free bearing interfaces is shown in Figure 3.4.9. These images are SEM photomicrographs of FIB sections performed on pin linkage microen-

gines. The gaps between gear and flange surfaces characteristically fill with debris on drive gears, and are free from debris or any evidence of wear on load gears. All wear debris observations suffer from the fact that in the current test setup, all engines continue to receive drive signals until all engines on a die fail. In this way, a gear may be permitted to vibrate for a significant period after being considered a failure. Future testing will be conducted to alleviate this condition and provide more detailed snapshot at early wear debris observations. Such observations

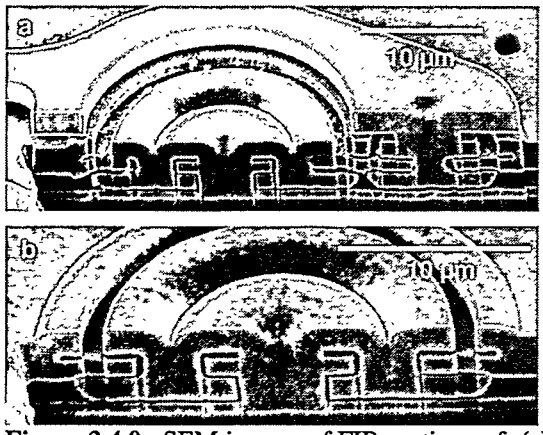

Figure 3.4.9. SEM images of FIB sections of (a) a drive gear hub and a drive pin and (b) a load gear hub from a pin linkage microengine operated to failure.

have been made at other locations on the engine, namely shuttles that reciprocate between guides.

Pin linkage shuttles have a pin joint at the link between the Y shuttle (Fig. 3.4.3) and its link arm. This link is accompanied by structures anchored to the substrate, which serve to restrain the shuttle and link arm both laterally and vertically. The long guide at the shuttle includes a vertical oblong dimple extending downward. The horizontal surfaces at the link arm are planar. The surface between these guides and the actuating structures is an additional site where wear can occur on pin linkage engines. This wear is shown in Figure 3.4.10a to occur both at the half-round guide and the long shuttle guide. The wear track shown on the right in Figure 3.4.10a is further magnified in Figures 3.4.10b and 3.4.10c. The extent of the reciprocation is such that the long shuttle guide with the dimples contacts only the shuttle and the half-round guides contact only the link arm.

We optically inspected 99 pin linkage microengines and found that 57% had wear tracks. All had wear debris much like we observed previously which we attributed to adhesive wear. Tracks were observed on microengines with only 2000 cycles of stress. However, many microengines had over 10^6 (one near 10^9) cycles with no wear tracks. The data were sorted according to the drive frequency, number of cycles to

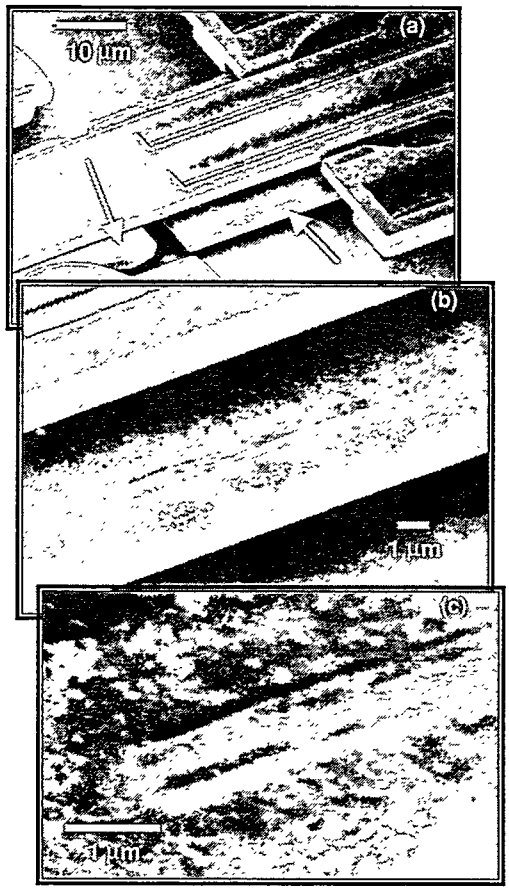

Figure 3.4.10. Wear debris and deep grooving of the shuttle from the dimples in the guides at successively higher magnification. These images were from a pin linkage microengine stressed at 1720 Hz for 290,000 cycles

failure and whether a track was observed and no pattern was found. Wear track formation appears to be a random occurrence.

In several cases, optical examination of microengines being exercised with a drive cycle indicated that the Y shuttle was incapable of movement. Often, this is accompanied by other indicators such as cyclic flexing of the shuttle resulting in vertical displacement, or movement of the Y link arm up to the link pin under the action of the X shuttle. The X shuttle operates normally in all cases where it has been excised from the rest of the system.

Figure 3.4.11 shows a high tilt angle view of the pin linkage region of such an engine. Proximity or contact, although recorded where possible, is not a certain indicator of adherence between rubbing surfaces in our experience. At high tilt, the dimple (high magnification - upper right) appears not to be in contact with the shuttle although severe wear debris has been generated. The half round guide (lower right) appears to be in contact with the link arm.

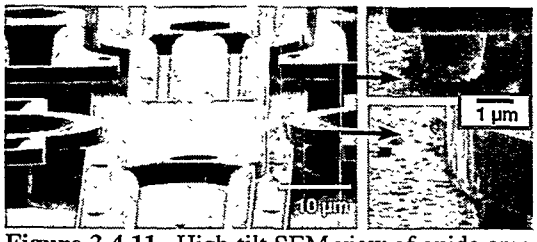

Figure 3.4.11. High-tilt SEM view of guide area and magnified views of guides.

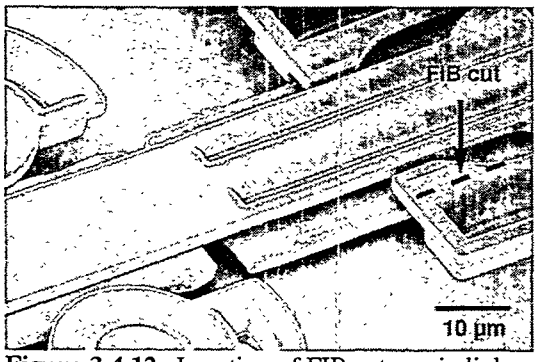

Figure 3.4.12. Location of FIB cut on pin linkage guide.

Frequently, the shuttle was severely grooved on one side and less damaged on the other, indicating that the shuttle was canted during operation. The dimples appeared to have horizontal, smooth bottoms as indicated by control samples. FIB sections of one shuttle indicate asperities from rubbing which correspond to grooves in the shuttles.

In several instances, the FIB was successfully used to sever the connection between the portion of the guide supporting the dimple and the shuttle. A view of the placement of such a cut is shown in Figure 3.4.12.

Two effects were observed. When the dimple was stuck to the shuttle, as the ion beam milled through the last remaining thickness of the guide, the springs of the comb drive restored the shuttle to its equilibrium position, carrying the remnant of the guide and stuck dimple as shown in Figure 3.4.13. Subsequent operation of these engines was restored by FIB cuts such as these.

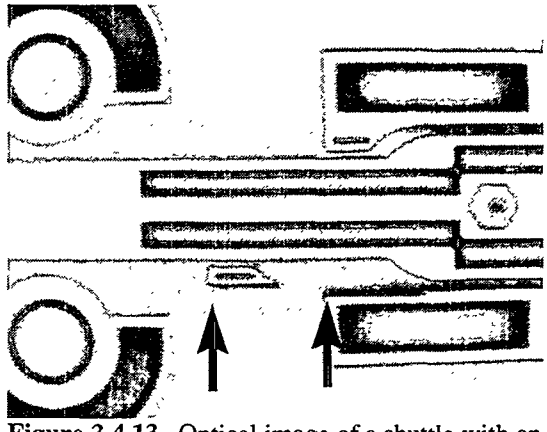

Figure 3.4.13. Optical image of a shuttle with an attached dimple that was freed from the anchored portion of the guide by a FIB cut. The shuttle moved to the left with no external force applied to the engine.

Linkage pins attached to the Y shuttles and receiver holes in the connecting arms also show some evidence of directional wear. This has been corroborated by FIB sectioning and is shown in the SEM images

of Figures 3.4.14 and 3.4.15. Pin wear was predominantly on faces perpendicular to the direction of motion of the shuttle. The worn receiver hole in Figure 3.4.15 is viewed from the top surface, and the control sample is viewed from the bottom surface, which was exposed when it was lifted off. The wear resulting form operation is quite evident.

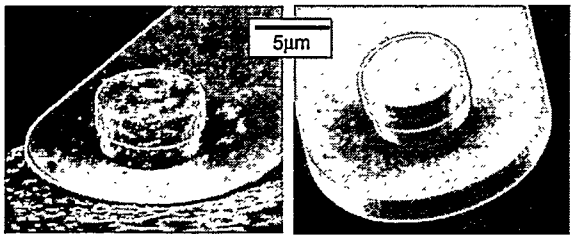

Figure 3.4.14. Linkage pins from a failed engine (left) and from a control sample (right).

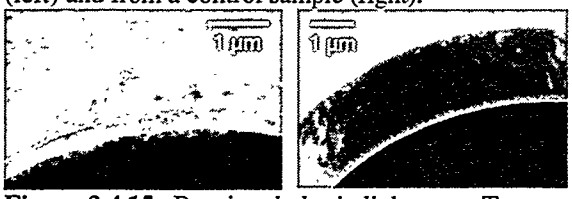

Figure 3.4.15. Receiver holes in link arms. Top view on engine worn to failure (left) and view of bottom surface of engine which was never operated (right).

Figure 3.4.16 is an SEM image at 0° tilt angle that shows a typical result for pin joint receiver holes in drive gears in both flex linkage and pin linkage microengines tested to failure. The wear debris is generated somewhat more severely at drive pins than at drive hubs. Many receiver holes show this appearance of material having been "scooped out" from the bore on one side and wear debris piled up in another site—effectively changing the location of the hole. Compare this to the round appearance of the hub attachment pillar and lower hub flange on the right of the image. This engine failed into a rocking mode; it did not seize up completely. A magnified view of this hole is shown in Figure 3.4.17.

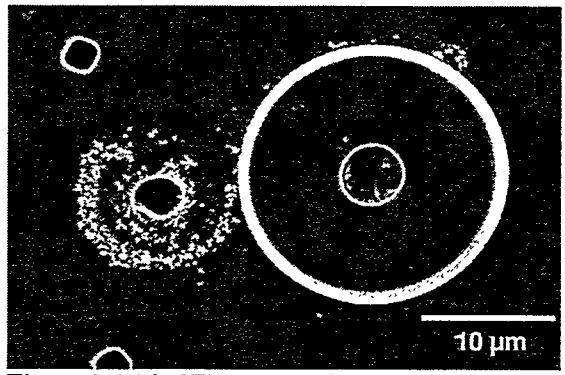

Figure 3.4.16. SEM image of receiver hole in drive gear exhibiting severe wear.

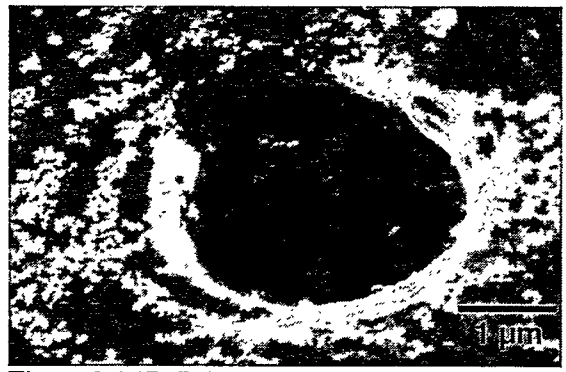

Figure 3.4.17. Drive gear receiver hole in a pin linkage microengine tested to failure.

FA Summary

Both pin linkage and flex linkage microengines driving load gears experienced significant wear which was most severe at pins and receivers in the drive gear, and also frequently found on drive gear hubs. No instance of wear debris has been observed on load gear hubs of pin linkage microengines driving loads. Significant wear has been found at locations unique to the pin linkage microengines, such as pins and holes and restraining guides and shuttles. The occurrence of debris on the Y shuttle guides of the flex linkage engines has been somewhat lower. The guides on the flex linkage engine have 0.5-micron spacing and are not clamped with a dimple from the upper layer of polysilicon.

Model Development

It is critical that a failure model be developed that describes the observed physics of failure and allows prediction of ultimate failure in any final design. To do so the failure modes must be established from statistically significant data.

Failure Modes

We have observed that wear is a primary failure mechanism in microengines (see sections 3.3 and 3.10 in this report). Using a wear variable for adhesive wear provided a good fit to the previous data. One typically describes adhesive wear as having a low contact pressure and abrasive wear with a high contact pressure [43]. In reality, wear is a combination of these processes with adhesion producing debris that can then abrade the rubbing surfaces. For this reason, we will refer to low and high contact pressure effects rather than trying to classify the wear process.

Low contact pressure effects

At low contact pressures, the wear model developed in section 3.3 describes the data quite well. The equation describing the wear was

$$R_{f(lcp)} = \left(\frac{1}{2\pi}\right)\left(\frac{1}{c}\right)\frac{V_c}{rF_N} \qquad (1)$$

where c was a wear variable, V_c was the critical volume to seize the microengine, r was the radius of the pin joint, and F_n was the normal force. (lcp refers to low contact pressure while hpc stands for high contact pressure)

If we consider wear in the guide region, we can substitute $2\pi r$, the wear length of equation 1, with the new wear length of the guide which is $4r'$, where r' is the radius of the hub center to the pin joint. Therefore, the equation for failure due to guides would be

$$R_{f(lcp)g} = \left(\frac{1}{4}\right)\left(\frac{1}{c}\right)\frac{V_c}{r' F_N} \qquad (2)$$

We found good agreement between the data and the model if we used the c of adhesive wear

$$c = \frac{K}{9\sigma_{yp}} \qquad (3)$$

where K is the adhesive wear constant and σ_{yp} is the uniaxial yield strength.

High contact pressure effects

High contact pressure (hcp) wear (example shown in Figure 3.4.19) may take place where a hard asperity on one surface gouges or wears another mating surface. This is commonly called two-body wear. Likewise a hard particle trapped between two surfaces can lead to gouging and wear in what is called three-body wear. We will assume that work-hardened asperities or particles

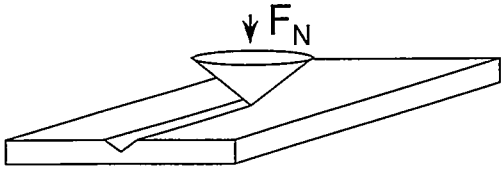

Figure 3.4.18. Example of how hcp wear occurs. An assumed conical asperity gouges a prismatic wear track in the polysilicon of the shuttle.

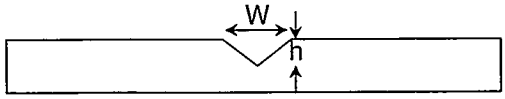

Figure 3.4.19. Definitions of groove parameters used in hcp wear derivations.

may result in the gouging seen in the surface of the wearing surface and will further assume that the shape of this asperity is roughly conical and that only a single asperity actually makes contact and creates the wear. The penetration of this asperity will be such that the normal force, F_N applied to it divided by the contact area, A is equal to the flow stress in the polysilicon. Thus,

$$F_N = 3A\sigma_{yp} \qquad (4)$$

Given that the asperity is assumed to be conical, the contact area, A, can be written as:

$$A = \frac{\pi}{4} W^2 \tag{5}$$

And hence the forces balance when:

$$F_N = \frac{3\pi}{4} W^2 \sigma_{yp} \tag{6}$$

where the width of the groove is given as W.

The hcp wear volume, V_{hcp} swept out by the per cycle is then given as:

$$V_{hcp} = Wh\Delta L\alpha \tag{7}$$

where the height of the groove is given as h and the total wear length is given as ΔL. The constant α is the reciprocal of the total number of cycles to produce the wear track of height, h, and width, W. Replacing the wear length with its value given in equation (2) yields:

$$V_{hcp} = 4r' RWh\alpha \tag{8}$$

By substituting the value for W obtained by inverting equation (6) into the expression for the hcp wear volume in equation (8) we may write:

$$V_{hcp} = \sqrt{\frac{64F_N}{3\pi\sigma_{yp}}} hr' R\alpha \tag{9}$$

Just as for lcp wear, when the wear volume equals some critical volume (described below) we would expect the device to fail. Thus, we can use equation (9) setting V_{hcp} to V_c and R to $R_{f(hcp)g}$ (the number of revolutions to failure for high-contact-pressure wear in the guide) to get:

$$R_{f(hcp)g} = \frac{V_c}{\alpha hr'} \sqrt{\frac{3\pi\sigma_{yp}}{64F_N}} \tag{10}$$

Resonance Effects

The true normal force on the guide will vary with excitation frequency, ω, as the critical frequency, ω_o, for resonance is approached due to variations in forces caused by the inertia of the system and the tolerance in the pin joints. The joints have approximately 50% tolerance as measured by the total diametrical gap divided by the joint size.

In such a case, the normal force, F_N on the guide will increase as the frequency approaches the critical frequency as [44]:

$$F_N = F_n \left[\frac{1}{\sqrt{\left[1 - \left(\frac{\omega}{\omega_o}\right)^2\right]^2 + \left(\frac{1}{Q}\frac{\omega}{\omega_o}\right)^2}} \right] \tag{11}$$

where the term in large square brackets represents a "magnification factor" caused by approach to resonance and

F_n is the nominal force applied to the guide,

Q is the "quality factor" of the damped harmonic mechanical system and

ω/ω_o is the ratio of the driving frequency to the resonant frequency of the system.

Combined wear model:

Combining equations (3), (10) and (11) we now arrive at the description for the reliability of a MEMS actuator failing due to lcp and hcp wear occurring between the guide and the Y-shuttle of the microengine. The mechanism that leads to the earliest failure will predominate.

$$R_{f(lcp)g} = \left(\frac{1}{4}\right)\left(\frac{1}{c}\right)\frac{V_c}{r'F_n}\times \left[\sqrt{\left[1-\left(\frac{\omega}{\omega_o}\right)^2\right]^2+\left(\frac{1}{Q}\frac{\omega}{\omega_o}\right)^2}\right] \quad (12)$$

$$R_{f(hcp)g} = \frac{V_c}{8\alpha h r'}\times \sqrt{\frac{3\pi\sigma_{yp}}{F_n}}\sqrt{\left[1-\left(\frac{\omega}{\omega_0}\right)^2\right]^2+\left(\frac{1}{Q}\frac{\omega}{\omega_0}\right)^2} \quad (13)$$

The formula for the number of revolutions to failure when the wear occurs mainly in the pin joint of the drive gear was derived in section 3.3 of this report.

Note that there are no adjustable fit parameters. The physical constant variables that are material dependent are known or can be estimated. The other variables have been measured or calculated.

V_c, the critical volume of adhered material, can be estimated from known physical parameters [46] by calculating the size of an asperity needed to stop the motion of the guide after an adhered junction occurs (Figure 3.4.18b). The cross-sectional area of such a junction that can just stop the motion of the shuttle is given as:

$$A_c = F_\ell / \sigma_{yp} \quad (15)$$

where A_c is the "critical area" of the adhered junction and F_ℓ is the longitudinal force exerted by the moving shuttle. F_ℓ was measured by displacing a cantilever beam with known physical parameters with the shuttle. The maximum drive voltage of 80V was used to produce a force of 11.8 μN.

If one assumes a roughly cubic mass of material with this critical area, then the critical volume of this mass is given by:

$$V_c = A_c^{3/2} = \left[F_\ell / \sigma_{yp}\right]^{3/2} \quad (16)$$

For the values of force and yield strength given in table 3.4.3, we calculate a value of 9.75×10^{-4} μm^3 for V_c.

The normal force was calculated using a model of a single layer comb. The maximum levitation force at a voltage of 80 V was determined to be 39 μN. Since this is the value at one extreme, we used an average value of 19.5 μN.

The adhesive wear constant for polysilicon on polysilicon hasn't been measured. The value in Table 3.4.3 was an estimate from experiments of ceramic on ceramic wear.

Comparison to Model

Table 3.4.3 has the values of the model parameters and the corresponding references. Figure 3.4.20 shows the measured

Table 3.4.3. Failure Model Parameters

Variable	Parameter	Value	Ref.
σ_{yp}	uniaxial yield strength	1.2×10^{-3} N/μm^2	[5]
K	adhesive wear constant	4×10^{-7}	[45]
V_c	critical volume	9.75×10^{-4} μm^3	calculated
r'	Hub to pin joint radius	17 μm	design
F_n	Normal force	19.5 μN	calculated
ω_o	Resonant freq.	1150 Hz	measured
Q	Quality factor	1.1	measured
F_ℓ	Longitudinal force	11.8 μN	measured
α	Cycle constant	3.5×10^{-6}	measured
H	Height of track	67 nm	measured

reliability data as compared to the various models. The data are bounded between the two lcp wear models. The pin-joint wear model assumes the dominant wear occurs in the pin joint of the drive gear. In the linkage wear model, the assumption is that the dominant wear occurs in the Y-shuttle linkage. The linkage hcp wear model describes wear occurring in the Y-shuttle linkage.

It is surprising that the high-contact-pressure model did so poorly. We definitely have observed wear tracks. However, we also observed large amounts of wear particles. It is possible that a particle lodged between the dimple and the shuttle formed the track and then broke off leading to more low contact pressure wear.

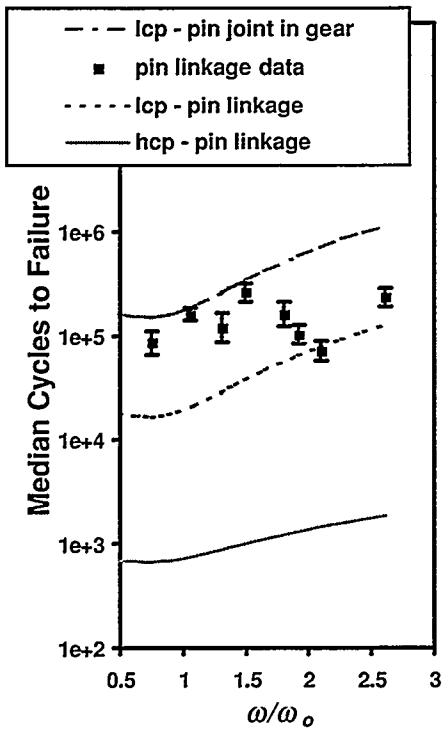

Figure 3.4.20. Pin linkage data compared to the various wear models.

Conclusions

We have determined that the pin mechanism linkage is less reliable than the flexure linkage. This was due to the tight tolerance (0.5 μm) of the guides that prevent vertical motion. We observed excessive wear debris and wear tracks due to the rubbing of the dimple and the moving shuttle. The wear tracks appear on microengines with low accumulated cycles and high accumulated cycles. Many microengines failed with no observable wear tracks.

We have presented an contact-pressure wear model which bounds the data indicating that the failures were a combination of wear occurring in the drive gear pin joint and wear occurring between the dimple and the Y shuttle.

[41] D. M. Tanner, W. M. Miller, W. P. Eaton, L. W. Irwin, K. A. Peterson, M. T. Dugger, D. C. Senft, N. F. Smith, P. Tangyunyong and S. L. Miller, "The Effect of Frequency on the Lifetime of a Surface Micromachined Microengine Driving a Load," *1998 IEEE International Reliability Physics Proceedings, IRPS 98*, pp. 26-35 (1998).

[42] E. J. Garcia and J. J. Sniegowski, "Surface micromachined microengine", Sensors and Actuators A, **Vol. 48**, 1995, pp. 203-214.

[43] J. A. Collins, *Failure of Materials in Mechanical Design*, New York, John Wiley & Sons, Inc., 1981.

[44] C. R. Freberg and E. N. Kemler , *Elements of Mechanical Vibration, 2nd ed.*, New York, John Wiley & Sons, Inc. (1949).

[45] Ernest Rabinowicz, *Friction and Wear of Materials*, 2nd ed., New York, John Wiley & Sons, Inc., 1995.

[46] W. N. Sharpe, Jr., B. Yuan, R. Vaidyanathan and R. L. Edwards, "Measurements of Young's Modulus, Poisson's Ratio and Tensile Strength of Polysilicon," *Proc. MEMS 97, 10th IEEE Inter. Workshop on MicroElectroMechanical Systems*, pp. 424-429.

3.5 Actuator reliability

In order to determine the reliability of the actuators and linkage assembly separate from the reliability of the microengine, we designed a gearless microengine (see section 2.2). We performed an experiment that showed the actuator/linkage was 4 orders of magnitude more reliable than the entire microengine that includes the gear. Geared microengines have shorter lifetimes primarily due to the wear debris accumulation in the pin joint and hub of a gear.

Experiment

The structure used in this experiment consists of linkage arms connected to an electrostatic actuator. It is identical to the standard microengine, but is fabricated without the gear. A view of the linkage arm connection is shown in Figure 3.5.1. The etch hole was located where the pin joint normally connects to the gear. When this device is run with a 17 μm radius, the actuators clamp [47] making the motion appear to be box-like. To prevent clamping, we adjusted our model-based parameters for a radius of 12.6 μm.

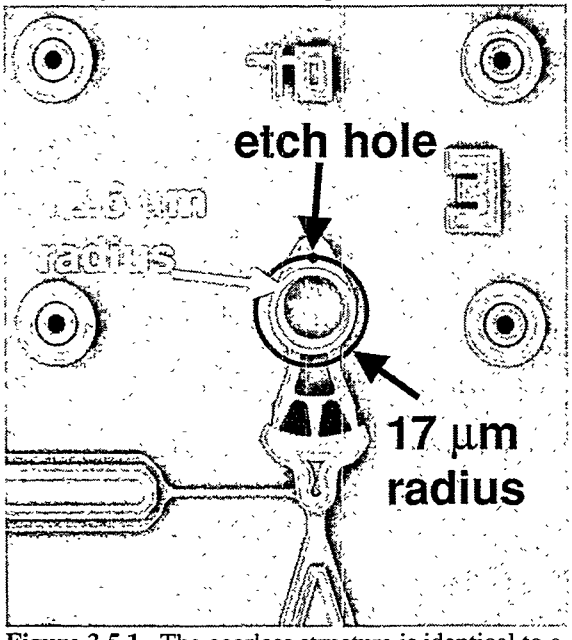

Figure 3.5.1. The gearless structure is identical to a standard microengine except it lacks a gear. An etch hole marks the pin joint location. In a standard microengine, the etch hole would follow the 17 μm radius circle. For this experiment, the etch hole followed a 12.6 μm radius circle.

We stressed eleven of these structures at a frequency of 1720 Hz. The parameter in the Super μDriver code (section 1.6) that was changed to yield a smaller radius was the ratio kr/a, which was set to 1350. In the ratio, k is the spring constant, r is the radius of the circle, and a is the electrostatic constant. A longitudinal force of 0.1 μN was implemented in the drive signals.

Results

The results were quite favorable and indicated much longer life for a gearless microengine. The test was stopped with seven failures after 4 months of continuous operation for an accumulation of 17.8 billion cycles. Four structures were still operating at the end of the test.

Figure 3.5.2 shows the failure data. The median time to failure was 4 billion cycles with a sigma of 1.7. This sigma is very high compared to our typical failure data indicating a spread in the distribution. Geared microengines at this frequency typically fail at 10^5 cycles.

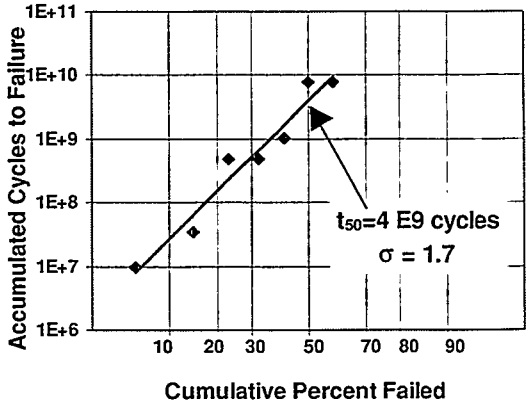

Figure 3.5.2. The lifetime data of the gearless structure has a median time to failure of 4 billion cycles.

The failure mode in the last two failed structures was investigated and determined to be adhesion in the guides of the actuators.

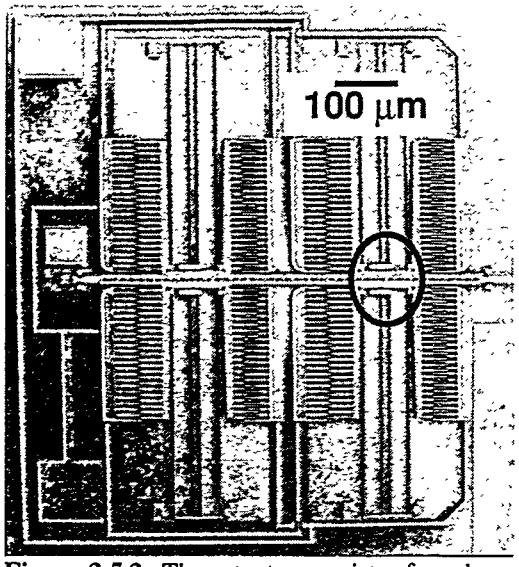

Figure 3.5.3. The actuator consists of combs connected to a moving shuttle anchored through restoring springs. The guides in the circled region anchor the springs.

Figure 3.5.3 shows the entire actuator. The circled region consists of guides that constrain the moving shuttle and anchor the springs.

A close-up of this region in the X actuator on a failed structure with roughly 7.8 billion cycles is shown in Figure 3.5.4. The locations where we suspected adhesion are noted with black arrows. We used a manual prober to gently poke the point indicated by the white arrow. The shuttle bounced back to near rest position after the poke indicating that our suspicion was correct.

The separation between the guides and the shuttle must be 1 micron when fabricated. Arcs (seen in Figure 3.5.4) were designed on each side of the shuttle to achieve this 1-micron design rule. When the shuttle moves out of rest position, the separation distance was reduced to 0.5 micron.

The freed shuttle was imaged in the SEM but no definite signs of adhesion could be pinpointed. A clear line-of-sight was not

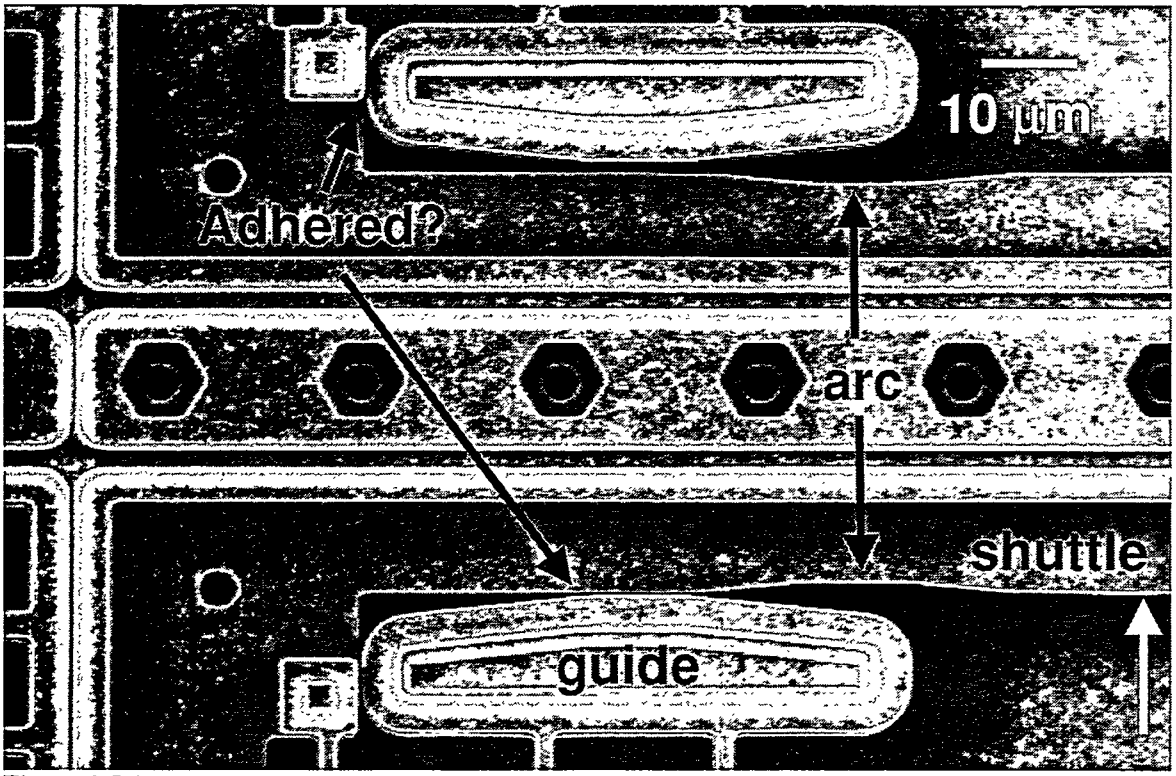

Figure 3.5.4. This view of the failed gearless microengine shows the two locations where there was suspicion of adhesion. A poke with the manual prober at the point indicated by the white arrow released the shuttle.

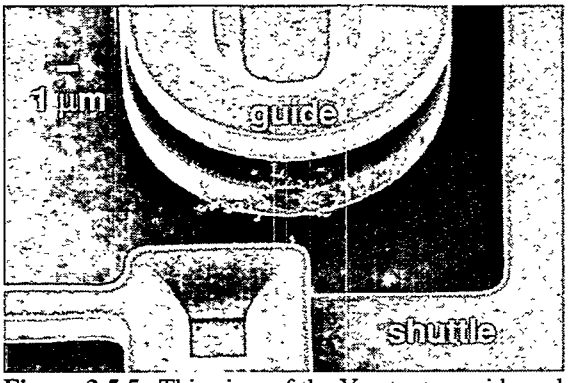

Figure 3.5.5. This view of the Y actuator guide and shuttle shows impact wear generated during operation.

available for the most likely spot (along the shuttle-guide interface).

The Y actuator on this microengine showed signs of impact wear. Figure 3.5.5 shows a view of the guide where the shuttle impacted presumably from clamping.

Although we thought clamping was eliminated from this test, analysis shows impact wear in some devices indicating clamping. The Y shuttle is extremely sensitive to this mechanism which propelled the development of a newer non-clamping actuator (sections 3.6 and 3.13).

Conclusions

The actuator/linkage assembly of a microengine is four orders of magnitude more reliable than the gear. Even with the reduced radius, clamping was observed.

The weak link in the microengine is the gear with its rubbing-surface separations of nominally 0.5 microns. Reductions in wear debris either through some type of surface coating or other material would improve the performance of the gear.

---

[47] S. L. Miller, M. S. Rodgers, G. LaVigne, J. J. Sniegowski, P. Clews, D. M. Tanner, K. A. Peterson, "Failure Modes in Surface Micromachined MicroElectroMechanical Actuators," *Proc. 1998 IEEE International Reliability Physics Symposium,* Reno, NV, 1998, pp. 17-25.

3.6 Drive Signal Study

Drive signals are an important aspect of MEMS actuators, for without them the devices do not function. How well do drive signals need to be optimized for a given device? Do variations in the devices themselves contribute to their reliability? These are questions that we addressed in a study of drive signals and variations in devices and how this relates to reliability.

The spring constant (kr/a) on 26 geared microengines and 26 gearless microengines was measured. All of these devices were from the same wafer. The spread of kr/a is large for the geared engine (Figure 3.6.1). This is probably due to stiction in the pin and hub region. Since the geared devices often do not return to their normal rest position once the voltage signals have been removed. The gearless engines (Figure 3.6.2) show much less variation in kr/a. Both types of devices show a peak at 1300.

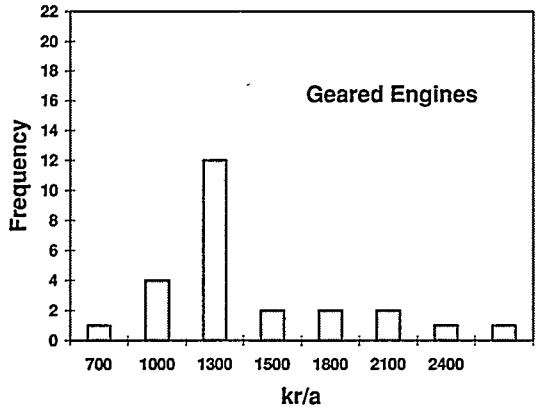

Figure 3.6.1. Distribution of kr/a values for geared microengines.

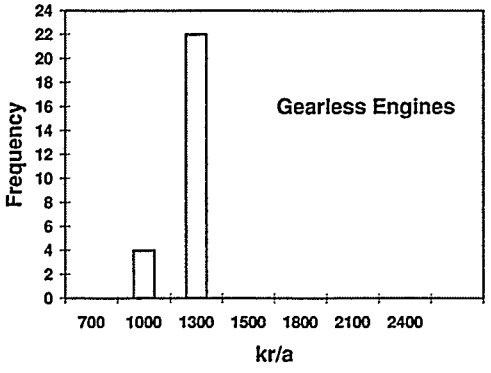

Figure 3.6.2. Distribution of kr/a values for gearless microengines

The resonant frequency (ω_0) was also required for a lifetime experiment to be performed on these devices. Since this test is destructive to the device and the parameter is known to be consistent from part to part only three devices were used. The voltage for these three parts ranged from 1000 to 1150 Hz for an average of 1081Hz (6793 radians/sec).

Lifetime experiments were performed on the geared microengines using average kr/a value for all the devices and the individual kr/a measured for that device. Figure 3.6.3 shows the results of the lifetime experiment using the average kr/a value. Figure 3.6.4 shows device lifetimes when using the kr/a measured for the individual device. The re-

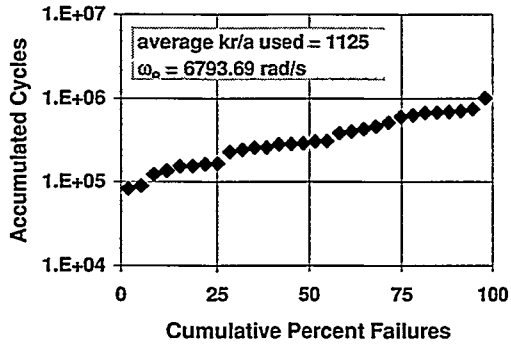

Figure 3.6.3. Device failures using average kr/a values.

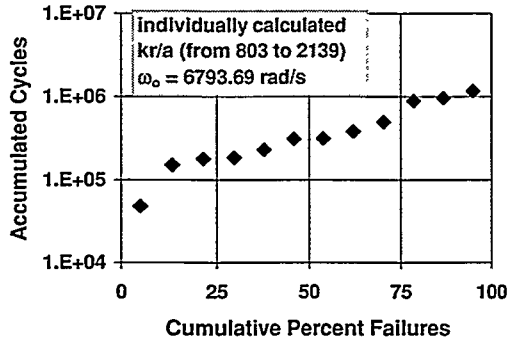

Figure 3.6.4. Device failures using individual kr/a values.

sults are of the same order of magnitude, therefore we can deduce that having a finely tuned kr/a for the device does not effect the overall reliability of the device.

The development of the image capture and analysis tools (Section 1.9) provided the capability to further study the effects of drive signals on microengine performance. Smooth rotational motion (theta vs. time) measurements and angular error measurements can easily be made. This provided a way to determine how well the gear stayed in synchronization with the drive signal. This information can be used to determine slip-stick behavior, friction coefficients, and possibly be used to determine the reliability of the device.

A series of images were acquired from four geared microengines. Three of the engines were from the kr/a measurement experiment and the fourth came from a prior lifetime experiment. This microengine had already accumulated approximately two billion cycles with the other three parts having less than a few tens of cycles.

Image sets for analysis were taken at 100 Hz with the stress cycles occurring at 1720 Hz. An initial set of baseline images was taken for each microengine except for the two billion-cycle device. Measurements of theta vs. time and angular error were made on each device.

The microengine shown in Figure 3.6.5 failed very quickly. The plot shows that the device is sticking after only 60 000 cycles. The position that the device failed at is indicated by the first point in the 100 000 cycle plot. This device show a rapid degradation in the angular error (Figure 3.6.6) after only 60 000 cycles. This can be contrasted with the device shown in Figures 3.6.7 and 3.6.8. This device degraded much more slowly. The theta vs. time plot shows that this device moves at a fairly constant rate. It should be noted that several points on the graphs are points that where misidentified by the

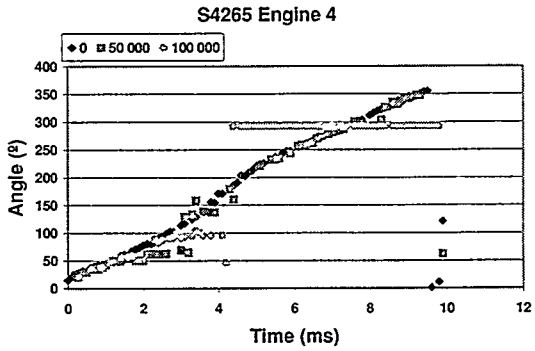

Figure 3.6.5. θ versus time graph for microengine stressed at 1720 Hz.

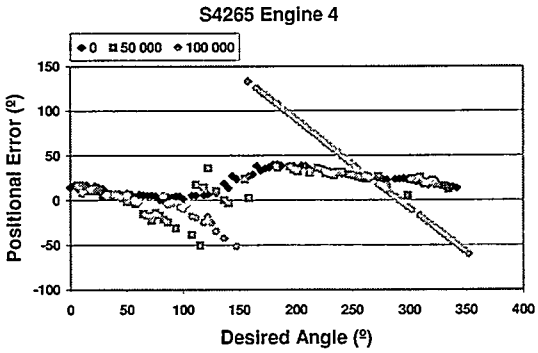

Figure 3.6.6. Plot of angular error measurment.

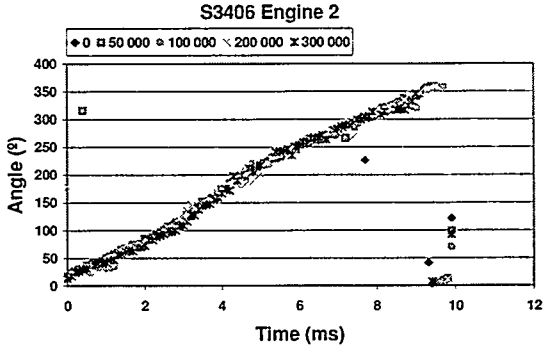

Figure 3.6.7. θ versus time graph for microengine stressed at 1720 Hz.

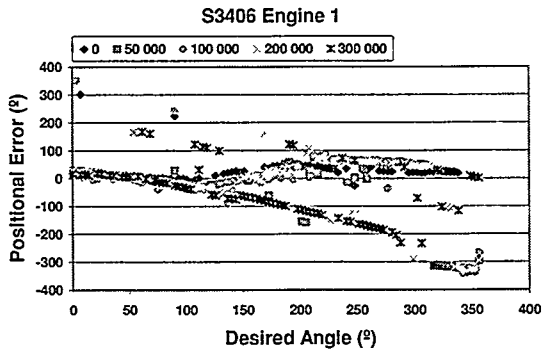

Figure 3.6.8. Plot of angular error measurment.

search algorithm. The points show up as random points on the plots. Both of these devices failed early in their expected lifetime.

Data was also taken on a microengine that had accumulated 2 billion cycles. The theta vs. time and angular error plots are shown in Figures 3.6.9 and 3.6.10. This device's motion appears to still be extremely smooth. This device also lacks the characteristic hump that is evident in the angular error plots of the other devices.

A gearless microengine was used to determine how well the drive signals were optimized for these devices. A plot of circular position is shown in Figure 3.6.11. This plot shows that at 100 Hz the drive signals are well matched to the device. At 1000 Hz we begin to see some irregularities. The images at 1720 Hz could not be interpreted due to a large amount of blurring. It does appear however that something about the system changes as we approach the resonance of the system and go beyond it.

Conclusions

Experiments have shown that an average kr/a value can be used for lifetime test without effecting the reliability of the devices being tested. The image analysis tools that have been developed have allowed us to gain further insight into device behavior at operational speed. The small humps in the angular error measurement warrant further investigation, as this may be an indicator of expected lifetime. Device behavior needs to be examined more closely at higher speeds to determine what types of changes to drive signal parameters are needed or if additional variables need to be accounted for.

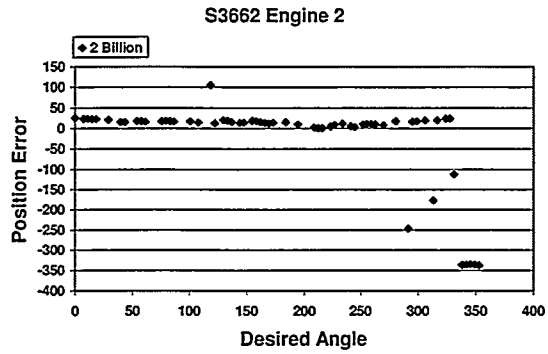

Figure 3.6.9. θ versus time graph for microengine stressed at 1720 Hz.

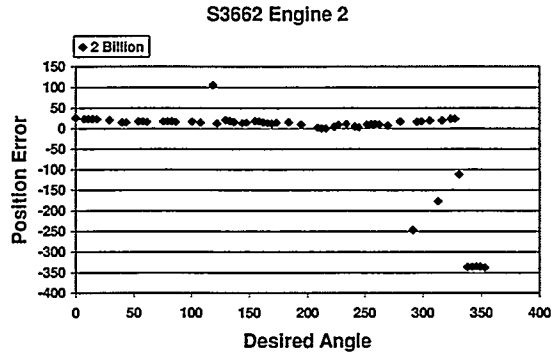

Figure 3.6.10. Plot of angular error measurment.

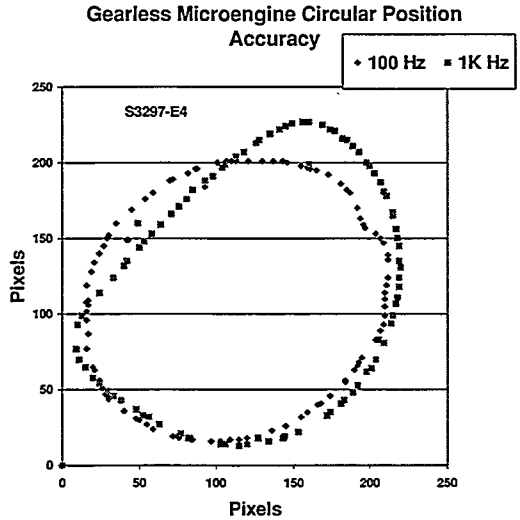

Figure 3.6.11. Matching drive signals to engine motion on a gearless microengine.

3.7 Temperature Cycling

Potential effects on reliable MEMS operation due to thermal expansion of the polysilicon components were analyzed. Modeling results indicate that this should not be a significant failure mechanism. Experiments were carried out which verified that temperature cycling had no detrimental effects on the reliable operation of the Sandia micro-engine.

Thermal Expansion Model

An analysis using a simple first-order model was performed to examine possible effects on reliable MEMS operation due to the thermal expansion of the polysilicon components. The change in length Δl due to a temperature change ΔT is well-approximated by

$$\frac{\Delta l}{l} = \alpha \Delta T \qquad (1)$$

where α is the linear coefficient of expansion. For polysilicon, $\alpha \approx 3 \times 10^{-6}$ /°C. The minimum in-plane space that can be fabricated using the present MEMS (SUMMiT) technology is about 1.0 micron.

First consider the case of two polysilicon components that are free to move (like gears) and can expand in any direction. For two of these to touch as a result of thermal expansion, it would require that the product of the temperature increase and the length of the polysilicon component, i.e., $l\Delta T$, be at least 3.33×10^{5} um·°C (1 um/3×10^{-6} /°C). For a temperature increase from room temperature to 200°C, this would require components on the order of 1.85 mm, which is very large.

If one end of both components were fixed, such that they were free to expand only in one direction towards each other, then for these to touch, the $l\Delta T$ product would have to be at least 1.67×10^{5} um·°C (0.5 um/3×10^{-6} /°C). For a temperature increase from room temperature to 200°C, this would require the components be on the order of 925 um, which is still very large.

Actually this simple analysis is somewhat conservative in that it ignores the thermal expansion of the silicon substrate, which would tend to move fixed components on the surface further apart. This would not be a factor for out-of-plane thermal expansion (normal to the surface).

In summary, these rudimentary calculations indicate that thermal expansion is unlikely to cause MEMS to fail to operate over a reasonable temperature range. This is particularly true for the Sandia micro-engine, for which the drive gear is only 80 um in diameter. This conclusion was borne out in the experimental studies described below. However, other thermal effects may be more subtle, e.g. deformation, which may result in sub-optimal operation or reduced operating lifetimes. These types of effects would require much more detailed study.

Experimental set-up

The testing began with 20 functional micro-engines on seven die packaged in 20-pin ceramic DIPs. Rather than sealing the packages with metal lids, glass microscope slides were attached with tape, which permitted observing the micro-engine operation and provided some protection from handling. All the parts used in these tests were taken from lot TP16501A-02-02.

The environmental test chamber used for all testing (Model 8000, Delta Design, Inc.) has two temperature chambers and a transfer carriage for moving the sample parts between chambers. One chamber was continually maintained at the selected low-temperature set-point, while the other chamber was kept at the selected high temperature. Transfer between the chambers took only a few seconds.

During the temperature cycling tests, the signals required to operate the micro-

engines were not applied, that is, the micro-engines were not running. After the temperature cycling was completed the micro-engines were tested to see if they were still functional.

Test 1

This test consisted of three temperature shock cycles between -55 °C and +75°C. For each cycle the micro-engines were kept at -55 °C for two hours and +75°C for two hours. After three cycles, the parts were removed and kept at room temperature for two hours prior to testing.

All 20 of the micro-engines were still functional upon completion of the temperature cycling. In fact, one micro-engine that previously had been non-functional was found to be operational. It is very likely that the thermal stresses created during heating and cooling cycles might be sufficient to free a stuck member of the micro-engine.

Test 2

This test consisted of four temperature shock cycles between -55 °C and +200°C. The same micro-engine samples were tested that were used in the previous temperature cycling test.

For each cycle the micro-engines were kept at -55 °C for approximately one hour. Due to electrical problems with the automatic carriage transport mechanism, the transfer of the sample parts between the two temperature chambers had to be initiated manually. As a result, the time the parts were kept at +200°C varied for each of the four cycles: 15 hours, 1 hour, 1.75 hours, and 0.5 hour. After four cycles, the parts were removed and kept at room temperature for one hour prior to testing.

All 20 of the originally functional micro-engines were still working upon completion of this second round of temperature cycling. The additional part that started to operate after the first temperature cycling test was also functional, as well.

Hot chuck test

To demonstrate that the Sandia micro-engine will operate over a wide temperature range, an experiment was performed using a whole wafer (TP15603-01-07) mounted in a Cascade wafer probe system. The signals to operate the micro-engines where provided through adjustable electrical probes. The chuck on which the wafer rested could be heated or cooled.

While continuously observing a running micro-engine, the wafer was heated from room temperature (25°C) to 150°C in about 12 minutes. Nothing unusual was seen in the micro-engine operation. At 150°C, the micro-engine was stopped and restarted several times without any problem. Several micro-engines, known to be functional at room temperature, were probed and found to be operational at 150°C, as well.

The wafer was then cooled to 0°C in less than 14 minutes, again while a running micro-engine was continuously monitored. The micro-engine was stopped and restarted several times at 0°C. Again, the micro-engine operated flawlessly.

Conclusion

Temperature cycling in the range of -55 °C to +200°C has been shown to have no detrimental effects on the operation of the Sandia micro-engine. These experimental results are in agreement with a modeling analysis showing that thermal expansion of the polysilicon components should not cause MEMS to fail to operate in this range.

3.8 Shock tests on the microengine

In order to find the susceptibility of our MEMS devices to shock, tests were performed using haversine shock pulses in the range from 500g to 40Kg (up to twenty times the requirement for our typical system). The microengine performed quite well at these high levels with a majority functioning after the stress.

Some of our observations follow. Debris moved at levels greater than 4000g causing shorts in the actuators. Bond wire and packaging problems surfaced there also. The die-attach bond failed at 10Kg allowing the die to slam into the package lid. At 20 Kg we began to observe structural damage. Ceramic packages fractured at 40Kg.

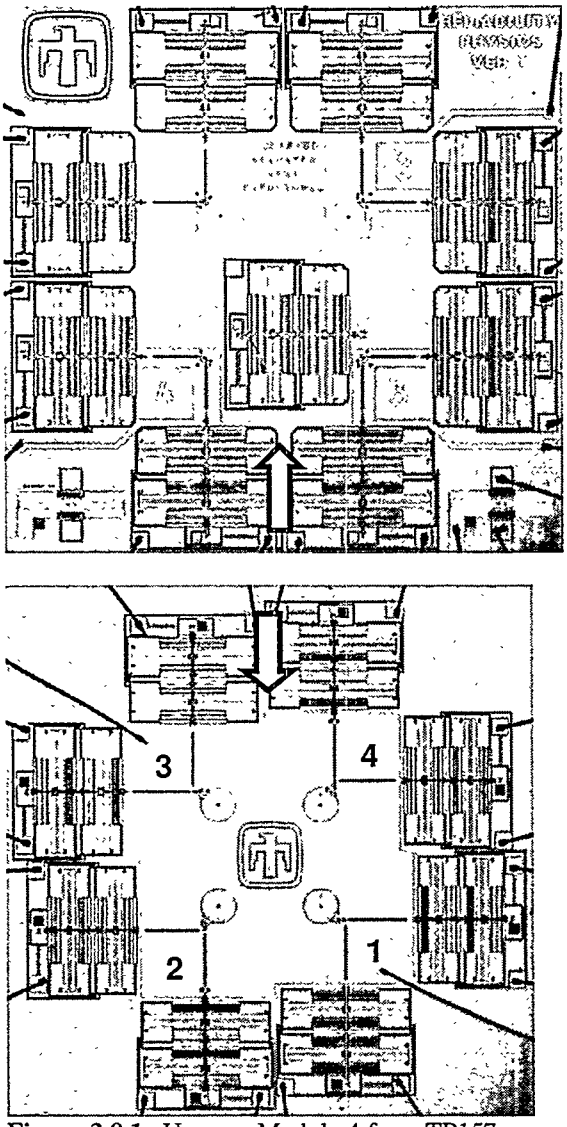

Figure 3.8.1. Upper – Module 4 from TP157 consists of two microengines driving load gears and two simple microengines. Lower - Module 1 from TP084 consists of four microengines driving load gears. The arrow indicates the direction of shock impact.

Experiment

Module description

We used a module consisting of four microengines; two of the microengines were attached to load gears to simulate real-world conditions. Module 4 from TP157 and module 1 from TP084 were used in this test. A complete description of the TP157 MEMS module can be found in section 2.5 of this report. Module 1 from TP084 consisted of four microengines driving load gears. Both modules are shown in Figure 3.8.1.

There were two major differences in the modules used. Module 1 from TP084 was an older version microengine with no vertical constraint. Module 4 from TP157 used the newer microengine design with guides that provide vertical constraint.

Each module was attached inside a 24-pin DIP ceramic package. A typical package without a cover is shown in Figure

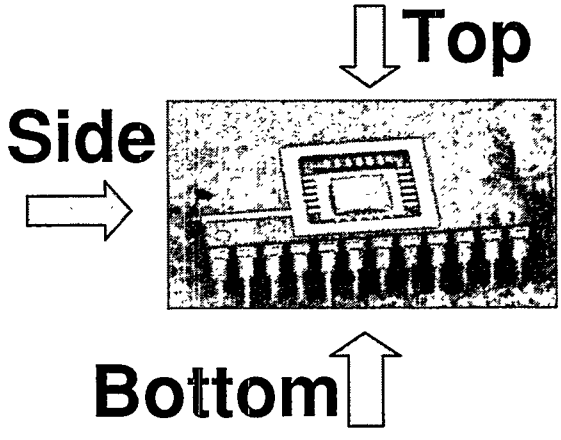

Figure 3.8.2. Photo of a typical packaged die that was shocked in the three orientations indicated.

3.8.2. For the shock test, metal lids were taped to the packages to prevent particle contamination of the MEMS devices. We used three directions of shock impact, designated top, bottom, side, and also shown in Figure 3.8.2.

Each functioning microengine was visually documented before the shock by capturing video images. We captured nine images per microengine. Four images were captured for each actuator, either X or Y, corresponding to different sections of the shuttle and comb mechanism. The final image was of the gear.

Calculations

In this discussion, the vulnerability to shock environments were calculated using simple models and Newtonian physics. Damping in the air environment was not included but may be a factor in reducing the shock effects. These calculations are most certainly worst case.

The Sandia designed microengine was selected as a test device because it performs actuation on all of the present designs. The microengine has all the components needed for evaluation: springs that flex, gears that are anchored, and clamps and spring stops to maintain alignment.

The first step is to calculate the mass of the moving structures. Figure 3.8.3 shows the comb, shuttle, and spring structure. The structure is anchored in eight places near the inner guides and circled in black in the figure. The mass was calculated as area × thickness × density of polysilicon and is shown in Table 1. Each structure is composed of the poly1poly2 laminate plus a

Table 3.8.1. Mass of moving structure

	Area $(\mu m)^2$	Mass (μg)	No.	Full mass (μg)
Shuttle	30,866	.324	1	.324
Comb	5,760	.0604	8	.483
Springs	4,736	.0497	4	.199
			Total:	1.01

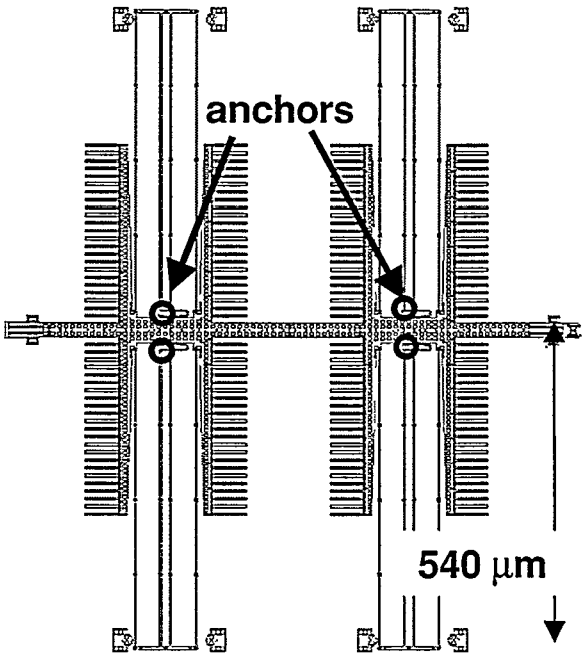

Figure 3.8.3 The moving components of the microengines actuator include combs, shuttle, and springs. The arrows and circles indicate where the springs are anchored.

poly3 layer which yields an overall thickness of 4.5 μm. The density of polysilicon is 2.33 g/cm^2 or 2.33 x 10^{-6} μg/μm^3

Once the mass is known, it is straightforward to calculate force due to acceleration from a shock. For example, the force from a 2000g, delta function shock would be

$$F = ma = (1.01\ \mu g)(2000g)(9.8\ m/sec^2 g)$$
$$= 19.7\ \mu N \qquad (1)$$

The crucial factor is determining where this force acts on microengine components and how much deflection occurs before fracture. For any material, fracture occurs when the stress applied exceeds the fracture strength. For polysilicon, a conservative estimate of the fracture strength is 1.5 GPa [48]. We can use beam-bending equations to get a handle on the effect. The stress on a simple cantilever beam is given by

$$\sigma = FLt/2I \qquad (2)$$

σ is the applied stress, F is the force applied to the end of the cantilever of length L, t is the thickness of the beam in the direction of

the force, and I is the moment of inertia. For a rectangular beam

$$I = bt^3/12 \quad (3)$$

(b is the width) and for a cylinder

$$I = \pi D^4/64 \quad (4)$$

(D is diameter). Combining equations (2) and (4) for rectangular beams, yields

$$F = \sigma bt^2/6L \quad (5)$$

where if the applied stress is 1.5 GPa, then this force will fracture the beam.

Another useful equation regarding beam bending is the deflection, δ, of a beam with applied force which yields

$$\delta = FL^3/3EI \quad (6)$$

where E is Young's modulus generally set to 155 GPa or 0.155 N/μm^2.

Now for the case of the microengine, in-the-plane shocks should be well mitigated by spring stops and guides so we expect to see no damage. There may be stiction problems for surfaces coming into contact. However, by far the greatest vulnerability is due to an out-of-the-plane shock. Most of the comb actuators have no constraints to motion out of the plane.

A large shock from the top would allow the massive shuttle and combs to rise in relation to the substrate. There are eight anchors connected to the springs to hold the structure down. The springs are free to bend giving rise to misalignment and with a large enough shock could produce a spring fracture.

A shock from the bottom would push the shuttle, combs and springs down 2 μm into the substrate allowing stiction to take effect. A plot the deflection equation (6) is shown in Figure 3.8.4 for accelerations of interest. Also shown on the plot are possible failure modes.

For this out-of-plane motion, the simple model is that the force is distributed over the eight-anchored spring beams. These beams are 540 μm long (L), 4.5 μm thick (t), and 2 μm wide (b). For stiction to occur, the beams must flex only 2 μm towards the substrate, which could be achieved by a shock of 100 g. Misalignment can occur when the combs and shuttle move away from the substrate by roughly 10 μm from a shock of 400g. Using equation 5, a force of 18.8 μN would break an individual spring beam and deflect it 419 μm. Because we have eight springs, the force is distributed implying that we may see spring fracture at 150 μN or 15,200 g.

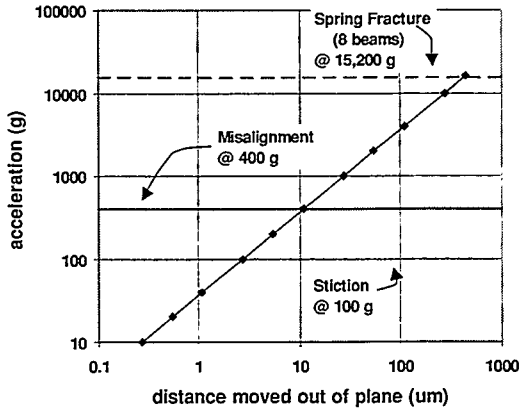

Figure 3.8.4. The plot shows where the problem accelerations may arise. Air-damping effects were ignored.

Shock levels and spectra

The calculations gave guidance on what shock levels should be used. The experiment matrix with the total number of functioning microengines tested at each level is shown in Table 3.8.2. This total number was composed of two types of microengines as mentioned earlier.

Table 3.8.2. Number of microengines tested at each shock level.

Level	Bottom	Top	Side
500g	8	8	8
1,000g	7	8	7
4,000g	4	5	3
10,000g	5	8	6
20,000g	6	7	6
40,000g	4	8	4

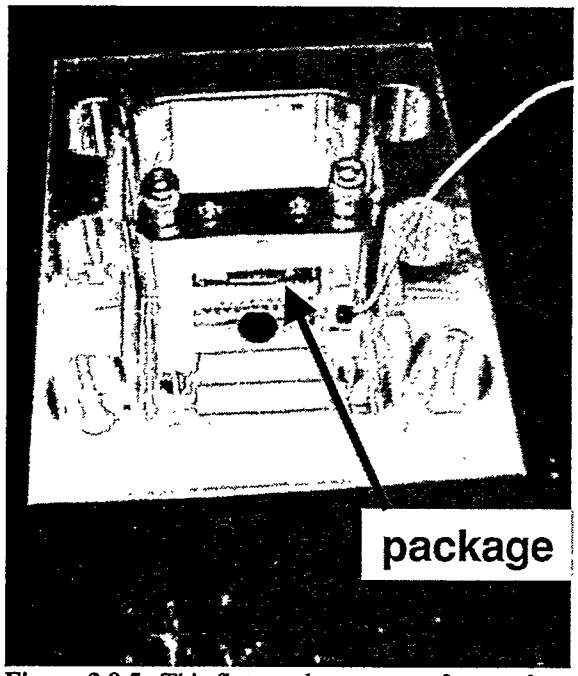

Figure 3.8.5. This fixture clamps up to four packages for the shock table tests.

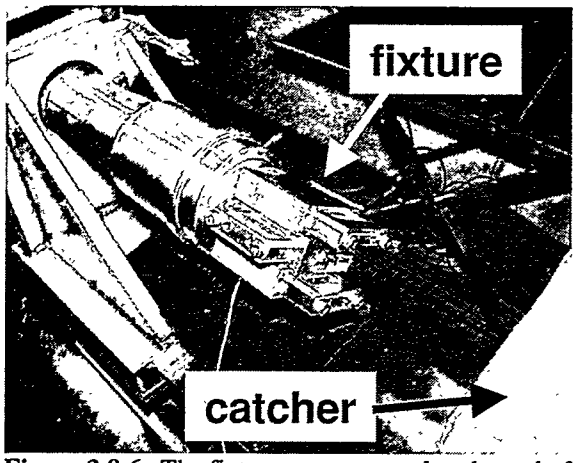

Figure 3.8.6. The fixture was mounted at the end of the Hopkinson bar and was blown into the catcher after the shock.

The MEMS devices were unpowered during the test. A maximum of four packages was clamped into a fixture as shown in Figure 3.8.5. The fixture was implemented with acceleration sensors and then attached to the shock table. The three orientations were achieved by rotating the fixture on the table.

For shock levels above 10 Kg, a fixture was designed that attached to a Hopkinson bar. Two packages could be tested in two orientations at each shock level. The fixture is shown mounted to the end of the bar in Figure 3.8.6. The shock actually blows the fixture off the end of the bar and into a foam-filled catcher.

The shock table produced the haversine shock pulses for levels ≤ 10 Kg with 1 ms pulse widths. For levels > 10 Kg , a Hopkinson bar produced pulse widths of roughly 0.2 ms. Typical spectra are shown in Figure 3.8.7. The ringing seen in the lower spectrum was due to the fixture holding the packages.

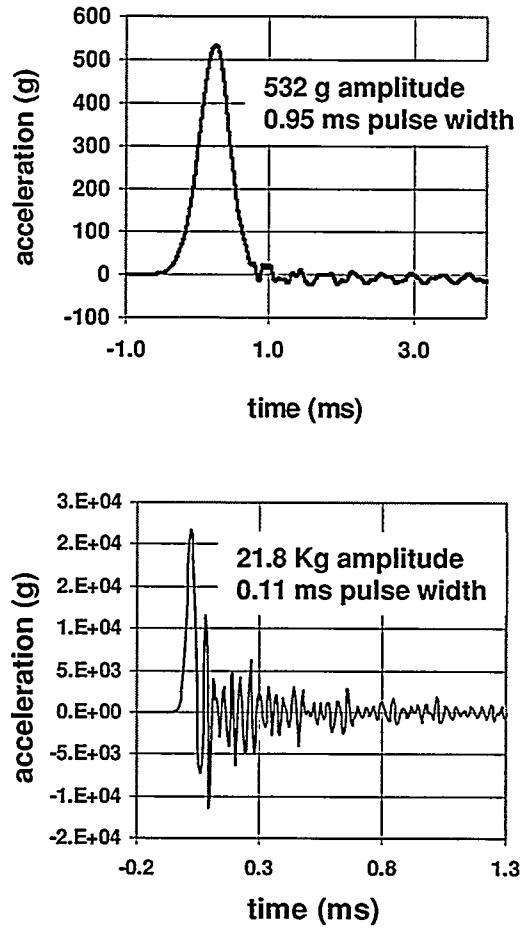

Figure 3.8.7. The upper spectrum was from a shock table impact and the lower spectrum was from the Hopkinson bar.

Results

Preliminary results indicate that these MEMS devices are quite robust. Levels of 500g and 1000g didn't even budge specks of debris on the die. In general, dice are extremely clean with very little particle contamination. However, slivers of polysilicon from the sawed edges of the die can break off (typically from handling) and contribute to debris. All 24 microengines at 500g and 22 microengines at 1,000g functioned after test with no damage. No stiction or comb misalignment was observed.

At 4000g, 11 out of 12 microengines functioned. However, we began to see bond wire problems in the package. Two rockers (a bottom impact and a side impact) functioned when manually probed, thus bypassing the package. A rocker is a microengine that doesn't make a complete revolution, but is not adhered so it can rotate through a small angle. The one failure moved slightly when first powered but then stuck. Debris on the surface of the die moved slightly due to the shock at 4,000g.

Although the 10Kg level had 90% pass the test (17 out of 19), we once again observed two rockers, one from a top impact and one from a side impact. The side impact produced a hairline crack in the package, which propagated during handling to short two power signals. Cutting the bond wires eliminated the short and produced a functioning microengine. The top-impact rocker simply functioned when manually probed indicating signal loss through the package.

The two failures at 10Kg were under top impact. The die actually broke away from the package and slammed into the metal lid. The broken die and package interior is shown in Figure 3.8.8. Note the imprint of the die into the die attach material. Each die was treated with a coupling agent to prevent stiction after the release. The failure occurred primarily because the coupling agent weakened the bond at the die-package interface. This die attach failure was observed in only one package out of three subjected to top impact.

Also at 10Kg, debris moved substantially. The edge of the die exposes polysilicon layers, which flake off easily to produce debris. The TP084 module had beam-like alignment marks located near the streets, which were freed due to handling producing debris. This debris has the potential to short out the actuators in the microengine.

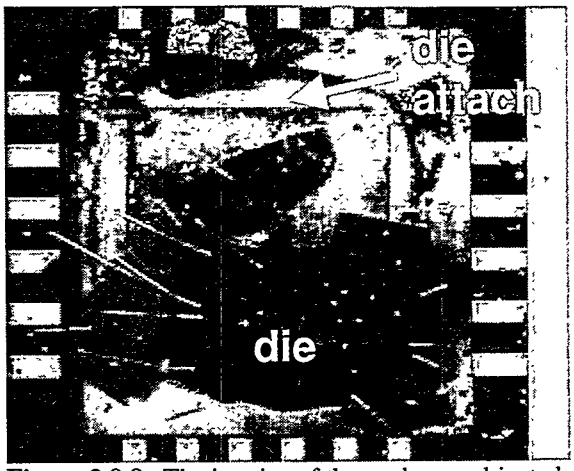

Figure 3.8.8. The interior of the package subjected to 10Kg from top impact shows the broken die and the imprint of the die in the die attach.

The tests were successful at 20Kg, with 14 out of 19 microengines functioning after the test, but we began to observe structural damage. Three large gears (320-μm diameter) broke away from the substrate as shown in Figure 3.8.9 due to a bottom impact, but the microengines still functioned after test. One set of linkages was lost (Figure 3.8.10) in a top impact producing a failed microengine.

The other four failures at 20Kg were rocked but did not rotate. Probing was unsuccessful in these cases to revive the microengine. Rocking is typically observed due to either asperity contact in the rubbing surfaces or signal loss in the actuators. Further investigation will be required to assess these failures.

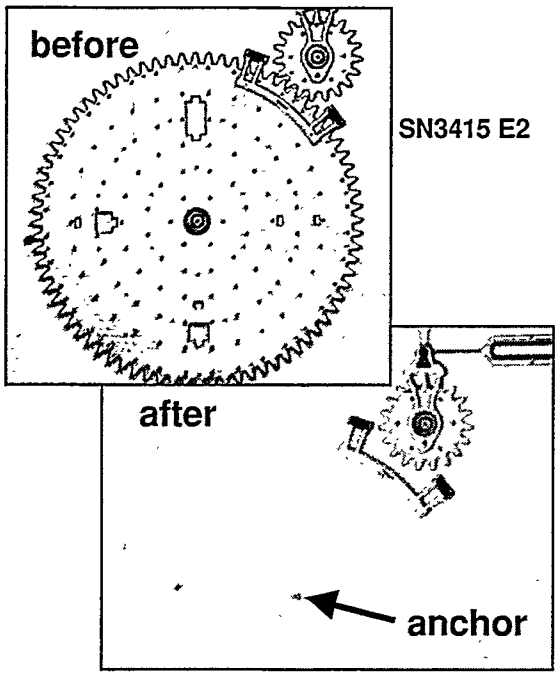

Figure 3.8.9. A bottom impact of 20Kg broke the anchor of the large gear. The microengine composed of the two actuators and drive gear still functioned in this case.

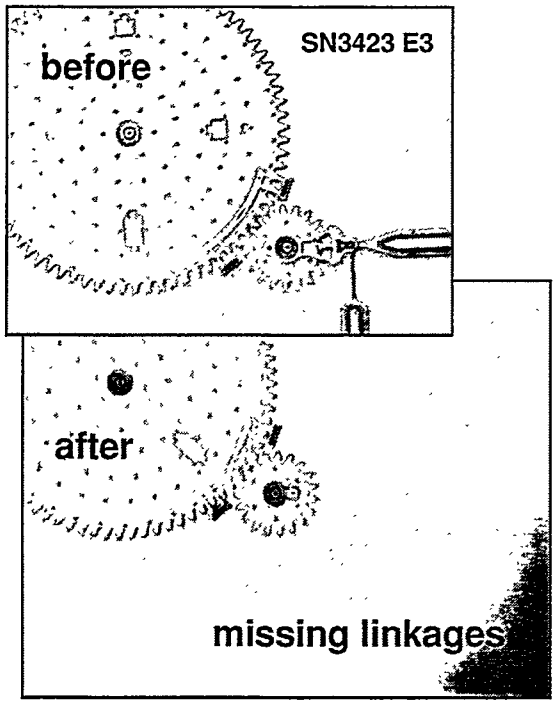

Figure 3.8.10. The linkage arms were removed with a 20Kg top impact.

One of the microengines at 20Kg had debris shorting out the actuation. Removal of the debris by careful probing fixed the short and the microengine functioned.

There were no severe die attach failures at 20 Kg from top impact although in two packages the dice were loose and held on only by the bond wires. It is uncertain if this happened from the shock or during handling after the test.

The extreme level of 40Kg shattered all four of the ceramic packages. An example of package fracture after bottom impact is shown in Figure 3.8.11. All 8 microengines stressed in a top impact were destroyed due to die attach failure. Surprisingly, two dies survived (one from bottom impact and one from side impact) and were lifted from the fractured packages. One is shown in Figure 3.8.12 where the bond wires are visible along the edge of the die. After careful removal of the bond wires, two microengines actually functioned, one from each die. There was a large amount of debris on the surfaces that may have hampered the functionality of the other microengines.

The bottom impact die at 40Kg started with four functioning microengines. After the test, one of the microengines functioned, two of the microengines failed as rockers, and the other microengine was shorted due to debris.

The side impact die at 40Kg also started

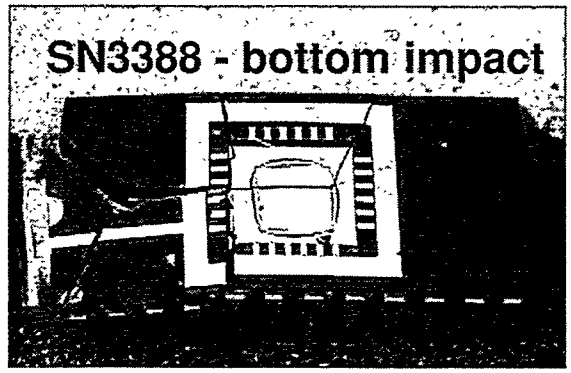

Figure 3.8.11. The 40Kg impact from the bottom fractured the package. The die was removed and tested.

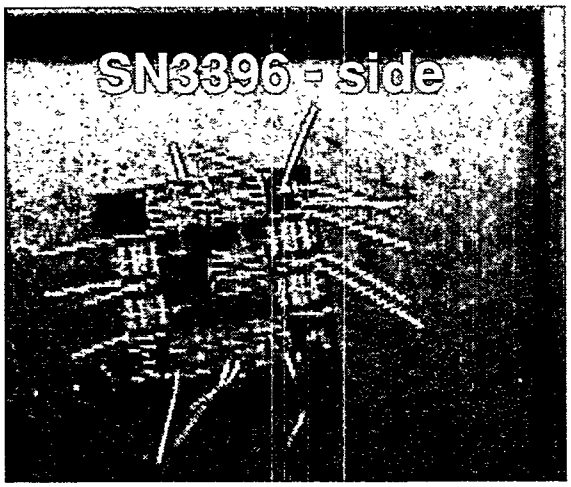

Figure 3.8.12. This die was removed from a fractured package subjected to 40Kg shock impact.

with four functioning microengines. After the test, one of the microengines functioned, one microengine failed due to a broken drive gear anchor (the actuators still worked), one microengine failed due to a broken flexure in the linkage arms (again, the actuators work), and one microengine may have been shorted due to debris.

More failure analysis will be included in conference proceedings [49] because it was incomplete at the deadline for this publication.

Comparison to prediction

We predicted stiction and misalignment at 100g and 400g respectively. This was not observed at any of the shock levels. The calculation did not include air damping which with these small masses may have a large effect.

The prediction of fracture at 15Kg was seen in the structural damage at 20Kg.

Conclusions

These MEMS devices are extremely robust in shock environments. At levels twenty times the typical requirement for our systems, some of the microengines functioned after test.

Debris from the die edges and alignment marks moved at the levels greater than 10Kg causing shorts in the actuators. This may be the cause of the rocker problem.

Many of the structural effects could be fixed with simple design changes such as larger anchors for large gears or wider flexures. However, ceramic packages will fracture at 40Kg.

---

[48] W. N. Sharpe, Jr., K. T. Turner, and R. L. Edwards, "Tensile Testing of Polysilicon," *Experimental Mechanics*, vol. 39, no.. 3, 1999, pp. 162-170.

[49] Danelle Tanner, Karen Helgesen, Jeremy Walraven, Lloyd Irwin, and Fred Brown, , "MEMS reliability in a shock environment," *IRPS 2000*, to be published.

3.9 Vibration tests of the microengine

In order to find an upper bound on susceptibility to vibration, the tests performed were four times the requirement for our typical system. The microengine performed quite well at these high levels with 17 out of 22 functioning after the stress.

Three of the failures had power signals shorting to ground. We suspect that this was not due to vibration because three of our controls exhibited the same type of failure. The controls were simply stored in a benign nitrogen environment.

Experiment Description

We used a module consisting of four microengines; two of the microengines were attached to load gears to simulate real-world conditions. Module 4 from TP157 was used in this test. A complete description of this MEMS module can be found in subsection 2.5 of this report.

The module was attached inside a 24-pin DIP ceramic package. A typical package without a cover is shown in Figure 3.9.1. For the vibration test, metal lids were taped to the packages to prevent contamination of the MEMS devices.

We used three modes of vibration, designated top/bottom, short side, and long side, and also shown in Figure 3.9.1. With the top/bottom vibration, possible problem areas were stiction to the substrate or misalignment of the movable shuttle and combs. The microengines are fairly well constrained by guides and spring stops against movement in the plane of the die. However, resonance effects could well be an issue for the short side and long side vibrations.

The orientation of the die relative to the vibration is shown in Figure 3.9.2. In both long side and short side orientation, actuators will be vibrated parallel or perpendicular to typical shuttle movement. When the motion is parallel, the shuttle and gear could move. However, with perpendicular motion the shuttle hits the guides.

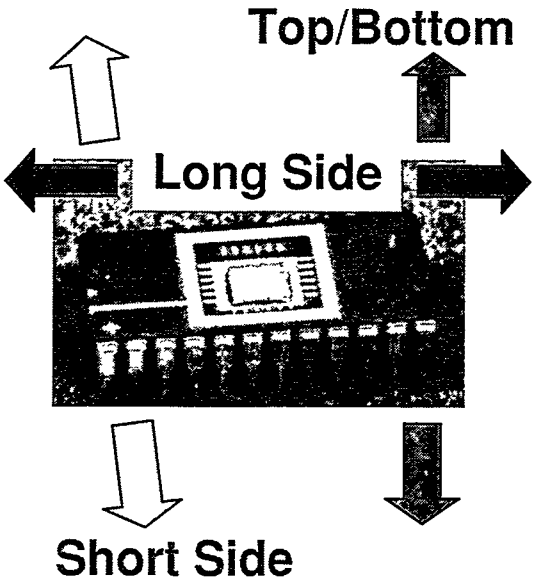

Figure 3.9.1 Photo of a typical packaged die that was vibrated in the three orientations indicated.

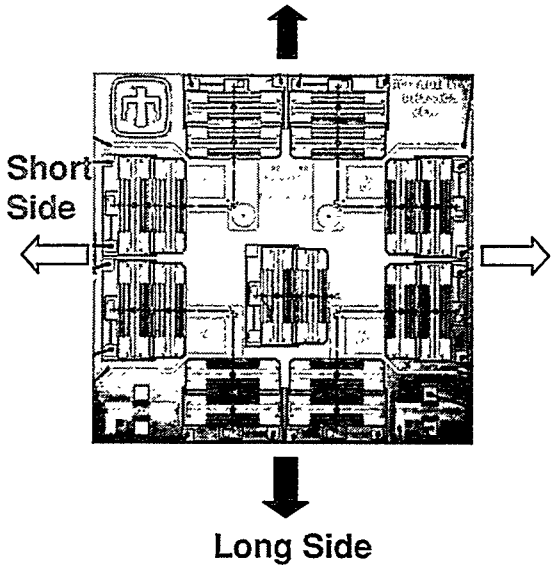

Figure 3.9.2 Orientation of the die relative to the vibration.

Each functioning microengine was visually documented before the vibration by capturing video images. We captured nine images per microengine. Four images were

captured for each actuator, either X or Y, corresponding to different sections of the shuttle and comb mechanism. The final image was of the gear.

Because this test was interested in establishing an upper bound to the susceptibility of MEMS devices to vibration, we chose a spectrum that was nearly four times the typical system vibration requirement. Our design stress was a white noise spectrum with frequency components from 20 Hz to 2000 Hz and a power spectral density of 0.8 g^2/Hz. This range includes the resonant frequency of the microengine. The duration of the test was three minutes.

The vibration spectra are shown in Figure 3.9.3, which includes the system requirement, the stress design, and the actual spectrum measured during the test. The rms values were calculated from the square root of the power spectral density times bandwidth.

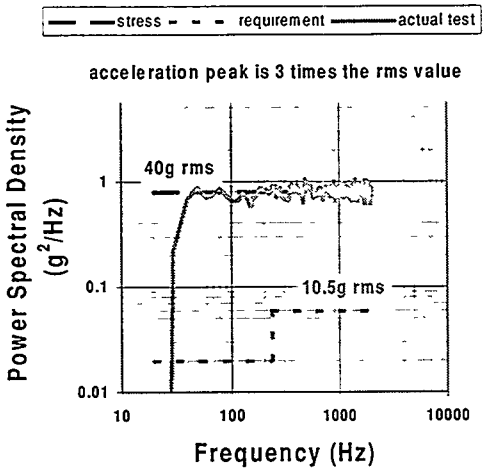

Figure 3.9.3 The graph of vibration spectra shows the requirement at 10.5g rms, the 40g rms design stress and the spectrum measured during the actual test.

The rule of thumb for the peak acceleration is three times the rms value, which was 120g for this test.

The MEMS devices were unpowered during the test. The packages were clamped into a fixture as shown in Figure 3.9.4. The fixture was then attached to a mounting cube

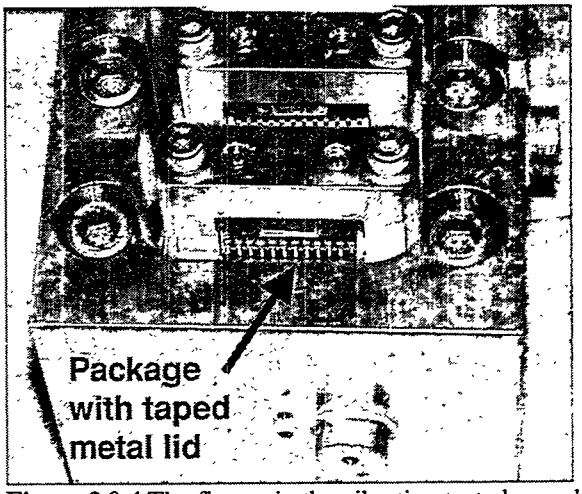

Figure 3.9.4 The fixture in the vibration test clamped the packages in place to prevent movement.

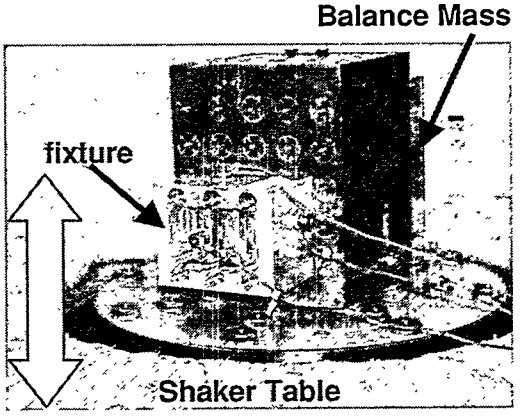

Figure 3.9.5 This photograph of the shaker table shows the fixture attached to the mounting cube for long side vibration. The arrow indicates the vibration direction.

on the shaker table shown in Figure 3.9.5. The arrow in the figure indicates vibration direction. The balance mass shown behind the mounting cube prevented out-of-plane stray oscillation. The three orientations were achieved by rotating the fixture on the mounting cube.

The initial test had five functioning microengines in the top/bottom orientation, five microengines in the long side orientation, and 4 microengines in the short side orientation.

Results

The initial test was highly successful with 13 out of the 14 on test surviving and working with no observable damage. We observed no stiction or misalignment problems in the microengines tested in the top/bottom orientation. The only overall effect noticed was a small change in the location of debris in the package. The debris was a sliver of polysilicon, probably from the edge of the die. Figure 3.9.6 shows the before and after images of debris movement. The vibration direction was long side as indicated in the figure.

There was a packaging failure in one case due to a short in the power signal bond wire. The microengine was run on a manual prober, thus bypassing the package, and it functioned properly.

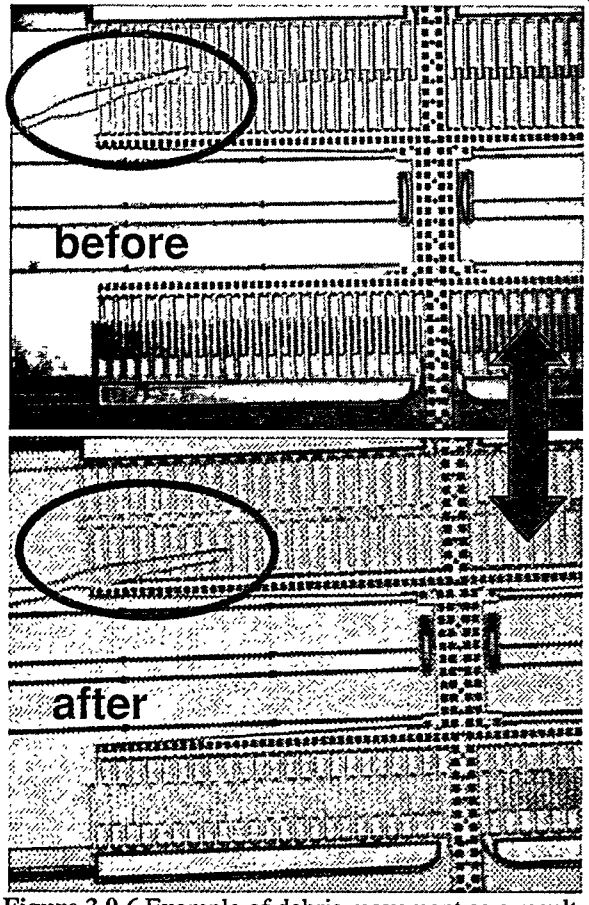

Figure 3.9.6 Example of debris movement as a result of the vibration. The arrow indicates the long side vibration direction.

The only microengine failure was due to a broken pin joint as seen in Figure 3.9.7. In order to investigate this effect, a repeat of the long side vibration test was conducted. The results of stressing 16 additional microengines resulted in NO broken pin joints.

Was there enough force in this test to break a pin joint? We can estimate the forces involved in the vibration assuming that the peak acceleration is 120g. The mass of the moving shuttle, combs, and springs is 1 μg. If we simply use $F = ma$, the peak force from the vibration was 1.2 μN. This force used with the spring equation, $F = kx$, where k was experimentally determined [50] to be 0.083 N/m will yield displacement. Assuming that the shuttle is not attached to the gear, the displacement would be 14 μm. A typical force used to rotate the microengine is 10 to 15 μN and typical displacements are 34 μm. Our only other observation [51] (see also Section 3.3 in this report) of broken pin joints was due to wear under accelerated conditions, not simple functionality tests. Hence, this acceleration due to

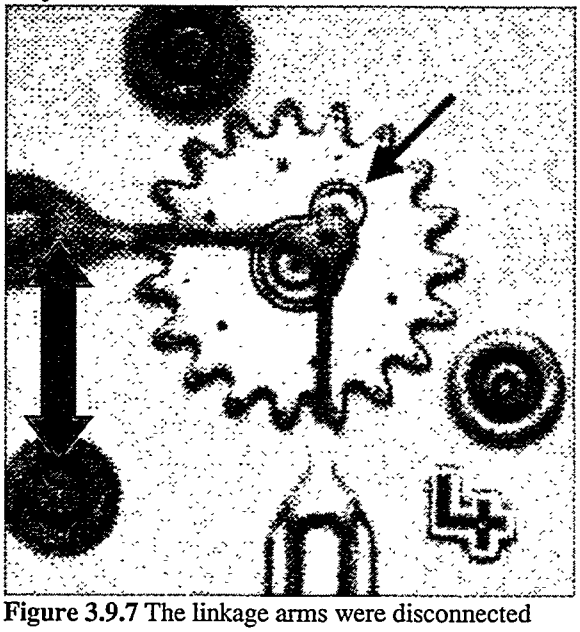

Figure 3.9.7 The linkage arms were disconnected from the gear thereby breaking the pin joint in the region indicated by the arrow. The double-tipped arrow indicates long-side vibration direction.

the vibration was not enough to break a pin joint.

There were eight functioning microengines on the repeat test. Four survived the test indicating an overall success of 17 out of 22 microengines. Three of the four failures in the repeat experiment had one power signal line shorted to ground. We suspect that this was not due to vibration because three of our controls exhibited the same type of failure. The controls were simply stored in a benign nitrogen environment. More failure analysis will be included in conference proceedings. [52]

Conclusions

Vibration tests at four times the requirement were successful with 17 out of 22 microengines functioning properly. Three of the failures were due to shorting of the power signal lines. Three of our controls also had this shorting failure indicating that it quite possibly is not due to vibration.

It appears that vibration will not be a big issue in qualifying MEMS for our systems.

[50] Norman F. Smith, William P. Eaton, Danelle M. Tanner, and James J. Allen, "Development of characterization tools for reliability testing of MicroElectro-Mechanical system actuators," *Proc. of SPIE*, Santa Clara, September 1999, to be published.

[51] Danelle Tanner, William Miller, William Eaton Lloyd Irwin, Ken Peterson, Michael Dugger, Donna Senft, Norman Smith, Paiboon Tangyunyong, and Samuel Miller, "The Effect of Frequency on the Lifetime of a Surface Micromachined Microengine Driving a Load," *IEEE International Reliability Physics Symposium Proceedings*, March 30 – April 2, 1998, pp. 26-35.

[52] Danelle Tanner, Karen Helgesen, Jeremy Walraven, Lloyd Irwin, Dan Gregory, and John Stake, "MEMS reliability in a vibration, environment," *IRPS 2000*, to be published.

3.10 Humidity

Humidity is shown to be a strong factor in the wear of rubbing surfaces in polysilicon micromachines. We demonstrate that very low humidity can lead to very high wear without a significant change in reliability. We show that the volume of wear debris generated is a function of the humidity in an air environment. As the humidity decreases, the wear debris generated increases. For the higher humidity levels, the formation of surface hydroxides may act as a lubricant.

The dominant failure mechanism of rubbing silicon surface micromachining (SMM) has been identified as wear. The wear debris was found to be amorphous oxidized silicon. Large slivers (approximately 1 micron in length) of debris observed at the low humidity level were also amorphous oxidized silicon. Using transmission electron microscopy (TEM), we observed that the wear debris forms spherical and rod-like shapes.

We compared the effect of humidity on wear for two surface treatment processes: a fluorinated silane chain, (FTS) and supercritical CO_2 dried ($SCCO_2$). The microengines using the $SCCO_2$ process were found to be less reliable than those released with the FTS process under two humidity levels.

Introduction

Reliability studies and predictions are becoming crucial to the success of MicroElectroMechanical System (MEMS) as commercial applications are developed. There have been extensive reliability studies by Maudie et al. identifying possible failure mechanisms in MEMS pressure sensors [53] and sensors exposed to harsh environments [54]. The lifetime experiments of Texas Instruments' Digital Micromirror Device (DMD) investigated unique failure mechanisms [55]. The DMD projection system has an array of hinged mirrors and has demonstrated 1.7×10^{12} mirror cycles with no hinge fatigue failures. However, most of the MEMS products on the market are sensors (pressure, acceleration, and chemical) that do not have rubbing surfaces. In both sensors and the DMD example, issues like friction and wear are minimal.

For many MEMS devices, especially actuators, normal operation requires surfaces to come into contact and rub against one another. In these cases wear of the rubbing surfaces becomes a reliability issue. One of the first experiments to show wear as a dominant failure mechanism was performed by Gabriel et al [56]. They ran polysilicon microturbines [57] and gears at rotational speeds up to 600,000 rpm. A focused air jet directed at the turbine induced the rotation. They estimated dynamic coefficients of friction between polysilicon and silicon ranging in value from 0.25 to 0.35. The wear was extensive enough to cause misalignment followed by wedging of the device.

The objective of the present study is to determine the fundamental correlation between environmental humidity and the lifetime of the microengine. Our previous work with microengines was performed in ambient conditions, typically 30% to 40% relative humidity. A secondary objective was to investigate the role of two different surface treatment processes and their impact on microengine reliability. These processes will be discussed in the next section.

Experimental Approach

Sample Preparation

Surface micromachined MEMS are mechanical structures fabricated from deposited thin films. The structures are encased in sacrificial layers (typically SiO_2) until ready for use. The oxide film is etched by hydrofluoric acid (HF) to yield a "released" sam-

ple. There are several strong adhesive forces that act on the structures during the drying stage of the release [58]. These include capillary, electrostatic, and van der Waals. Capillary forces dominate at these dimensions and processes have been developed to reduce or eliminate the forces for successful operation of the MEMS structure [59].

Coupling agent coatings such as alkysilanes have been used to increase the hydrophobicity of the polysilicon surface, thus eliminating capillary forces [60]. The most studied silane coatings deposited on silicon are octadecyltrichlorosilane (OTS) precursor molecules having a chemical formula of $C_{18}H_{37}SiCl_3$. Additionally, a fluorinated chain, perfluorodecyltrichlorosilane (FTS, $C_6F_{13}CH_2SiCl_3$), has been studied by Alley et al. [61]. Application of a coupling agent requires preparation of the polysilicon surface by an oxidation step (H_2O_2), resulting in an oxide layer a few nanometers thick.

An alternate approach to applying a coupling agent prevents the formation of a meniscus by eliminating the liquid phase in the drying process. This method is supercritical CO_2 drying [62] and it has been successfully applied to surface micromaching.

In these experiments we used samples that had either an FTS surface treatment or samples that were supercritically dried ($SCCO_2$). The $SCCO_2$ samples had no specific oxidation step, but were in an air environment that would promote growth of a native oxide.

Microengine Lifetime Experiment

This study used the electrostatically driven microactuator (microengine) developed at Sandia National Laboratories [63]. The microengine consists of orthogonal linear comb drive actuators mechanically connected to a rotating gear as seen in Figure 3.10.1. By applying voltages, the linear displacement of the comb drives was transformed into circular motion. The X and Y linkage arms are connected to the gear via a pin joint. The gear rotates about a hub, which is anchored to the substrate.

A die with four microengines (see section 2.2) was designed and fabricated for this experiment. There was one gearless microengine on the module for setup and calibration purposes, but it was not run in the experiment. The dice were packaged with taped glass covers to prevent particle contamination during handling. The packages were then stored in a dry nitrogen environment prior to testing. The covers were removed during the test to expose the microengines to the local environment. The SHiMMeR [64] tester was used to provide electrical signals to large numbers of packaged microengines and to optically inspect them for functionality.

A humid environment was achieved by bubbling dry laboratory compressed air through a large bottle of deionized water. The humid air that exited the bottle was then piped into the environmental chamber surrounding the packaged parts. A humidity sensor located inside the chamber controlled the airflow to maintain humidity levels to within ±1 % RH at 25°C. A General Eastern humidity monitor (Model HYGRO M4) using chilled mirror technology measured the dew point. All dew point values were converted to percent relative humidity at 25°C. We performed lifetime tests at six humidity levels, 1.8%, 10%, 24%, 31%, 39%, and 68% RH at 25°C for the FTS coated devices and two humidity levels, 1.8% and 31% RH at 25°C for the $SCCO_2$ devices as shown in Table 3.10.1.

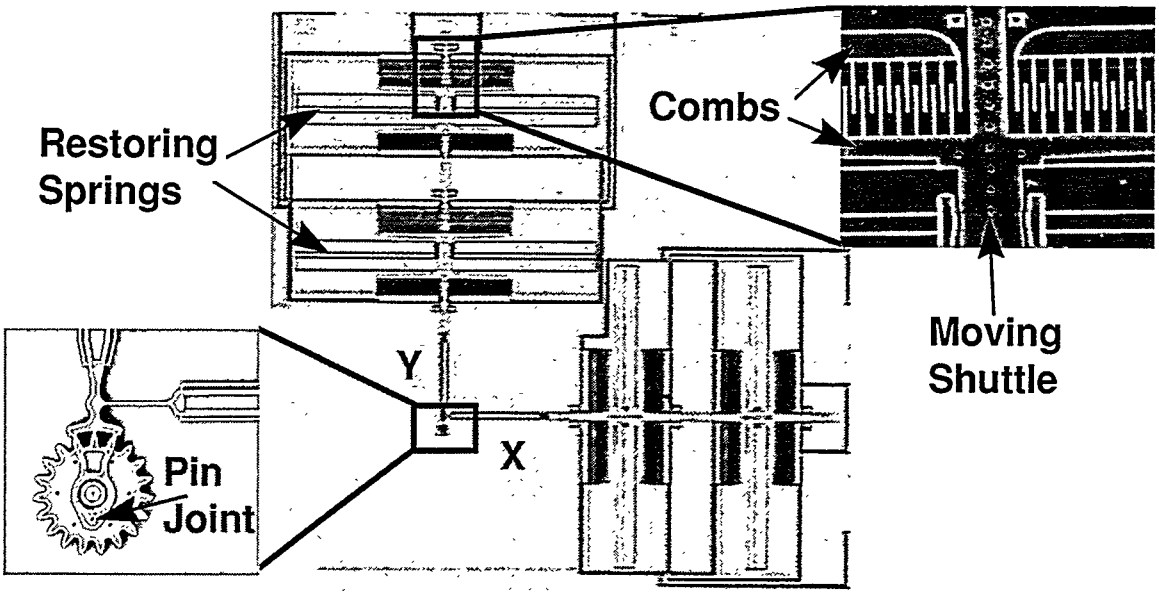

Figure 3.10.1. Sandia microengine with expanded views of the comb drive (top right) and the rotating gear (bottom left).

For each test, we operated the microengines with the same drive parameters at a frequency of 1720 Hz, slightly higher than the resonant frequency of 1500 Hz. We have found that operation near resonance causes increased wear [7]. The microengines were stressed with large drive forces to accelerate the failure times. The stress intervals followed roughly the same sequence for all the experiments. The sequence was 2000, 4000, 8000, 16000, ..., rotation cycles of the drive gear per stress interval. If more than 4 parts failed during a particular stress interval, we stressed the microengines for the same number of cycles as the previous interval to achieve better resolution in the number of cycles to failure. The devices were stressed at high speed and then slowed to 1 Hz to inspect for functionality. A failure was defined as the inability of the microengine drive gear to make a complete revolution at the 1 Hz inspection speed. During the inspection interval, we noted any observed changes or degradation in the motion of the gears for our records.

Table 3.10.1. Series of humidity experiments performed.

Humidity (%RH@25°C)	Surface Treatment	No. parts tested
1.8	FTS	28
1.8	FTS	30
10	FTS	44
24	FTS	29
31	FTS	29
39	FTS	22
68	FTS	31
1.8	$SCCO_2$	16
31	$SCCO_2$	33

Data Analysis

Because the parts were observed at fixed inspection times, common to all the parts, the results fall into the category of reliability data called "interval" data. Reliability analysis of interval data typically uses either the Weibull or lognormal statistical distributions to fit the data. Both distributions work quite well. However, the choice of the distribution should be based on the failure mechanism the data is describing. The Weibull is an extreme value or "weak link"

distribution that applies when many small defect sites compete with each other to be the one that causes the earliest failure. The lognormal distribution is based on a proportional growth model, where at any instant in time, the process undergoes a random increase in degradation that is proportional to its present state [65]. The multiplicative effect of all these random growth events build up to failure. The microengine failures are known to be due to an accumulation of wear debris and hence, the lognormal distribution represents the best choice based on the physics of failure.

The first step in the data analysis was ordering the failure data from low to high values of total accumulated cycles. We then plotted the accumulated cycles to failure against the cumulative percent failure for each humidity level. A linear regression of the lognormal data resulted in an estimate of t_{50}, the median cycles to failure. The estimate for the lognormal shape parameter, σ, was also determined.

The data from each of the experiments could be described by a simple unimodal distribution such as seen in Figure 3.10.2. The regression analysis yielded a median of 4×10^5 cycles to failure with a correlation coefficient of 0.98. The shape parameter, σ, was determined to be 0.2. The above analysis was completed for each experiment and a value for the median and sigma of each distribution was calculated. We performed nine experiments during which a total of 262 parts failed. A larger number of experiments were performed with the FTS process simply because of their greater availability.

Table 3.10.2 has the results of lognormal fits to all of the humidity experiments. The data is also graphically represented in Figure 3.10.3 with 95% confidence bounds represented by error bars. The figure shows a rather flat dependence on humidity for the FTS-coated microengines with the exception near 0%. The $SCCO_2$ data shows the failure

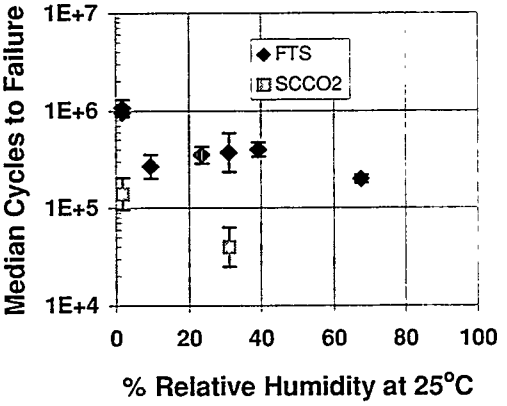

Figure 3.10.2. Lognormal distribution of accumulated cycles to failure for the 40% RH stress. The early failure, with less than 10^5 cycles, was omitted from the regression analysis.

Table 3.10.2. Results of median number of cycles to failure from all humidity experiments performed.

Humidity (%RH @ 25°C)	Surface Treatment	Median and sigma	
		t_{50}	σ
1.8	FTS	9.60E+05	0.107
1.8	FTS	1.07E+06	0.196
10	FTS	2.67E+05	0.3
24	FTS	3.51E+05	0.22
31	FTS	3.70E+05	0.39
39	FTS	4.00E+05	0.16
68	FTS	1.99E+05	0.11
1.8	$SCCO_2$	1.40E+05	0.37
31	$SCCO_2$	3.98E+04	0.69

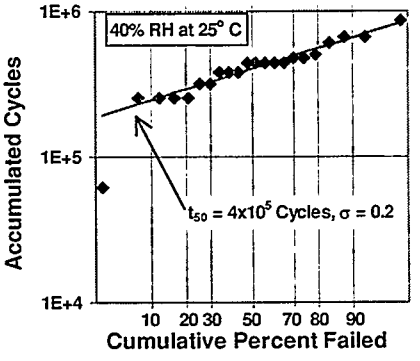

Figure 3.10.3. The effect of humidity on the lifetime of the microengines shows a rather flat distribution with the exception near 0%. The y error bars represent 95% confidence bounds. The microengines were stressed with large forces to accelerate failures in these experiments.

roughly an order of magnitude earlier, indicating a less reliable microengine.

The behavior of the microengines tested at levels of 10% RH and above followed a consistent pattern. Initially the microengines ran smoothly. With the accumulation of cycles, the operation of the microengines became sticky and jerky (stick-slip behavior) at inspection frequencies. Some of the microengines would actually work through the sticky behavior and become smooth again. Near the end of life, the rotation became more erratic until the microengine failed by sticking, rocking back and forth through a small angle, or breaking a pin joint. We observed broken pin joints (connects the linkage arm to the gear as shown in Figure 3.10.1) in only 6% of the failures for devices at levels of 10% RH and above. There were no broken pin joints in the $SCCO_2$ experiment at 31% RH.

The values shown in Figure 3.10.3 are comparable to previous data used in the development of a predictive reliability model based on the fundamental principles of wear coupled to a resonating system (see sections 3.3 and 3.4). In this work, the stickiness of the gear motion was attributed to the interaction of asperities on the rubbing surfaces. Asperities could break off causing wear debris or adhering particles which would result in a seized gear.

A contributing factor to failure values of less than 10^6 cycles lies in the design of the microengines tested. It has been experimentally determined that the Y comb drive "linearly clamps" during a portion of rotation of the gear [66]. The clamping was due to the force from the fringing fields at the ends of the comb fingers that occur when the combs are fully engaged. This effect increased the force on the drive pin joint by an unknown amount. In addition, in order to accelerate failures the longitudinal drive signal force was five times larger than the minimum force needed to simply run the microengine.

The behavior of the microengines tested at levels near 0% was quite different. In this low humidity case, there was a dramatic increase in the amount of wear debris, regardless of the coating method. We first noticed the formation of wear debris after accumulation of roughly 10^5 cycles. The debris was typically thrown out from the hub and collected on the gear face and surrounding substrate. In general, the gear hubs were worn down and the gears exhibited severe wobble during operation. In 55% of the failures (31% for $SCCO_2$), the pin joint actually wore down and was severed.

We suspect that the large wear rate removes any asperities that would cause the gear to seize in the same manner as the higher humidity levels. Therefore, wear of polysilicon would continue until the pin joint is worn away, causing failure at a much higher number of cycles. The increase in median cycles to failure that was observed at 1.8% RH in Figure 3.10.3 resulted from this change in failure mechanism even though the wear was increased greatly.

Failure Analysis

Scanning Electron Microscopy (SEM)

FTS Treatment: The dominant failure mechanism for these microengines has been identified as wear. The major effects of the wear process were either pin joint wear-out causing the linkage arm to break away from the gear or accumulation of wear debris causing the microengine to seize. The overwhelming effect of the humidity was demonstrated by the amount of wear debris observed. The volume of debris increased dramatically as we lowered the humidity.

In Figure 3.10.4, we show a comparison of the gears of microengines stressed in air environments of 39%, 24%, and 1.8% RH at 25°C. These microengines were stressed to failure at 862,000, 746,000, and 742,000 accumulated cycles, respectively, yet the microengine with the most accumulated cycles has the least amount of wear debris. In the 39% RH case, there is a small amount of debris located around the hub. The 24% RH case shows more noticeable wear debris around the hub and on the linkage arm. The debris in the 1.8% case includes large accumulations near the gear teeth. Debris has been thrown out and collected on the hub face, at the tips of the gears, on the linkage arm, in the etch-release holes, and onto the substrate area outside of the gear face. These images are characteristic of observations at different humidity levels.

Using a field emission SEM to further magnify and characterize the wear debris, we again noticed a difference between the 39% and the 1.8% RH case. Figure 3.10.5 shows a magnified view of the hub of a microengine that failed at 510,000 cycles at 39% RH. The box region has been magnified further to illustrate the debris morphology. The wear debris appears to be 200 to 500 nm agglomerates which string together with other agglomerates to form chains of 1 μm or longer.

For comparison, we investigated the hub of a microengine stressed to failure after 642,000 cycles in 1.8% RH at 25°C. This hub is shown in Figure 3.10.6. The first item to note (indicated by an arrow) is the radial offset in the gear and hub due to the large amount of wear between the hub and the mating gear. The offset caused a wobble in the motion of the gear at the inspection frequency of 1 Hz. Note also that the entire hub is covered with particulate wear debris. This is shown more fully in the lower image of Figure 3.10.6, which is a higher magnifi-

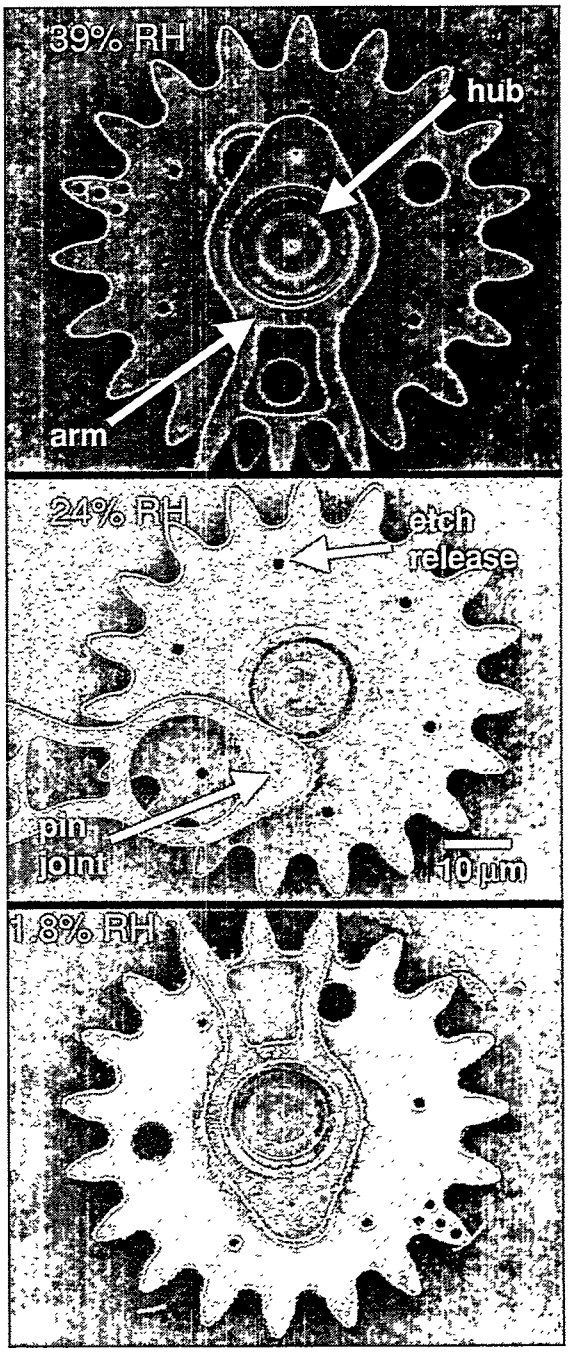

Figure 3.10.4. SEM images of various microengine gears stressed under different humidity conditions 39%, 24%, and 1.8% RH at 25° C. The microengines were stressed for roughly the same number of cycles, but the amount of wear debris for each humidity was dramatically different. (FTS)

cation of the box region. There are no stringy agglomerates in the 1.8% RH case.

$SCCO_2$ Treatment: Just as in the FTS treatment, the dominant failure mechanism was associated with wear. As shown in Figure 3.10.7, the amount of wear debris on the face of the gear far exceeded that observed in the FTS case at the humidity level of 1.8% RH. This engine failed at 600,000 cycles. The gap around the hub was an indication of severe wear.

Closer examination revealed particulate wear debris in spherical and rod-like agglomerations. The 31% RH experiment had very little wear debris, in part because of fewer revolutions of 510,000 cycles. The debris did not form stringy agglomerates as in the FTS case.

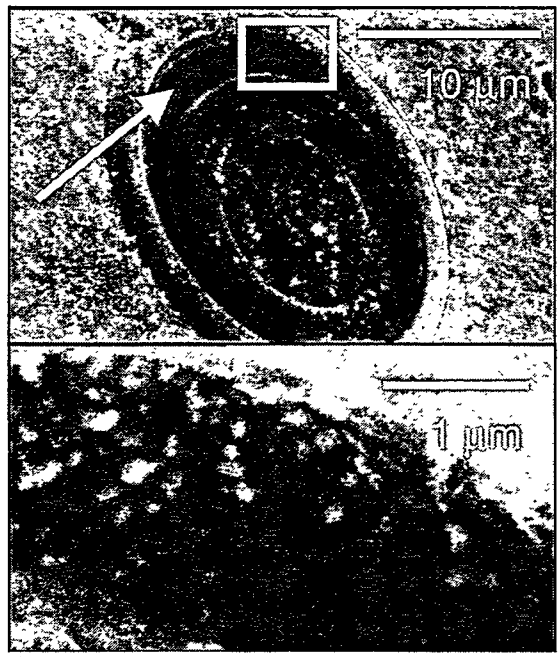

Figure 3.10.6. SEM magnified view of the inner gear region on a microengine stressed to failure after 642,000 cycles at 1.8% RH. The wear debris formed particulate matter, each smaller than 100 nm. (FTS)

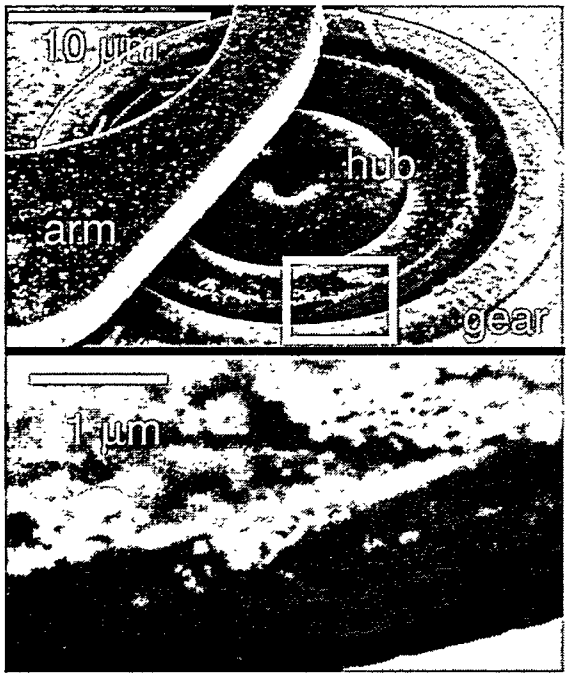

Figure 3.10.5. SEM magnified view of the hub region on a microengine that failed at 510,000 accumulated cycles during the 39% humidity test shows the morphology of the wear debris. (FTS)

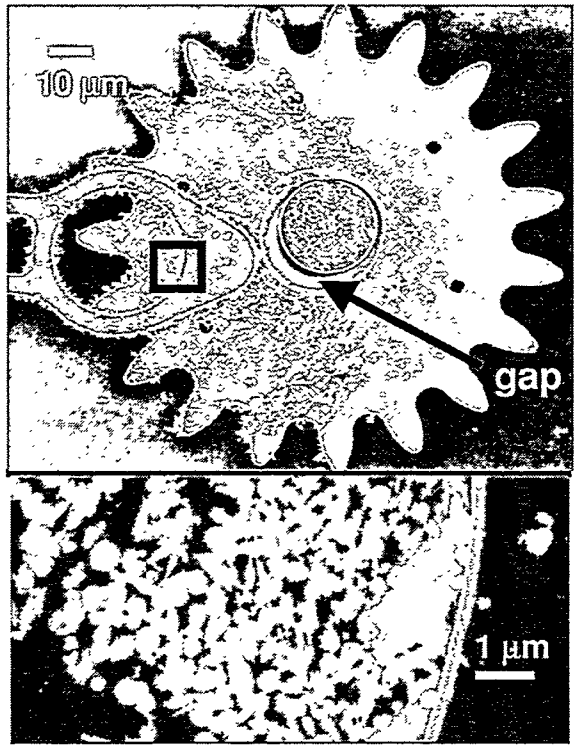

Figure 3.10.7. SEM image of a microengine that failed at 600,000 cycles at 1.8% RH illustrates the wear debris produced. The gap near the hub is an indication of severe wear. Note the morphology of the wear debris in the lower magnified image. ($SCCO_2$)

Focused Ion Beam (FIB)

FTS Treatment: To investigate the effect of wear, FIB cross sections were performed on a sample from each humidity level. Shown in Figure 3.10.8 are cross sections taken from a control (top), 39% RH (middle), and 1.8% RH (bottom) samples. The control sample was tested for functionality, but was not stressed. Because debris is not shown in the control sample we believe the debris was caused by wear, not the FIB cut. The 39% RH microengine was stressed to failure at 606,000 cycles and the 1.8% RH microengine was stressed to failure at 542,000 cycles. In the 39% RH case, we observed mostly pin joint wear as shown with the notched diameter. The wear of the pin joint was accompanied by a reduction in the pin joint opening, probably due to a buildup of debris. For the 1.8% RH experiment the wear was observed in both the pin joint and the hub. The pin joint diameter eventually broke in the majority of samples tested (32 times out of 50 samples) for the 1.8% case.

Using high resolution SEM, closer observation of the pin joint of the 10% RH microengine stressed to failure at 510,000 cycles reveals adhesion of the wearing surfaces (Figure 3.10.9). This was our first observation of adhered surfaces, which yielded clear evidence of the cause of failure. As indicated on the right hand side of Figure 3.10.9, the adhered region is approximately 0.7 μm long.

Transmission Electron Microscopy (TEM)

TEM was employed to attain a better understanding of the morphology and composition of the wear debris and the gear wear surface. Wear debris has been studied at 1.8% and 39% RH at 25°C, using a Phillips

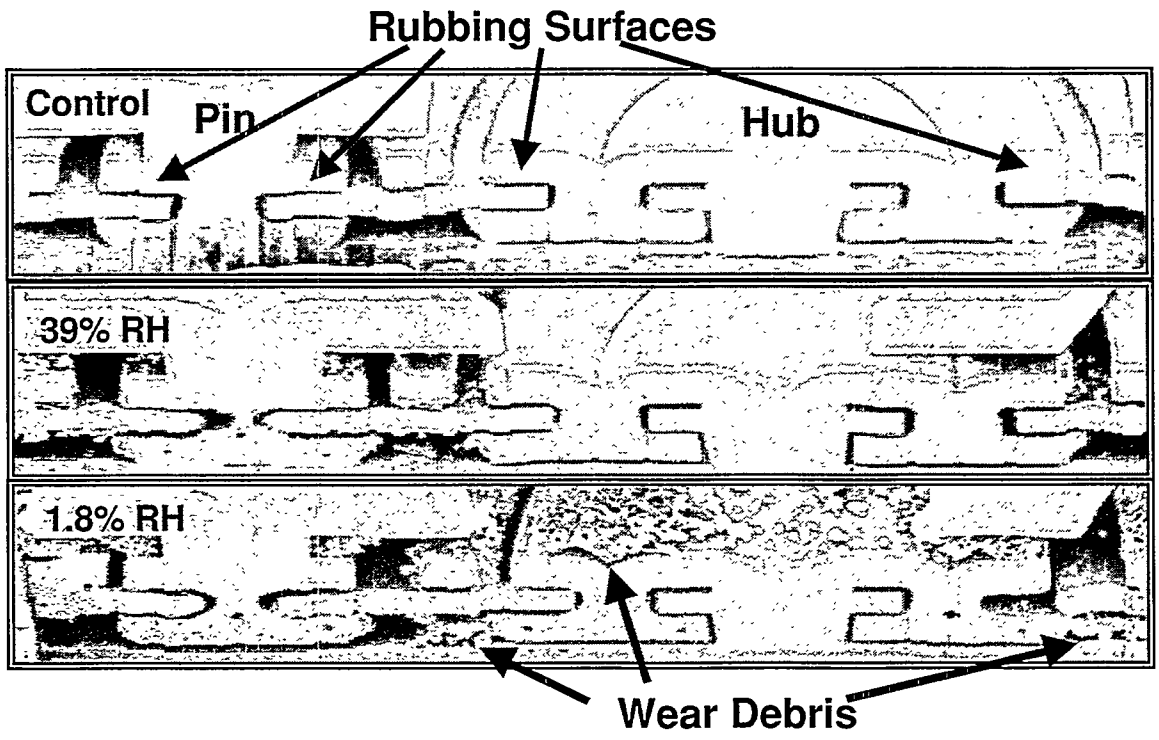

Figure 3.10.8. SEM images of the control, the 39% RH sample and the 1.8% RH sample illustrate the amount of wear debris created in each experiment. Arrows indicate the rubbing surfaces. In both stressed samples, the pin joint has been worn down from its fabricated 3-μm diameter. (FTS)

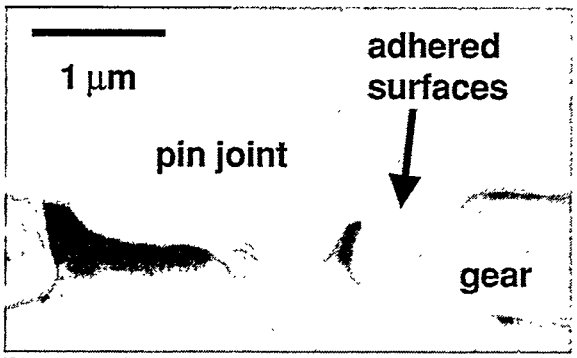

Figure 3.10.9. SEM magnified view of the pin joint region in a FIB cross section shows the area where the two surfaces adhered causing the microengine to seize. This microengine was tested at 10% RH at 25°C. (FTS)

CM30 300keV TEM with an attached energy dispersive x-ray spectroscopy (EDS) system. Plan-view samples were prepared for analysis by using polyacetate film to remove the gear from the package. The underlying gear surface thus revealed was then coated with an amorphous carbon film. These samples were transferred to a TEM grid by removal of the polyacetate film with acetone. The adhering gear and debris were used for analysis.

Gears from two microengines tested to failure at 1.8% RH were examined in plan-view. These engines accumulated 642,000 and 742,000 cycles prior to failure. As illustrated in the SEM micrograph of Figure 3.10.4, large amounts of wear debris are produced in this environment. The analysis of wear debris found outside the gear, adhering to the gear teeth, and inside etch release holes of both gears showed the debris to be either spherical or rod-like in geometry. Figure 3.10.10 shows spherical particles ranging from 100 nm to ~250 nm in diameter. Also shown are rod-like debris particles with diameters ranging from 20 to 50 nm and lengths up to 0.5 μm. The morphology of both the spherical and rod-like structures was determined by tilting the wear debris along its axis through angles of 50° to 60°. These images (not shown) did not illustrate

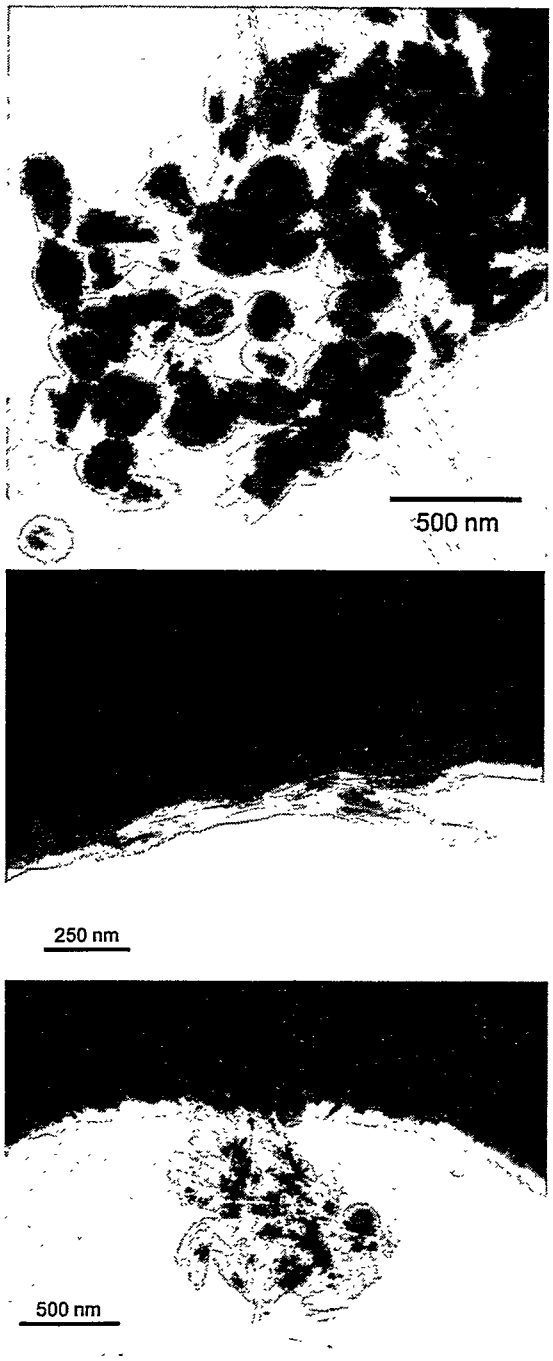

Figure 3.10.10. Spherical and rod-like debris morphologies from outside the gear (top), adhering to the gear tooth (middle) and inside an etch release hole (bottom). Note the region inside the spherical debris. (FTS)

significant deviation from either the spherical or rod-like shapes.

High resolution TEM did not indicate the formation of boundaries in larger wear particles. However, the smaller particles may have agglomerated to form the larger debris.

Identification of Wear Debris

Using TEM in conjunction with EDS, the wear debris has been identified as amorphous oxidized silicon with either spherical or rod-like morphologies. EDS spectrums taken from wear debris found outside the gear, adhering to the gear teeth, and inside etch release holes revealed high concentrations of carbon, oxygen and silicon. Diffraction patterns (Figure 3.10.11) taken from these locations showed broad ring–like patterns typical of amorphous materials. The lack of diffraction spots or speckled rings from these areas indicate no polysilicon was worn directly away from the hub or pin joint regions during testing.

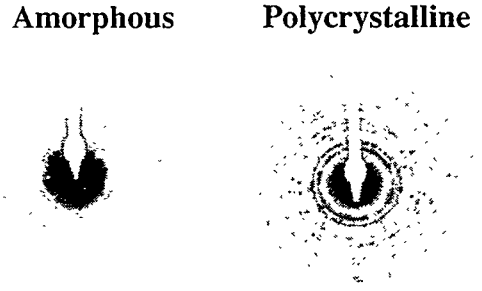

Figure 3.10.11. Diffraction patterns illustrating the amorphous structure of wear debris (left) compared to a diffraction pattern of the polysilicon gear tooth (right).

Figure 3.10.12 illustrates an EDS spectrum typical of debris analyzed from all three regions. High concentrations of carbon result from the thin carbon film used for sample preparation.

Although EDS indicated the elemental constituents of the wear debris, we could not distinguish the stoichiometry of oxidized silicon using this technique. Missing from the spectrum is any indication of fluorine from the FTS coating. The coating was only a few nanometers thick implying that the volume of FTS is quite small which would make the peak from fluorine indiscernible.

Large slivers of wear debris were observed on some of the microengines tested at 1.8% RH. TEM analysis of a sliver from a microengine stressed to 4,192,000 cycles indicated that the debris was composed of agglomerates of spherical and rod-like particles. These particles maintain their morphology even with failure cycles five to ten times greater than microengines in our previous analysis. EDS in conjunction with diffraction analysis showed the presence of oxidized silicon with **no** indication of polysilicon. The slivers of oxidized silicon were thrown out of the hub region after severe wear had occurred.

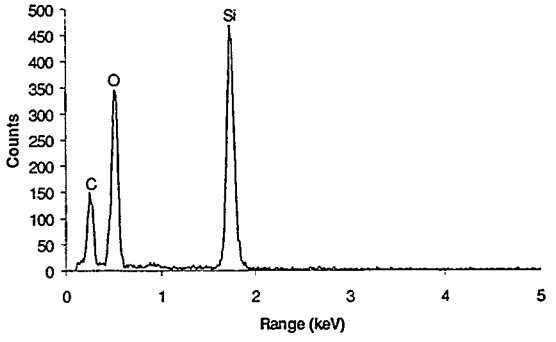

Figure 3.10.12. EDS spectra of wear debris found outside the gear. Note the strong presence of oxygen and silicon.

Discussion

Our experiments have shown that wear of the polysilicon surfaces contributed to the failure of the microengines. Performing these experiments in air with varying humidity introduced effects that will be discussed below. Chemical interactions as a result of rubbing are referred to as tribochemistry and tribochemical reactions influence friction coefficients as well as wear mechanisms and wear rates [67].

We have divided the discussion into the pertinent issues of comparison of the surface treatment methods, quantifying the volume of wear, and discussing the wear debris.

$SCCO_2$ vs. FTS

The reliability data indicated that the $SCCO_2$ drying-process produced microengines, which were less reliable because of early failure times at both high and low humidity levels. The difference could be due to differences in coefficient of friction (COF) between the two treatments. Early work by Gabriel [56] using air-dried turbines measured the dynamic COF between polysilicon and silicon near 0.3. Work by Srinivasan et al. [68] suggests that nanometer thick surface treatments can act as a boundary lubricant and reduce the dynamic COF between FTS-coated polysilicon surfaces to 0.08. The normal force in Srinivasan's experiments was roughly 5 μN and total number of cycles was in the 10^5 to 10^6 range, which is applicable to what the microengines experience.

Quantifying Wear

To estimate the volume of wear material one can either measure the volume of the wear debris or measure the missing volume in the worn device. We chose the latter and used the FIB cross sections (Figure 3.10.8) from FTS-coated devices to estimate the volume worn for the humidity levels of 1.8%, 10%, 24%, and 39% RH at 25°C.

The locations exhibiting the most wear were the hub and pin joint areas so we made our estimates there. Measurements of the diameter of worn hubs, gears, and pin joints were made. The cross sectional area was calculated and compared to the control to yield a value for worn area. This value was then multiplied by the thickness to yield the volume of the material worn away. The technique assumes that the wear is symmetrical around the hub and pin joint, which we know, is improper. Therefore, we estimated the error in the technique as ± 20% of the calculated worn area. The wear volume was normalized by the total number of cycles to failure to yield wear rate which is shown in Figure 3.10.13 as a function of percent relative humidity at 25°C.

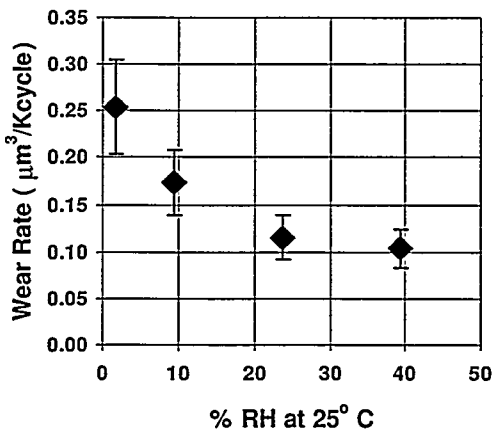

Figure 3.10.13. This plot of wear rate of FTS-coated microengines as a function of humidity shows the increase in wear rate as humidity decreases. (FTS)

The wear rate shown in Figure 3.10.13 agrees with studies of a SiC/SiC system [69] where the decrease in wear rate has been attributed to a tribochemical reaction leading to the formation of a protective film of hydrated amorphous silica. Gee et al. investigated silicon nitride sliding on silicon nitride [70] and the main mechanism of wear was the tribochemical oxidation of the silicon nitride to form silicon oxide. The wear rate increased in drier conditions in the silicon nitride case also.

For the case of polysilicon sliding on polysilicon, Mizuhara and Hsu [71] reported the formation of surface hydroxides which may protect the surface from additional wear at high humidity. In this case, the mechanical wear produced dangling silicon bonds. Water reacted with this surface to form Si-OH and Si-H. Zanoria et al. [72]

also reported that the rubbing-enhanced reaction of Si with water vapor generated Si-OH groups. The mechanism of Si → SiOH → SiO_2 → hydrated SiO_2 provided a lubricating film to protect the surface [73].

We believe that the humidity promotes hydration of the silicon surface, which provides lubrication for our rubbing surfaces.

Wear Debris Formation

Wear debris typically forms when asperities from the sliding surfaces contact and break [74]. The localized temperature at the asperity (flash temperature) was expected to elevate. Whether that temperature was high enough to accelerate oxide growth is uncertain. Because of the large presence of oxidized silicon and the absence of crystalline polysilicon in the debris, we conclude that rubbing and reaction with the environment already oxidized the material removed by wear. The broken oxidized silicon asperities could then agglomerate into larger pieces throughout the cycling of the gear, forming spherical and rod-like debris. The formation of cylindrical sliding wear debris on silicon in humid conditions and elevated temperatures in macro-scale wear experiments has been observed [23].

The wear debris from higher humidity tests formed an elongated stringy agglomeration. The lower humidity experiments produced wear debris that was more particulate.

Conclusions

We have shown that the amount of wear debris generated in sliding micromachined polysilicon surfaces is a function of the humidity in an air environment. As the humidity decreases, the volume of wear debris generated increases. For the higher humidity levels, the formation of surface hydroxides may act as a lubricant resulting in lower amounts of wear debris. At lower levels of humidity, 1.8% and 10% RH, formation of hydroxides is reduced, resulting in large amounts of wear debris.

The dominant failure mechanism has been identified as wear. The major effects of the wear process were that either the pin joint wore out causing the linkage arm to break free of the gear or the accumulation of wear debris caused mechanical interference which seized the microengine. The wear debris has been identified as amorphous oxidized silicon, both in small and large agglomerates. **No** polysilicon was observed in any portion of the wear debris.

The FTS treatment process produced microengines that were more reliable than microengines with the $SCCO_2$ treatment, which can be attributed to the FTS film acting as a lubricant.

[53] T. Maudie, "Testing Requirements and Reliability Issues Encountered with Micromachined Structures," *Proceedings Of 2nd International Conference on Microstructures and Microfabricated Systems,* **95-27**, 1995, pp. 223-230.

[54] T. Maudie, D. J. Monk, D. Zehrbach, and D. Stanerson, "Sensor Media Compatibility: Issues and Answers," *Proceedings of Sensors Expo,* Anaheim, CA, 1996, pp. 215-229.

[55] Douglass, M. R., "Lifetime Estimates and Unique Failure Mechanisms of the Digital Micromirror Device (DMD)," *IEEE International Reliability Physics Symposium Proceedings,* Reno, NV, 1998, pp. 9-16.

[56] K. J. Gabriel, F. Behi, and R. Mahadevan, "In situ Friction and Wear Measurements in Integrated Polysilicon Mechanisms," *Sensors and Actuators,* **A21-A23**, 1990, pp. 184-188.

[57] M. Mehregany, K. J. Gabriel, and W. S. N. Trimmer, "Integrated fabrication of polysilicon mechanisms," *IEEE Trans.*

Electron Devices, **ED-35**, 1999, pp. 719-723.

[58] R. Maboudian and R. T. Howe, "Critical Review: Adhesion in surface micromechanic structures," *Journal Vac. Sci. Technol.,* **B 15(1)**, Jan/Feb 1997, pp. 1-20.

[59] R. Maboudian and R. T. Howe, "Stiction reduction processes for surface micromachines," *Tribology Letters,* **3**, 1997, pp. 215-221.

[60] M. R. Houston, R. T. Howe, and R. Maboudian, *in 8th Int. Conf. On Solid-State Sensors and Actuators (Transducers '95) and Eurosensors IX,* **Vol.1** Stockholm, June 1995, pp. 210-213.

[61] R. L. Alley, R. T. Howe, and K. Komvopoulos, *Proceedings of the IEEE Solid-State Sensor and Actuator Workshop,* Hilton Head, SC, 1992, pp. 202-207.

[62] G. T. Mulhern, D. S. Soane, and R. T. Howe, *in Proc. 7th Int. Conf. on Solid-State Sensors and Actuators (Transducers '93),* Yokohama, June 1993, pp.296-299.

[63] E. J. Garcia and J. J. Sniegowski, "Surface micromachined microengine", Sensors and Actuators A, **Vol. 48**, 1995, pp. 203-214.

[64] D. M. Tanner, N. F. Smith, D. J. Bowman, W. P. Eaton, K. A. Peterson, " First Reliability Test of a Surface Micromachined Microengine Using SHiMMeR," *Proceedings SPIE Symposium on Micromachining and Microfabrication,* **Vol. 3224**, Austin, 1997, pp 14-23.

[65] Paul A. Tobias and David Trindade, *Applied Reliability,* New York, Van Nostrand Reinhold, 1986, ch. 5, pp. 93-101.

[66] S. L. Miller, M. S. Rodgers, G. LaVigne, J. J. Sniegowski, P. Clews, D. M. Tanner, K. A. Peterson, "Failure Modes in Surface Micromachined MicroElectroMechanical Actuators," *Proc. 1998 IEEE International Reliability Physics Symposium,* Reno, NV, 1998, pp. 17-25.

[67] T. E. Fischer and W. M. Mullins, "Ceramics, friction, and chemistry," *CHEMTECH,* **23:2** (1993), pp. 27-31.

[68] U. Srinivasan, J. D. Foster, U. Habib, R. T. Howe, R. Maboudian, D. C. Senft, and M. T. Dugger, "Lubrication of Polysilicon Micromechanisms with Self-Assembled Monolayers," *Proc. IEEE Solid-State Sensor Actuator Workshop,* Hilton Head, SC, USA, 1998, pp. 156-161.

[69] J. Takadoum, Z. Zsiga, M. Ben Rhouma, and C. Roques-Carmes, "Correlation between friction coefficient and wear mechanism of SiC/SiC system," *Journal of Material Science Letters,* **13,** 1994, pp. 474-476.

[70] M. G. Gee and D. Butterfield, "The combined effect of speed and humidity on the wear and friction of silicon nitride," *Wear,* **162-164,** 1993, pp. 234–245.

[71] K. Mizuhara and S. M. Hsu, "Tribochemical Reaction of Oxygen and Water on Silicon Surfaces," *Wear Particles,* Elsevier Science Publishers (D. Dowson et. al. Editors), 1992, pp. 323-328.

[72] E. S. Zanoria, S. Danyluk, and M. J. McNallan, "Formation of Cylindrical Sliding-Wear Debris on Silicon in Humid Conditions and Elevated Temperatures," *Tribology Transactions,* **38**, 1995, pp.721-727.

[73] M. N. Gardos, "Advantages and Limitations of Silicon as a Bearing Material for MEMS Applications," *Tribology Issues and Opportunities in MEMS,* Kluwer Academic Publishers, Netherlands, ed. by B. Bhushan, 1998, pp. 341-365.

[74] E. Rabinowicz, *Friction and Wear of Materials,* New York, John Wiley & Sons, Inc., 1995.

3.11 Storage life

In order to determine the reliability of dormant microengines, we started a set of experiments that investigated microengine functionality after storage for a period of time. We've seen an encouraging increase in lifetime by using a different die attach in packaging that does not outgas as much as the previous attach.

In experiments to determine the minimum force required to move a stuck microengine, we have observed that the required force was reduced with weekly operation of the microengines. Over time, the required force approached a minimum value, and then remained constant.

Experiments

Storage and functionality

We selected microengines from lot TP122 module 8 (section 2.2) which consists of three microengines and one gearless microengine. The microengines were screened for functionality at a speed of 1 Hz.

In October of 1997, we verified functionality of 14 microengines and then stored them in a dry-nitrogen environment. Every week the microengines were removed from the environment, tested under ambient laboratory conditions (30-40%RH), and returned to the environment.

In June of 1998, we started another test with TP122 microengines, however, these were packaged using a different die attach. Eighteen microengines were stored in the 0% RH nitrogen environment and seventeen were stored in a 60% RH nitrogen environment.

In September of 1999, we started yet another four more tests with TP122 microengines using the newer die attach. To investigate whether weekly stimulation might free up a stuck device, longer-term tests were started. These tests would check functionality only once a month, once every three months, once every six months, and once every year.

Minimum force

The purpose of the experiment was to determine the minimum force required to actuate freshly released microengines. A small force was used first and the force was gradually increased until the drive gear rotated fully. The microengines were never exposed to forces greater than the required minimum for actuation. The hope was to see a relationship between the minimum actuation force and storage time. Our suspicion was that the actuation force would increase with storage time if a degradation phenomenon was occurring. With this information, we would be able to predict the storage life of the devices from initial measurements.

Five microengines from lot TP122 module 8 were stored in a dry-nitrogen environment (less than 0.4% RH, the minimum of our chilled-mirror system) and 4 were stored in a 60% RH nitrogen environment.

Drive signal parameters

In order to measure the minimum actuation voltage, changes to the rotation equations were necessary. The typical drive signal equations were originally developed by Miller et al. [75] and are also detailed in section 1.7 of this report.

We wanted to calculate the forces that an engine would see while it was stuck. We did this by first neglecting all dynamic terms for this static case. The ratio of the dynamic terms to the static terms at low frequencies was 10^{-4} to 10^{-5}, which is negligible. With this modification, the static drive equations become:

$$V_x^2(\theta(t)) = \frac{1}{\gamma}\frac{kr}{a}\left(\begin{array}{l}\left(\frac{F_r}{kr}+\gamma^2\right)\sin(\theta)\\ +\frac{F_l}{kr}\cos(\theta)\end{array}\right) \quad (1)$$

$$V_y^2(\theta(t)) = \frac{kr}{a}\left(\begin{array}{l}1-\left(\frac{F_r}{kr}+1\right)\cos(\theta)\\ +\frac{F_l}{kr}\sin(\theta)\end{array}\right) \quad (2)$$

An algorithm was created to solve the equation for all the voltage pair combinations and record the highest force obtained for each angle increment. Several methods were used to calculate the forces to check for accuracy. There is not currently a good method for measuring force in the μN range, which constrains us to calculate the forces based on assumptions of the engine's geometry and friction.

A new software program, Micro Step Driver, was written that uses the static equations to operate the engines, and can be indexed through the rotation of the drive gear like a stepper motor. This is useful in studying the nuances of the engine's rotation. By stepping the microengine, we have good control of gear location and applied drive voltages. If an engine was sticking at a certain angle, it could be indexed around, then given a higher force value at that angle until the engine breaks free. By using this method, we can begin to quantify the amount of force required to free the stuck engine. We were limited to the maximum voltages generated by the amplifier boards.

Figure 3.11.1 is a screen shot of the front panel for Micro Step Driver. Using this

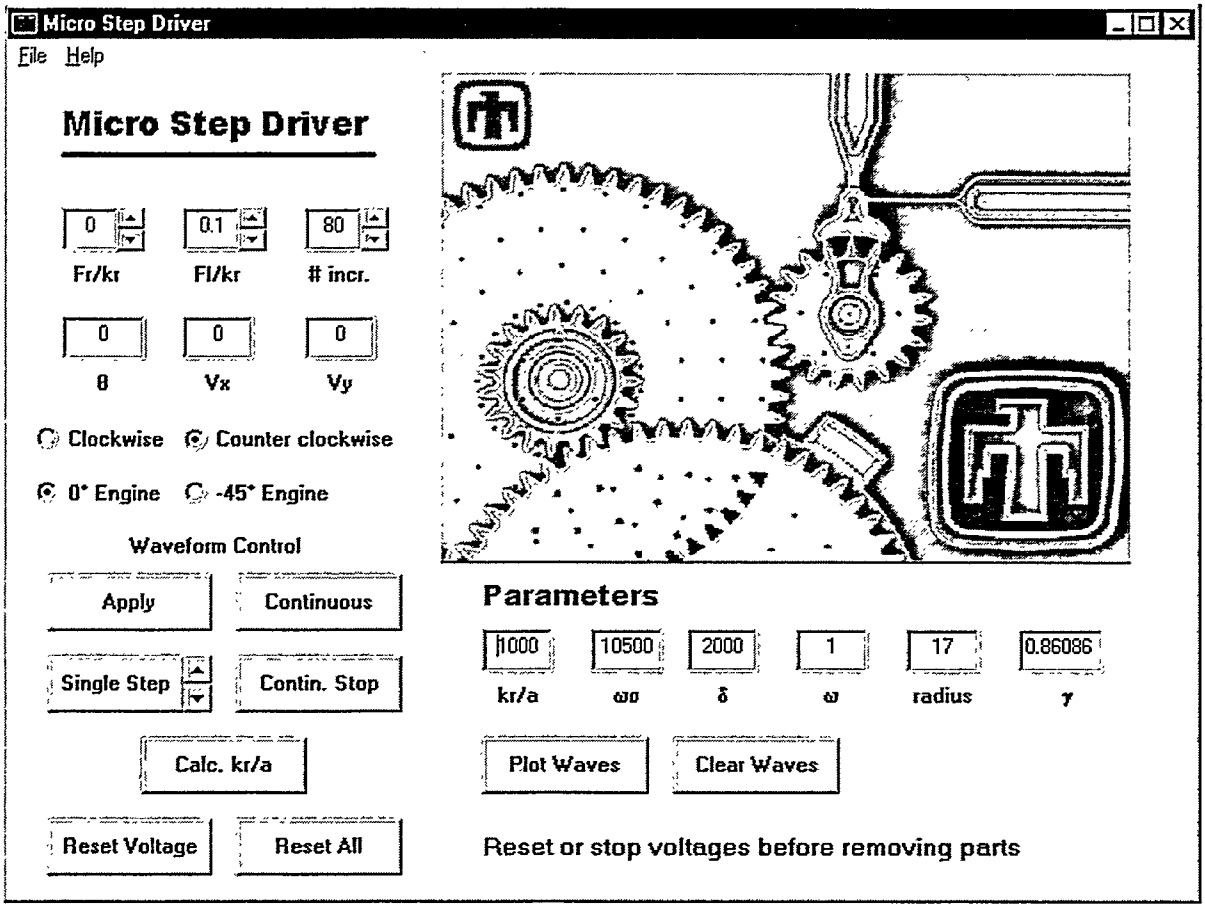

Figure 3.11.1. This screen shot of the Micro Step Driver shows all the adjustable parameters and the waveform control options.

program, it is possible to single step, run continuous, alter parameters, jump immediately to a given angle of rotation, and view the waveforms. This program was designed for the static or quasi-static regime by neglecting dynamic effects. It should not be used at frequencies above 5 Hz.

Results

Storage life functionality

The results from all of the experiments can be presented in one graph shown as Figure 3.11.2. The longest running experiment has lost the majority of microengines. It is specified as 'old' in the graph to signify the use of the older die attach material. The median time to failure is 400 days (1.1 year), which is not acceptable for most applications.

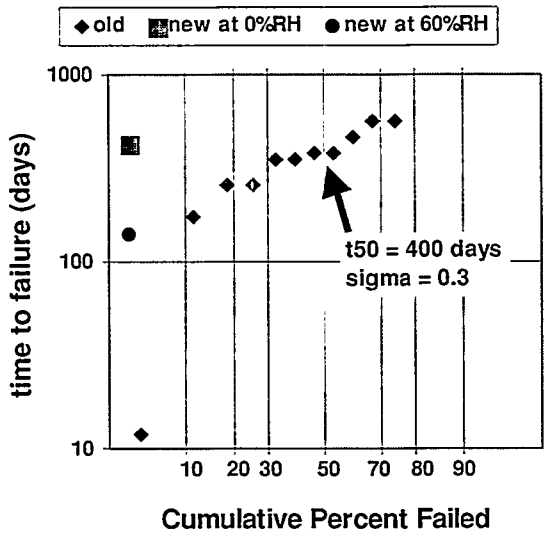

Figure 3.11.2. The failure time plot shows the median failure time of the old die attach to be 400 days. Also shown on the plot are the single failures of the new die attach at low and high humidity.

There has only been one failure in both 'new' die-attach cases of low and high humidity. There is no way to accurately predict a time to failure for the new die-attach cases. However, a worst case can be predicted if we assume that these first failures are the beginning of the distribution and assume a value for the shape parameter, σ. Both of these assumptions have faults. If the first failure of the new die-attach cases were outside the main distribution (early defect) as in the old die-attach case, then the prediction would be lower than the actual value. In previous experimentation with the microengine, we have observed wear as our failure mechanism and shape parameters ranging from 0.3 to 0.4. The shape parameter may be different for the failure mechanism associated with adhesion in dormant microengines. The following table shows the predictions of median lifetime using the range of shape parameters from wear failures.

Table 3.11.1. These predictions of median time to failure were calculated using assumed shape parameters.

σ	t_{50} (yr) (0%RH)	t_{50} (yr) (60%RH)
0.3	4.1	1.3
0.4	6.2	4.7

From the predictions in the table, it appears that the dry storage is better than wet storage. We may also see four to six times improvements in median lifetime using the new die attach. However, these predictions are highly suspect until much more data is available.

In the monthly testing of microengines, there have been no failures after the first three months. Based on the weekly test with the newer die attach, we would not expect a failure before several hundred days unless the failure mechanism is different.

Minimum force

After eight weeks of the minimum actuation force test, we can see the initial results and trends. The data from both 60% RH (WET) and 0% RH (DRY) are shown in Figures 3.11.3 and 3.11.4. In the graphs, minimum actuation voltage was plotted for

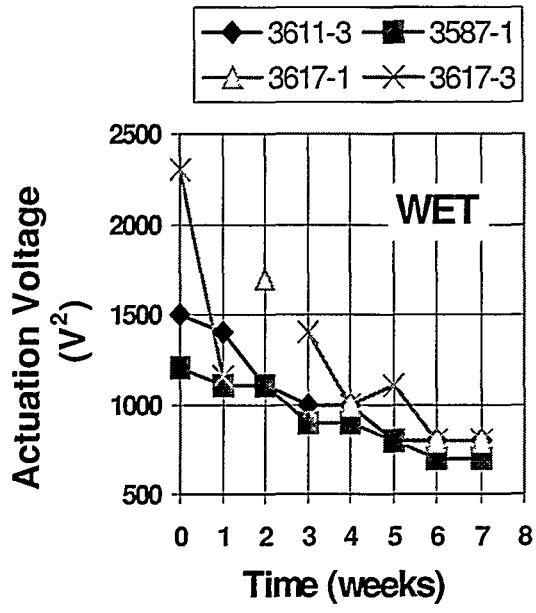

Figure 3.11.3. The actuation voltage needed to just barely move the microengine through a full rotation is plotted against the weekly intervals. These microengines were stored in a wet nitrogen environment.

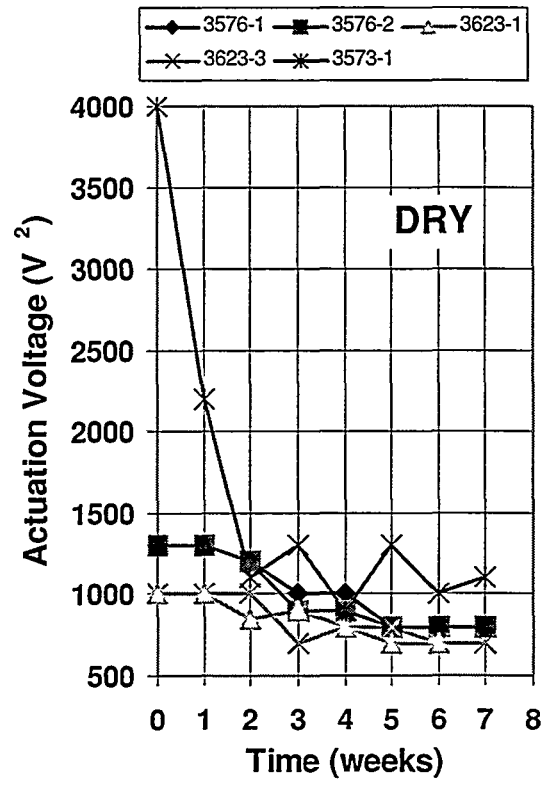

Figure 3.11.4. The actuation voltage needed to just barely move the microengine through a full rotation is plotted against the weekly intervals. These microengines were stored in a dry nitrogen environment.

each weekly inspection. In this case, the engines were characterized with force values $F_l = F_r = 0$, and kr/a was varied to achieve different voltages. This method used only one parameter (kr/a) to change the amplitude of the drive signals. The parameter was increased in steps until the microengine rotated freely and that value was plotted. The force is proportional to this minimum actuation voltage squared, but we were unable to calculate the magnitude due to unknown frictional forces and angle uncertainties. (Note: This is **not** standard operation where kr/a is a constant. For standard operation in our storage life tests, we typically set $F_r = 0$ and $F_l/kr = 0.3$.)

In both cases, we see some engines that require higher voltages initially, and then fall in line with the others with time. We also see engines that oscillate from a high value to a low from week to week. The actuator voltage increments were 100 V^2 implying that these oscillations were significant. There were microengines that showed intermittent operation (3617-1 and 3617-3, note the missing data points and connecting lines in the figure). They would work perfectly one week, then rock the next week, and then work the following week.

The results from the minimum force versus time experiment were contrary to the assumptions of how these microengines fail during storage. It was assumed that surface forces would cause the rubbing surfaces of the drive gear to stick. This type of effect has been seen on a few microengines that have not been run for some time. However, it was thought that the stiction force would grow in magnitude over time and the minimum required force for actuation would increase.

Current results after eight weeks of testing indicate that the actuation forces have

leveled off over time from initially high values. This looks like the "break in" phenomenon that we frequently see in macrosystems, for example an automobile engine.

Conclusions

There is still much more to be done in determining the reliability of dormant microengines. We have made a start, by showing that the die attach used in packaging has an effect. The new die attach case has a highly speculative "worst case" median time of failure of 4.1 years which is an encouraging improvement over 1.1 years. The wet storage may be worse than the dry storage. More failures must be observed over time before we can make valid predictions.

The true advances in the dormancy issue will come with an understanding of the physics of failure. Once the mechanism is identified then we can determine a method to accelerate the failure. This is the one case where an acceleration parameter is crucial, for we do not have the time to perform experiments for many years to verify dormant functionality.

---

[75] S. L. Miller, J. J. Sniegowski, G. LaVigne, and P. J. McWhorter, "Friction in Surface Micromachined Microengines", *Proc. SPIE Smart Electronics and MEMS*, **Vol. 2722**, p. 197-204(Feb. 1996).

3.12 Friction device and environments

To quantify friction in micromachine contacts and examine debris generation as a function of environment, a friction structure was operated in dry and humid environments. This structure brings sidewall surfaces into contact in pure sliding, and is designed to allow both of the contacting surfaces to be examined after testing. Tests were performed in dry and humid air, and nitrogen. The friction coefficient was slightly higher in dry environments than humid environments, but debris generation was very different in dry versus wet conditions. Devices that were run at 40% relative humidity generated large amounts of debris in $5x10^5$ cycles, while those run in dry conditions exhibited very low debris generation.

This result is a contradiction of what was observed in section 3.10 with experiments on the microengine. It is possible that three-body wear effects caused by trapped debris in the microengine contributed to the large volume of debris. Additionally, the wear rate is influenced by contact pressure and the local contact pressure of the friction device was much higher than the microengine.

Introduction

Major progress has been made with this project in examination of SMM device failure mechanisms. Tests of the Sandia microengine have suggested design modifications to improve the durability of devices, and explored effects of various environments on device performance. One area that is difficult to explore with complex devices such as the Sandia microengine is friction forces at contact surfaces. Dynamic analysis of the microengine can yield information on the overall friction forces, but the presence of many moving interfaces and the complex geometry of surfaces makes detailed knowledge of the contact conditions at a specific interface impossible. The sidewall friction structure was designed to permit quantitative measurement of friction forces and to simplify the contact geometry so that observations could be associated with a known contact pressure in an isolated region of the surface. This device can be used to examine the performance of surface treatments, effects of environment, contact pressure, interfacial velocity, etc. The main limitation of the experimental system is that quantification of friction requires a large amount of image acquisition and processing, and can not yet be performed in parallel for multiple devices. For the purpose of the present work, we ran several friction devices in dry and humid air, as well as dry and humid nitrogen. Image data was acquired for friction measurement, and the contact surfaces were examined with SEM to compare debris evolution characteristics in the different environments.

Experiment Description

Sidewall Friction Device

A portion of the mask set used to create the sidewall friction device is shown in Figure 3.12.1. The device consists of two or-

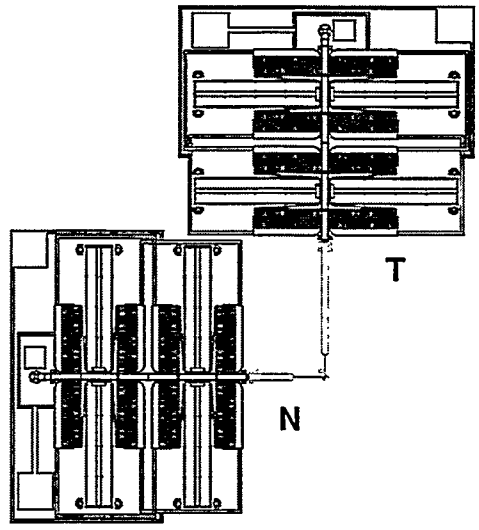

Figure 3.12.1. The sidewall friction device consists of two comb actuators (labeled N and T) connected to a movable beam.

thogonal electrostatic comb actuators connected to a movable beam. The beam is constructed of polysilicon layer 2, and is suspended above the substrate by the folded spring suspensions on the comb actuators. A post is formed by etching through sacrificial oxide layers 1 and 2 so that a polysilicon layer 3 deposition forms a structure which is anchored to the substrate and has a cylindrical geometry facing the beam. A SEM picture of the beam and post in their rest positions is shown in Figure 3.12.2. The device is actuated by using a DC voltage on the 'N' comb to bring the beam into contact with the post, and then applying a waveform to the 'T' comb to slide the beam against the post.

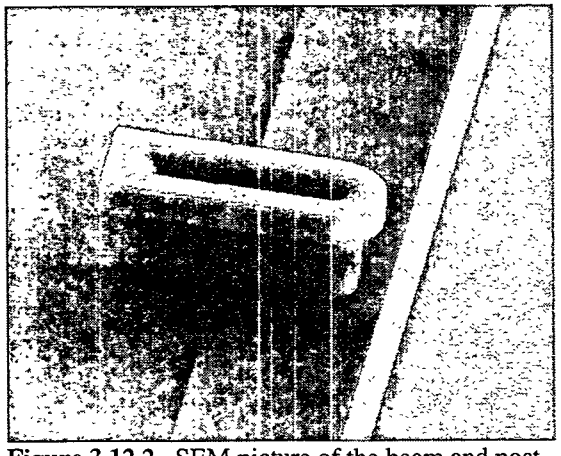

Figure 3.12.2. SEM picture of the beam and post in the sidewall friction device. The beam is 2 μm wide and the radius of curvature of the cylindrical face of the post is 2 μm.

Obtaining Displacement Data

The simplest waveform used to oscillate the beam against the post is a square wave, and this waveform was used in the experiments described here. Using a square wave, we are interested in the maximum amplitude of the beam motion for a given voltage (force) applied to the 'T' comb. The time sequence of signals to the device is illustrated schematically in Figure 3.12.3. The signal to the 'N' comb is a constant DC voltage in this experiment, as shown by the "load" signal in the figure. The square wave to the 'T' comb is also shown. To obtain displacement, a strobe light is fired before the voltage change (as indicated in Figure 3.12.3), and an image is captured of the position of the beam at this point in time. This process is repeated for several successive cycles. Immediately following image capture at this phase, the strobe is flashed and images captured at a position 180 degrees out of phase with the first measurement, for the same number of measurements. A sample of the images captured with the optical microscope, strobe, CCD camera and frame grabber is shown in Figure 3.12.4. The im-

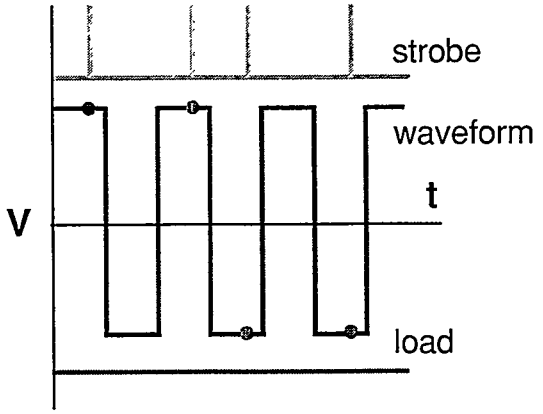

Figure 3.12.3. Schematic representation of the relationship between various signals applied to the sidewall device to obtain displacement versus time while sliding.

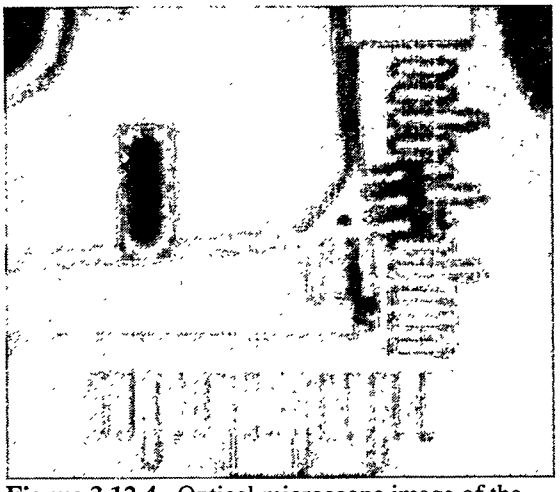

Figure 3.12.4. Optical microscope image of the post area of the sidewall device, acquired by flashing a strobe and storing a frame of image data.

ages acquired during an experiment are stored to a folder along with an index file, which contains the elapsed time and file name for each image file that was acquired. The contents of this folder are then processed using a macro in an image-processing program (Optimas version 6.2, by Media Cybernetics). The macro locates the post and the dot at the end of the beam for each image, and calculates the relative X and Y position coordinates of each. A new text file is created by the macro, which contains the time, image file name, and position of the dot relative to the post for each image. This displacement as a function of time information is reduced further to yield forces as a function of time.

Converting Displacement to Force

Equilibrating the force exerted by an electrostatic comb drive and the force required to bend the comb spring suspensions and the cantilever beam yields

$$F_C = \frac{\eta \varepsilon_0 h}{g} V^2 = (k_c + k_b)\delta \qquad (3.12.1)$$

where n is the number of fingers, ε_0 is the dielectric constant, h is the height of the fingers, g is the gap between fingers, V is the relative voltage between the opposing teeth of the comb, k_c is the stiffness of the comb suspension springs, k_b is the stiffness of the beam in bending, and δ is the displacement of the comb from its rest position. Equation (3.12.1) indicates that a plot of comb displacement versus the square of applied voltage should yield a line of slope equal to

$$\frac{\eta \varepsilon_0 h}{g(k_c + k_b)} = \frac{a}{(k_c + k_b)} = \Delta \qquad (3.12.2)$$

The calibration process prior to performing friction measurements consists of measuring the slope of displacement versus voltage for each comb actuator, and the displacement amplitude in the absence of contact between the beam and the post, δ_0. Therefore, the comb force may be expressed as

$$F_c = V^2(k_c + k_b)\Delta \qquad (3.12.3)$$

If we now use the notation k_c^T to refer to the stiffness of the comb springs for the 'T' actuator, Δ^T the slope of displacement versus voltage squared for the 'T' actuator, and so on, the normal force exerted by the 'N' comb may be expressed as

$$F_N = (V^N)^2(k_c^N + k_b^T)\Delta^N \qquad (3.12.4)$$

A force balance on the device when the beam is in contact with the post, compared to a force balance in the absence of contact, gives the friction drag force f_d

$$f_d = (k_c^T + k_b^N)(\delta_0 - \delta)^T \qquad (3.12.5)$$

The reaction force between the beam and the post, in response to the force exerted by the 'N' comb, is simply

$$F_R = F_N \frac{l}{l_1} \qquad (3.12.6)$$

where l is the length of the beam at the end of the 'T' comb, and l_1 is the distance between the beam base and the point where the post makes contact. The friction coefficient μ is then f_d/F_R, or

$$\mu = \frac{f_d}{F_R} = \frac{l_1(k_c^T + k_b^N)(\delta_0 - \delta)^T}{l(k_c^N + k_b^T)(V^N)^2\Delta^N} \qquad (3.12.7)$$

In this expression, all parameters are measured in the experiment except the dimensions associated with the stiffness terms (k_b and k_c) and the length associated with where the beam contacts the post (l_1). From beam theory, stiffness $k=3EI/l^3$ where moment of

inertia $I=bh^3/12$. In the latter relationship, b is the thickness of the polysilicon film that makes up the beam element, and h is the width of the beam element in the plane of the film and parallel to the direction in which it is deflected. The main sources of error in friction coefficient are therefore determination of these beam dimensions, particularly h which is cubed in the expression for the moment of the beam.

Environmental Testing Conditions

Friction structures were coated with perfluorodecyltrichlorosilane (PFTS) and packaged according to procedures described elsewhere in this report for Sandia microengines. Packaged parts were tested in the single package environmental cell described in section 1.5. Ambient atmospheric pressure was 12.5 psia, and ambient temperature was 25ºC. Dry air or nitrogen was supplied to a manifold at 10 psig, and flow meters controlled the flow of this supply gas to a desiccant column or a deionized water column. Gas exiting from these columns was mixed to generate the desired water vapor concentration.

Experiments were performed on friction devices run in dry air, dry nitrogen, humid air, and humid nitrogen. The dry environments contained 1 % relative humidity (370 ppmv) or less, and the wet environments contained 40 % relative humidity (15,000 ppmv). Contact force was typically 20 μN, which is near the low end of the range of forces that can be accurately measured with the present device geometry. Devices were run at 100 Hz for approximately $5x10^5$ total accumulated cycles. The sliding distance was typically 30-40 μm per cycle (twice the track length of 15-20 μm). Table 3.12.1 contains the device numbers used for these experiments, and the environments in which they were run. The suffix after the serial number indicates which of the four devices on the module were used for the test.

Table 3.12.1. Environmental test conditions for friction device

Device	Environment
2988-2	dry air
2993-2	dry air
2984-2	dry nitrogen
3013-1	dry nitrogen
2988-1	40% RH air
3010-1	40% RH air
3010-2	40% RH air
3013-2	40% RH nitrogen
3015-1	40% RH nitrogen
3015-2	40% RH nitrogen

Results and Discussion

Friction Coefficient

A sample displacement versus time plot for a device run in dry air is shown in Figure 3.12.5. The figure shows the relative position of the "dot" on the beam as a function of time during the test. Larger displacement amplitude corresponds to smaller friction coefficient, and a small run-in portion can be seen at the beginning of the test where the friction coefficient gradually increases up to $1x10^5$ cycles, resulting in smaller displacement amplitude. The friction coefficient calculated at the end of the test, where displacement remains constant, is 0.06 in this

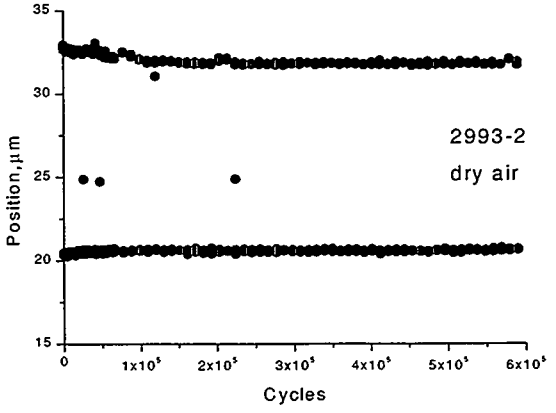

Figure 3.12.5. This graph shows the relative position of the beam as a function of cycles or time during the test.

environment. This is in good agreement with Srinivasan et. al. [76], where a friction coefficient of 0.08 was measured between PFTS-treated planar surfaces in air. Frictional behavior in humid air and humid nitrogen was similar (μ~0.02 near the end of the $5x10^5$ cycle test), although the displacement did not remain uniform over the course of the test. In humid environments, devices would begin to stick at approximately 10^5 cycles. The device could usually be made to continue operating by briefly removing and reapplying the normal load, but would begin to stick again shortly after reapplying the load. Accumulation of material could be observed by optical microscopy in the contact region of the beam in humid environments, at the ends of the contact area. No such accumulation was observed for tests run in dry conditions. This contradiction with the experiments in section 3.10 is addressed in the discussion of wear behavior.

Wear Behavior

Scanning electron microscope examination of the worn surfaces from devices tested in dry air revealed very little damage or debris accumulation. The contact region of the beam from a test in dry air is shown in Figure 3.12.6. A small amount of debris accumulation can be seen on the top of the beam, but very little damage has occurred to the beam surface. In contrast, the worn surface of a beam from a test in humid air is shown in Figure 3.12.7. This figure shows a large amount of wear debris generation, so much so that thinning of the beam can be seen in the image. The differences in wear behavior can be rationalized in terms of the known effect of water on the tribology of silicon ceramics. Adsorbed water can react with the surface of silicon ceramics to form a low-shear hydrated oxide layer. This layer has lower shear strength than the bulk ceramic, and acts to reduce the friction coefficient in environments containing water vapor. Since the layer has lower shear strength, higher wear rate is typically observed in environments where water vapor is present.

There are two issues that remain to be resolved as a result of this work. First, the mechanism described above would be present on unlubricated silicon surfaces. It is not yet known how the PFTS film influences this process, and what the degradation mechanisms of the coating are. Second, the results described for the friction structure are exactly opposite to those observed with a large number of Sandia microengines tested as part of this project (section 3.10). One likely explanation for the differences is that a low shear layer formed on microengine surfaces would be constrained to a large ex-

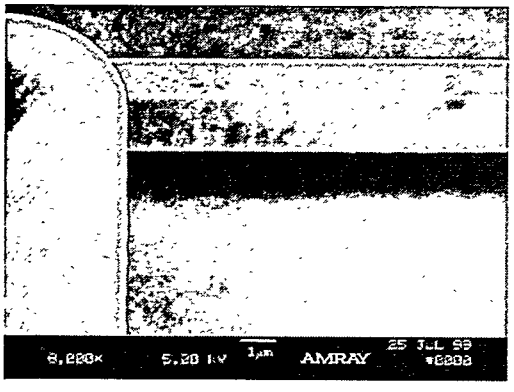

Figure 3.12.6. Worn surface of a beam from a device tested in dry air.

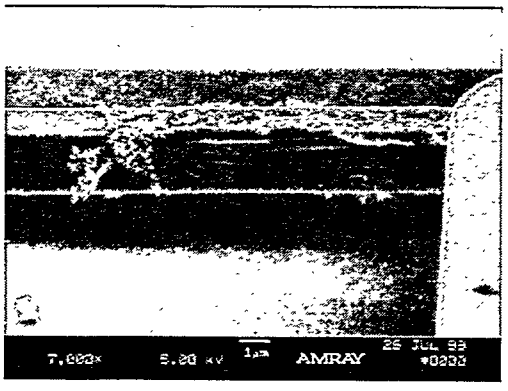

Figure 3.12.7. Worn surface of a beam from a device tested in 40% relative humidity air.

tent to remain between the sliding surfaces, due simply to the geometry of the device and location of contacting surfaces. In contrast, the friction device has a more "open" geometry that allows any debris generated to escape easily from the contact zone. This third body trapping phenomenon has been observed in macroscopic systems, where geometries that trap lubricious debris exhibit lower friction and wear compared with designs that allow debris to escape. Another possible explanation is that the local contact pressures at contact points are much higher in the friction device than the microengine, and at this pressure the low shear film cannot sustain the applied load and is removed rapidly by wear. This argument is consistent with the fact that the surfaces in contact in the friction device have roughly an order of magnitude larger RMS roughness than planar surfaces (30 nm versus about 3 nm), and at least some of the load is born by the smoother surfaces in the microengine. A more thorough discussion of the discrepancy will be published [77].

Conclusions

The sidewall friction device permits quantification of friction coefficient between sidewall surfaces in a surface micromachined device. Friction measurements on PFTS-treated structures are in agreement with those reported for a micromachined friction device having contact between planar surfaces. Wear surfaces from tests in dry and 40 % relative humidity air and nitrogen suggest that low friction and high wear rate are associated with environments containing water vapor. Slightly higher friction, but lower wear rate is exhibited in dry conditions. These observations can be explained in terms of the role of water vapor in the friction and wear of silicon ceramics, but are opposite to the observed effect of water vapor on debris generation in the Sandia microengine (see reference 77 for more discussion of the discreapancy). It is clear that contact pressure and the ability of structures to retain third bodies (wear debris) is critical to the performance of structures in various environments. These effects will be the subjects of additional research with the friction device.

[76] U. Srinivasan, J.D. Foster, U. Habib, R.T. Howe, and R. Maboudian, D.C. Senft and M.T. Dugger, Transducer Research Foundation, Inc., June 7-12 1998, Hilton Head, SC.

[77] M. T. Dugger, G. A. Poulter, and J. A. Ohlhausen, "Surface passivation for reduced friction and wear in surface-micromachined devices," Proceedings for the Fall MRS Symposium, Boston, MA, Dec. 1999, to be published.

3.13. Non-clamping actuator lifetime

Running the non-clamping actuator significantly below resonance (500 Hz) improved the lifetime of the microengine. The median time to failure was 3 x 10^9 for the majority of devices. This is a four order of magnitude improvement from the old clamping style run at 860 Hz. Running near or above resonance reduces the lifetime significantly, possibly because the drive signals do not take the dynamics of a microengine with finite tolerances into account properly.

Experiments

As discussed in section 2.3, guide dimples on the new actuator limited the lifetime of the microengines. A newer version without the dimples was fabricated (see section 2.4) and used in these experiments.

1720 Hz with guides

We stressed 19 microengines from wafer 3, module 3 from lot TP16501A at a frequency of 1720 Hz. The technique described in section 1.7 was implemented to determine the normalized spring constant and resonant frequency from a small sample of 3 microengines. The value for kr/a was 1530. The resonant frequency was 6911 radians/sec (1100 Hz). A small longitudinal force of 0.3 was used for F_l/kr.

Our observation was that these microengines were quite jerky, and the shuttles seemed to be binding excessively.

1720 Hz without guides

We stressed 33 microengines from wafer 3, module 3 from lot TP16501A at a frequency of 1720 Hz. The value for kr/a was 1530. The resonant frequency was 6911 radians/sec (1100 Hz). A small longitudinal force of 0.3 was used for F_l/kr.

500 Hz without guides

We stressed 21 microengines from wafer 11, module 4 from lot TP15701A at a frequency of 500 Hz. This is an identical module to the one used in the first two experiments. However, in this case a gearless microengine without guides was used to determine the normalized spring constant and resonant frequency from a large sample of 28 microengines. The value for kr/a was 1125. The resonant frequency was 8168 radians/sec (1300 Hz). We believe that without the guides the frictional forces were reduced, thus yielding a different value for kr/a and resonant frequency. A small longitudinal force of 0.3 was used for F_l/kr.

Results

1720 Hz with guides

Our expectation was that this non-clamping actuator would be much more reliable than the early design. However, as seen in Figure 3.13.1, the time to failure was worse than we typically observed. Notice the bimodal distribution signifying two populations. The line through the data points is our fit to the bimodal distribution. The data must be deconvoluted to analyze it properly. The straight lines in the figure represent the two populations. The lower population has a median time to failure, t_{50}, of 5.4 x 10^4 with a shape parameter, σ, of 0.2. The upper population has t_{50} equal to 3.4 x 10^5 with σ equal to 0.1.

As noted earlier, we observed binding in the guides of these actuators. We suspect that the lower population failed due to guide problems and the upper population was perhaps a different failure mode due to the difference in σ. Failure analysis has not been completed.

The guide problem prompted us to perform an identical experiment without the guides to determine the effect of the guides.

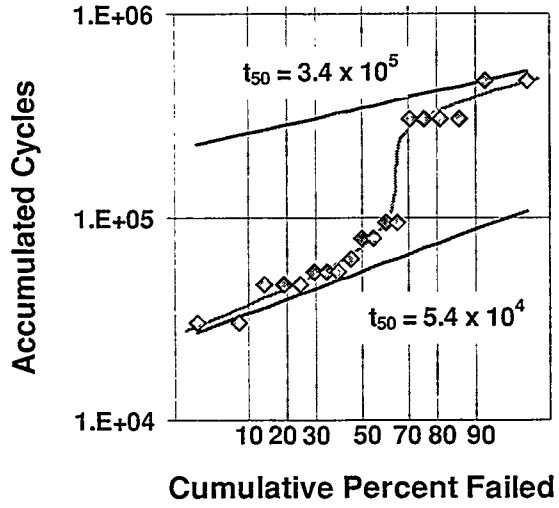

Figure 3.13.1. The data from the 1720 Hz experiment with guides was bimodal representing two populations. The median time to failure for each population is shown on the graph.

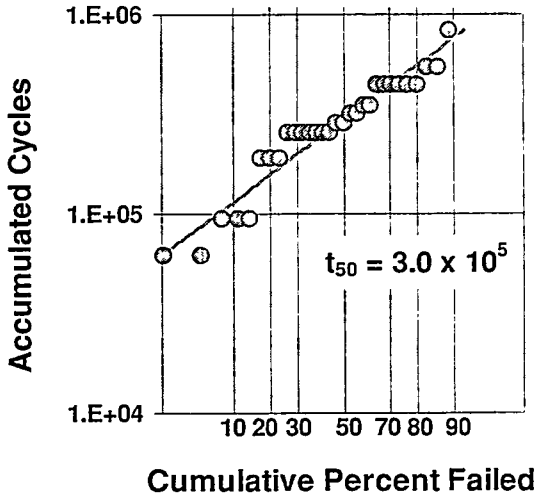

Figure 3.13.2. Most of the data from the 1720 Hz experiment without guides is shown with the median time to failure. However, three microengines continued to run until the experiment was halted. They had over two billion operational cycles.

The guides were broken off of a sample of microengines by a probe tip and the next experiment was attempted.

1720 Hz without guides

As seen in Figure 3.13.2, the bimodal distribution vanished, but the time to failure was not substantially improved. The fit to the distribution has a time to failure, t_{50}, of 3.0 x 10^5 with a shape parameter, σ, of 0.3. There were three microengines that didn't fail even after a total of over two billion accumulated cycles.

As seen throughout this report, we periodically observe some extremely long-lived microengines. We suspect that the drive signal parameters are well suited for these, which yields long life. A larger sample size typically yields more long-lived devices.

At this point we started investigating the drive signal parameters in greater detail. We found that at higher frequencies, the circular motion of the linkage arms was degraded as shown in Figure 3.6.11. This prompted us to experiment with lower frequencies.

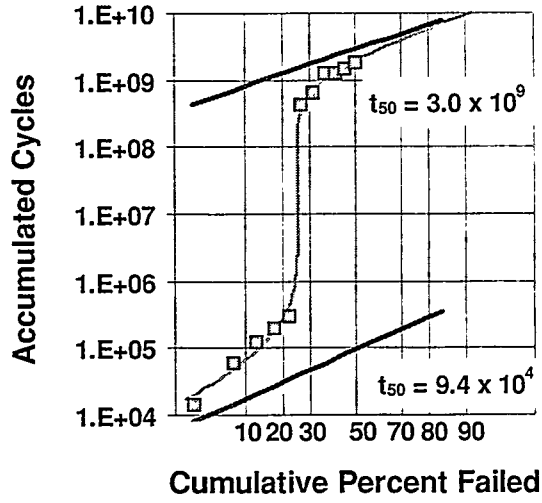

Figure 3.13.3. The first eleven failures from the 500 Hz experiment without guides show a bimodal distribution. The important aspect here is that the majority of microengines fall in the upper long-lived population.

500 Hz without guides

The data in Figure 3.13.3 shows clearly that frequency makes a substantial differ-

ence. We once again observe a bimodal distribution, however, this time the majority of microengines have run above a billion cycles. Ten microengines were still running at the time of publication.

The data must be deconvolved in the same manner to predict median time to failures for both populations. For the long-lived distribution, t_{50} was determined to be 3.0 x 10^9 cycles with σ equal to 0.4. The lower 'defect' population has t_{50} equal to 9.4 x 10^4 cycles with σ equal to 0.6.

Conclusions

Running the new actuator significantly below resonance (500 Hz) greatly improved the lifetime of the microengine. The median time to failure was a **four order of magnitude** improvement from the old clamping style run at 860 Hz.

Running the microengine at high frequency affected the lifetime. It was found that guides, a source of friction, decreased the lifetime also. We believe that running near or above resonance reduced the lifetime significantly because the drive signals do not take the dynamics of the microengine with finite tolerances into account properly.

Intentionally Left Blank

Chapter 4. Summary

4.1 Failure modes and mechanisms discovered
4.2 Reliability design rules

Intentionally Left Blank

4.1 Failure modes and mechanisms discovered

We have observed failure in both operating and non-operating cases. Certain failure modes are catastrophic and have been readily pinpointed. Others are more elusive such as the existence of intermittence in microengines, particularly those that are stored in benign environments.

Although most of our experiments were performed with microengines, we believe that these failure modes can be generalized to any MEMS device with rubbing surfaces or surfaces in close contact.

Operating

Wear

By far the major failure mechanism that we have observed in operating microengines is wear. The polysilicon rubbing surfaces in the pin joint and hub region of the microengine are most susceptible to wear. These regions are quite constrained with gaps of 0.5 microns or less. Once the wear debris is produced, it cannot escape the region and then participates in three-body wear.

Surprisingly, humidity helps to mitigate this effect by acting as a lubricant (see section 3.10 and [78]). As the humidity decreases, the amount of wear debris produced increases. The optimum region to operate a microengine for low wear was between 30 to 60 %RH at 25° C.

However, there are contradictory results as to the effect of humidity. Using the friction device, which allows escape of the debris and runs with a different contact pressure, there is less debris at low humidity.

Adhesion

Rubbing surfaces wear and typically fail by adhesion. The device no longer operates as it was designed to. In the case of the microengine, failure is defined as the inability to make a complete revolution. Some of the signs of adhesion are sticking, rocking, or seizing of microengines. Each of these will be addressed.

The behavior of the microengines as they were stressed followed a consistent pattern. Initially the microengines ran smoothly. With the accumulation of stress, the operation of the microengines became erratic at inspection frequencies, with occasional sticking followed by release. Some of the microengines would actually overcome the sticky behavior and become smooth again. Near the end of a microengines life, rotation became more erratic until the microengine failed by seizing or rocking back and forth through a small angle.

Sticking

Sticking appears to be the precursor to failures by rocking or seizing. In normal operation of the microengines at the inspection frequency of 1 Hz, some of the gears rotate very smoothly. Others have a point in the rotation where the gear sticks momentarily. As the microengine is stressed over time these sticky points may remain or disappear. We believe this to be a surface effect, either due to small asperities or a small region where the adhesive properties are different.

Rocking

This mode of failure occurs when the microengine gear cannot make a complete revolution, but rocks through an angle. There could be two possible causes: either one or more signal lines have failed or there is a sticky spot or fixed particle in the gear hub or pin joint, which impedes motion.

In some of the shock and vibration experiments, packages were cracked which shorted out signal lines. The microengines rocked in those cases until a probe assured power to the pads.

As discussed in the sticking section, asperities could prevent the gear from making a

full rotation. If the gear is near the end of life, wear debris buildup could be the culprit. Additionally, certain regions of the microengine wear out unevenly from other regions of the microengine. This preferential wearing can cause the gear to rotate in a non-circular fashion. Depending on the degree of wear in the hub or pin joint region, the pin joint can extend into the worn region and rock about that given area.

Seizing

A seized microengine is a permanent failure. The seizure point is typically in the gear hub or pin joint region. These are the regions of tighter tolerances. In a few instances, such as that shown in Figure 4.1.1, we have located the seized region. The rubbing surfaces were adhered over a small region.

However, we cannot rule out the effect of wear debris. This debris may cause the mobile portion of the gear to become wedged into the anchoring portion resulting in a loss of microengine functionality. Another possibility is the accumulation of debris in critical areas (pin joint, hub) that may cause the microengine to seize due to the excessive build up of this debris.

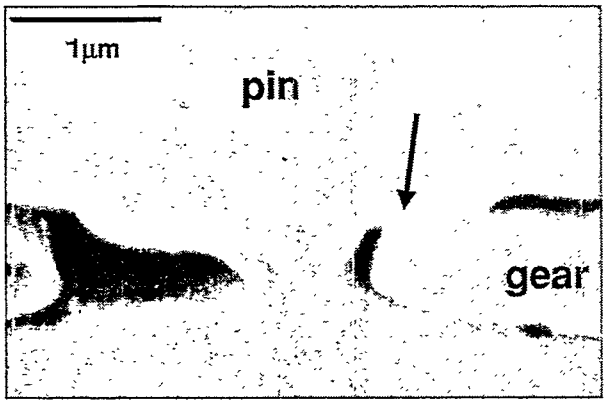

Figure 4.1.1. The arrow indicates the 0.7-μm long region of adhered surfaces.

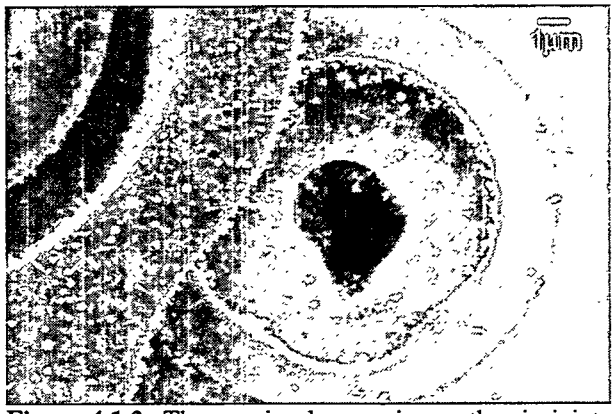

Figure 4.1.2. The noncircular wearing on the pin-joint hole was due to actuator clamping.

Actuator clamping

This is basically a design issue that was corrected in later designs. The Y actuator was found to clamp when the gear was in the upper region of its rotation [79]. This resulted in larger forces on the pin joint than expected and contributed to wear in the pin joint as seen in Figure 4.1.2 (see also, the discussion in section 3.3).

Failures above resonance speeds

Even with the removal of actuator clamping by using the new design, early lifetimes (10^5 cycles) were observed at low forces. If we run significantly below resonance, for example, 500 Hz, then lifetimes of over a billion cycles were observed for the majority of the microengines. We believe that the drive signals (see section 1.7) do not fully describe the complete dynamics near resonance and above. Hence, this mismatch induces wear in the microengine through the creation of unbalanced forces.

Particulate contamination

Particulate contamination outside the clean room environment, where performance analysis or packaging is conducted, can naturally be expected to have a serious effect on devices where small gaps and large voltages are

required. Particulate contamination has been a minor problem and typically promotes shorting of the actuators.

In shock and vibration environments, particulate contamination can be a major problem. These environments cause the particles to move and can short out working devices. Of particular concern is the edge of the die where the polysilicon layers are free to peel and crack which forms rather large debris.

Fused components

A condition that results from inadvertent contact of structural and electrical members has been observed in comb fingers. The relatively high voltages employed make arcing possible in these cases, and attachments resembling a weld can result. These attachments are occasionally small enough to be subsequently freed without extensive damage, but more often are permanent as shown in Figure 4.1.3. The use of guides has been shown to prevent this failure mode, but typically introduces more rubbing surfaces, which increases wear.

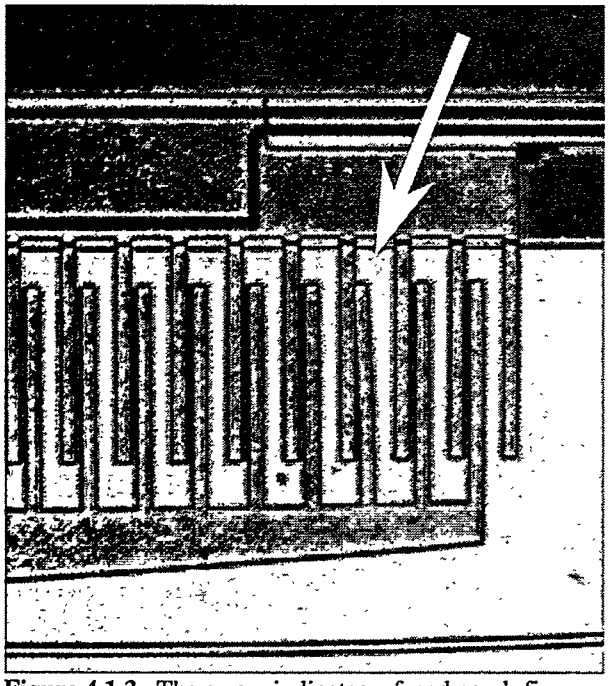

Figure 4.1.3. The arrow indicates a fused comb finger.

Non-operating

Release

A bad release process can result in failed devices. If all of the sacrificial oxide was not etched away, the devices will not work. This was rarely a problem, but could be significant on a large device if the proper number of etch release holes are not used.

Stiction

Stiction results from capillary forces that are large at these dimensions. Surface coatings that make the surface hydrophobic typically achieve stiction reduction. Alternate methods are super critical CO_2 drying or freeze sublimation.

Surface coatings utilize many chemistry processes that may or may not be well understood. Development of a consistent, repeatable, reliable process is ongoing.

Some microengines start right up after the release while others require a 'slight poke' with the manual prober to function. These microengines may be side by side on the same die. There are many unresolved issues surrounding the stiction problem.

Packaging

Functional microengines whether with surface coatings or dried, still have to make it through the sometimes harsh next step of packaging. Die-attach techniques that work well for electronics may be death to MEMS devices. The handling and oven curing can also lead to failure.

Dormancy

One of the really disturbing failure modes is that of dormancy, when these microengines fail during storage in a benign environment. Experiments have shown that the die attach used really matters (section 3.11).

There is also a pattern emerging that dry storage is better that wet (roughly 60% RH) storage. Certainly, de Boer [80] has shown that the adhesion between a polysilicon beam and the polysilicon surface increased exponentially between 30 to 90% RH.

The issue of intermittence also arises in these dormancy experiments. There have been occasions where a previous failed part begins to function again. The only difference between the two tests was time in storage.

---

[78] M. N. Gardos, "Advantages and Limitations of Silicon as a Bearing Material for MEMS Applications," *Tribology Issues and Opportunities in MEMS,* Kluwer Academic Publishers, Netherlands, ed. by B. Bhushan, 1998, pp. 341-365.

[79] S. L. Miller, M. S. Rodgers, G. LaVigne, J. J. Sniegowski, P. Clews, D. M. Tanner, K. A. Peterson, "Failure Modes in Surface Micromachined MicroElectroMechanical Actuators," *Proc. 1998 IEEE International Reliability Physics Symposium,* Reno, NV, 1998, pp. 17-25.

[80] M. P. de Boer, P. J. Clews, B. K. Smith, and T. A. Michalske, "Adhesion of Polysilicon Microbeams in Controlled Humidity Ambients," *Materials Research Society Proceedings*, Vol. 518, pp. 131-136, 1998.

4.2 Reliability design rules

In our experiments over the last three years, we have discovered some failure modes and pitfalls to avoid. The major rules to follow will be discussed here.

Prevent wear

The major operational failure mechanism was wear so any technique or design that prevents wear would produce longer life. A major step in this regard would be the development of a microscale lubricant.

Lubrication

Henck [81] studied lubricants ranging from self-assembled monolayers (SAMs), to fluids, to solid lubricants in attempts to lubricate the Digital Micromirror Device™ (DMD). He found that vapor-deposited SAMs of perfluorodecanoic carboxylic acid were the best lubricant for the DMD. However, the DMD has contacting surfaces but no rubbing surfaces as in the microengine.

For rubbing surfaces, both Senft [82] and Srinivasan et al. [83] have observed lowered coefficient of friction for SAM coated devices. The wear properties are still under investigation.

Use a little humidity

As shown in section 3.10, humidity levels of 30 to 60% RH act as a lubricant and reduce the formation of wear debris. Although low humidity devices lasted a little longer than comparable devices at high humidity, the loss of volume at low humidity produced severe wobble in the drive gear, which would degrade performance.

In practice, most MEMS devices will be sealed in hermetic packages. Once again, the need for a lubricant presents itself.

Minimize rubbing surfaces

Wear only takes place in regions where two surfaces contact due to a normal force and move in relation to one another. In the case of the microengine, the pin joint region on the drive gear was subjected to large forces making it the weak link. The hub of the drive gear also experienced these forces and the resulting wear debris caused problems. In contrast, we rarely see debris in the hub regions of larger load gears because the normal forces here are so small (see section 3.3).

Another region of rubbing surfaces in the microengine is in the shuttle guides that constrain the motion. There are four shuttle guides in each actuator as shown in Figure 4.2.1. The inner guides are also anchors for the springs. The outer guides were the ones removed to yield circular motion of the gearless microengine (section 3.3.13). We have observed wear at all locations.

The use of springs that are stiff in the orthogonal direction could prevent unwanted motion and eliminate the need for guides or at least allow for an increase in the gap, diminishing contact and wear.

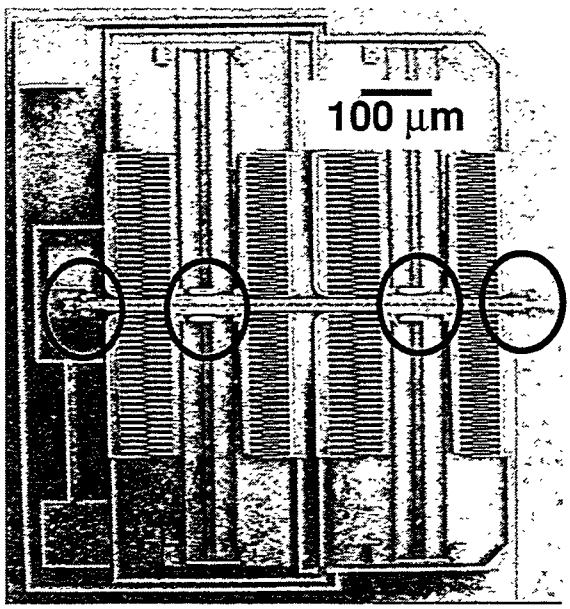

Figure 4.2.1. This image shows the location of the four shuttle guides in a typical actuator.

Eliminate dimples on shuttle clamps

Clamps, shown in Figure 4.2.2, have been used to prevent vertical (out of the plane) displacement of the shuttle mechanism in the actuator. Adding a dimple on the clamp reduces the displacement between the dimple and the moving surface below it to 0.5 microns. However, due to shuttle levitation, this provides another rubbing surface and failure mode (see section 3.4).

In order to prevent wobble, clamps with dimples on load gears have been used with no detrimental effects. An alternate method to control wobble that has met with success is to add a dimple to each gear tooth as in Figure 4.2.3.

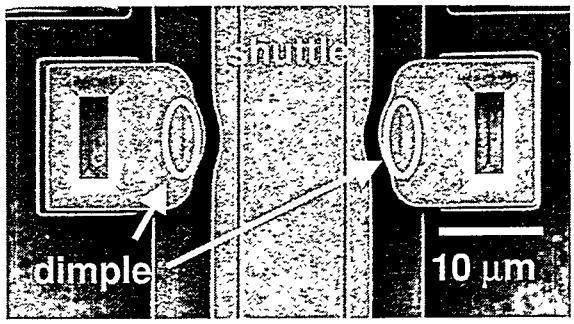

Figure 4.2.2. The SEM image of a shuttle clamp shows the location of the dimple.

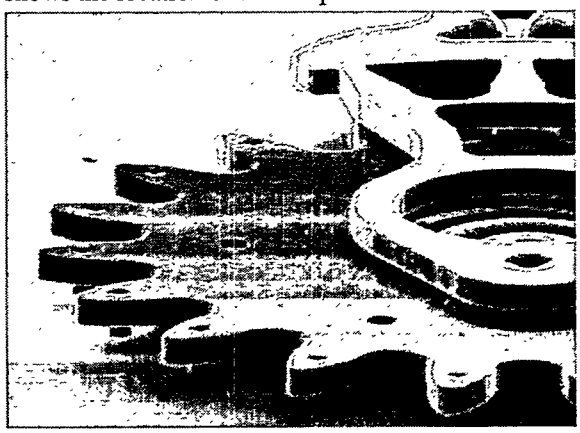
Figure 4.2.3. This high-tilt SEM image of a gear shows the dimple location on each gear tooth.

Minimize impact or rubbing force

The uncontrolled force due to a clamping actuator provided impact to the pin joint and promoted noncircular wearing (see Figure 4.1.2). Impact will produce wear debris (Figure 3.5.5) and ultimately reduce the reliability of the device. The best way to prevent impact is to design non-clamping actuators.

Additionally, well-defined and understood drive signals will reduce impact. As an example, Miller et al. [84] showed that the use of square waves to drive a microengine will reduce the number of start/stop cycles to on the order of 10. In contrast, microengines operated using model-based signals have demonstrated millions of start/stop cycles, a five order of magnitude increase in start/stop endurance.

For the microengine, it is good practice to ramp up to full speed slowly over a few cycles. This will lessen the effect of impact forces.

A reduction in the force used to move the drive gear would minimize wear. This can be achieved by using a pure tangential force with no radial force on the pin joint. The work discussed in section 3.6 described the methods to implement pure circular motion of the linkage arms. Using these methods and a lower frequency of operation, the lifetime of the non-clamping microengine was increased to billions of cycles for the majority of the samples (section 3.13).

Throw out the debris

We believe that a major contributor to failure due to wear is the result of three-body wear. This wear takes place when a debris particle gets caught between the rubbing surfaces and promotes additional wear debris. The dramatic influence of third body wear upon tribological processes is well known [85]. If the initial wear debris particle were removed from the rubbing surfaces, the devices may run longer.

Promote clean environments

After MEMS devices are released the surrounding environment can wreck havoc on

reliability. Any particulate matter can easily short out a comb finger or prevent viable operation.

The packaging environment was shown to affect the reliability of microengines (section 3.11). To promote packaging reliability, care must be taken to select the proper die attach that doesn't outgas.

Shock and vibration environments promoted movement of any debris on the surface. Of particular concern is the observed flaking of layers near the edge of the die, creating debris that may lead to failure. Figure 4.2.4 shows a large layer flake, which could easily short the comb fingers. A sealing method to prevent flaking or complete removal of these flakes will be necessary.

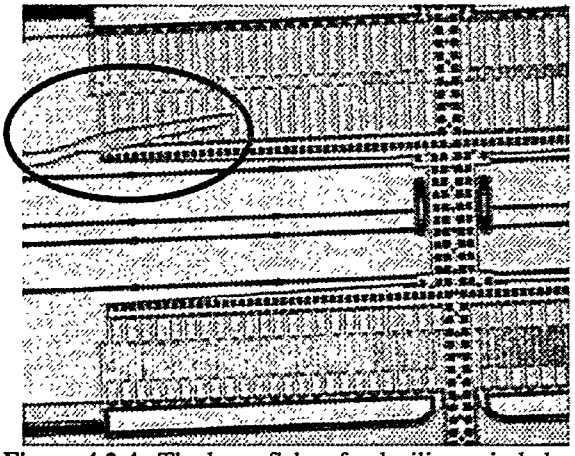

Figure 4.2.4. The large flake of polysilicon circled in this optical image could easily short the comb fingers.

Prevent shorting of voltage components

This is a case where guides or stiffer springs may be used. Springs that are compliant in their direction of motion, but stiff in other directions are needed here. As mentioned earlier, guides can be a source of rubbing surfaces, increasing wear. The use of physical stops, which prevent contact between the components, is recommended. A long structure is especially susceptible to small rotations that may cause shorting.

Anchor according to mass

In the shock environments, many of the large gears broke away from the substrate. Gears are presently fabricated with identical hubs for ease of the design. Larger gears should have proportionately larger anchors to maintain attachment.

[81] Steven A. Henck, "Lubrication of digital micromirror devices," *Tribology Letters*, **3**, (1997), pp. 239-247.

[82] D. C. Senft and M. T. Dugger, 'Friction and wear in surface micromachined tribological test devices,' *Proceedings SPIE Symposium on Micromachining and Microfabrication,* **Vol. 3224**, Austin, 1997, pp 31-38.

[83] U. Srinivasan, J. D. Foster, U. Habib, R. T. Howe, R. Maboudian, D. C. Senft, and M. T. Dugger, "Lubrication of Polysilicon Micromechanisms with Self-Assembled Monolayers," *Proc. IEEE Solid-State Sensor Actuator Workshop,* Hilton Head, SC, USA, 1998, pp. 156-161.

[84] S. L. Miller, M. S. Rodgers, G. LaVigne, J. J. Sniegowski, P. Clews, D. M. Tanner, K. A. Peterson, "Failure Modes in Surface Micromachined MicroElectroMechanical Actuators," *Proc. 1998 IEEE International Reliability Physics Symposium,* Reno, NV, 1998, pp. 17-25.

[85] Irwin L. Singer, "How Third-Body Processes Affect Friction and Wear," MRS Bulletin, Vol. 23, No. 6, June 1998.

Distribution

1	MS	0303	Michael Callahan, 15402
1		0329	David Plummer, 2100
1		0329	Fernando Bitsie, 2614
1		0329	Marcus Craig, 2614
1		0329	Ernest Garcia, 2614
1		0329	Andres Jojola, 2614
1		0329	Andrew Oliver, 2614
1		0329	Frank Peter, 2614
1		0329	Marc Polosky, 2614
1		0329	Ed Vernon, 2614
1		0333	Tom Buchheit, 1835
1		0340	Wendy Cieslak, 1832
1		0340	Michael Dugger, 1832
1		0405	Todd Jones, 12333
1		0405	Kevin Maloney, 12333
1		0405	Heather Schriner, 12333
1		0405	Keri Sobolik, 12333
1		0405	Mary Young, 12333
1		0429	John Stichman, 2100
1		0434	Jeff Everett, 12333
1		0434	Ed Fronczak, 12334
1		0455	Laura Gilliom, 6232
1		0481	Scott Holswade, 2168
1		0481	Kent Meeks, 2168
1		0481	Beth Potts, 2168
1		0482	Victor Johnson, 2161
1		0482	Shawn Kerr, 2161
1		0482	Jay Vinson, 2161
1		0492	James Cates, 12332
1		0492	Kenneth Chen, 12332
1		0492	Michael Dvorack, 12332
1		0492	Donald Lewis, 12332
1		0492	Douglas Loescher, 12332
1		0492	Ed Mauldin, 12332
1		0492	Daryl McCollister, 12332
1		0492	David Olson, 12332
1		0492	Daniel Summers, 12332
1		0492	James Wolcott, 12332
1		0523	James Harris, 1733
1		0525	Thom Fischer, 1732
1		0525	Paul Plunkett, 1734
1		0527	Paul Royer, 1731
1		0527	Fred Sexton, 1730
1		0535	Larry Dalton, 2615
1	MS	0603	Albert Owyoung,1710
1		0603	Olga Blum Spahn, 1712
1		0603	Stanley Kravitz, 1713
1		0603	Randy Shul, 1713
1		0603	Charles Sullivan, 1713
1		0603	Thomas Zipperian, 1713
1		0633	Jack Dobrian, 12363
1		0634	Sandra Chavez, 12361
1		0634	Ron Hahn, 12361
1		0635	Bob Goetsch, 12361
1		0635	Glenn Kuswa, 12365
1		0741	Sam Varnado, 6200
1		0746	Robert Cranwell, 6411
1		0829	Kathleen Diegert, 12335
1		0830	Jim Henderson, 12335
1		0830	Tom Kerschen, 12335
1		0830	Don Wright, 12335
1		0874	Carol Sumpter, 1702
1		0874	Robert Blewer, 1705
1		0874	Dave Palmer, 1716
1		0874	Paul Dressendorfer, 1726
1		0959	Kenneth Peterson, 1471
1		0972	Paul Schanwald, 5722
1		0986	Joseph Perry, 2691
1		1071	David Myers, 1703
1		1071	Ted Dellin, 1704
1		1071	Mike Knoll, 1730
1		1072	K.K. Ma, 1735
1		1072	Richard Beegle, 1737
1		1072	Frank Hewlett, 1737
1		1072	Vic Yarberry, 1737
1		1073	Wilson Barnard, 1736
1		1073	Dale Kemper, 1736
1		1073	Ronald Anderson, 1738
1		1073	Michael Daily, 1738
1		1073	George Dulleck, 1738
1		1073	Dave Peterson, 1738
1		1073	Kurt Wessendorf, 1738
1		1074	Ron Jones, 1721
1		1074	Paul Resnick, 1722
1		1077	Harry Weaver, 1720
1		1077	Linda Cecchi, 1722
1		1077	Matt Hankins, 1722
1		1078	Paul McWhorter, 1702
1		1079	David Williams, 1700
1		1080	Jim Allen, 1725

Distribution (continued):

1	MS	1080	Steve Barnes, 1725
1		1080	Maarten de Boer, 1725
1		1080	Michael Burg, 1725
1		1080	Chris Dyck, 1725
1		1080	Matt Edmonds, 1725
1		1080	Jim Fleming, 1725
1		1080	Paul Galambos, 1725
1		1080	Daniel Gutierrez, 1725
1		1080	Jay Jakubczak, 1725
1		1080	Tom Krygowski, 1725
1		1080	Siv Limary, 1725
1		1080	John McBrayer, 1725
1		1080	Nathan Masters, 1725
1		1080	Sam Miller, 1725
1		1080	Steve Montague, 1725
1		1080	Murat Okandan, 1725
1		1080	David Reyes, 1725
1		1080	Steve Rodgers, 1725
1		1080	Jeff Sniegowski, 1725
1		1080	Bevin Staple, 1725
1		1081	Duane Bowman, 1728
1		1081	Craig Carmignani, 1728
1		1081	Joseph Clement, 1728
1		1081	William Eaton, 1728
1		1081	William Filter, 1728
1		1081	Karen Helgesen, 1728
1		1081	Lloyd Irwin, 1728
25		1081	William Miller, 1728
1		1081	David Monroe, 1728
1		1081	Michael Rightley, 1728
1		1081	Norman Smith, 1728
1		1081	Scot Swanson, 1728
25		1081	Danelle Tanner, 1728
1		1081	Lila Zurzolo, 1728
1		1081	Richard Anderson, 1739
1		1081	Daniel Barton, 1739
1		1081	Paiboon Tangyunyong, 1739
1		1081	Jeremy Walraven, 1739
1		1082	Robert Mitchell, 1726
1		1082	Cathy Reber, 1726
1		1083	Jim Schwank, 1727
1		1083	Peter Winokur, 1727
1		1083	Steve Witczak, 1727
1		1084	Reid Bennett, 1723
1		1084	Scott Habermehl, 1723
1	MS	1084	Sita Mani, 1723
1		1084	Peggy Clews, 1724
1		1084	Dale Hetherington, 1724
1		1084	Patrick Nelson, 1724
1		1084	Brad Smith, 1724
1		1084	Harold Stewart, 1724
1		1084	Paul Smith, 1726
1		1137	Marge Peterson, 6534
1		1137	William Stubblefield, 6534
1		1202	Ann Campbell, 5911
1		1407	David LaVan, 1835
1		1407	Richard Salzbrenner, 1835
1		1413	Terry Michalske, 1115
1		1421	John Sullivan, 1112
1		1425	Marion Scott, 1707
1		1425	Steve Martin, 1715
1		0188	LDRD, 4001
1		9018	Central Technical Files, 8940
2		0899	Technical Library, 4916
1		0161	Patent & Lic. Office, 11500
1		0612	Review & Approval, 4912 For DOE/OSTI